Shear instabilities in shallow-water magnetohydrodynamics

Julian Mak

Submitted in accordance with the requirements for the degree of Doctor of Philosophy

The University of Leeds

Department of Applied Mathematics

July 2013

Abstract

The interaction of horizontal shear flows and magnetic fields in stably stratified layers is central to many problems in astrophysical fluid dynamics. Motions in such stratified systems, such as the solar tachocline, may be studied within the shallow-water approximation, valid when the horizontal length scales associated with the motion are long compared to the vertical scales. Shallow-water systems have the advantage that it captures the fundamental dynamics resulting from stratification, but there is no explicit dependence on the vertical co-ordinate, and is thus mathematically simpler than the continuously stratified, three-dimensional fluid equations. Here, we study the shear instability problem within the framework of shallow-water magnetohydrodynamics.

A standard linear analysis is first carried out, where we derive theorems satisfied by general basic states (growth rate bounds, semi-circle theorems, stability criteria, parity results), investigate the instabilities associated with idealised, piecewise-constant profiles (the vortex sheet and rectangular jet), and investigate the instabilities associated with two prototypical smooth profiles (hyperbolic-tangent shear-layer and Bickley jet); these are studied via analytical, numerical and asymptotic methods. The nonlinear development of the instabilities associated with the smooth profiles is then investigated numerically, focussing first on the changes to the nonlinear evolution arising from MHD effects, before investigating the differences arising from shallow-water effects. We finally investigate the interplay between MHD and shallow-water effects on the nonlinear evolution.

子曰：“學而不思則罔, 思而不學則殆”[0]

〈〈論語 · 為政〉〉

[0]“He who learns but does not think is lost; he who thinks but does not learn is in danger” – Confucius, *Analects* 2.15

Acknowledgements

First and foremost I would like to thank my supervisors, David Hughes and Stephen Griffiths, for introducing me to this interesting research topic, as well as their continued support, guidance and patience with this thesis and my academic development over the past four years. I would also like to thank my undergraduate supervisors, Djoko Wirosoetisno, Miguel Moyers-Gonzalez, and my pastoral advisor John Bolton for encouraging me to pursue PhD studies fives years ago.

I further extend my thanks to the following people for discussions and contribution that have improved parts of this thesis: Steve Tobias and Sam Hunter for discussions of the properties possessed by shallow-water systems; Eyal Heifetz for comments on the counter-propgating Rossby wave mechanism that appears in Chapter 5; Andrew Gilbert for discussions that improved Chapter 5, and for the anti-dynamo result in Chapter 7; Ben Hepworth and Laura Burgess, for a template of their nonlinear code that served as a starting point of the nonlinear code I wrote to generate the results in Chapter 6 and 7; and my examiners David Dritschel and Chris Jones for comments that clarified some technical points and improved the presentation of the thesis. I would also like to thank Pat Diamond, Nic Brummell, Pascale Garaud, as well as Yusuke Kosuga, Erica Rosenblum, Toby Wood, CJ Donnelly and other participants of the six week 2010 International Summer Institute for Modelling in Astrophysics summer programme that contributed significantly to my early academic development.

On a more personal note, I would like to thank my family, staff and student members at Leeds mathematics department, and my friends from outside the department for their continued support and encouragement during my time at Leeds.

This work was supported by the STFC doctoral training grant ST/F006934/1.

Notation

$\boldsymbol{B}_3$	three-dimensional magnetic field, $\boldsymbol{B}_3 = (b_x, b_y, b_z)$
$\boldsymbol{b}$	two-dimensional magnetic field, $\boldsymbol{b} = (b_x, b_y)$
$\boldsymbol{B}$	magnetic flux in shallow-water, $\boldsymbol{B} = (h_t b_x, h_t b_y)$
c	phase speed, $c = c_r + \mathrm{i}c_i$
F	Froude number, $F = \mathcal{U}/\sqrt{g\mathcal{H}}$
g	gravitational acceleration
H	equilibrium fluid depth
h	the free surface displacement
h_B	bottom topography
h_t	total fluid height $h_t = H_0 + F^2 h$
j	vertical component of current, $j = \boldsymbol{e}_z \cdot (\nabla \times \boldsymbol{B}_3)$
M	inverse Alfvén-Mach number, $M = \mathcal{B}/\mathcal{U}$
P	total pressure
p	gas pressure
Q, q	potential vorticity, $q = \omega/h_t$
U_0	the basic state velocity
$\boldsymbol{u}_3$	three-dimensional velocity field, $\boldsymbol{u}_3 = (u, v, w)$
$\boldsymbol{u}$	two-dimensional velocity field, $\boldsymbol{u} = (u, v)$
$\boldsymbol{U}$	momentum in shallow-water, $\boldsymbol{U} = (h_t u, h_t v)$
α	streamwise wavenumber
ρ	density
ω	vertical component of vorticity, $\omega = \boldsymbol{e}_z \cdot (\nabla \times \boldsymbol{u}_3)$
∇	gradient operator
∇_z	gradient operator with z-component omitted
D/Dt	material derivative
$(\cdot)'$	$\mathrm{d}(\cdot)/\mathrm{d}y$

Contents

List of Figures

List of Tables

Chapter 1

Introduction

Geophysical and astrophysical systems are often density stratified, with flows characterised by motions that have a long horizontal length scale compared with the vertical scale. The dynamics of such systems are often studied under the shallow-water approximation (e.g., Pedlosky 1987, §3; Salmon 1998, §2; Vallis 2006, §3; Bühler 2009, §1); this constitutes a set of two-dimensional equations with no explicit dependence on the vertical co-ordinate, a mathematical simplification compared with the continuously stratified three-dimensional system. The shallow-water equations capture the fundamental dynamics of density stratification, supporting slow, vortical motions as well as fast, wave motions, and interactions thereof.

The hydrodynamic shallow-water equations have often been used as a model for geophysical and astrophysical systems, such as the Earth's ocean (e.g., Vallis, 2006, part IV) or Jupiter's weather layer (e.g., Cho & Polvani, 1996a; Showman, 2007). They are also used as a simplified model for exploring the fundamental fluid dynamics underlying geophysical and astrophysical systems, for example: vortex and wave dynamics in uniformly rotating systems (e.g., Sadourny, 1975; Young, 1986; Ripa, 1987; Farge & Sadourny, 1989; Ford, 1994; Polvani *et al.*, 1994; Stegner & Dritschel, 2000; Ford *et al.*, 2000; Mohebalhojeh & Dritschel, 2001; Lahaye & Zeitlin, 2012; Plotka & Dritschel, 2012); jet formation in differentially rotating systems (e.g., Cho & Polvani, 1996a,b; Showman, 2007; Scott & Polvani, 2008; Dritschel & Scott, 2011; Showman & Polvani, 2011); wave-wave or wave-mean flow interaction (e.g., Ripa, 1982; Bühler & McIntyre, 1998; Bühler, 2000; Bühler & McIntyre, 2003; Bühler, 2009); shear instabilities (e.g., Satomura, 1981; Griffiths *et al.*, 1982; Paldor, 1983; Ripa, 1983; Hayashi & Young, 1987; Balmforth, 1999; Dritschel *et al.*,

1999; Mohebalhojeh & Dritschel, 2000; Poulin & Flierl, 2003; Dritschel & Vanneste, 2006).

In this thesis we shall be concentrating on shear instabilities. To study the behaviour of shear flows at a fundamental level, we shall investigate instabilities of parallel shear flows in planar geometry. Instability of parallel shear flows in the hydrodynamic (not necessarily shallow-water) setting is by now a well-established topic, often included as chapters in monographs dedicated to instabilities (Lin, 1955; Betchov & Criminale, 1967; Chandrasekhar, 1981; Drazin & Reid, 1981; Schmid & Henningson, 2001; Criminale *et al.*, 2003) or geophysical fluid dynamics (e.g., Pedlosky 1987, §7; Vallis 2006, §6; Bühler 2009, §7). Instabilities associated with shear flows leads to the breakdown of the flow, formation of coherent structures, and eventual transition into turbulence via secondary instabilities (e.g., Schmid & Henningson, 2001). The breakdown of the flow and transition to turbulence has implications for mixing of momentum, vorticity, passive scalars, density (if stratification is present) and so forth, so it is of theoretical as well as physical interest to study shear flow instabilities. For example, see the recent review by Smyth & Moum (2012) for recent advances in shear instability research in geophysical fluid dynamics. Shear instabilities in the hydrodynamic shallow-water setting have been investigated by numerous authors. It is known that instability may result from the basic flow profile possessing non-monotonic (potential) vorticity gradients (e.g., Ripa, 1983; Ford, 1994; Balmforth, 1999; Dritschel *et al.*, 1999; Poulin & Flierl, 2003; Dritschel & Viúdez, 2007), as in the incompressible system, but also from gravity wave interaction (e.g., Satomura, 1981; Griffiths *et al.*, 1982; Paldor, 1983; Ripa, 1983; Hayashi & Young, 1987; Balmforth, 1999; Dritschel & Vanneste, 2006). The formation of vortices resulting from the instability then also emit gravity waves (e.g., Dritschel *et al.* 1999; Mohebalhojeh & Dritschel 2000; Poulin & Flierl 2003; Dritschel & Vanneste 2006; see also Ford 1994; Polvani *et al.* 1994; Ford *et al.* 2000 for example on gravity wave emission by shallow-water vortices), something that is absent in the incompressible setting.

Many astrophysical systems are stratified, thin in terms of aspect ratios, and are ionised. The interaction of the fluid motion with a background magnetic field in such systems require the magnetohydrodynamic (MHD) description; one interest then is a MHD analogue of the shallow-water equations as a simplified model for investigating the interplay between stratification and MHD effects. To this end, the shallow-water MHD system (SWMHD) was derived by Gilman (2000), and we shall be investigating the dynamics of shear flows in the SWMHD system.

Often we shall have in mind the solar tachocline as an example of such an astrophysical system.

From helioseismology (see, for example, the review by Christensen-Dalsgaard & Thompson 2007), it was inferred from observational data relatively recently that, in the Sun, the latitudinal differential rotation (faster at the equator and slower at the poles) holds true along radial lines throughout the convection zone, whilst the inner radiative zone rotates roughly in solid body rotation; a representation of this inversion for the angular rotational period is given in Figure 1.1. This naturally leads to a thin transition region (of depth approximately $0.03R_{\text{sun}}$) of strong shear located at approximately $0.7R_{\text{sun}}$; this region was termed the tachocline by Spiegel & Zahn (1992). In particular, the lower portion of the tachocline that is within the radiative zone is known to be strongly stratified, and the assumptions that go into the shallow-water description are well satisfied in this region. For completeness, some data estimated by Gough at $0.7R_{\text{sun}}$ are reproduced here in Table 1.1; this will be used to estimate the magnitude of certain non-dimensional parameters in Chapter 2. The tachocline is regarded as an important piece of the jigsaw in understanding the global solar dynamics. Its mere existence has led to a re-assessment of the underlying fluid dynamical behaviour due to fluid/magnetic coupling, leading to questions on how the tachocline is maintained, generally known as the tachocline confinement problem (e.g., Spiegel & Zahn, 1992; Gough & McIntyre, 1998; Garaud, 2007; Wood & McIntyre, 2011; Wood *et al.*, 2011). The tachocline is generally seen as the seat of the solar dynamo, contributing to the strengthening of the magnetic field via differential rotation (e.g., Tobias & Weiss, 2007). The issue of instabilities associated with the differential rotation profile and its physical consequences is also of relevance (e.g Gilman & Cally, 2007; Dikpati *et al.*, 2009; Zaqarashivili *et al.*, 2010). We refer the reader to the book "The solar tachocline" (edited by Hughes, Rosner & Weiss, 2007) for a comprehensive and relatively recent review of the current research problems associated with the tachocline.

Since the derivation by Gilman (2000), the SWMHD equations have been studied both from a theoretical and modelling point of view. They have been shown to possess a hyperbolic as well as Hamiltonian structure (De Sterck, 2001; Dellar, 2002, 2003b; Rossmanith, 2002). The MHD modifications to wave motions supported by the hydrodynamic shallow-water system have also been derived (Schecter *et al.*, 2001; Zaqarashivili *et al.*, 2008; Heng & Spitkovsky, 2009). To date, the principal aim of studies of shear flow instabilities in SWMHD have been to investigate in detail the global aspect of the instability, employing spherical geometry and model differential rotation profiles as the basic shear flow (Dikpati & Gilman, 2001; Rempel & Dikpati, 2003; Dikpati *et al.*, 2003; Dikpati & Gilman, 2005). These authors considered basic state profiles that only depend on latitude, and they investigated the effects of different magnetic field strengths, varying physical

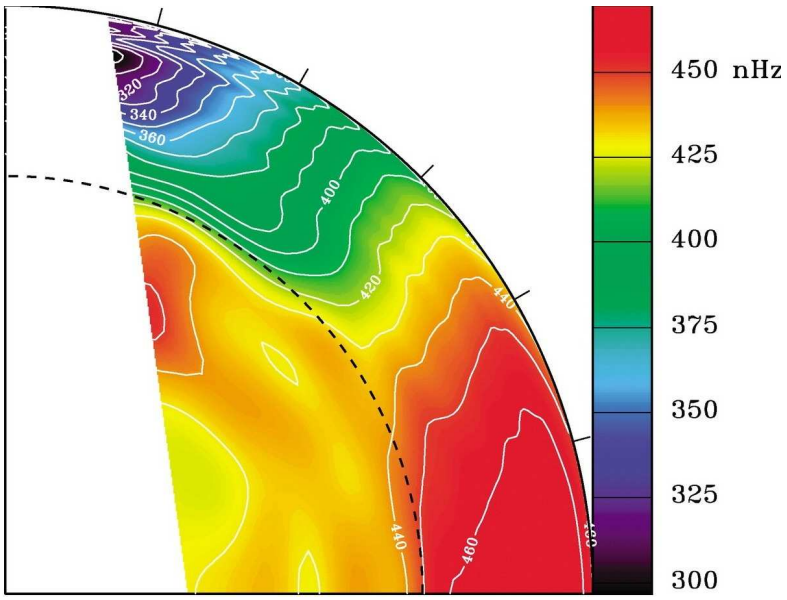

Figure 1.1: Angular velocity profile inferred from helioseismology, taken from the LSV group at HAO, NCAR (`http://www.hao.ucar.edu/research/lsv/lsv.php`, convection page). 450nHz and 325 nHz translates roughly to rotation periods of 26 and 36 days. The tachocline is indicated by the dashed line.

Quantity	meaning	value at $R = 0.7R_{\text{sun}}$	units (cgs units)
R_{sun}	Solar radius	6.95×10^{10}	cm
Ω_{pole}	angular frequency at pole	2.0×10^{-6}	s^{-1}
Ω_{equator}	angular frequency at equator	2.9×10^{-6}	s^{-1}
ρ	density	0.21	g cm^{-3}
N	buoyancy frequency	8×10^{-4}	s^{-1}
c	sound speed	2.3×10^{7}	cm s^{-1}
g	gravitational acceleration	5.4×10^{4}	cm s^{-2}
μ_0	magnetic permeability	1	
η	magnetic diffusivity	4.1×10^{2}	$\text{cm}^2\ \text{s}^{-1}$
ν	kinematic viscosity	2.7×10^{1}	$\text{cm}^2\ \text{s}^{-1}$
κ	thermal diffusivity	1.4×10^{7}	$\text{cm}^2\ \text{s}^{-1}$

Table 1.1: Some physical parameters given in Gough (2007) for the Sun at $R = 0.7R_{\text{sun}}$.

structure of the background magnetic field, and the dependence on the gravity parameter (their G, which will be seen to be related to our Froude number F as $G \sim F^{-2}$; see Dikpati & Gilman 2001; Rempel & Dikpati 2003; Dikpati *et al.* 2003).

These previous studies of shear instabilities have focussed on the global instabilities. To complement these previous studies, we focus here on local instabilities, with the aim to examine the shear flow instability problem in a more general context. For this, we consider here the instability problem of plane parallel shear flows in the single-layer SWMHD system. We ask the general question: how are the well known fluid instabilities of plane parallel shear flows modified by MHD and shallow-water effects?

We begin in Chapter 2 with a derivation of the SWMHD equations, and, in planar geometry with appropriate boundary conditions, highlight the conservation laws and wave modes possessed by this system. We study the onset of instability via a linear analysis, and derive in Chapter 3 the governing eigenvalue equation, as well as some general results valid for suitably differentiable profiles. At a sufficiently local level, most flows may be modelled as either a shear layer or a jet. In Chapter 4 we consider the instability characteristics of idealised versions of these shear layer and jet profiles, namely, the vortex sheet and the rectangular jet. It is known such piecewise-constant profiles reveal features that have analogues in the corresponding smooth cases, and the resulting problem benefit from the fact the problem may be solved completely or asymptotically. In Chapter 5 we consider two prototypical flow profiles often employed for studying the instability characteristics of shear layers and jets, the hyperbolic-tangent shear layer and the Bickley jet. To highlight several features of interest, we first solve the eigenvalue problem numerically. We consider the instability mechanism, where there is an interpretation of the instability mechanism in terms of a pair of counter-propagating Rossby waves; we see how this paradigm is modified when MHD and shallow water effects are present. The long-wave asymptotic procedure of Drazin & Howard (1962) is generalised to the SWMHD system, and these analytical, asymptotic results complement the numerical results presented earlier. The nonlinear evolution of unstable smooth shear flows is then studied numerically. Chapter 6 focusses on the incompressible cases, with a review of the numerical techniques and known results in the literature. It is known that the vortices normally formed from the hydrodynamic evolution may be destroyed by MHD effects, depending on the field strength and on the size of the magnetic diffusivity parameter. An investigation of the disruption on the dependence of the background field strength and dissipation parameter is

carried out, and we provide estimates of the boundaries between the different regimes. Chapter 7 deals with the modifications introduced by shallow-water effects. Some numerical issues are highlighted, before an investigation into the parameter dependence of the nonlinear evolution. Detailed conclusion and discussion are given at the end of each chapter, and a brief conclusion and suggestions for future work are given in Chapter 8.

Chapter 2

The shallow-water MHD equations

For self-containment purposes, we reproduce here a derivation of the shallow-water MHD (SWMHD) equations (see also Gilman, 2000; Dellar, 2003a). Anticipating the discussions in the later chapters, we also provide derivations of the conservations laws and wave solutions for this system.

2.1 Derivation

We consider a magneto-fluid with a free surface at $z = h(x, y, t)$ with undisturbed free surface at $z = 0$, lying over some topography (describing real topography, underlying dynamical effects or otherwise) $z = -H(x, y)$. The total fluid column height is given by $h_t = H + h$; see Figure 2.1. We focus on dynamics at a sufficiently local level so that the Rossby number (measuring the relative importance between inertia and rotational effects) is large, so that the Coriolis term is relatively small and may be neglected as a simplification. The three-dimensional incompressible, ideal MHD equations describing the dynamics of a thin layer of electrically conducting fluid of constant density ρ, with gravitational acceleration, are given by

$$\frac{\partial \boldsymbol{u}_3}{\partial t} + \boldsymbol{u}_3 \cdot \nabla \boldsymbol{u}_3 = -\frac{1}{\rho_0}\nabla p + (\nabla \times \boldsymbol{B}_3) \times \boldsymbol{B}_3 - g\boldsymbol{e}_z, \tag{2.1a}$$

$$\frac{\partial \boldsymbol{B}_3}{\partial t} + \boldsymbol{u}_3 \cdot \nabla \boldsymbol{B}_3 = \boldsymbol{B}_3 \cdot \nabla \boldsymbol{u}_3, \tag{2.1b}$$

$$\nabla \cdot \boldsymbol{u}_3 = 0, \tag{2.1c}$$

$$\nabla \cdot \boldsymbol{B}_3 = 0. \tag{2.1d}$$

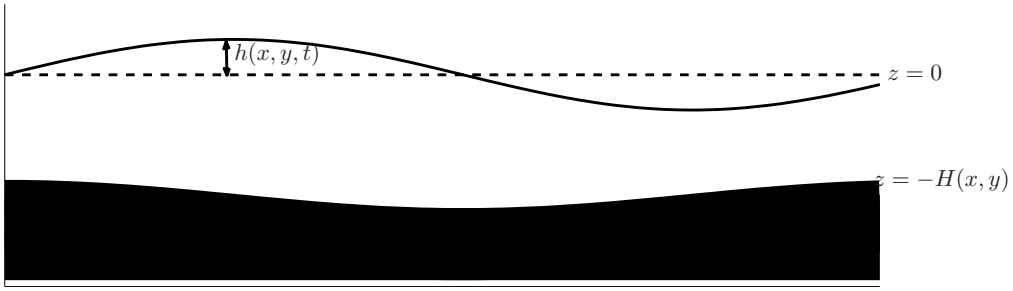

Figure 2.1: Physical set up of the problem.

Here, the subscript '3' denotes the full three-dimensional quantity, and $\boldsymbol{B}_3$ is given in units of velocity, so $\boldsymbol{B}_3 = \boldsymbol{B}^*/\sqrt{\mu_0\rho_0}$, where μ_0 is the permeability of free space.

To proceed with the derivation, we note that the momentum equation (2.1a) may be written as

$$\frac{\partial \boldsymbol{u}_3}{\partial t} + \boldsymbol{u}_3 \cdot \nabla \boldsymbol{u}_3 = -\frac{1}{\rho_0}\nabla P + \boldsymbol{B}_3 \cdot \nabla \boldsymbol{B}_3 - g\boldsymbol{e}_z, \tag{2.2}$$

where $P = p + |\boldsymbol{B}_3|^2/2$, the sum of the gas and magnetic pressure. We assume that the typical horizontal length scale $\mathcal{L}$ is much greater than the typical vertical length scale $\mathcal{H}$, so that the aspect ratio $\epsilon = \mathcal{H}/\mathcal{L}$ is small. Now, the $\epsilon \ll 1$ approximation justifies the neglect of the vertical acceleration, and the leading order balance in the vertical momentum equation is assumed to be

$$\frac{\partial P}{\partial z} = -\rho_0 g, \tag{2.3}$$

which may be termed magneto-hydrostatic balance. Integrating (2.3), we obtain

$$P = -\rho_0 g z + P_0, \tag{2.4}$$

where P_0 is to be fixed by the boundary conditions. Across the free surface, pressure should be continuous; we take the pressure to be zero above the free surface without loss of generality, and so

$$P(x,y,z,t) = \rho_0 g[h(x,y,t) - z]. \tag{2.5}$$

Denoting ∇_z as the gradient operator with the z-component omitted, we see that

$$\frac{1}{\rho_0}\nabla_z P = g\nabla_z h. \tag{2.6}$$

Now, because the $\nabla_z h$ terms are independent of z, this means we may also assume u, v, b_x and b_y are also z-independent, and so the horizontal momentum equation becomes

$$\frac{\partial \boldsymbol{u}}{\partial t} + \boldsymbol{u} \cdot \nabla_z \boldsymbol{u} = \boldsymbol{b} \cdot \nabla_z \boldsymbol{b} - g\nabla_z h. \tag{2.7}$$

Here $\boldsymbol{u} = (u, v)$ and $\boldsymbol{b} = (b_x, b_y)$. The dependency in the vertical co-ordinate z does not appear explicitly, which highlights an important feature of the shallow-water equations: if the fields are initially depth independent, they will remain so for all subsequent time (e.g., §2.3 of Salmon 1998 or §3.1 of Vallis 2006).

Now, integrating $\nabla \cdot \boldsymbol{u}_3 = 0$ over the fluid depth gives

$$[w]_{z=-H}^{z=h} = -h_t \nabla_z \cdot \boldsymbol{u}, \tag{2.8}$$

with $h_t = H + h$. Since w is just the material derivative of the position of a particular element, we have

$$[w]_{z=-H}^{z=h} = \left(\frac{\partial}{\partial t} + \boldsymbol{u}_3 \cdot \nabla\right)[H + h(x, y, t)] = \left(\frac{\partial}{\partial t} + \boldsymbol{u} \cdot \nabla_z\right) h_t. \tag{2.9}$$

Putting the two together, we obtain

$$\frac{\partial h_t}{\partial t} + \nabla_z \cdot (h_t \boldsymbol{u}) = 0. \tag{2.10}$$

For the induction equation (2.1b), assuming b_z is small compared to b_x and b_y, there is only explicit evolution of the horizontal magnetic field, with the governing equation given by

$$\frac{\partial \boldsymbol{b}}{\partial t} + \boldsymbol{u} \cdot \nabla_z \boldsymbol{b} = \boldsymbol{b} \cdot \nabla_z \boldsymbol{u}. \tag{2.11}$$

Finally, from the condition $\nabla \cdot \boldsymbol{B}_3 = 0$,

$$\frac{\partial b_z}{\partial z} = -\nabla_z \cdot \boldsymbol{b}. \tag{2.12}$$

Integrating over the fluid depth gives

$$[b_z]_{z=-H}^{z=h} = -h_t \nabla_z \cdot \boldsymbol{b}. \tag{2.13}$$

We make two further additional assumptions. The lower boundary is taken to be a perfect conductor, and it is assumed that the free surface starts off as a field line. By Alfvén's theorem, field lines are frozen into the fluid, and the free surface thus remains a field line. The full three-dimensional field should be locally parallel to the vertical boundaries. So, letting $\boldsymbol{n}$ be the normal vector to the vertical boundaries, we require $\boldsymbol{B}_3 \cdot \boldsymbol{n} = 0$, and hence

$$(b_x, b_y, -h_t \nabla_z \cdot \boldsymbol{b}) \cdot (-\partial h/\partial x, -\partial h/\partial y, 1) = -\nabla_z \cdot (h_t \boldsymbol{b}) = 0. \tag{2.14}$$

In summary, the single layer SWMHD equations in Cartesian co-ordinates are given by

$$\frac{\partial \boldsymbol{u}}{\partial t} + \boldsymbol{u}\cdot\nabla\boldsymbol{u} = \boldsymbol{b}\cdot\nabla\boldsymbol{b} - g\nabla h, \tag{2.15a}$$

$$\frac{\partial \boldsymbol{b}}{\partial t} + \boldsymbol{u}\cdot\nabla\boldsymbol{b} = \boldsymbol{b}\cdot\nabla\boldsymbol{u}, \tag{2.15b}$$

$$\frac{\partial h}{\partial t} + \nabla\cdot(h_t\boldsymbol{u}) = 0, \tag{2.15c}$$

$$\nabla\cdot(h_t\boldsymbol{b}) = 0, \tag{2.15d}$$

where the subscript on the gradient operator has been dropped. It will be seen later that the divergence-free condition (2.15d), if satisfied initially, is preserved by the dynamics, and thus serves as a constraint for the initial condition; hence we do have five equations for five variables, subject to a constraint. Note that it is $\partial h/\partial t$ that appears since h is the only quantity in $h_t = H + h(x, y, t)$ that is time dependent. This set of equations is only dependent on the two horizontal variables, but there is a vertical structure in that w and b_z are not necessarily zero, but are related to the horizontal divergence of $\boldsymbol{u}$ and $\boldsymbol{b}$ respectively.

It should be noted that a vector identity may be used to rewrite the induction equation (2.15b) in the form

$$\frac{\partial \boldsymbol{b}}{\partial t} = \nabla\times(\boldsymbol{u}\times\boldsymbol{b}) + (\nabla\cdot\boldsymbol{u})\boldsymbol{b} - (\nabla\cdot\boldsymbol{b})\boldsymbol{u}. \tag{2.16}$$

Neither $\boldsymbol{u}$ or $\boldsymbol{b}$ are divergence-free by themselves; rather, it is $\boldsymbol{u}_3$ and $\boldsymbol{B}_3$, reconstructed from the relations (2.8) and (2.13), that are divergence-free.

2.2 Properties

For completeness we provide an overview of the basic properties satisfied by the SWMHD equations, highlighting some important points that will be discussed in the later chapters.

2.2.1 Non-dimensional form

A common approach is to rescale the problem to obtain a non-dimensional set of equations. Taking then

$$\boldsymbol{u}\to\mathcal{U}\boldsymbol{u}, \qquad \boldsymbol{b}\to\mathcal{B}\boldsymbol{b}, \qquad h\to\mathcal{H}h, \tag{2.17}$$

we shall also choose to scale time by the advective time rather than the Alfvén time, so we also have

$$\frac{\partial}{\partial t} \to \frac{1}{\mathcal{T}}\frac{\partial}{\partial t} = \frac{\mathcal{U}}{\mathcal{L}}\frac{\partial}{\partial t}, \qquad \nabla \to \frac{1}{\mathcal{L}}\nabla. \tag{2.18}$$

Rescaling accordingly gives

$$\frac{\partial \boldsymbol{u}}{\partial t} + \boldsymbol{u}\cdot\nabla\boldsymbol{u} = M^2\boldsymbol{b}\cdot\nabla\boldsymbol{b} - \frac{1}{F^2}\nabla h, \tag{2.19a}$$

$$\frac{\partial \boldsymbol{b}}{\partial t} + \boldsymbol{u}\cdot\nabla\boldsymbol{b} = \boldsymbol{b}\cdot\nabla\boldsymbol{u}, \tag{2.19b}$$

$$\frac{\partial h}{\partial t} + \nabla\cdot(h_t\boldsymbol{u}) = 0, \tag{2.19c}$$

$$\nabla\cdot(h_t\boldsymbol{b}) = 0. \tag{2.19d}$$

The two non-dimensional parameters are then the inverse Alfvén-Mach number $M = \mathcal{B}/\mathcal{U}$, a measure of the relative importance of the Lorentz force term and the fluid inertia term, and the Froude number $F = \mathcal{U}/\sqrt{g\mathcal{H}}$, a measure of how strong gravity is (it will be seen that F is related to the speed of gravity waves). A further rescaling of $h \to F^2 h$ results in the set of equations

$$\frac{\partial \boldsymbol{u}}{\partial t} + \boldsymbol{u}\cdot\nabla\boldsymbol{u} = M^2\boldsymbol{b}\cdot\nabla\boldsymbol{b} - \nabla h, \tag{2.20a}$$

$$\frac{\partial \boldsymbol{b}}{\partial t} + \boldsymbol{u}\cdot\nabla\boldsymbol{b} = \boldsymbol{b}\cdot\nabla\boldsymbol{u}, \tag{2.20b}$$

$$F^2\frac{\partial h}{\partial t} + \nabla\cdot(h_t\boldsymbol{u}) = 0, \tag{2.20c}$$

$$\nabla\cdot(h_t\boldsymbol{b}) = 0, \tag{2.20d}$$

where $h_t = H + F^2 h$ is the total fluid depth. The Froude number now appears in the mass and flux conservation equations rather than the momentum equations. The two-dimensional incompressible MHD equations are recovered when $F = 0$, $H = 1$ (with h identified with the pressure p). Furthermore, the hydrodynamic equations are obtained when $M = 0$.

To get a rough estimate of M and F for the tachocline we use the parameters given in Table 1.1. We take the typical velocity and length scales as

$$\mathcal{T} = \frac{\Omega_{\text{pole}} + \Omega_{\text{equator}}}{2}, \qquad \mathcal{L} = 2\pi \times 0.7 R_{\text{sun}} \qquad \Rightarrow \qquad \mathcal{U} = \frac{L}{T} \approx 1.3 \times 10^5 \text{ cm s}^{-1} \tag{2.21}$$

We first estimate M. There is some uncertainty in the magnetic field strength B^* in the tachocline, but a likely range is $10^3 G \lesssim B^* \lesssim 10^5 G$. This leads to

$$\mathcal{B} = \frac{B^*}{\sqrt{\mu_0\rho_0}} \text{ cm s}^{-1} \approx 2.2 \times 10^{3-5} \text{ cm s}^{-1}, \tag{2.22}$$

and so we have

$$0.01 \lesssim M \lesssim 1. \tag{2.23}$$

For the Froude number, instead of just taking $\mathcal{H}$ and work out $F = \mathcal{U}/\sqrt{g\mathcal{H}}$, we consider a slightly different approach that is often employed in geophysical fluid dynamics; this approach was also the one adopted by, for example, Dikpati & Gilman (2001). In the hydrodynamic case, there is a formal analogy between linearised shallow-water system and the linearised primitive equations, and the shallow-water gravity waves $\sqrt{g\mathcal{H}_0}$ correspond to the fastest gravity waves in the continuously stratified case, given by $N\mathcal{H}_1/\pi$ (e.g., Gill, 1982, §6.11). Taking $\mathcal{H}_1 = 0.03R_{\text{sun}}$, this implies $N\mathcal{H}_1/\pi \approx 5 \times 10^5$ cm s^{-1}, and thus giving

$$F \approx 0.25. \tag{2.24}$$

The equivalent depth $\mathcal{H}_0$ in this case is approximately 5×10^6 cm (or 50 km).

This implies that the large-scale magnetic field is weak relative to the large-scale flow, and that the system is strongly constrained by stratification effects. Although we have estimates for F and M for the tachocline, we will not restrict ourselves to these parameters as we are interested in the more general shear flow instability problem.

2.2.2 Conserved quantities

In line with the domain set up considered later, we consider the case where the domain is periodic in x and bounded by perfectly conducting impermeable walls in y, with no underlying topography (so $H = 1$). Now we have $h_t = 1 + F^2 h$, we first note that integrating the divergence-free condition (2.20d) over the domain leads to the restriction

$$[h_t b_y]_{y=-L_y}^{y=L_y} = 0. \tag{2.25}$$

This is satisfied for example if we take no normal flux boundary conditions

$$b_y = 0 \quad \text{on} \quad y = \pm L_y. \tag{2.26}$$

This, together with no normal flow boundary conditions

$$v = 0 \quad \text{on} \quad y = \pm L_y, \tag{2.27}$$

implies the condition

$$\frac{\partial h}{\partial y} = 0 \quad \text{on} \quad y = \pm L_y \tag{2.28}$$

from the y-component of the momentum equation. We then have the following conservation laws:

Mass conservation

$$\frac{\mathrm{d}}{\mathrm{d}t} \iint h_t \, \mathrm{d}x\mathrm{d}y = - \iint \nabla \cdot (h_t \boldsymbol{u}) \, \mathrm{d}x\mathrm{d}y = 0, \tag{2.29}$$

since the domain is periodic in x and $v = 0$ on the y-boundaries.

Momentum conservation

$$\begin{aligned} \frac{\mathrm{d}}{\mathrm{d}t} \iint h_t u \, \mathrm{d}x\mathrm{d}y &= - \iint \left[\nabla \cdot (h_t u \boldsymbol{u}) + h_t \frac{\partial h}{\partial x} \right] \mathrm{d}x\mathrm{d}y - M^2 \iint b_x \nabla \cdot (h_t \boldsymbol{b}) \, \mathrm{d}x\mathrm{d}y \\ &= - \iint \frac{\partial}{\partial x} \left(F^2 \frac{h^2}{2} + h \right) \mathrm{d}x\mathrm{d}y = 0, \end{aligned} \tag{2.30}$$

owing to periodicity in x, and $v = 0$ as well as $b_y = 0$ on the y-boundaries. Note that the divergence-free condition (2.15d) is required for momentum conservation.

$$\begin{aligned} \frac{\mathrm{d}}{\mathrm{d}t} \iint h_t v \, \mathrm{d}x\mathrm{d}y &= - \iint \left[\nabla \cdot (h_t v \boldsymbol{u}) + h_t \frac{\partial h}{\partial y} \right] \mathrm{d}x\mathrm{d}y - M^2 \iint b_y \nabla \cdot (h_t \boldsymbol{b}) \, \mathrm{d}x\mathrm{d}y \\ &= - \iint \frac{\partial}{\partial y} \left(F^2 \frac{h^2}{2} + h \right) \mathrm{d}x\mathrm{d}y \\ &= - \int \left[F^2 \frac{h^2}{2} + h \right]_{-L_y}^{+L_y} \mathrm{d}x, \end{aligned} \tag{2.31}$$

again, owing to periodicity, and $v = 0$ as well as $b_y = 0$ on the y-boundaries. As above, the divergence-free condition (2.15d) is again required for conservation. The loss of y-momentum conservation here is related to the fact that we no longer have translational invariance in y. In the incompressible limit $F = 0$, the extra contribution happens to vanish as long as there is no net difference in the mean pressure on the side walls. We note in passing that the presence of underlying topography also results in extra contributions to the momentum budget.

Flux conservation

Similar to the above manipulations, we have

$$\frac{\mathrm{d}}{\mathrm{d}t} \iint h_t b_x \, \mathrm{d}x\mathrm{d}y = - \iint \nabla \cdot (h_t b_x \boldsymbol{u}) \, \mathrm{d}x\mathrm{d}y - \iint u \nabla \cdot (h_t \boldsymbol{b}) \, \mathrm{d}x\mathrm{d}y = 0, \tag{2.32}$$

and

$$\frac{\mathrm{d}}{\mathrm{d}t}\iint h_t b_y \,\mathrm{d}x\mathrm{d}y = -\iint \nabla\cdot(h_t b_y \boldsymbol{u})\,\mathrm{d}x\mathrm{d}y - \iint v\nabla\cdot(h_t\boldsymbol{b})\,\mathrm{d}x\mathrm{d}y = 0, \tag{2.33}$$

using periodicity in x, $v = 0$ and $b_y = 0$ on the y-boundaries. The divergence-free condition (2.15d) is again necessary for conservation.

Total energy conservation

The total energy of the system evolves as

$$\begin{aligned}\frac{1}{2}\frac{\mathrm{d}}{\mathrm{d}t}\iint \left[h_t(|\boldsymbol{u}|^2 + M^2|\boldsymbol{b}|^2) + F^2h^2\right]\,\mathrm{d}x\mathrm{d}y \\ = -\iint \nabla\cdot\left\{h_t\boldsymbol{u}\left(\frac{|\boldsymbol{u}|^2 + M^2|\boldsymbol{b}|^2}{2} + h\right)\right\}\,\mathrm{d}x\mathrm{d}y \\ + M^2\iint h_t\boldsymbol{b}\cdot\nabla\left(ub_x + vb_y\right)\,\mathrm{d}x\mathrm{d}y,\end{aligned} \tag{2.34}$$

where the energy contributions on the left hand side of (2.34) are the kinetic energy, the magnetic energy, and the potential energy; notice that the kinetic and magnetic energy is multiplied by the total height and is cubic in nature, whereas the potential energy only involves the deviation from the rest state. In the incompressible limit $F = 0$, the potential energy contribution disappears, whilst in the hydrodynamic limit $M = 0$, the magnetic contribution disappears. The first integral vanishes because of periodicity and $v = 0$ on the boundaries. Performing an integration by parts on the second integral,

$$\begin{aligned}\iint\left[h_t b_x\frac{\partial}{\partial x}\left(ub_x + vb_y\right)\right]\,\mathrm{d}x\mathrm{d}y = \left[h_t b_x(ub_x + vb_y)\right]_{x=0}^{x=L_x} + \left[h_t b_y(ub_x + vb_y)\right]_{y=-L_y}^{y=L_y} \\ - \iint (ub_x + vb_y)\nabla\cdot(h_t\boldsymbol{b})\,\mathrm{d}x\mathrm{d}y = 0,\end{aligned} \tag{2.35}$$

owing to periodicity, $b_y = 0$ on the boundary, and the divergence free condition. Thus the total energy is conserved.

Divergence-free condition

All of the above conservation laws as written depend crucially on the fact that the divergence-free condition of the magnetic field (2.20d) holds for all time. It is therefore important to verify that the governing equation preserves this divergence-free condition during the evolution. This may

be shown by a brute force calculation by considering the time derivative of $\nabla \cdot (h_t \boldsymbol{b})$ and using the remaining equations as appropriate (index notation here is useful). A cleaner way to show this (due to Sam Hunter, private communication) is to observe that

$$\begin{aligned}
\nabla \times (\boldsymbol{u} \times h_t \boldsymbol{b}) &= h_t \boldsymbol{b} \cdot \nabla \boldsymbol{u} - h_t \boldsymbol{b}(\nabla \cdot \boldsymbol{u}) - \boldsymbol{u} \cdot \nabla (h_t \boldsymbol{b}) + \boldsymbol{u}[\nabla \cdot (h_t \boldsymbol{b})] \\
&= h_t \boldsymbol{b} \cdot \nabla \boldsymbol{u} - h_t \boldsymbol{u} \cdot \nabla \boldsymbol{b} - \boldsymbol{b}[\nabla \cdot (h_t \boldsymbol{u})] + \boldsymbol{u}[\nabla \cdot (h_t \boldsymbol{b})] \\
&= h_t \frac{\partial \boldsymbol{b}}{\partial t} + \boldsymbol{b} \frac{\partial h_t}{\partial t} + \boldsymbol{u}[\nabla \cdot (h_t \boldsymbol{b})] \\
&= \frac{\partial}{\partial t}(h_t \boldsymbol{b}) + \boldsymbol{u}[\nabla \cdot (h_t \boldsymbol{b})],
\end{aligned} \tag{2.36a}$$

so

$$\frac{\partial}{\partial t} \nabla \cdot (h_t \boldsymbol{b}) = \nabla \cdot [\nabla \times (\cdots) + \boldsymbol{u}(\nabla \cdot (h_t \boldsymbol{b}))]. \tag{2.36b}$$

The divergence of a curl is zero, and so if $h_t \boldsymbol{b}$ is divergence free at $t = 0$, the subsequent evolution will keep the fields divergence free. Another way to show this property is to observe that the induction equation may be written as

$$\frac{\partial (h_t \boldsymbol{b})}{\partial t} + \nabla \cdot (h_t \boldsymbol{u}\boldsymbol{b} - h_t \boldsymbol{b}\boldsymbol{u}) = 0, \tag{2.37}$$

as in De Sterck (2001), using the tensor notation $(\boldsymbol{u}\boldsymbol{b})_{ij} = u_i b_j$. Taking a divergence also shows that the divergence-free condition is preserved in time by the dynamics.

Equations in transport variables

Another equivalent and potentially useful way of writing the SWMHD equations is in terms of the transport variables $(\boldsymbol{U}, \boldsymbol{B}, h) = (h_t \boldsymbol{u}, h_t \boldsymbol{b}, h)$. Equations given by (2.20) may then be written as

$$\frac{\partial \boldsymbol{U}}{\partial t} + \nabla \cdot \left(\frac{\boldsymbol{U}\boldsymbol{U}}{h_t} - M^2 \frac{\boldsymbol{B}\boldsymbol{B}}{h_t} \right) + h_t \nabla h = 0, \tag{2.38a}$$

$$\frac{\partial \boldsymbol{B}}{\partial t} + \nabla \cdot \left(\frac{\boldsymbol{U}\boldsymbol{B}}{h_t} - \frac{\boldsymbol{B}\boldsymbol{U}}{h_t} \right) = 0, \tag{2.38b}$$

$$F^2 \frac{\partial h}{\partial t} + \nabla \cdot \boldsymbol{U} = 0, \tag{2.38c}$$

$$\nabla \cdot \boldsymbol{B} = 0. \tag{2.38d}$$

We have used the divergence-free condition implicitly when writing the equations in this form. The remaining h terms may also be included in the divergence term if there is no underlying topography. Then it may be checked that mass, momentum, flux and energy conservation are as

before by using the analogous boundary conditions given by

$$V = 0, \quad B_y = 0 \quad \text{and} \quad \frac{\partial h}{\partial y} = 0 \quad \text{on} \quad y = \pm L_y. \tag{2.39}$$

This shows that, at least in the ideal case, we have the expected conservation laws. We will be interested in solving the SWMHD equations numerically to investigate the nonlinear evolution in due course. It will be seen that there are some subtle issues regarding the choice of solving the equations in velocity or transport variables and the dissipation terms that are to be inserted. In the ideal case there is no big difference between the two formulations; we will use the velocity variable formulation in the linear analysis and discuss why we might want to use the transport variable formulation over the velocity variable formulation in the numerical investigation in Chapter 7.

Other quantities and their associated conservation laws

In the shallow-water system with $M = 0$, the potential vorticity

$$q = \frac{\omega}{h_t}, \qquad \omega = \frac{\partial v}{\partial x} - \frac{\partial u}{\partial y}, \tag{2.40}$$

is materially conserved, satisfying $Dq/Dt = 0$, with $D/Dt = \partial/\partial t + \boldsymbol{u} \cdot \nabla$. When $M \neq 0$ however this is no longer true, as the Lorentz force term is generally rotational. Instead, it is the flux function $h_t \boldsymbol{b} = \boldsymbol{e}_z \times \nabla A$ that is materially conserved, satisfying $DA/Dt = 0$.

The SWMHD system also possesses a Hamiltonian structure, as demonstrated by Dellar (2002). Choosing the state variables, constructing the Hamiltonian and equipping it with a Poisson bracket (with associated Poisson tensor), conserved quantities may be derived in a systematic manner. Furthermore, the representation is in fact a non-canonical one, and as such there are extra Casimir invariants that corresponds to non-trivial conservation laws; in this case the Casimir invariants are related to the flux function A. One notable invariant that the Hamiltonian formulation reveals is the global cross-helicity given by

$$\iint h_t \boldsymbol{u} \cdot \boldsymbol{b} \, \mathrm{d}x\mathrm{d}y, \tag{2.41}$$

again, the condition (2.20d) is necessary for conservation.

2.2.3 Waves

The type of waves supported by the SWMHD equations, including the effect of rotation, have been previously investigated (Schecter *et al.*, 2001; Zaqarashivili *et al.*, 2008; Heng & Spitkovsky,

2009). To obtain the dispersion relation governing wave motion, we consider again the simplified case where the equations are posed in a channel, with no topography, and take as basic state

$$\boldsymbol{u}_0 = \boldsymbol{e}_x, \qquad \boldsymbol{b}_0 = \boldsymbol{e}_x, \qquad h = 0. \tag{2.42}$$

Linearising about this basic state, we obtain

$$\frac{\partial u}{\partial t} + \frac{\partial u}{\partial x} - M^2\frac{\partial b_x}{\partial x} + \frac{\partial h}{\partial x} = 0, \tag{2.43a}$$
$$\frac{\partial v}{\partial t} + \frac{\partial v}{\partial x} - M^2\frac{\partial b_y}{\partial x} + \frac{\partial h}{\partial y} = 0, \tag{2.43b}$$
$$\frac{\partial b_x}{\partial t} + \frac{\partial b_x}{\partial x} - \frac{\partial u}{\partial x} = 0, \tag{2.43c}$$
$$\frac{\partial b_y}{\partial t} + \frac{\partial b_y}{\partial x} - \frac{\partial v}{\partial x} = 0, \tag{2.43d}$$
$$F^2\left(\frac{\partial h}{\partial t} + \frac{\partial h}{\partial x}\right) + \frac{\partial u}{\partial x} + \frac{\partial v}{\partial y} = 0. \tag{2.43e}$$

The boundary conditions $v = b_y = \partial h/\partial y = 0$ suggest we consider solutions of the form

$$(u, b_x, h) = (u_0, b_{x,0}, h_0)\cos\left(\frac{n\pi y}{L}\right)\mathrm{e}^{\mathrm{i}(kx-\omega t)}, \tag{2.44a}$$
$$(v, b_y) = (v_0, b_{y,0})\sin\left(\frac{n\pi y}{L}\right)\mathrm{e}^{\mathrm{i}(kx-\omega t)}, \tag{2.44b}$$

which leads to the algebraic system

$$\begin{pmatrix} k-\omega & 0 & -kM^2 & 0 & k \\ 0 & k-\omega & 0 & -kM^2 & \mathrm{i}n\pi/L \\ -k & 0 & k-\omega & 0 & 0 \\ 0 & -k & 0 & k-\omega & 0 \\ k & -\mathrm{i}n\pi/L & 0 & 0 & F^2(k-\omega) \end{pmatrix} \begin{pmatrix} u_0 \\ v_0 \\ b_{x,0} \\ b_{y,0} \\ h_0 \end{pmatrix} = 0. \tag{2.45}$$

The dispersion relation is then

$$(k-\omega)[(k-\omega)^2 - k^2M^2]\left[F^2(k-\omega)^2 - F^2k^2M^2 - k^2 - \frac{n^2\pi^2}{L^2}\right] = 0. \tag{2.46}$$

The first bracket corresponds to the $u_0 = v_0 = 0$ case which is not a wave mode of interest here. The second bracket is associated with the Alfvén branch which has dispersion relation and eigenfunctions given by

$$\omega_A = k \pm Mk, \qquad u = \mp b_x, \quad v = \mp b_y, \quad h = 0. \tag{2.47}$$

The last bracket is associated with magneto-gravity waves. The dispersion relation is given by

$$\omega_{mg} = k \pm \frac{\sqrt{k^2 + F^2M^2k^2 + n^2\pi^2/L^2}}{F}, \tag{2.48a}$$

and the eigenfunctions are given by

$$\begin{aligned}
u =& \pm h_0 \frac{Fk\sqrt{k^2 + F^2M^2k^2 + n^2\pi^2/L^2}}{k^2 + n^2\pi^2/L^2} \cos\left(\frac{n\pi y}{L}\right) \cos(kx - \omega t), \\
v =& \mp h_0 \frac{F(n\pi/L)\sqrt{k^2 + F^2M^2k^2 + n^2\pi^2/L^2}}{k^2 + n^2\pi^2/L^2} \sin\left(\frac{n\pi y}{L}\right) \sin(kx - \omega t), \\
b_x =& - h_0 \frac{k^2F^2M}{k^2 + n^2\pi^2/L^2} \cos\left(\frac{n\pi y}{L}\right) \cos(kx - \omega t), \\
b_y =& h_0 \frac{k(n\pi/L)F^2M}{k^2 + n^2\pi^2/L^2} \sin\left(\frac{n\pi y}{L}\right) \sin(kx - \omega t), \\
h =& h_0 \cos\left(\frac{n\pi y}{L}\right) \cos(kx - \omega t).
\end{aligned} \tag{2.48b}$$

When $F \to 0$, we see that the gravity waves become infinitely fast and are effectively filtered out of the system. These exact wave solutions are used later in Chapter 7 as a check for the numerical routines.

Chapter 3

Linear theory: eigenvalue problem and general theorems

3.1 Linearisation and eigenvalue problem

The non-dimensional SWMHD equations are given by

$$\frac{\partial \boldsymbol{u}}{\partial t} + \boldsymbol{u}\cdot\nabla\boldsymbol{u} = -\nabla h + M^2\boldsymbol{b}\cdot\nabla\boldsymbol{b}, \tag{3.1a}$$

$$\frac{\partial \boldsymbol{b}}{\partial t} + \boldsymbol{u}\cdot\nabla\boldsymbol{b} = \boldsymbol{b}\cdot\nabla\boldsymbol{u}, \tag{3.1b}$$

$$F^2\frac{\partial h}{\partial t} + \nabla\cdot(h_t\boldsymbol{u}) = 0, \tag{3.1c}$$

$$\nabla\cdot(h_t\boldsymbol{b}) = 0, \tag{3.1d}$$

where $h_t = H + F^2 h$ is the total fluid depth. For the linear problem considered here, the basic state and perturbation are chosen to satisfy the divergence free condition (3.1d), so it need not be considered explicitly. Above a topography of the form $H(y)$, we consider a basic state

$$h = 0, \qquad \boldsymbol{u} = U_0(y)\boldsymbol{e}_x \qquad \text{and} \qquad \boldsymbol{b} = B_0(y)\boldsymbol{e}_x, \tag{3.2}$$

so that the basic magnetic field profile is initially aligned with the basic flow profile. We then consider perturbations in h, $\boldsymbol{u} = (u, v)$ and $\boldsymbol{b} = (b_x, b_y)$ to this basic state. The linear evolution is

then described by

$$\left(\frac{\partial}{\partial t}+U_0\frac{\partial}{\partial x}\right)u+U_0'v=-\frac{\partial h}{\partial x}+M^2\left(B_0\frac{\partial b_x}{\partial x}+B_0'b_y\right), \tag{3.3a}$$

$$\left(\frac{\partial}{\partial t}+U_0\frac{\partial}{\partial x}\right)v=-\frac{\partial h}{\partial y}+M^2B_0\frac{\partial b_y}{\partial x}, \tag{3.3b}$$

$$\left(\frac{\partial}{\partial t}+U_0\frac{\partial}{\partial x}\right)b_x+B_0'v=U_0'b_y+B_0\frac{\partial u}{\partial x}, \tag{3.3c}$$

$$\left(\frac{\partial}{\partial t}+U_0\frac{\partial}{\partial x}\right)b_y=B_0\frac{\partial v}{\partial x}, \tag{3.3d}$$

$$F^2\left(\frac{\partial}{\partial t}+U_0\frac{\partial}{\partial x}\right)h+H\left(\frac{\partial u}{\partial x}+\frac{\partial v}{\partial y}\right)+H'v=0, \tag{3.3e}$$

where a prime denotes differentiation with respect to y.

Since the coefficients of the system of linear PDEs given by (3.3) are only functions of y, we may consider modal solutions of the form

$$\xi(x,y,t)=\mathrm{Re}\{\hat{\xi}(y)\exp[\mathrm{i}\alpha(x-ct)]\}, \tag{3.4}$$

where α is the (real) wavenumber and c is the phase speed, so that $\omega=\alpha c$ is the wave frequency. We shall be considering a temporal analysis in which α is real and $c=c_r+\mathrm{i}c_i$ is complex; we then observe that such a modal solution grows like $\exp(\alpha c_i t)$. Equations (3.3) reduce to an eigenvalue problem given by the following system of equations, after dropping the hatted notation,

$$\mathrm{i}\alpha(U_0-c)u+vU_0'=-\mathrm{i}\alpha h+M^2(B_0'b_y+\mathrm{i}\alpha B_0b_x), \tag{3.5a}$$

$$\mathrm{i}\alpha(U_0-c)v=-h'+\mathrm{i}\alpha M^2B_0b_y, \tag{3.5b}$$

$$\mathrm{i}\alpha(U_0-c)b_x-U_0'b_y=\mathrm{i}\alpha B_0u-B_0'v, \tag{3.5c}$$

$$\mathrm{i}\alpha(U_0-c)b_y=\mathrm{i}\alpha B_0v, \tag{3.5d}$$

$$\mathrm{i}\alpha(U_0-c)F^2h+\mathrm{i}\alpha u+(Hv)'=0. \tag{3.5e}$$

This system may in fact be reduced to a single second order ODE. Eliminating in favour of v gives a single governing differential equation given by

$$\left[\frac{S^2(Hv)'}{(U_0-c)^2HK^2}\right]'-\left[\frac{\alpha^2S^2}{H(U_0-c)^2}-\frac{U_0'}{H(U_0-c)}\left(\frac{S^2}{(U_0-c)^2K^2}\right)'+\frac{Q_0'S^2}{(U_0-c)^3K^2}\right]Hv=0, \tag{3.6}$$

where $Q_0=-U_0'/H$ is the background potential vorticity, and

$$S^2(y)=(U_0(y)-c)^2-M^2B_0^2(y),\qquad K^2(y)=1-F^2S^2(y). \tag{3.7}$$

We note that equation (3.6) remains unchanged under $\alpha \to -\alpha$, so we may therefore take $\alpha \geq 0$ without loss of generality; thus unstable modes have $c_i > 0$. The ODE (3.6) may be singular in the domain if c is purely real; here, we shall be interested only in instabilities, so this will not be an issue.

The eigenvalue equation (3.6) may be cast into a more compact form. Following Howard (1961), we consider the transformation $Hv = (U_0 - c)^n G$. Equation (3.6) then becomes

$$\left[\frac{(U_0-c)^{2n}\Sigma^2}{HK^2}G'\right]' - \alpha^2(U_0-c)^{2n}\Sigma^2\frac{G}{H} + (n-1)\left[\frac{U_0'(U_0-c)^{2n-1}\Sigma^2}{(K^2)'} + n\frac{(U_0')^2(U_0-c)^{2n-2}\Sigma^2}{K^2} - \frac{Q_0'(U_0-c)^{2n-1}\Sigma^2}{HK^2}\right]\frac{G}{H} = 0. \tag{3.8}$$

We see that taking $n = 1$ gives us the much simplified equation

$$\left[\frac{S^2}{K^2}\frac{G'}{H}\right]' - \alpha^2 S^2\frac{G}{H} = 0, \tag{3.9}$$

which we shall use for the remainder of the linear analysis. In the shallow-water, hydrodynamic limit ($M = 0$), equation (3.6) reduces to equation (3.4) of Balmforth (1999). In the two-dimensional incompressible MHD limit ($F = 0$ and $H = 1$), (3.9) reduces to equation (3.5) of Hughes & Tobias (2001).

We will consider equation (3.9) in either an unbounded domain, for which $|G| \to 0$ as $|y| \to \infty$, or in a bounded domain with rigid side walls, where $G = 0$. Either way, for given real α, (3.9) is then an eigenvalue problem for the unknown phase speed $c = c_r + \mathrm{i}c_i$.

In the hydrodynamic case ($M = 0$), there is an analogy between the shallow-water equations and the compressible Euler equations (e.g., Vallis 2006, §3.1, or Bühler 2009, §1.6). We may thus draw on the previous results of shear instabilities in the compressible hydrodynamic system in order to compare with our results.

3.2 Growth rate bound

A bound on the instability growth rate may be obtained by manipulating equations (3.3) in a manner analogous to that adopted by, for example, Griffiths (2008). The rate of change of the total disturbance energy is given by the combination

$$Hu^* \times (3.3a) + Hv^* \times (3.3b) + (M^2 Hb_x^*) \times (3.3c) + (M^2 Hb_y^*) \times (3.3d) + h \times (3.3e),$$

where * denotes complex conjugate. On adopting the form (3.4) for the perturbations, the real part of this expression gives

$$\begin{aligned}\alpha c_i \left[H\left(|u|^2+|v|^2+M^2|b_x|^2+M^2|b_y|^2\right)+F^2|h|^2\right] = \\ -\,\mathrm{Re}\left[HU_0'\left(vu^*-M^2b_x^*b_y\right)+M^2HB_0'\left(vb_x-u^*b_y\right)\right]-\mathrm{Re}\frac{\partial}{\partial y}(Hvh^*).\end{aligned} \tag{3.10}$$

On integrating over the y domain, employing the boundary condition on v, and manipulating the remaining terms on the right hand side using the fact that $\pm 2\mathrm{Re}(pq^*) \leq |p|^2+|q|^2$ yields

$$\alpha c_i \int E\,\mathrm{d}y \leq \frac{1}{2}(\max|U_0'|+M\max|B_0'|)\int H\left(|u|^2+|v|^2+M^2|b_x|^2+M^2|b_y|^2\right)\,\mathrm{d}y \tag{3.11}$$

with E is equal to the square bracket quantity on the left hand side of equation (3.10). Adding an extra $F^2|h|^2$ term to the integrand on the right hand side respects the inequality, so we obtain the following bound on the growth rate:

$$\alpha c_i \leq \frac{1}{2}(\max|U_0'|+M\max|B_0'|). \tag{3.12}$$

Thus the growth rate of a modal solution is bounded above by the average of the maximum shear and the maximum current. In the absence of a magnetic field, this reduces to the well-known bound in hydrodynamics (Høiland, 1953; Howard, 1961).

3.3 Semicircle theorems

In a classic paper, Howard (1961) proved that, for incompressible, hydrodynamic parallel shear flows, the wave speed c of any unstable mode must lie within a semi-circle in the complex plane determined by properties of the basic state flow. Subsequently, semi-circle theorems have been derived for several other hydrodynamical and hydromagnetic systems (e.g., Kochar & Jain, 1979a,b; Collings & Grimshaw, 1980; Watson, 1981; Hayashi & Young, 1987; Shivamoggi & Debnath, 1987; Thuburn & Haynes, 1996; Hughes & Tobias, 2001; Zaqarashivili *et al.*, 2010). In a similar manner, semi-circle theorems may be derived for the SWMHD system.

Multiplying equation (3.9) by G^*, integrating over y and using the boundary conditions gives the

$$\int \frac{S^2}{K^2}\frac{|G'|^2}{H}\,\mathrm{d}y+\alpha^2\int\frac{S^2|G|^2}{H}\,\mathrm{d}y=0. \tag{3.13}$$

The imaginary part of (3.13) gives

$$c_i\int(U_0-c_r)\chi\,\mathrm{d}y=0, \qquad \text{where} \qquad \chi=\frac{|G'|^2}{H|K|^4}+\alpha^2\frac{|G|^2}{H}\geq 0. \tag{3.14}$$

Equation (3.14) immediately yields Rayleigh's result that, for unstable modes, c_r lies in the range of U_0 (i.e. $U_{0,\min} \le c_r \le U_{0,\max}$). Note this formal bound is independent of F.

On using equation (3.14), the real part of (3.13) gives

$$(c_r^2 + c_i^2) \int \chi \, \mathrm{d}y = \int \chi \left(U_0^2 - M^2 B_0^2\right) \, \mathrm{d}y - F^2 \int \frac{|S|^4}{H|K|^4} |G'|^2 \, \mathrm{d}y, \tag{3.15}$$

which implies that

$$0 \le (c_r^2 + c_i^2) \int \chi \, \mathrm{d}y \le \left(U_0^2 - M^2 B_0^2\right)_{\max} \int \chi \, \mathrm{d}y. \tag{3.16}$$

Thus the complex wave speed c of an unstable eigenfunction must lie within the semi-circle defined by

$$(c_r^2 + c_i^2) \le \left(U_0^2 - M^2 B_0^2\right)_{\max}. \tag{3.17}$$

Another semi-circle bound may be obtained, by using the inequality

$$0 \ge \int (U_0 - U_{0,\max})(U_0 - U_{0,\min}) \chi \, \mathrm{d}y.$$

Substituting from (3.14), deriving an inequality from (3.15) and dropping the integral multiplying F^2 leads to the expression

$$0 \ge \left[c_r^2 + c_i^2 - (U_{0,\min} + U_{0,\max}) c_r + U_{0,\min} U_{0,\max} + M^2 (B^2)_{\min}\right] \int \chi \, \mathrm{d}y, \tag{3.18}$$

which gives another semi-circle bound: the speed c of an unstable eigenfunction must lie within the region defined by

$$\left[c_r - \frac{U_{0,\min} + U_{0,\max}}{2}\right]^2 + c_i^2 \le \left[\frac{U_{0,\max} - U_{0,\min}}{2}\right]^2 - M^2 (B^2)_{\min}. \tag{3.19}$$

Thus, taking these results together, the eigenvalue c of an unstable mode must lie within the intersection of the two semi-circles defined by (3.17) and (3.19). In the absence of magnetic field, semi-circle (3.19) lies wholly within semi-circle (3.17), and we recover the well-known result of Howard (1961).

A drawback of the above approach is that the bounds do not contain the Froude number F. It is possible to include F into the semi-circle bounds using similar manipulations to that used by Pedlosky (1964), but this does not tighten the bounds; see the Section 3.5 for details.

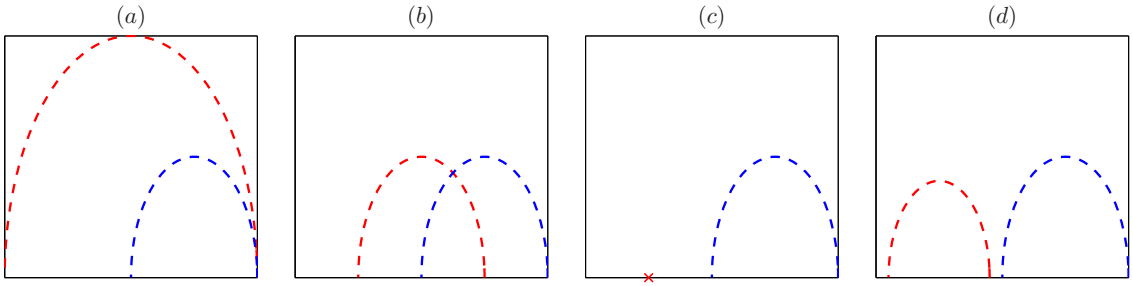

Figure 3.1: Four possible regimes for the semicircle bounds (3.17) and (3.19). They could: (a) completely overlap; (b) partially overlap; (c) shrink to a point; (d) be disjoint. For the latter two cases, the intersection region is empty, so there are no normal mode instabilities.

3.3.1 Stability criteria

As observed by Hughes & Tobias (2001), for non-zero magnetic field there is the possibility of the two semi-circles overlapping, being disjoint, or indeed ceasing to exist; see Figure 3.1. Thus, in addition to giving eigenvalue bounds for unstable modes, these results also provide sufficient conditions for stability. From (3.17) and (3.19) it follows that the basic state is linearly stable if any one of the following three conditions is satisfied:

$$M|B_0| \geq |U_0| \qquad \text{everywhere in the domain;} \tag{3.20}$$

$$M|B_0|_{\min} \geq \frac{|U_{0,\max} - U_{0,\min}|}{2}; \tag{3.21}$$

$$\frac{U_{0,\max} + U_{0,\min}}{2} - \sqrt{\left(\frac{U_{0,\max} - U_{0,\min}}{2}\right)^2 + M^2(B_0^2)_{\min}} \geq \sqrt{\left(U_0^2 - M^2 B_0^2\right)_{\max}}. \tag{3.22}$$

This result is equivalent to that given in Hughes & Tobias (2001) for incompressible MHD.

3.4 Parity results

In the hydrodynamic case, it is known that, when the basic state possesses certain symmetries, the allowed form of eigenvalues or the eigenfunctions to the instability problem is appropriately restricted (see, for example, Drazin & Howard, 1966). Similar results may be generalised to SWMHD if we further assume that $B_0^2(y)$ and $H(y)$ are even functions about $y = 0$.

Following Howard (1963), when $U(y)$ is odd about $y = 0$, we notice that (3.9) is unchanged under $c \to -c$ and $G(y) \to G(-y)$. By considering the conjugate equation, we see that an unstable eigenfunction must be accompanied by eigenvalues of the form $c = \pm c_r \pm \mathrm{i}c_i$, so unstable solutions are either standing waves ($c_r = 0$) or a pair of counter-propagating waves with the same phase speed. As argued by Howard (1963), the symmetry in the basic state implies there is no preferred direction for wave propagation, consistent with the form the eigenvalues are allowed to take.

Now consider the case when $U(y)$ is even about $y = 0$. Then it is seen that

$$G_e(y) = \frac{1}{2}\left[G(y) + G(-y)\right] \qquad \text{and} \qquad G_o(y) = \frac{1}{2}\left[G(y) - G(-y)\right] \tag{3.23}$$

are also eigenfunctions of (3.9). If we now take G_o multiplied by (3.9) with $G = G_e$, and subtract from G_e multiplied by (3.9) with $G = G_o$, integrating over the y-domain gives

$$[G_e' G_o - G_o' G_e]_{-L_y}^{L_y} = 0, \tag{3.24}$$

owing to the imposed boundary conditions on the eigenfunction. The Wronskian of G_e and G_o is equal to zero implies that the two functions are linearly dependent throughout the domain. This cannot be the case so one of them is identically zero, and therefore we conclude the eigenfunction corresponding to a particular eigenvalue is either an even or odd function about $y = 0$.

3.5 Discussion

Equation (3.8) **for other values of** n

Here and in later chapters, we consider the $n = 1$ case in equation (3.8), leading to equation (3.9) from which we obtain the semi-circle theorems and parity results. Howard (1961) noticed that by taking different values of n, notably the $n = 0$ and $n = 1/2$ cases, different results could be obtained.

In the absence of MHD effects, the $n = 0$ case does indeed give us a generalisation of Rayleigh's criterion for the $F = 0$ case, as noted already by Balmforth (1999). When MHD effects are present, the usual manoeuvre (e.g., Drazin & Reid, 1981, §22) gives an expression involving c which needs to change sign over the domain for there to be an instability (e.g., Hughes & Tobias,

2001). This is of minimal use since we need to solve the full problem before we can use the criterion.

A different approach may yet give stability theorems. A method due initially to Arnol'd (1966a) considers using wave activity invariants and deducing formal stability results that can, in certain cases, be extended to nonlinear stability. Briefly, following Shepherd (1990), we consider the non-canonical Hamiltonian representation of a system (fluid systems written in the Eulerian formalism generally require the non-canonical representation), given by

$$\frac{\partial u}{\partial t} = \mathsf{J}\frac{\delta \mathcal{H}}{\delta u}, \tag{3.25}$$

where u is the state vector, $\mathcal{H}$ is the Hamiltonian functional, and J is the symplectic (Poisson) operator. In the canonical representation, $u = (p, q)$, where p and q are the generalised co-ordinates (usually momentum and position), and we see that

$$\mathsf{J} = \begin{pmatrix} -1 & 0 \\ 0 & 1 \end{pmatrix}. \tag{3.26}$$

The benefit with using the non-canonical representation is that it makes explicit the Casimir invariants associated with the kernel of J. For example, in two-dimensional incompressible hydrodynamics, the Casimirs are functions of vorticity. By Noether's theorem, conservation laws are associated with symmetries (and vice-versa), and in the incompressible hydrodynamic system, the Casimirs are associated with the particle relabelling symmetry (e.g., Salmon, 1998, §7). In the hydrodynamic shallow-water system, the Casimirs are $\mathcal{C} = \int f(q)\,\mathrm{d}S$, where f is an arbitrary function of the potential vorticity q (e.g., Shepherd, 1990); in the SWMHD system, the Casimirs are of the form

$$\mathcal{C} = \int [f(A) + h_t g(A)]\,\mathrm{d}S, \tag{3.27}$$

where $h_t = H + F^2 h$, and f and g are arbitrary functions of the flux function A, defined as $h_t \boldsymbol{b} = \boldsymbol{e} \times \nabla A$ (Dellar, 2002).

The observation then is that, for a steady basic state U_0, we have

$$\frac{\partial U_0}{\partial t} = \mathsf{J}\left.\frac{\delta \mathcal{H}}{\delta u}\right|_{u=U_0} = 0. \tag{3.28}$$

Now, the Hamiltonian functional $\mathcal{H}$ and the Casimir functional $\mathcal{C}$ are both invariants of the system, and so we have

$$\left.\frac{\delta \mathcal{H}}{\delta u}\right|_{u=U_0} = -\left.\frac{\delta \mathcal{C}}{\delta u}\right|_{u=U_0} \tag{3.29}$$

where the minus sign is by convention, and from this we may work out the Casimir functionals $\mathcal{C}$. Then we construct the wave activity functional

$$\mathcal{A}(u) = \mathcal{H}(u) - \mathcal{H}(U_0) + \mathcal{C}(u) - \mathcal{C}(U_0), \tag{3.30}$$

which is an invariant of the dynamics; $\mathcal{A}$ here is sometimes called the pseudo-energy. $\mathcal{A}$ may be further augmented by other conserved functionals, such as along-stream momentum (relevant here for the shear flow problem). The point is that, under the small amplitude approximation, this quantity can serve as a Hamiltonian for the linearised dynamics, act as a norm to measure disturbance growth, and hence provide a means to obtain formal stability criteria for linear stability. Furthermore, it is usually quadratic, and so in certain cases, additional convexity estimates can result in nonlinear, Lyapunov-type stability criteria. In the incompressible hydrodynamic case for plane parallel shear flows, it was shown that Rayleigh's condition comes from considering the pseudo-energy (e.g., Salmon, 1998, §7), whilst the Rayleigh–Fjørtoft condition comes from augmenting the pseudo-energy with an additional momentum functional. These may also be promoted to nonlinear stability conditions and appear as special cases of Arnol'd's theorems.

The idea of using wave activity invariants in various disguises has been employed previously by various authors (e.g., Taylor, 1915; Blumen, 1970; Satomura, 1981; Eliassen, 1983; Ripa, 1983). The advantage of using the Hamiltonian structure is that wave activities may be derived in a systematic manner, as well as making obvious the links with the underlying structure of the system of equations and its associated symmetries/conservation laws. There have been several works that invoke the Hamiltonian structure explicitly (e.g., Holm *et al.*, 1985; McIntyre & Shepherd, 1987; Dritschel, 1988; Shepherd, 1990, 1992; Vladimirov & Moffatt, 1995; Vladimirov *et al.*, 1996; Nycander, 2003; Shepherd, 2003), and it would certainly be worth investigating whether such a procedure can yield a result for the SWMHD system.

For the $n = 1/2$ case, using manipulations similar to Chimonas (1970), the growth rate bound (3.12) may be obtained. The method used in the main body of this chapter is substantially cleaner and more intuitive, and since we do not obtain a new result, a presentation of the working has been omitted.

Further extensions to the semi-circle theorem(s)

The two semi-circle bounds (3.17) and (3.19) are independent of F, and it would be desirable to obtain a formal bound that includes F dependence to reflect the fact that we are considering a shallow-water system. The term of interest in equation (3.15) is

$$F^2 \int \frac{|S^2|^2}{H|K^2|^2}|G'|^2 \,\mathrm{d}y, \tag{3.31}$$

and we are interested in bounding this term. The simplest thing to do is to maximise or minimise $|S^2|^2$. However, a minimisation procedure yields

$$|S^2|^2 = [(U_0 - c_r)^2 - (c_i^2 + M^2 B_0^2)] + 4c_i^2(U_0 - c_r)^2 \geq 4c_i^2(U_0 - c_r)^2, \tag{3.32}$$

which does not have a positive non-zero lower bound.

We could however consider bounding $|S^2|^2$ from above. This gives

$$\begin{aligned} |S^2|^2 = [(U_0 - c_r)^2 - (c_i^2 + M^2 B_0^2)] + 4c_i^2(U_0 - c_r)^2 &\leq (1 + 4c_i^2)(U_0 - c_r)^2 \\ &\leq (1 + 4c_i^2)(U_{0,\max} - U_{0,\min})^2 \end{aligned} \tag{3.33}$$

since $U_{0,\min} \leq c_r \leq U_{0,\max}$. After taking a modulus sign accordingly, the semi-circle result (3.19) is modified to

$$\begin{aligned} \left(c_r - \frac{U_{0,\max} + U_{0,\min}}{2}\right)^2 + [1 - 4F^2(U_{0,\max} - U_{0,\min})^2]c_i^2 \\ \leq (U_{0,\max} - U_{0,\min})^2 \left(\frac{1}{4} + F^2\right) - M^2(B_0^2)_{\min}. \end{aligned} \tag{3.34}$$

This manipulation is similar to that of Pedlosky (1964), except in his case a Poincaré inequality was also used. This formal bound is worse than the original formal semi-circle bounds as it becomes less strict as F increases, to such a point where the ellipse becomes ill-defined.

A similar manipulation modifies the semi-circle (3.17) to

$$0 \leq (c_r^2 + c_i^2) \leq (U_0^2 - M^2 B_0^2)_{\max} - F^2(1 + 4c_i^2)(U_{0,\max} - U_{0,\min})^2, \tag{3.35}$$

where in this case a change of sign is required.

We have attempted to adapt the elegant method used by Kochar & Jain (1979a) to our case. The original method was successful in including the stratification term (the term multiplied by the Richardson number) in the case considered by Howard (1961) to give a semi-ellipse theorem.

Similar approaches have been tried here and we were unsuccessful in generating something similar for the shallow-water or MHD cases. The method of Barston (1980) has also been attempted (working in the Lagrangian formulation and considering relevant supremum or infimum of the associated operators) but nothing new has been derived from employing that formalism.

Chapter 4

Instabilities of piecewise-constant profiles

There are many variations of the shear flow instability problem that may be studied, with different profiles of the magnetic field, parameter values, and so forth. We restrict ourselves to the simpler case where there is no topography ($H = 1$) and the background magnetic field is uniform ($B_0 = 1$, so that M is now our measure of the field strength). This simplifies the problem somewhat and in certain limits reduces to problems that have been previously studied in the incompressible and/or hydrodynamic case. With these restrictions, equation (3.9) becomes

$$\left[\frac{S^2}{K^2}G'\right]' - \alpha^2 S^2 G = 0, \tag{4.1}$$

where, again, $S^2 = (U_0 - c)^2 - M^2$, and $K^2 = 1 - F^2 S^2$. We seek solutions in an unbounded domain, with

$$|G| \to 0 \qquad \text{as} \qquad |y| \to \infty. \tag{4.2}$$

We consider velocity profiles $U_0(y)$ that are piecewise-constant. In addition to allowing for the problem to be solved analytically, such profiles usually reveal some features that are present in the analogous smooth profiles, which we consider in Chapter 5.

If $U_0(y)$ is discontinuous at $y = y_0$, then the eigenfunction G must satisfy two jump conditions at $y = y_0$. In the usual way (e.g., Drazin & Reid, 1981, §23), denoting η to be the cross-stream displacement (so $v = D\eta/Dt$), the (linearised) kinematic boundary condition implies

$$[\eta]_{y_0^-}^{y_0^+} = \left[\frac{v}{U_0 - c}\right]_{y_0^-}^{y_0^+} = [G]_{y_0^-}^{y_0^+} = 0. \tag{4.3a}$$

The free surface displacement (and so pressure) must also be continuous at $y = y_0$. The corresponding condition on G is most easily derived by integrating (4.1) across $y = y_0$, yielding

$$\left[\frac{S^2}{K^2}G'\right]_{y_0^-}^{y_0^+} = 0. \tag{4.3b}$$

4.1 Vortex sheet

We first consider the velocity profile

$$U_0(y) = \begin{cases} +1, & y > 0, \\ -1, & y < 0. \end{cases}$$

Then, for $y \neq 0$, (4.1) becomes $G'' - \alpha^2 K^2 G = 0$. Using (4.2) and (4.3a), we thus find

$$G(y) = \begin{cases} \exp\left(-\alpha K_+ y\right), & y > 0, \\ \exp\left(+\alpha K_- y\right), & y < 0, \end{cases} \tag{4.4}$$

where

$$K_\pm = \sqrt{1 - F^2[(1 \mp c)^2 - M^2]}, \qquad \mathrm{Re}\,(K_\pm) > 0. \tag{4.5}$$

The second jump condition (4.3b) then implies an eigenvalue relation for c:

$$\frac{(1-c)^2 - M^2}{K_+} + \frac{(1+c)^2 - M^2}{K_-} = 0. \tag{4.6}$$

Note that c is independent of wavenumber α, so any unstable mode with $c_i > 0$ has an unbounded growth rate as $\alpha \to \infty$. This is an artefact of considering ideal fluids; viscosity will act preferentially on small scales and remove this unphysical behaviour.

There are several special cases. When $F = M = 0$, we recover the classical Kelvin–Helmholtz instability with $c = \pm\mathrm{i}$. When $F = 0$ but $M \neq 0$, (4.6) reduces to the incompressible MHD case with $c^2 = -(1 - M^2)$, a result due to Michael (1953). The Kelvin–Helmholtz instability is stabilized when $M \geq 1$, which might be expected physically as the disturbance has to do work to bend the field lines. When $M = 0$ but $F \neq 0$, we obtain the classical hydrodynamic shallow-water case, which is analogous to two-dimensional compressible hydrodynamics. The Kelvin–Helmholtz instability is stabilized when $F \geq \sqrt{2}$ (Bazdenkov & Pogutse, 1983; Miles, 1958), which might be expected physically as the disturbance has to do work to move the free surface against gravity. Thus, increasing F or M in the absence of the other is stabilising.

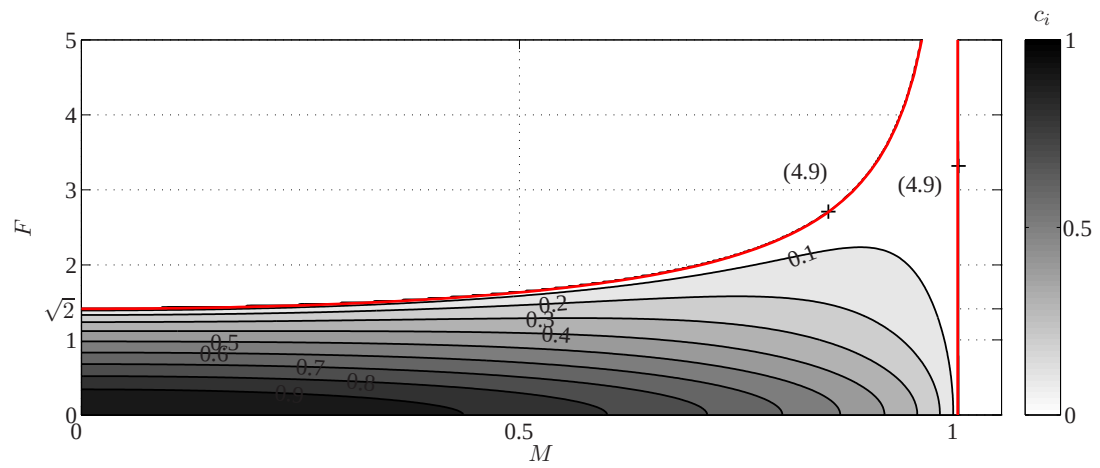

Figure 4.1: Contours of $\mathrm{Im}(c_\mathrm{v})$ given by the expression (4.8), with stability boundaries (4.9).

In the general case where F and M are both non-zero, (4.6) can be rearranged and squared to yield

$$c\{2(1+c^2-M^2)-F^2[(1-c)^2-M^2][(1+c)^2-M^2]\}=0. \tag{4.7}$$

Here we will ignore the degenerate case with $c=0$ that occurs when $M=1$. We have checked numerically that only two roots of (4.7) also satisfy (4.6); they are $c=\pm c_\mathrm{v}$, where

$$c_\mathrm{v}=\mathrm{i}\left[\frac{\sqrt{1+4F^2+4F^4M^2}-(1+F^2+F^2M^2)}{F^2}\right]^{1/2}. \tag{4.8}$$

Note that $\mathrm{Re}(c_\mathrm{v})=0$. A contour plot of $\mathrm{Im}(c_\mathrm{v})$ is shown in Figure 4.1. Using (4.8), we see that there is instability only if

$$M<1 \qquad \text{and} \qquad F<\sqrt{\frac{2}{1-M^2}}. \tag{4.9}$$

Although, at fixed M, increasing F is always stabilising, the critical value of F above which the flow is stable increases as M increases towards 1. Thus, although magnetic field and free surface effects are stabilising in isolation, together they can lead to instabilities at large values of F.

We have also solved the full equation (4.6) numerically via a Newton iteration scheme, and the roots associated with instability are described by c_v given by (4.8). No other modes of instability were found from solving numerically (4.6).

4.1.1 Asymptotic analysis: $M \approx 1$

The tongue region of instability at $M \lesssim 1$ may be further investigated via an asymptotic analysis. Writing $\mu = (1 - M^2) \ll 1$ and $F^2 = O(1)$, equation (4.7) is given by

$$0 = c^4 - 2\left[\frac{1}{F^2} + 2 - \mu\right] c^2 - \mu\left[\frac{2}{F^2} - \mu\right]. \tag{4.10}$$

We know the roots are stable when μ is non-positive, i.e. $M \geq 1$. The two dominant balances are $c^2 = O(1)$ and $c^2 = O(\mu)$. The $O(1)$ roots are real both at the leading order and at the next order correction and hence are ignored. The $O(\mu)$ roots take the form

$$c \sim \mathrm{i}\sqrt{\frac{1 - M^2}{1 + 2F^2}} \qquad \text{as} \qquad (1 - M^2) \to 0^+, \quad F^2 = O(1). \tag{4.11}$$

As expected, this root is stable when $M \geq 1$, in accordance with the stability criterion. For the case $F^2 = \epsilon^{-1} \gg 1$, if $\mu \ll \epsilon$, then we have (4.11) to leading order, and if $\mu \gg \epsilon$, we can show that the roots are real, so we consider the case $\mu = \lambda\epsilon$ with $\lambda = O(1)$. The dominant balance gives either $c^2 = O(1)$ or $c^2 = O(\epsilon^2)$, and again the $O(1)$ roots are real at leading order and at the next order correction so will be ignored. The $O(\epsilon)$ roots take the form

$$c^2 \sim \epsilon(1 - M^2)^2 \frac{1 - 2\lambda}{4}.$$

Notice that we require $\lambda > 1/2$ for instability, i.e.

$$F < \sqrt{\frac{2}{1 - M^2}},$$

and we recover one of our conditions in (4.9). Restoring the scalings of relevant terms, we have

$$c \sim \mathrm{i}\sqrt{\frac{1 - M^2}{2F^2} - \frac{(1 - M^2)^2}{4}} \qquad \text{as} \qquad F^{-2} \sim (1 - M^2) \to 0^+. \tag{4.12}$$

The exact result (4.8) and the asymptotic results (4.11) and (4.12) are plotted in Figure 4.2, and the quantitative agreement between the asymptotics and exact results is apparent.

4.2 Rectangular jet

We now consider the velocity profile

$$U_0(y) = \begin{cases} 1, & |y| < 1, \\ 0, & |y| > 1. \end{cases} \tag{4.13}$$

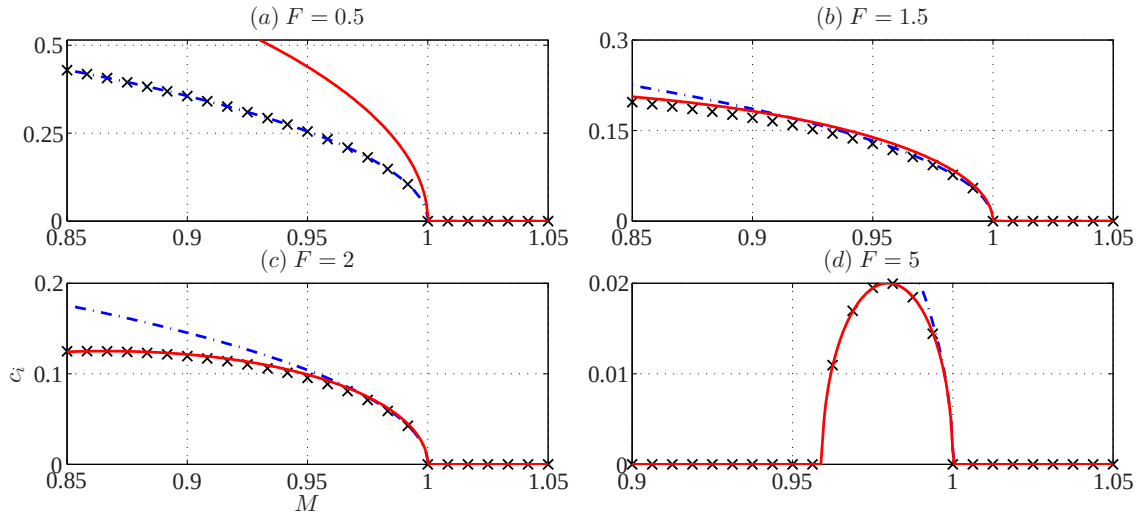

Figure 4.2: Comparison between the exact results (4.8), given by crosses, and the asymptotic results (4.11) and (4.12), given by the dot-dashed line and solid line respectively. Note the use of different axes here.

Then, (4.1) and (4.2) imply

$$G = \begin{cases} C_+ \exp\left(-\alpha K_0 (y-1)\right), & y > 1, \\ C_e \cosh(\alpha K_1 y) + C_o \sinh(\alpha K_1 y), & |y| < 1, \\ C_- \exp\left(+\alpha K_0 (y+1)\right), & y < -1, \end{cases} \tag{4.14}$$

for some C_+, C_-, C_e and C_o, where

$$K_0 = \sqrt{1 - F^2(c^2 - M^2)}, \qquad K_1 = \sqrt{1 - F^2[(1-c)^2 - M^2]}. \tag{4.15}$$

We consider modes that satisfy $\mathrm{Re}(K_0) > 0$, i.e. modes that decay at infinity.

Since the profile is even about $y = 0$, we may follow Rayleigh's formulation (e.g., Drazin & Reid, 1981, Q1.7) and consider eigenfunctions that are either even or odd. For the even mode, we have $C_o = 0$, and the matching conditions gives

$$\frac{c^2 - M^2}{K_0} + \frac{(1-c)^2 - M^2}{K_1} \tanh(\alpha K_1) = 0. \tag{4.16}$$

For the odd mode, we have $C_e = 0$, and matching gives

$$\frac{c^2 - M^2}{K_0} + \frac{(1-c)^2 - M^2}{K_1} \coth(\alpha K_1) = 0. \tag{4.17}$$

When there is no magnetic field, these equations reduce to special cases of results given by Gill (1965), who considered corresponding instabilities for two-dimensional compressible hydrodynamics.

Equations (4.16) and (4.17) will need to be solved numerically; here this is done using a Newton iteration scheme, tracking from the mode that exists at $M = 0$ and $F = 0$. Contours of $\mathrm{Im}(c_i)$ are shown in Figure 4.3 for a wide range of parameters. Here, $c_r > 0$, and two types of roots are found: roots that have fixed c_r are denoted by solid contours, and other roots that have varying c_r, found in the $\alpha \gg 1$, $F > 2\sqrt{2}$ regime, denoted by dashed contours. These roots have been found previously by Gill (1965) in the compressible hydrodynamic setting; by analogy, we will refer to these as supersonic modes. We observe for now these supersonic modes are weak instabilities. Other features displayed by Figure 4.3 include: (i) at large α (Figure 4.3*a*,*b*), the even and odd modes lead to instabilities of comparable strength, which mimic the vortex sheet of Figure 4.1; (ii) the even mode is generally more unstable than the odd mode; (iii) neither mode is unstable beyond a cutoff $M = 1/2$; (iv) for small α and moderate F (Figure 4.3*e*,*f*), there is a cutoff when M is smaller than $M = 1/2$. Using asymptotic analyses, we will now quantitatively describe properties (i) and (iv), and say something about property (ii).

4.2.1 Vortex sheet like behaviour at large α

Assuming we have $\mathrm{Re}(K_1) > 0$, and M and F are of moderate size, then we notice that $\tanh(\alpha K_1) \to 1$, so both (4.16) and (4.17) may be approximated by

$$\frac{-(c^2 - M^2)}{\sqrt{1 - F^2(c^2 - M^2)}} = \frac{(1-c)^2 - M^2}{\sqrt{1 - F^2[(1-c)^2 - M^2]}}. \tag{4.18}$$

Solving for $\tilde{c} \equiv c - \tilde{U}$ where $\tilde{U} = 1/2$, we notice the resulting equation is similar in form to the governing equation for the vortex sheet (4.6) up to extra numerical factors. The solution to (4.18) is seen to be given by

$$\tilde{c} = (c - \tilde{U}) = \mathrm{i}\left[\frac{\sqrt{1 + 4F^2\tilde{U}^2 + 4F^4M^2\tilde{U}^2} - (1 + F^2\tilde{U}^2 + F^2M^2)}{F^2}\right]^{1/2}. \tag{4.19}$$

The region where there is instability is given by

$$M < \frac{1}{2} \qquad \text{and} \qquad F < \sqrt{\frac{2}{1/4 - M^2}}. \tag{4.20}$$

Physically, a sufficiently localised short-wave disturbance would only ‘see’ one of the flanks of the jet, and thus resemble a vortex sheet instability. For the $M = 0$ case, this result is consistent with the condition given in Gill (1965).

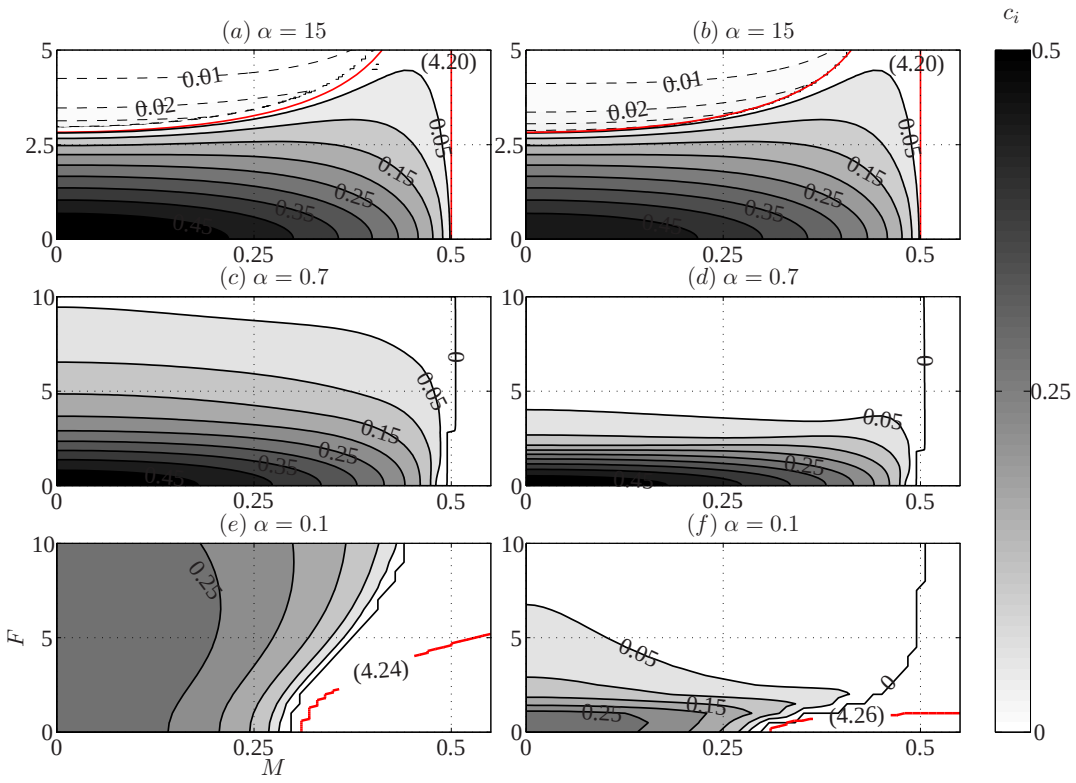

Figure 4.3: Contours of c_i, computed numerically for the even mode (equation (4.16), left column) and the odd mode (equation (4.17), right column) of the rectangular jet at some selected α. Note the different choice of axes used in the bottom panels. The stability boundary according to computed results is the contour labelled by '0'. The stability boundaries (4.20), (4.24) and (4.26) are plotted also in the appropriate panels.

Returning briefly to these supersonic instabilities that exists in the region beyond the cutoff given by conditions in (4.20), the interpretation by Gill (1965) is that, even though the modes are effectively isolated vortex sheet instabilities when $\alpha \gg 1$, when the stability boundary given by (4.20) is crossed, the isolated modes on one flank become radiating, interact with the mode on the other flank, and leading to instability. Such instabilities arising from interacting radiating waves is termed resonant over-reflection (e.g., McIntyre & Weissman, 1978; Benilov & Lapin, 2013)[1]. Although these instabilities exist, we observe that these have growth rates that are small, and thus have not investigated them in great detail here.

[1]This is in contrast to over-reflection, which does not necessarily lead to instability (e.g., Acheson, 1976).

4.2.2 Long-wave cutoff due to the magnetic field

Even mode

We consider the even mode first. Assuming that

$$\mathrm{Re}(K_1) > 0, \qquad \alpha \ll 1, \qquad \text{and} \qquad \alpha F \ll 1, \tag{4.21}$$

we have $\tanh(\alpha K_1) \approx \alpha K_1$, and (4.16) becomes

$$\frac{-(c^2 - M^2)}{\sqrt{1 - F^2(c^2 - M^2)}} = \alpha[(1-c)^2 - M^2]. \tag{4.22}$$

Suppose that $F^2 = O(1)$. If $M = O(1)$ also, then $c = \pm M$ at leading order, and c is real at the next correction. Letting $M^2 = \mu \ll 1$, the interesting results comes from taking $\alpha \sim \mu$, which gives, at leading order in μ,

$$c \sim \mathrm{i}\sqrt{\alpha - M^2} \qquad \text{as} \qquad M^2 \sim \alpha \to 0^+, \quad F^2 = O(1). \tag{4.23}$$

When $\mu = M^2 \ll \alpha$, we recover the result of Gill (1965). The presence of the magnetic field is to reduce the strength of the instability, and in this case to introduce a long-wave cutoff. The Froude number dependence comes in at the next correction.

Consider now $F^2 = \epsilon^{-1} \gg 1$. We let $\alpha \sim \epsilon^s$; to be consistent with the assumptions stated in (4.21), we need $s > 1/2$. Again, $M^2 = O(1)$ results in a real c, so we consider $M^2 = \mu \ll 1$. It may be checked that the balance that gives a non-zero c_i at leading order is $\mu \sim \epsilon \sim \alpha$. This implies $c \sim \epsilon^{1/2} \sim \alpha^{1/2}$, with the corresponding result

$$c \sim \mathrm{i}\left[\frac{\alpha^2 F^2}{2} - M^2 + \sqrt{\frac{\alpha^4 F^4}{4} + \alpha^2}\right]^{1/2} \qquad \text{as} \qquad M^2 \sim F^{-2} \sim \alpha \to 0^+. \tag{4.24}$$

We see that there is a long-wave cutoff due to the presence of a magnetic field. Notice also that, when F is small, expression (4.24) reduces formally to (4.23).

Figure 4.4 shows the computed growth rates over a range of α compared with the corresponding asymptotic results. The computed results are found by solving the full eigenvalue equation (4.16) with a Newton root finding method. Notice that the domain of validity of (4.24) requires $\alpha F^{-2} = O(1)$, consistent also with the numerical results given in the bottom panels of Figure 4.3. In both cases, we note that $c \sim \mathrm{i}\alpha^{1/2}$; we will see that the scaling is different for the odd mode.

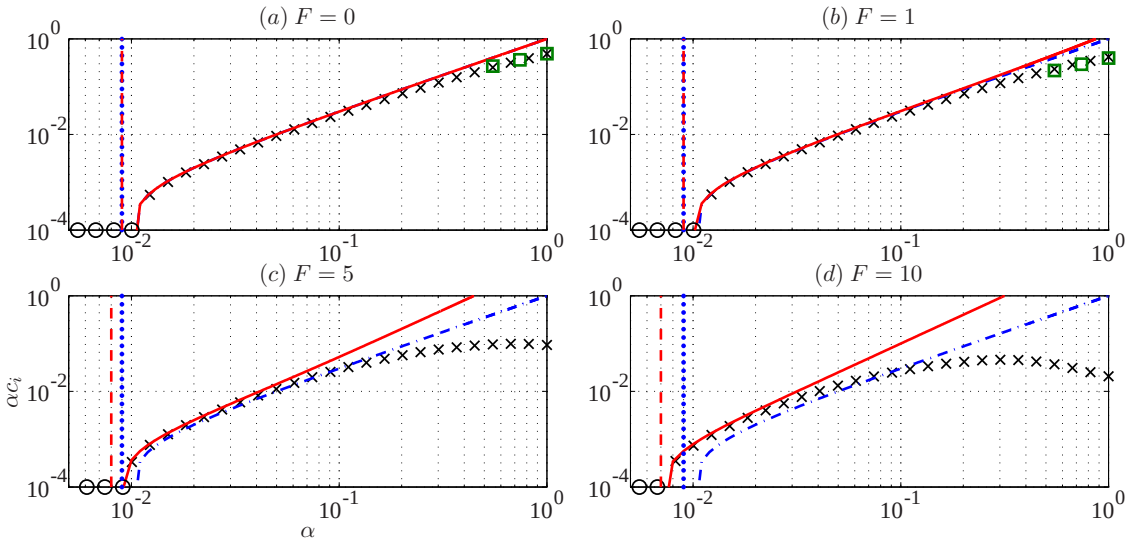

Figure 4.4: Comparison of the computed growth rates and the predicted growth rates from the asymptotic results, for the even mode of the rectangular jet at $M = 0.1$. The computed results are given by crosses (and circles when the computed result is smaller than what may be displayed at this axis choice), $\alpha\times$(4.23) is given by the dot-dashed line (cutoff plotted as vertical dotted line) and $\alpha\times$(4.24) is given by the solid line (cutoff plotted as vertical dashed line). The corresponding growth rate as predicted by the large α asymptotics (4.18) is plotted as squares when this growth rate is non-zero.

Odd mode

The analysis for the odd mode is entirely analogous except for some small complications. Using the assumptions in (4.21), the governing eigenvalue equation for the odd mode given by (4.17) may be approximated by

$$\frac{(1-c)^2 - M^2}{1 - F^2[(1-c)^2 - M^2]} = \frac{-\alpha(c^2 - M^2)}{\sqrt{1 - F^2(c^2 - M^2)}}. \tag{4.25}$$

Consider first the case where $F^2 = O(1)$. It may again be seen that $M^2 = O(1)$ gives real solutions at both leading order and at the next correction. Taking $M^2 = \mu \ll 1$, we again have $\mu \sim \alpha$ with leading order solution $c_0 = 1$, with the relevant asymptotic result

$$c \sim 1 + \mathrm{i}\left[\frac{\alpha}{\sqrt{1-F^2}} - M^2\right]^{1/2} \qquad \text{as} \qquad M^2 \sim \alpha \to 0,\ F^2 = O(1). \tag{4.26}$$

We immediately see there is a problem: the analysis is only valid for F^2 not close to 1, and we need to look in more detail at the case $F^2 = 1 + \epsilon$. We note that (4.26) suggests also a long-wave cutoff due to the magnetic field (with result plotted in Figure 4.3), that $c_i \sim \alpha^{1/2}$, and also that the growth rate should peak near $F^2 = 1$.

For $F^2 = 1 + \epsilon$, to get an instability we need to take $c = 1 + \epsilon c_1$, with $\mu^{1/2} \sim \alpha^{2/5} \sim \epsilon$ where $M^2 = \mu \ll 1$; the other choice is $\epsilon \sim \mu$, which gives a real c_1. The equation for c_1 is then given by the quintic equation

$$(c_1^2 - \nu)^2(2c_1 + 1) = -\lambda^2, \tag{4.27}$$

where ν and λ are $O(1)$ constants with $\mu = \nu\epsilon^2$ and $\alpha = \lambda\epsilon^{2/5}$. This unfortunately has no closed form solution. Even though we cannot solve for c_1 in closed form, we can say that c_1 is expected to be complex because of the numerical results presented in Figure 4.3. We observe that $c = 1 + \alpha^{2/5}c_1$ with $\mathrm{Im}(c_1) > 0$, which suggests the odd mode may be more unstable than the even mode at this $F \approx 1$ regime. We will revisit the possibility of the odd mode dominating in the next subsection.

For larger values of F, we let $F^2 = \epsilon^{-1} \gg 1$. On taking $M^2 = \mu \ll 1$, we obtain the result

$$c \sim 1 + \sqrt{\frac{\mathrm{i}\alpha}{F} + M^2} \qquad \text{as} \qquad \frac{1}{F^2} \sim M^{4/(2s+1)} \sim \alpha^{1/s} \to 0^+ \qquad (s > 1/2), \tag{4.28}$$

where s may be left as a free parameter, and this result now suggests there is no cutoff due to the magnetic field, as c_i is small but non-zero. The fact that there is no longer a cutoff at small α suggests also that in this high F small α regime, the odd modes are preferred over the even mode. We also notice that this result is formally equivalent to the result (4.26) in the large F limit.

We compare the numerical results from the full equation (4.17) to the asymptotic results given by equation (4.26) – equation (4.28) is the large F limit of (4.26) so has been omitted. We plot in Figure 4.5 the growth rate αc_i against α, and the agreement between the numerical and the asymptotic results is apparent. The scaling suggested by the $F^2 = 1 + \epsilon$ analysis has also been checked and agreement is observed.

4.2.3 Preferred mode of instability: even versus odd modes.

As we have noted, the odd mode may be the preferred mode of instability in certain regimes. To investigate this more thoroughly, we carried out a scan over (M, F, α) space, computing the eigenvalues corresponding to the even and the odd modes. This is converted into the regime diagram given by Figures 4.6 and 4.7, showing the regions in parameter space where one or the other mode is preferred.

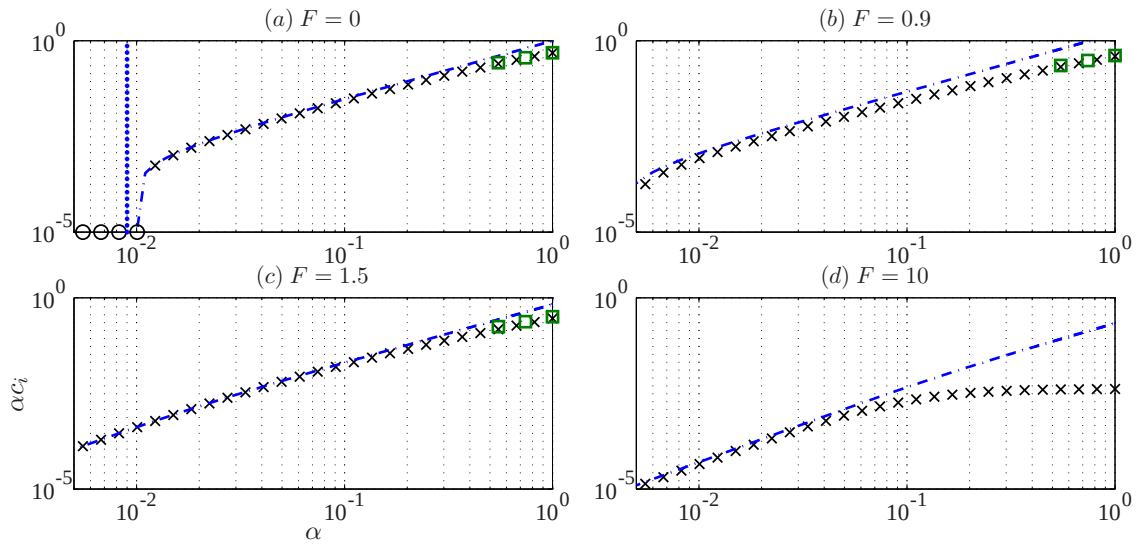

Figure 4.5: Comparison of the computed growth rates and the predicted growth rates from the asymptotic results, for the odd mode of the rectangular jet at $M = 0.1$. The computed results are given by crosses (and circles when the computed result is smaller than what may be displayed at this axis choice), $\alpha\times$(4.26) is given by the dot-dashed line (cutoff plotted as vertical dotted line). The corresponding growth rate as predicted by the large α asymptotics (4.18) is plotted as squares when this growth rate is non-zero.

The mode preference transition at small F may be quantified by a small F asymptotic analysis. First note that when F is zero, i.e. $K = 1$, the closed form solution to the equations for the even and odd modes may be found from equations (4.16) and (4.17), given respectively by

$$c_e^{(0)} = \frac{T \pm \sqrt{-T + M^2(1+T)^2}}{1+T}, \qquad c_o^{(0)} = \frac{1 \pm \sqrt{-T + M^2(1+T)^2}}{1+T}, \tag{4.29}$$

where $T = \tanh\alpha$. Notice that the two modes are equally unstable. The critical M above which there is no instability for any value of α may be shown to be $M_c = 1/2$, and there is a long-wave cutoff due to the magnetic field given by

$$\alpha_{c0} = \frac{1 - 2M^2 - \sqrt{1-4M^2}}{2M^2}. \tag{4.30}$$

This cutoff is plotted as α_{c0} in Figures 4.6 and 4.7.

Now, we let $F^2 = \epsilon \ll 1$ and assume that α and M are of moderate size. It may be shown that the appropriate form of the asymptotic solution is $c = c^{(0)} + F^2 c^{(1)} + O(F^4)$. Substituting this into (4.16), (4.17), and manipulating accordingly, we obtain

$$c_e^{(1)} = \mathrm{i}[T + T^2 + \alpha(T^2-1)]\frac{1 - T - 2\mathrm{i}\sqrt{T - M^2(1+T)^2}}{4(1+T)^4\sqrt{T - M^2(1+T)^2}} \tag{4.31a}$$

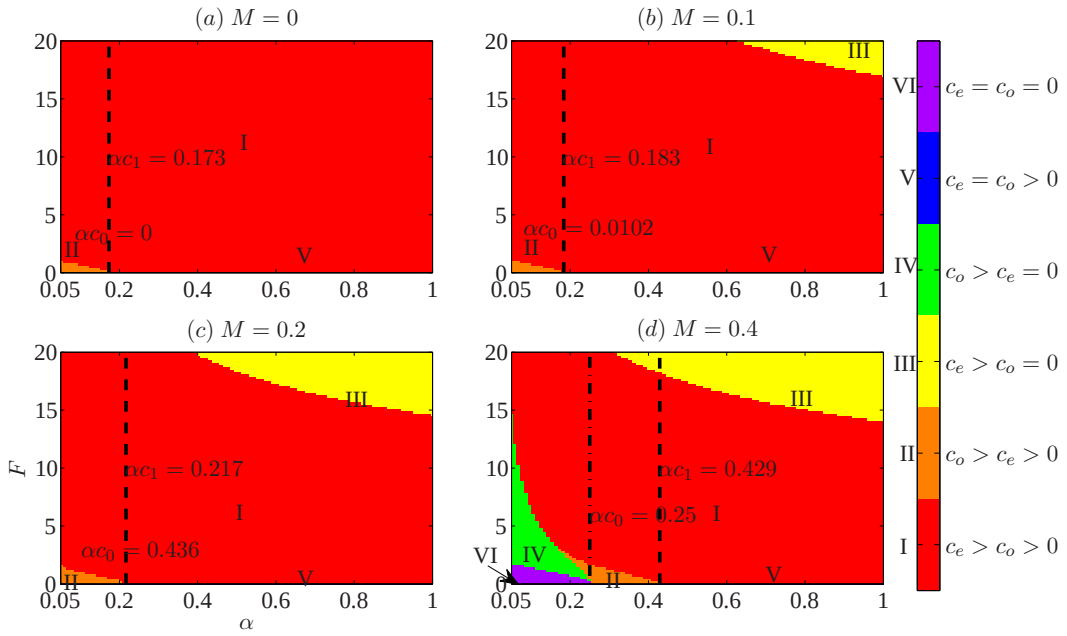

Figure 4.6: A plot over (α, F) space showing the different scenarios for the rectangular jet. Here, $c_e = \mathrm{Im}(c_e)$ and $c_o = \mathrm{Im}(c_o)$; see legend for the corresponding regime denoted by I–VI. The cutoff at $F = 0$ due to the magnetic field (4.30) is labelled as α_{c0} and is plotted as the dot-dashed line. The change of regime, i.e. where the even and odd mode are equally unstable, as predicted by the small F asymptotic analysis (4.32), is labelled as α_{c1} and plotted as the dashed line in the diagrams.

for the even mode, and

$$c_o^{(1)} = \mathrm{i}[T + T^2 + T\alpha(1 - T^2)]\frac{1 - T - 2\mathrm{i}\sqrt{T - M^2(1+T)^2}}{4(1+T)^4\sqrt{T - M^2(1+T)^2}} \tag{4.31b}$$

for the odd mode. If the expression inside the square root is negative or zero, i.e. there is no instability at leading order, then there is no instability also at the first correction. By considering the imaginary part of (4.31a) and (4.31b) appropriately, the value of α where the even and odd modes are equally unstable is then given by

$$\alpha_{c1} = \tanh^{-1}\left(\frac{3 - 4M^2 - \sqrt{8 - 32M^2}}{1 + 4M^2}\right), \tag{4.32}$$

and we see that $\mathrm{Im}(c_e^{(1)}) < \mathrm{Im}(c_o^{(1)})$ when $\alpha < \alpha_c$ and vice versa, i.e. the odd mode is more unstable than the even mode for sufficiently small α. This changeover value (4.32) is plotted as α_{c1} in Figures 4.6 and 4.7

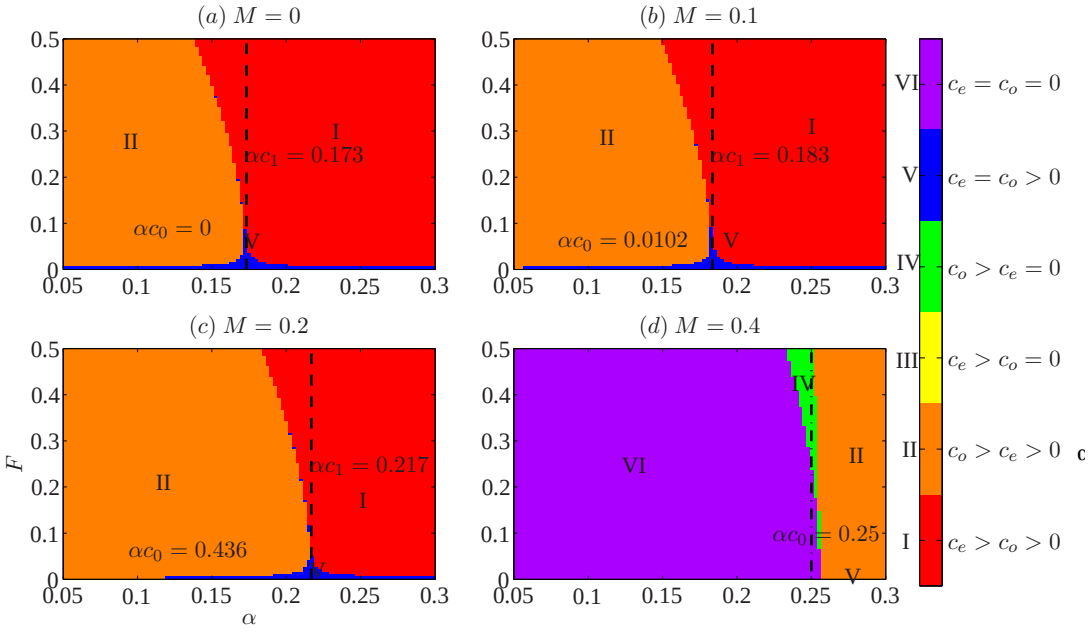

Figure 4.7: A zoomed in version of Figure 4.6.

4.2.4 Miscellaneous features

In Figures 4.4 and 4.5 we note that in certain cases there is a well-defined most unstable mode. We have tried to predict where the precise location for this optimal α will occur by considering expressions like $\partial(\alpha c_i)/\partial\alpha$, but without much success. We can however use the large and small α results to say when such a well-defined optimal α will exist, since if c_i goes to zero as $\alpha \to 0$ and $\alpha \to \infty$, there must be a well-defined optimal α. For the case $M = 0.1$ in Figures 4.4 and 4.5, the result (4.20) tells us that the F cutoff occurs at $F = 5/\sqrt{3} \approx 2.88$, which agrees with the appearance of the peaks in the respective figures.

4.3 Summary and discussion

For the vortex sheet, it was shown that closed form solutions may be written down for the root corresponding to instability, from which stability criteria may be derived. This instability is strongest when M and F are both zero. On increasing F or M when the other is zero, it is seen that the effect is to decrease the growth rate of the instability, consistent with energetic arguments. However, we also observe that there is a tongue region for F large and M close to 1, indicating

that somehow the individual stabilisation effects cancel each other out. An asymptotic analysis was carried out near the stability boundary $M = 1$ to investigate the behaviour of the instability in this tongue region.

For the rectangular jet, there were several features of note that we have found. For $\alpha \gg 1$, we found two types of instability, one that is like a vortex sheet instability, and the other is what we termed supersonic instabilities, previously found by Gill (1965) and now attributed to resonant over-reflection. We focussed on the vortex sheet instabilities, and found analytical expressions for these instabilities via an asymptotic analysis. The supersonic instabilities were observed to be weak instabilities so have not been investigated in great detail; it is certainly possible however to investigate them via an asymptotic procedure, as was done in Gill (1965). Numerically it was found that there are no instabilities when $M > 1/2$. For $\alpha \ll 1$, it was seen that there is a cutoff due to the magnetic field, and the locations of these cutoffs were found by an asymptotic procedure. Although it was found that the even mode is generally more unstable that the odd mode, via numerical and asymptotic procedures, we were able to find regions in parameter space where the odd mode is the strongest instability.

4.4 Appendix: Expressions for eigenfunctions

When the profile is piecewise-constant, the eigenfunction may be written down explicitly, given below. Note that the F dependence appears in $K^2 = 1 - F^2S^2 = 1 - F^2[(U_0 - c)^2 - M^2]$, and in the case $F = 0$, $\hat{h}$ is identified with $\hat{p}$, the pressure term in the incompressible case. Note the expressions for $\hat{h}$ remain formally at $O(1)$ in the limit of F tending to zero, and this is because of the rescaling $h = \tilde{h}/F^2$ we employed when we wrote down the full SWMHD equations in Chapter 2.

Note in these cases there are no vorticity or current perturbations except at the discontinuities.

Vortex sheet

$$U_0 = \begin{cases} +1, & y > 0 \\ -1, & y < 0 \end{cases} \tag{4.33a}$$

$$G = \begin{cases} e^{-\alpha K_+ y}, & y > 0 \\ e^{+\alpha K_- y}, & y < 0 \end{cases} \tag{4.33b}$$

$$\hat{v} = \begin{cases} +(1-c)e^{-\alpha K_+ y}, & y > 0 \\ -(1+c)e^{+\alpha K_- y}, & y < 0 \end{cases} \tag{4.33c}$$

$$\hat{b_y} = \begin{cases} Me^{-\alpha K_+ y}, & y > 0 \\ Me^{+\alpha K_- y}, & y < 0 \end{cases} \tag{4.33d}$$

$$\hat{u} = \begin{cases} -\mathrm{i}(1-c)K_+^{-1}e^{-\alpha K_+ y}, & y > 0 \\ -\mathrm{i}(1+c)K_-^{-1}e^{+\alpha K_- y}, & y < 0 \end{cases} \tag{4.33e}$$

$$\hat{b_x} = \begin{cases} -\mathrm{i}MK_+^{-1}e^{-\alpha K_+ y}, & y > 0 \\ +\mathrm{i}MK_-^{-1}e^{+\alpha K_- y}, & y < 0 \end{cases} \tag{4.33f}$$

$$\hat{h} = \begin{cases} +\mathrm{i}S_+^2K_+^{-1}e^{-\alpha K_+ y}, & y > 0 \\ -\mathrm{i}S_-^2K_-^{-1}e^{+\alpha K_- y}, & y < 0 \end{cases} \tag{4.33g}$$

Rectangular jet: even mode

$$U_0 = \begin{cases} 0, & y > 1 \\ 1, & |y| < 1 \\ 0, & y < -1 \end{cases} \tag{4.34a}$$

$$G = \begin{cases} +e^{-\alpha K_0 (y-1)}, & y > 1 \\ +\cosh(\alpha K_1 y)/\cosh(\alpha K_1), & |y| < 1 \\ +e^{+\alpha K_0 (y+1)}, & y < -1 \end{cases} \tag{4.34b}$$

$$\hat{v} = \begin{cases} -ce^{-\alpha K_0 (y-1)}, & y > 1 \\ +(1-c)\cosh(\alpha K_1 y)/\cosh(\alpha K_1), & |y| < 1 \\ -ce^{+\alpha K_0 (y+1)}, & y < -1 \end{cases} \tag{4.34c}$$

$$\hat{b_y} = \begin{cases} +Me^{-\alpha K_0 (y-1)}, & y > 1 \\ +M\cosh(\alpha K_1 y)/\cosh(\alpha K_1), & |y| < 1 \\ +Me^{+\alpha K_0 (y+1)}, & y < -1 \end{cases} \tag{4.34d}$$

$$\hat{u} = \begin{cases} +\mathrm{i}ce^{-\alpha K_0 (y-1)}, & y > 1 \\ +\mathrm{i}(1-c)\sinh(\alpha K_1 y)/\cosh(\alpha K_1), & |y| < 1 \\ -\mathrm{i}ce^{+\alpha K_0 (y+1)}, & y < -1 \end{cases} \tag{4.34e}$$

$$\hat{b_x} = \begin{cases} -\mathrm{i}Me^{-\alpha K_0 (y-1)}, & y > 1 \\ +\mathrm{i}M\sinh(\alpha K_1 y)/\cosh(\alpha K_1), & |y| < 1 \\ +\mathrm{i}Me^{+\alpha K_0 (y+1)}, & y < -1 \end{cases} \tag{4.34f}$$

$$\hat{h} = \begin{cases} +\mathrm{i}S_0^2 e^{-\alpha K_0 (y-1)}, & y > 1 \\ -\mathrm{i}S_1^2\sinh(\alpha K_1 y)/\cosh(\alpha K_1), & |y| < 1 \\ -\mathrm{i}S_0^2 e^{+\alpha K_0 (y+1)}, & y < -1 \end{cases} \tag{4.34g}$$

Rectangular jet: odd mode

$$U_0 = \begin{cases} 0, & y > 1 \\ 1, & |y| < 1 \\ 0, & y < -1 \end{cases} \tag{4.35a}$$

$$G = \begin{cases} +e^{-\alpha K_0 (y-1)}, & y > 1 \\ +\sinh(\alpha K_1 y)/\sinh(\alpha K_1), & |y| < 1 \\ -e^{+\alpha K_0 (y+1)}, & y < -1 \end{cases} \tag{4.35b}$$

$$\hat{v} = \begin{cases} -ce^{-\alpha K_0 (y-1)}, & y > 1 \\ +(1-c)\sinh(\alpha K_1 y)/\sinh(\alpha K_1), & |y| < 1 \\ -ce^{+\alpha K_0 (y+1)}, & y < -1 \end{cases} \tag{4.35c}$$

$$\hat{b_y} = \begin{cases} +Me^{-\alpha K_0 (y-1)}, & y > 1 \\ +M\sinh(\alpha K_1 y)/\sinh(\alpha K_1), & |y| < 1 \\ -Me^{+\alpha K_0 (y+1)}, & y < -1 \end{cases} \tag{4.35d}$$

$$\hat{u} = \begin{cases} +\mathrm{i}ce^{-\alpha K_0 (y-1)}, & y > 1 \\ +\mathrm{i}(1-c)\cosh(\alpha K_1 y)/\sinh(\alpha K_1), & |y| < 1 \\ +\mathrm{i}ce^{+\alpha K_0 (y+1)}, & y < -1 \end{cases} \tag{4.35e}$$

$$\hat{b_x} = \begin{cases} -\mathrm{i}Me^{-\alpha K_0 (y-1)}, & y > 1 \\ +\mathrm{i}M\cosh(\alpha K_1 y)/\sinh(\alpha K_1), & |y| < 1 \\ -\mathrm{i}Me^{+\alpha K_0 (y+1)}, & y < -1 \end{cases} \tag{4.35f}$$

$$\hat{h} = \begin{cases} +\mathrm{i}S_0^2 e^{-\alpha K_0 (y-1)}, & y > 1 \\ -\mathrm{i}S_1^2\cosh(\alpha K_1 y)/\sinh(\alpha K_1), & |y| < 1 \\ +\mathrm{i}S_0^2 e^{+\alpha K_0 (y+1)}, & y < -1. \end{cases} \tag{4.35g}$$

Chapter 5

Linear instabilities of smooth profiles

As a model for more realistic profiles, we consider in this chapter the instabilities associated with the hyperbolic-tangent shear layer and the Bickley jet. Again, for simplicity, we limit ourselves to the case of a uniform background magnetic field with no underlying topography. Linear instability calculations involving these two profiles are well documented in the literature in a wide variety of contexts (e.g., Lipps, 1962; Howard, 1963; Michalke, 1964; Drazin & Howard, 1966; Hazel, 1972; Drazin & Reid, 1981; Sutherland & Peltier, 1992, 1994; Hughes & Tobias, 2001) and provide a comparison and check on our results.

5.1 Numerical method

We seek a numerical solution of the eigenvalue equation (4.1), written as

$$G'' + \left[\frac{(S^2)'}{S^2} - \frac{(K^2)'}{K^2}\right] G' - \alpha^2 K^2 G = 0, \tag{5.1}$$

where, again, $S^2 = (U_0 - c)^2 - M^2$ and $K^2 = 1 - F^2 S^2$. Although the velocity profiles are technically defined over the entire real line, we solve the equation on the finite domain $y \in [-L_y, L_y]$. We will consider solutions that decay exponentially as $|y|$ becomes large, namely

$$G \sim \exp[-\alpha K y], \qquad \mathrm{Re}(K) > 0 \qquad \text{as} \qquad |y| \to \infty, \tag{5.2}$$

and the size of L_y chosen depends on the decay properties of the eigenfunction; we will be doubling L_y until the change in the computed eigenvalue is suitably small, such that

$|c(2L_y)|/|c(L_y)| < \epsilon$, for some choice of ϵ. We solve the second order ODE (5.1) by a shooting method, with matching imposed at $y = 0$, employing a generalised Newton method as the root-finding algorithm; the integration is started from $\pm L_y$, taking

$$\left.\frac{G'}{G}\right|_{-L_y} = -\alpha K_-, \qquad \left.\frac{G'}{G}\right|_{L_y} = -A\alpha K_+, \tag{5.3}$$

as the initialisation, where $K_\pm = 1 - F^2[(U(\pm\infty) - c)^2 - M^2]$, with $U(\pm\infty) = \pm 1$ for the shear layer and $U(\pm\infty) = 0$ for the jet. The constant A and the eigenvalue c accordingly until the matching errors at $y = 0$ are sufficiently small. To avoid singularities in the governing equation, we seek only unstable modes. The routines were written in MATLAB, using routine `ode113` as the integrator (an Adams-Bashforth type method with adaptive grid). Although the boundary conditions are functions of c, changing at every iteration, we generally have no problems with convergence provided that the initial guess is close to the true value. Solutions are initialised from $F = 0$, $M = 0$ at some fixed α using a known numerical result documented in, for example, Drazin & Reid (1981). Runs at new parameter values are then initialised using an estimate for the eigenvalue from previously calculated eigenvalues at nearby parameter values. The Bickley jet is even about $y = 0$ and hence the parity result of Section 3.4 holds, i.e. the eigenfunctions are either even or odd. In this case we need integrate only up to $y = 0$, with the imposition of either $G'(0) = 0$ (even mode) or $G(0) = 0$ (odd mode).

5.2 Hyperbolic-tangent shear layer

In this subsection, we consider the basic state velocity defined by

$$U_0(y) = \tanh(y), \qquad -\infty < y < \infty. \tag{5.4}$$

From inequality (3.12) we know that the growth rates αc_i associated with any instability are bounded above by $\max |U_0'|/2 = 1/2$; furthermore, from the stability criteria (3.20) or (3.21), this profile is stable when $M \geq 1$. From the parity results in Section 3.4, the eigenvalues associated with unstable eigenfunctions take the form $c = \pm c_r + \mathrm{i}c_i$. In the hydrodynamic case, instability exists only within the bandwidth $0 < \alpha < 1$, with a neutral mode at $\alpha = 1$ (e.g., Drazin & Reid, 1981, §31.10).

Figure 5.1 shows contours of c_i over the F and M parameter space at selected α, reflecting: (i) a relatively short wave disturbance (Figure 5.1a); (ii) the most unstable mode in the hydrodynamic

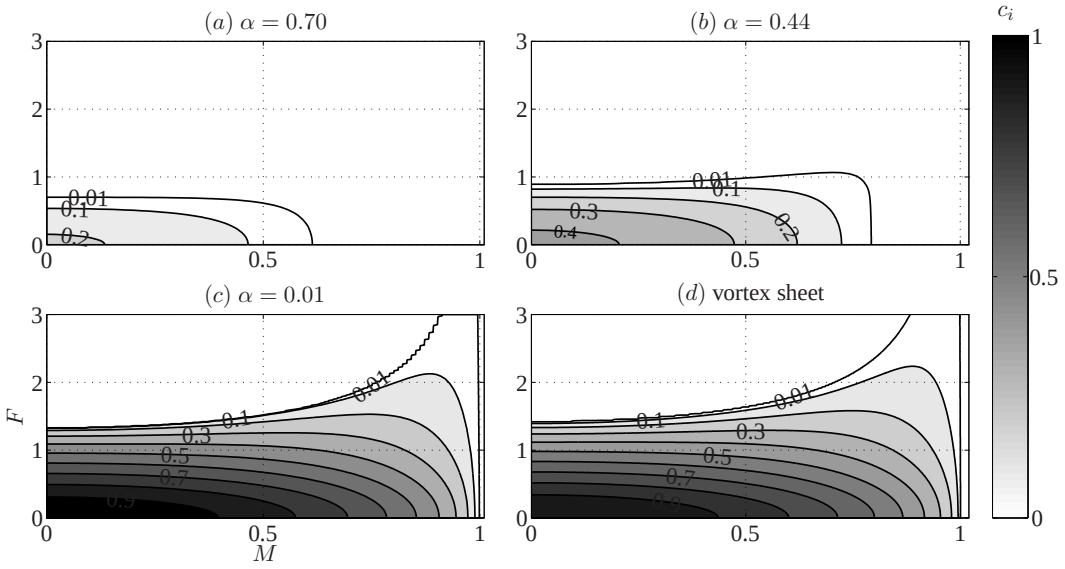

Figure 5.1: Contours of c_i over F and M parameter space at selected α. The results have been filtered so that only modes with $|c_r| < 10^{-3}$ are plotted. Figure 4.1 is reproduced here as panel(d) for comparison purposes.

incompressible case (Figure 5.1b); (iii) a long wave disturbance in panel (Figure 5.1c). Figure 4.1, the corresponding diagram for the vortex sheet profile, is reproduced here as the Figure 5.1(d) for comparison purposes. We should note that the results have been filtered so that only the low-frequency modes (here those with $|c_r| < 10^{-3}$) have been displayed; as explained below, there is also a distinct second mode of instability (with larger $|c_r|$), which is manifest at higher values of F. Figure 5.1(c) and (d) are remarkably similar, suggesting that long-wave instabilities for this velocity profile resemble the instabilities of a vortex sheet. This resemblance will be quantified via a long-wave asymptotic analysis in Section 5.5, in which we derive the more general result that long-wave instabilities of any shear layer profile resemble vortex sheet instabilities.

As described above, figure 5.1 is compiled by tracking the evolution of a particular mode of instability, using the incompressible hydrodynamic case $(F = M = 0)$ as the starting point. It is therefore important to ask whether there are additional, distinct modes of instability. Indeed, it is known that for both two-dimensional compressible hydrodynamics and shallow-water hydrodynamics, there is a second mode of instability, found by Blumen *et al.* (1975) and Satomura (1981) respectively. Compared to the first modes (those of Figure 5.1), which may be referred to as inflection point instabilities, these second modes (or supersonic modes for compressible

hydrodynamics) are observed to be weaker instabilities, possess a weaker spatial decay, and occur as a pair of propagating waves with phase speed $\pm c_r$. Inflection point instabilities can be attributed to interacting Rossby waves supported by the background shear (see, for example, the review by Carpenter *et al.*, 2012); by contrast, supersonic instabilities (absent in the $F < 1$ regime) can be attributed to gravity waves interacting with critical layers (e.g., Satomura, 1981; Hayashi & Young, 1987; Takehiro & Hayashi, 1992; Balmforth, 1999; Benilov & Lapin, 2013) and, indeed, can occur for linear shear flows, explicitly filtering out the possibility of Rossby waves due to the background shear. This is consistent with the theorem of Ripa (1983), which states that for instability, either the associated potential vorticity profile possesses an inflection point or that the flow is supersonic ($F > 1$) somewhere in the domain, conditions necessary for Rossby and/or gravity wave interaction leading to instability.

Such second mode instabilities can also be identified in the SWMHD system; some contours of c_i associated with these instabilities are presented in Figure 5.2. By analogy with the instabilities found in compressible MHD, we shall also refer to these modes as 'supersonic'. Figure 5.3 plots their growth rate over the unstable bandwidth at various sample parameter values. It can be seen that the supersonic instabilities generally have weaker growth rates than inflection point instabilities, consistent with the results of Blumen *et al.* (1975). As we shall see in Section 5.5, the relation between the two types of unstable modes can be explored in some detail in the small wavelength limit.

5.3 Instability mechanism in terms of counter-propagating Rossby waves

As mentioned above, inflection point instabilities can be attributed to interacting Rossby waves supported by the background shear. The constructive interference of a pair of Counter-propagating Rossby Waves (CRW) has been put forward as the mechanism leading to instability of shear flows in a variety of settings (e.g., Bretherton, 1966a; Hoskins *et al.*, 1985; Baines & Mitsudera, 1994; Heifetz *et al.*, 1999, 2004; Heifetz & Methven, 2005; Harnik & Heifetz, 2007; Heifetz *et al.*, 2009; Carpenter *et al.*, 2012). For the SWMHD system, it is therefore natural to enquire how this underlying mechanism is modified by shallow-water and MHD effects.

Let us first consider the incompressible, hydrodynamic case ($F = 0$, $M = 0$). Viewed

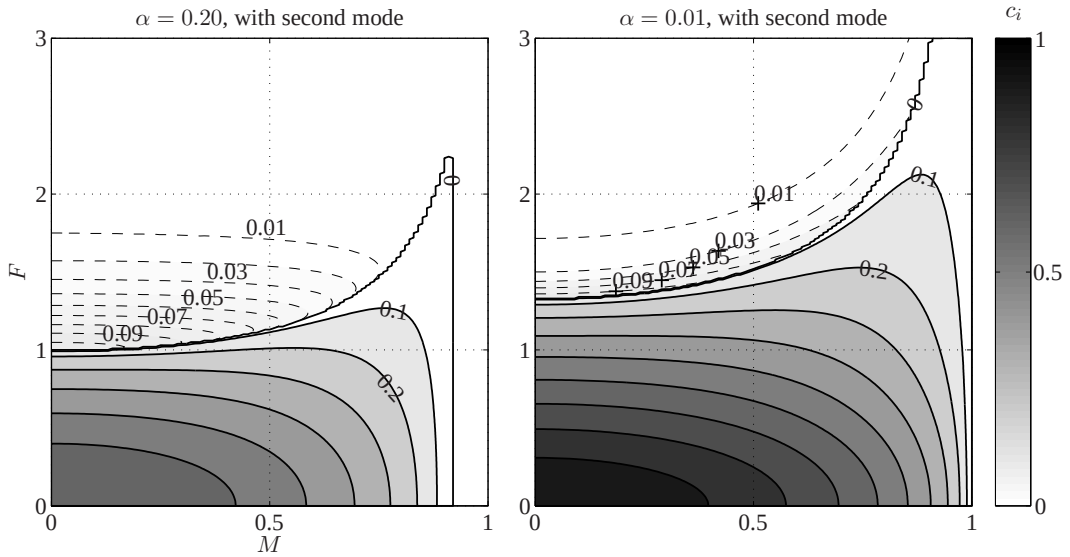

Figure 5.2: Contours of c_i over F and M parameter space at selected α. Inflection point instabilities with $|c_r| < 10^{-3}$ are plotted as solid lines while supersonic instabilities with $|c_r| > 10^{-3}$ are plotted as dashed lines.

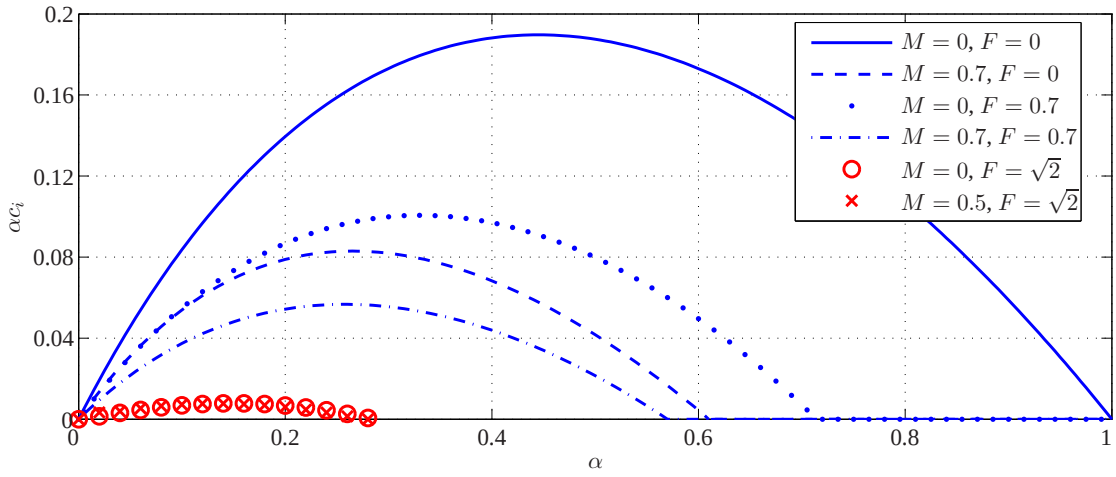

Figure 5.3: The growth rate over the unstable bandwidth at selected parameter values for $U_0(y) = \tanh(y)$. The inflection-point mode is plotted as lines and the supsersonic mode as markers.

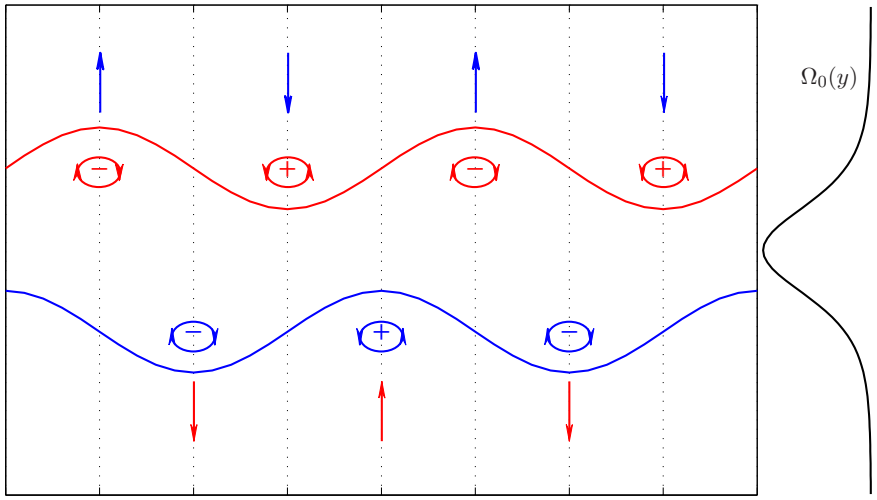

Figure 5.4: Basic CRW mechanism in schematic form, for the background velocity profile of $U_0 = \tanh(y)$, so the background vorticity profile is $\Omega_0 = -\text{sech}^2(y)$. Solid lines here depict the dynamics for the incompressible, hydrodynamic case. The contours are of the vorticity. Vorticity anomalies are shown by the closed solid curves, and the effect of these on the other contours, leading to instability, is shown by solid arrows.

individually, the Rossby waves are neutral. Its direction of propagation is determined by the vorticity profile, which in this case is related to the background flow. This in turn is seen to imply a wave propagation that is in the opposite direction to the background flow. A pair of CRW may then be held stationary by the background flow, become phase locked, and, depending on the phase shift, interfere constructively, leading to mutual amplification and hence instability. This is the scenario depicted in, for example, Figure 1 of Heifetz & Methven (2005). Schematically, these CRW are represented by the solid curves in figure 5.4, where each of the vorticity anomalies has an associated velocity, and where the configuration is such that the mutual influence of the two Rossby waves acts to increase the wave amplitude.

We plot in Figures 5.5 and 5.6 the relevant eigenfunctions for the most unstable mode at some sample values of F and M, with the Rossby waves represented by vorticity anomalies; the incompressible hydrodynamic case is displayed in panel (c) in the figures. Looking at Figure 5.5(c), the pattern is consistent with the schematic in Figure 5.4. So, at the simplest level, we observe that increasing F or M perturbs the patterns away from the optimal configuration for instability, thus leading to the observed stabilisation. We now quantify how the extra physics of

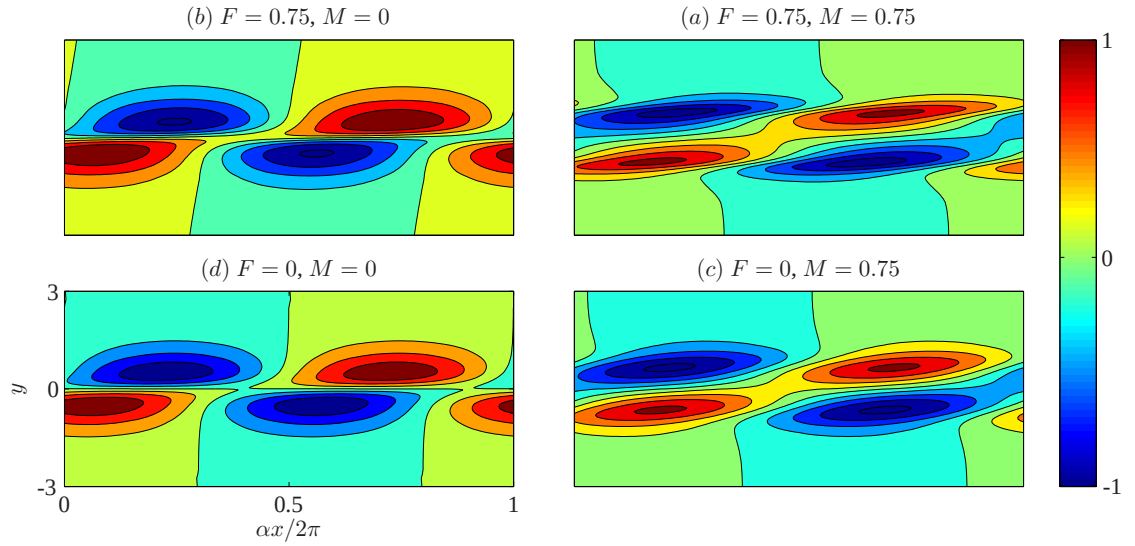

Figure 5.5: Vorticity eigenfunction of the most unstable mode of $U_0(y) = \tanh(y)$ at some selected parameters. Here and in subsequent diagrams of this type, red is positive and blue is negative. Notice the larger shift between the pair of waves as M is increased, and a slight tilting when F is increased.

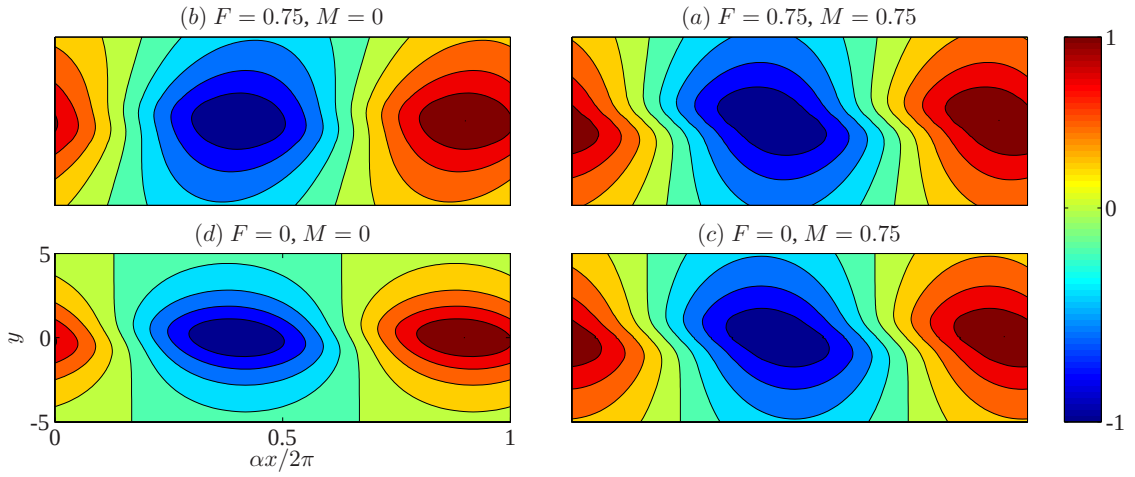

Figure 5.6: Height (pressure) eigenfunction of the most unstable mode of $U_0(y) = \tanh(y)$ at some selected parameters. Notice an increased tilting with increasing F.

the SWMHD system perturbs the patterns away from the optimum configuration.

So since Rossby waves are associated with vorticity anomalies, we consider the vorticity equation and see what can be inferred. The vorticity equation in two-dimensional incompressible

hydrodynamics is

$$\frac{D\omega}{Dt} \equiv \frac{\partial \omega}{\partial t} + \boldsymbol{u} \cdot \nabla \omega = 0. \tag{5.5}$$

Then, linearising about a basic shear flow $U_0(y)$ gives

$$\left(\frac{\partial}{\partial t} + U_0 \frac{\partial}{\partial x} \right) \omega = -v\Omega_0'. \tag{5.6}$$

Now, we note that v is related to the cross-stream displacement of the material contour η as

$$\left(\frac{\partial}{\partial t} + U_0 \frac{\partial}{\partial x} \right) \eta = v, \tag{5.7}$$

and so taking modal solutions of the form (3.4) then gives

$$\hat{\omega} = -\hat{\eta}\Omega_0. \tag{5.8}$$

This says that, in the incompressible hydrodynamic case, any vorticity anomalies are tied to the deformation of the material contour.

Here we work out the eigenfunction for ω and η associated with the most unstable mode from G, and compare the two in Figure 5.7. As a measure of the error, we calculate the relative L_2 error:

$$\text{rel. } L_2 \text{ error} = \frac{||\omega - (-\eta\Omega_0')||_{L_2}}{||\omega||_{L_2}}, \qquad ||(\cdot)||_{L_2} = \sqrt{\iint (\cdot)^2 \, \mathrm{d}x\mathrm{d}y}. \tag{5.9}$$

As we can see, the relative error is small, less than 1%; thus we can say with confidence that the vorticity budget equation captures all the vorticity contributions.

5.3.1 Modifications in the SWMHD case

The SWMHD vorticity equation is given by

$$\frac{D\omega}{Dt} = -(\nabla \cdot \boldsymbol{u})\omega + M^2 \boldsymbol{b} \cdot \nabla j + M^2 (\nabla \cdot \boldsymbol{b}) j, \tag{5.10}$$

where ω and j are the z-components of the vorticity, $\nabla \times \boldsymbol{u}$, and electric current, $\nabla \times \boldsymbol{b}$, respectively. Using equations (3.1c) and (3.1d), this can be written as

$$\frac{D\omega}{Dt} = F^2 \omega \frac{Dh}{Dt} + F^2 h \omega \nabla \cdot \boldsymbol{u} + M^2 (1 - F^2 j) \boldsymbol{b} \cdot \nabla j - M^2 h j \nabla \cdot \boldsymbol{b}. \tag{5.11}$$

On linearising about the basic state $\boldsymbol{U}_0 = U_0(y)\boldsymbol{e}_x$, $\boldsymbol{B}_0 = 1\boldsymbol{e}_x$, taking modal solutions of the form (3.4), we obtain the following expression for the vorticity budget:

$$\hat{\omega} = -\hat{\eta}\Omega' + F^2 \hat{h}\Omega + M^2 \frac{\hat{j}}{U_0 - c}, \tag{5.12}$$

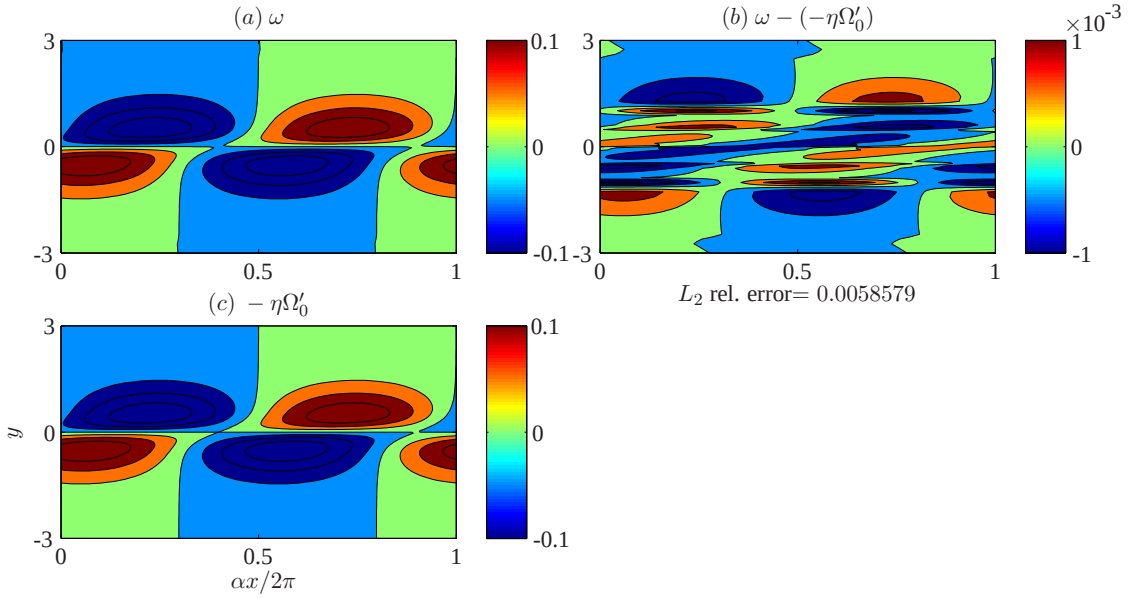

Figure 5.7: Vorticity contributions associated with the most unstable mode at $F = 0$, $M = 0$; panel (a) is also Figure 5.5(c). The small relative L_2 error given by (5.9) indicates that the vorticity anomalies come solely from deformation of the material contours.

where $\Omega_0 = -U_0'$ is the basic state vorticity. These three terms represent contributions due respectively to the deformation of the cross-stream displacement, to shallow-water and magnetic effects. Inspection of Figure 5.1 shows that the instability is most vigorous when $M = F = 0$ and that increasing either M or F when the other parameter is zero is stabilising; we therefore expect that the vorticity anomalies from the magnetic and shallow-water effects will counteract that associated with the deformation of the material contour.

CRWs modification when one of F or M is zero

Consider first the case where $F = 0$ (the incompressible MHD case). Equation (5.12) is given by

$$\hat{\omega} = -\hat{\eta}\Omega_0' + M^2 \frac{\hat{j}}{U_0 - c}. \tag{5.13}$$

We show in Figure 5.8 a typical result for $F = 0$ showing the physical form of the respective components associated with the most unstable mode at the particular parameter values.

We notice that the positive contribution to vorticity when $M \neq 0$ has a centre that straddles the two negative vorticity anomalies associated with the deformation of the material contour, and the same

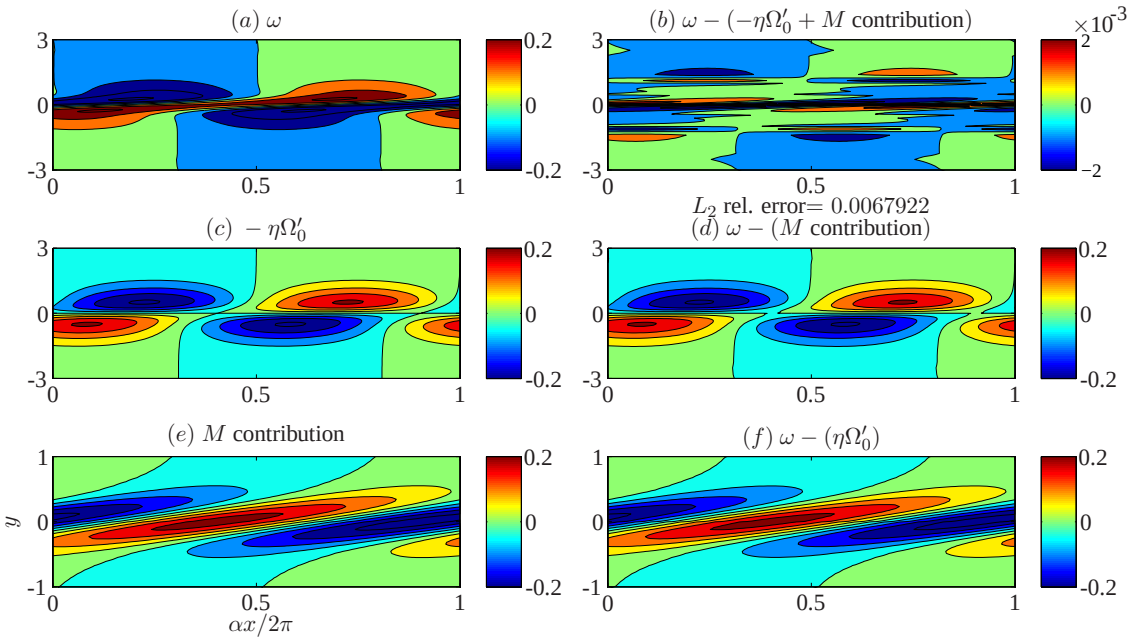

Figure 5.8: Vorticity contributions associated with the most unstable mode at $F = 0$, $M = 0.25$. Notice that unlike the hydrodynamic shallow-water case, the vorticity contribution due the MHD effects is the same order as the contribution due to the displacement of the material contour. Note also the bottom panels are zoomed in than the other panels.

is true half a wavelength along where the sign of the contributions are swapped. At the simplest level, we have a modification to the basic CRW mechanism, given in Figure 5.9. The location and the sign of the extra vorticity contribution is such that it counteracts the action associated with the underlying CRW mechanism and so is stabilising, consistent with the stabilisation observed previously.

The case where $M = 0$ (so the shallow-water, hydrodynamic case) may be considered in an analogous manner. Equation (5.12) in this case is given by

$$\hat{\omega} = -\hat{\eta}\Omega_0' + F^2\hat{h}\Omega_0. \tag{5.14}$$

This equation is a restatement of the conservation of potential vorticity, and may be derived from starting with $Dq/Dt = 0$ and linearising accordingly. We plot in Figure 5.10 a typical result for $M = 0$ showing the physical form of the components, again using the most unstable mode at this particular parameter value. A similar interpretation leads to a schematic like Figure 5.9, as in the $F = 0$ case. We note however that the vorticity anomalies arising from the perturbation

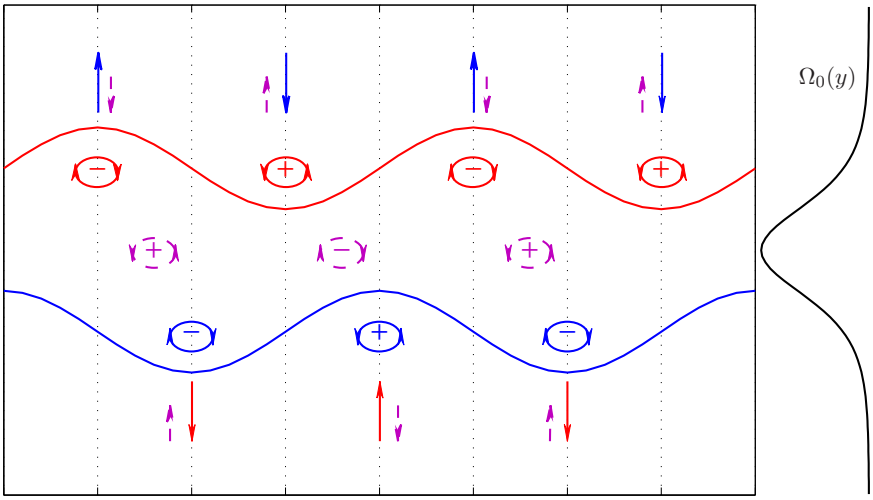

Figure 5.9: Modified CRW mechanism in pictorial form, with the background velocity profile $U_0 = \tanh(y)$. The solid contours are associated with the basic CRW mechanism, as in Figure 5.4. The closed dashed curves represent the additional vorticity anomalies due to the extra physical effects. The (stabilising) effect of these extra vorticity anomalies are shown by the dashed arrows.

of the material contour is the dominant contribution to the whole vorticity, larger than the extra contribution by an order of magnitude.

As a further verification of these ideas, we have also adopted a perturbative approach to the analysis of expression (5.12), approximating the shallow-water and magnetic contributions using the eigenfunction for $F = M = 0$. It can be readily seen that calculating $F^2\hat{h}\Omega_0$ using $\hat{h}$ is consistent with that obtained from the full linear equations (see Figure 5.11a, b). To obtain an estimate of the magnetic contribution, it is necessary to calculate $\hat{j}$ using the governing equations (3.3c) – (3.3d) with the velocity obtained when $F = M = 0$. This is slightly more involved than for $\hat{h}$, but can be shown to provide a consistent vorticity contribution; see for example Figure 5.11(c) and the numerically calculated contribution given in Figure 5.11(d). Thus the idea that shallow-water and magnetic effects act to shift the vorticity distribution from an optimal configuration for instability is confirmed.

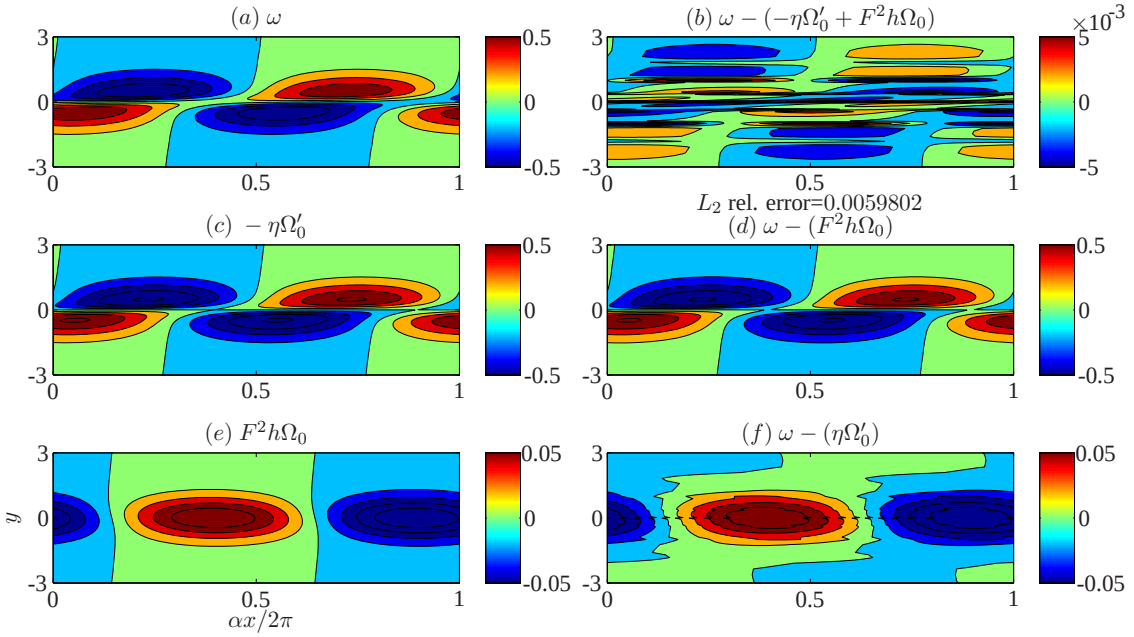

Figure 5.10: Vorticity contributions associated with the most unstable mode at $F = 0.5$, $M = 0$. Notice that the vorticity contribution due the presence of a free surface is much smaller than the contribution due to the displacement of the material contour.

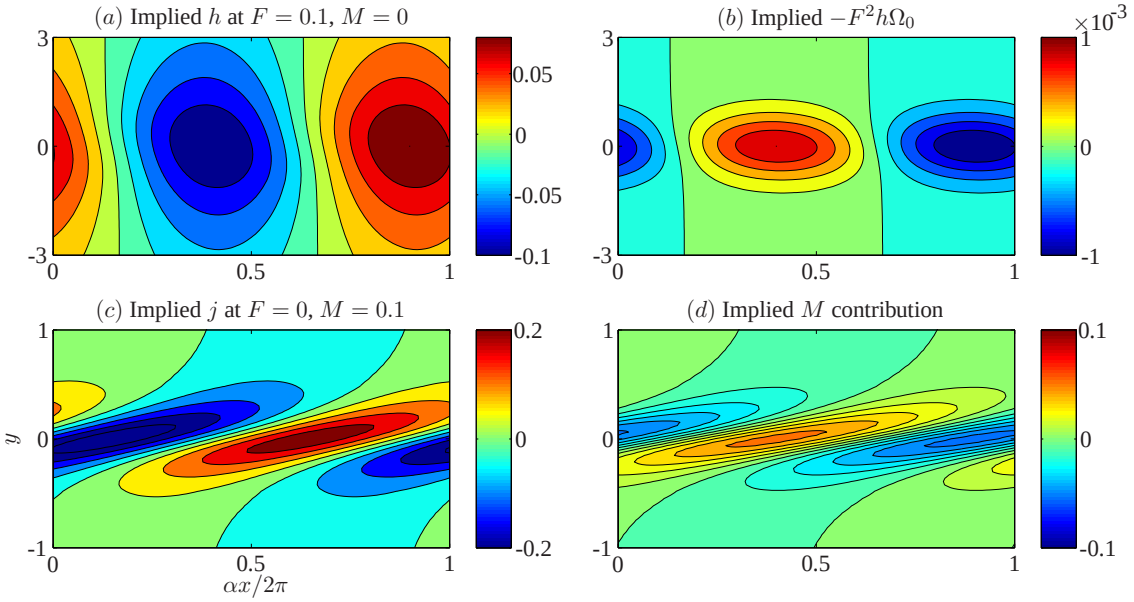

Figure 5.11: Vorticity contributions implied by the velocity eigenfunction calculated at $F = 0$, $M = 0$.

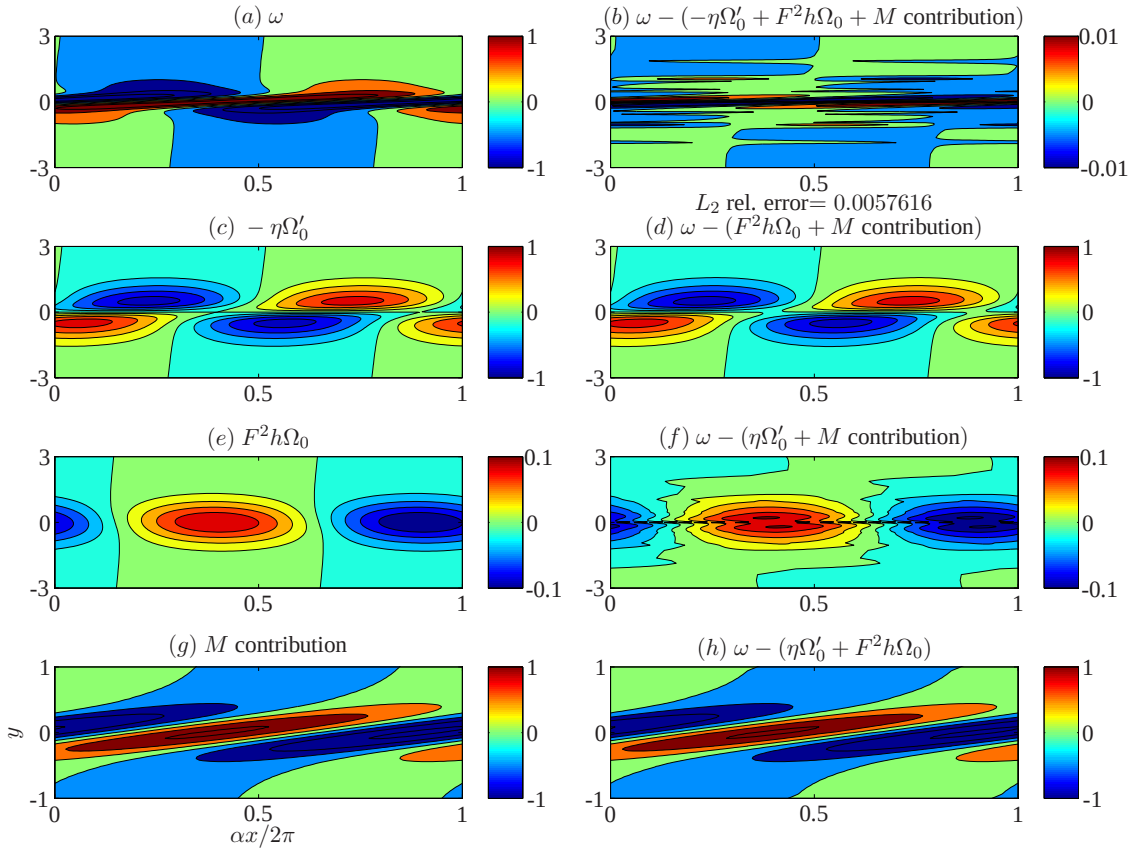

Figure 5.12: Vorticity contributions associated with the most unstable mode at $F = 0.5$, $M = 0.25$. Notice that, as observed before, the vorticity contribution from the MHD term is larger than the contribution from the shallow-water term, and both are such that they counteract the contribution from the deformation of the material contour.

CRWs modification in the full SWMHD case

The vorticity $\hat{\omega}$ and its three constituent components in expression (5.12) are shown in Figure 5.12 for the representative case of $M = 0.25$, $F = 0.5$. The contribution from the deformation of the material contour is consistent with that of Figure 5.5(a). Note that the extra contributions due to non-zero F or M have opposite signs of vorticity that straddle the appropriate peaks and troughs of the underlying vorticity anomalies due to the CRW mechanism, and its stabilising effect is as in the schematic given in Figure 5.9. We observe that the vorticity contribution associated with the M terms are an order of magnitude larger than the contributions due to F.

So we see that the underlying CRW mechanism, in the SWMHD system, necessarily generates vorticity anomalies that implies an action that counteracts the basic instability mechanism. There

are certain details that we have not accounted for, such as the acceleration of the waves from these induced anomalies which affects phase locking, fringe effects away from the peaks and troughs of the extra vorticity anomalies, and so forth; these are discussed at the end of this chapter.

5.4 Bickley jet

Here we consider the basic state velocity defined by

$$U_0(y) = \text{sech}^2(y), \qquad -\infty < y < \infty. \tag{5.15}$$

From inequality (3.12), the instability growth rates αc_i are bounded above by $\max|U_0'|/2 = 2/(3\sqrt{3})$; furthermore, from stability criterion (3.21), this velocity profile is stable when $M \geq 1/2$. For the incompressible hydrodynamic case, even and odd modes are unstable only in the respective bandwidths $0 < \alpha < 2$ and $0 < \alpha < 1$, with neutral modes at $\alpha = 2$ and $\alpha = 1$ respectively (e.g., Drazin & Reid, 1981, §31.9).

Figure 5.13 shows contours of c_i over (M, F) space for selected values of the wavenumber, tracking from the mode at $M = 0$, $F = 0$. The values of α are chosen to reflect: (i) the most unstable mode in the incompressible hydrodynamic case (Figure 5.13*a*,*b*); (ii) the mode with highest c_i in the incompressible hydrodynamic case (Figure 5.13*c*,*d*); (iii) a long-wave disturbance (Figure 5.13*e*,*f*). The magnetic field provides a stabilising influence, which is most pronounced at small values of the wavenumber α. This feature will be quantified later via a long-wave asymptotic analysis.

Figure 5.14 shows the growth rate of the modes over the unstable bandwidth at selected parameter values. In general, the even mode is more unstable than the odd mode. Though there are isolated regions where the odd modes are more readily destabilised, these do not necessarily correspond to the regions predicted by the stability analysis for the rectangular jet, described in Chapter 4. We have also performed some sample calculations in regions where the analysis for the rectangular jet suggests a preference for odd modes; however, we found no strong evidence to suggest that for the Bickley jet the odd modes are more unstable than the even modes in those regions. Thus, for this particular aspect of the problem, the stability properties of the piecewise-constant profile do not provide a quantitative guide to those of the smooth profile.

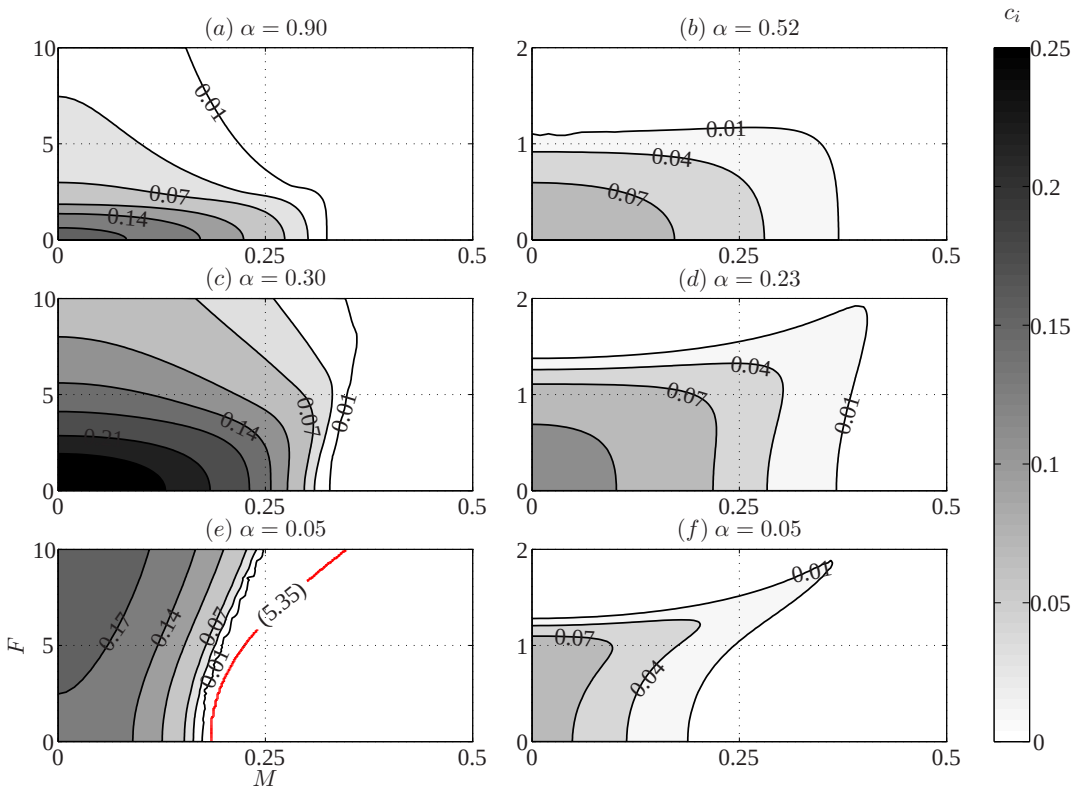

Figure 5.13: Contours of c_i over the F and M parameter space at selected α, for the even mode (left column) and the odd mode (right column) of $U_0(y) = \text{sech}^2(y)$. The predicted cut off from the asymptotic result (5.38) is plotted in panel (e).

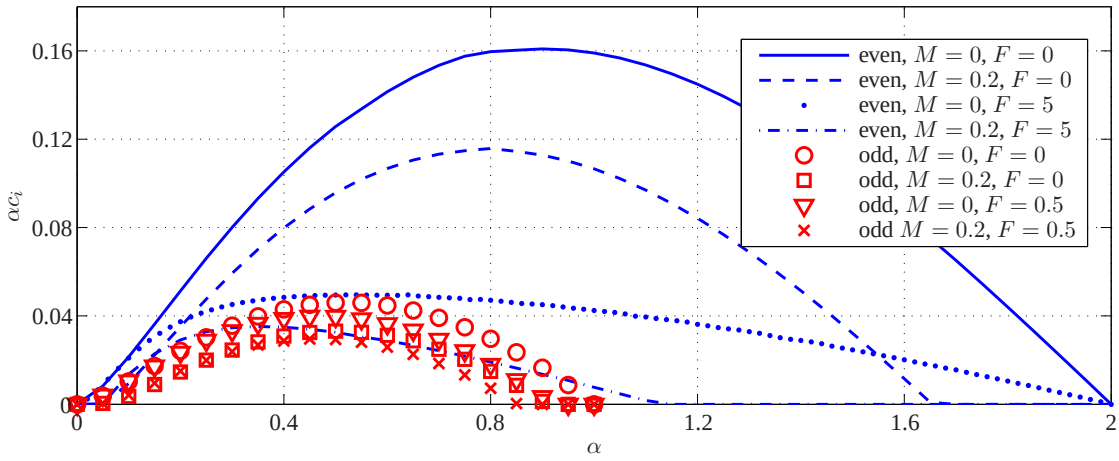

Figure 5.14: The growth rate over the unstable bandwidth at selected parameter values for $U_0(y) = \text{sech}^2(y)$. The even mode is plotted as lines and the odd mode as markers.

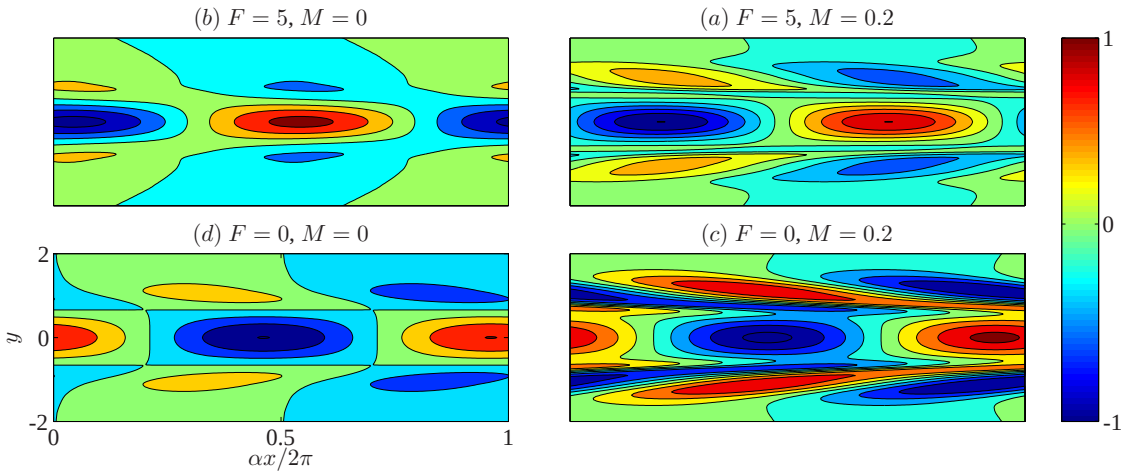

Figure 5.15: Vorticity eigenfunction of the most unstable even mode of $U_0(y) = \text{sech}^2(y)$, at some selected parameters.

A natural question to ask, prompted by the findings for rectangular jet in Chapter 4 and the shear layer earlier this chapter, is whether there are additional modes of instability to those shown in Figure 5.14, which were obtained from tracking modes starting from the incompressible, hydrodynamic case ($F = 0$, $M = 0$). We have performed a scan over (M, F) space at various values of the wavenumber α, with randomly generated initialisations chosen so that the initial guesses for c lie within the smallest rectangle containing the semi-circle (3.19). A substantial number of computations (20 different initialisations at over 200 different parameter values) were carried out, solving the governing eigenvalue equation with no parity imposed. Via this, admittedly non-exhaustive, procedure, we have not found any unstable mode that differs from the even and odd modes obtained by tracking from the starting point of $F = 0$, $M = 0$.

One question to ask is whether the CRW mechanism discussed earlier is applicable to the jet profile. For the jet case we may be tempted to say there are two pairs of Rossby waves, centred around each of the jet flanks. However, we should note that there is a change in wave behaviour in the middle of the jet, where the flow is at its maximum and $U'' < 0$, in contrast to inflection points where $U'' = 0$. The interaction of these Rossby waves are not straightforward because, for example, the flow is not necessarily holding the waves stationary any more. We do not pursue the Rossby wave interpretation as the instability mechanism for this profile, however, we provide plots of the eigenfunction for completeness (Figures 5.15 to 5.18).

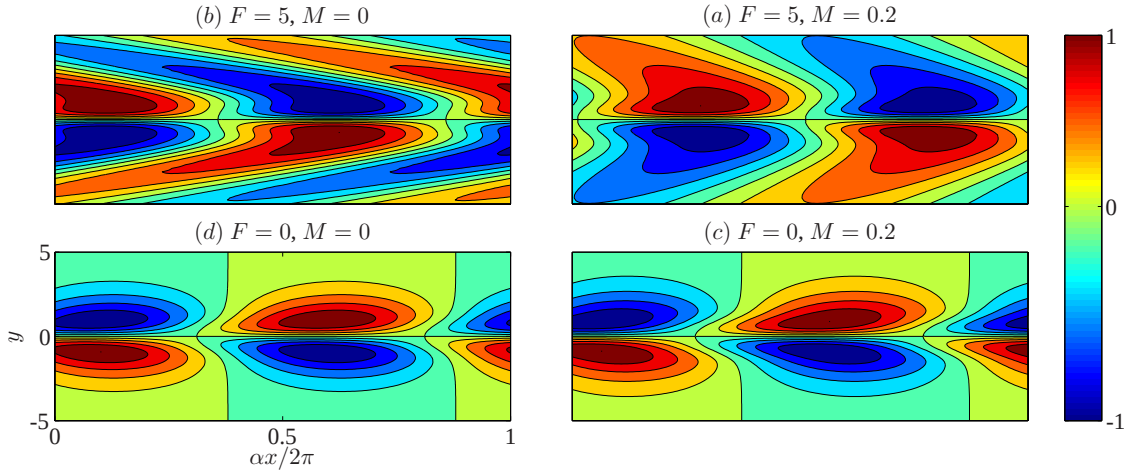

Figure 5.16: Height (pressure) eigenfunction of the most unstable even mode of $U_0(y) = \mathrm{sech}^2(y)$, at some selected parameters.

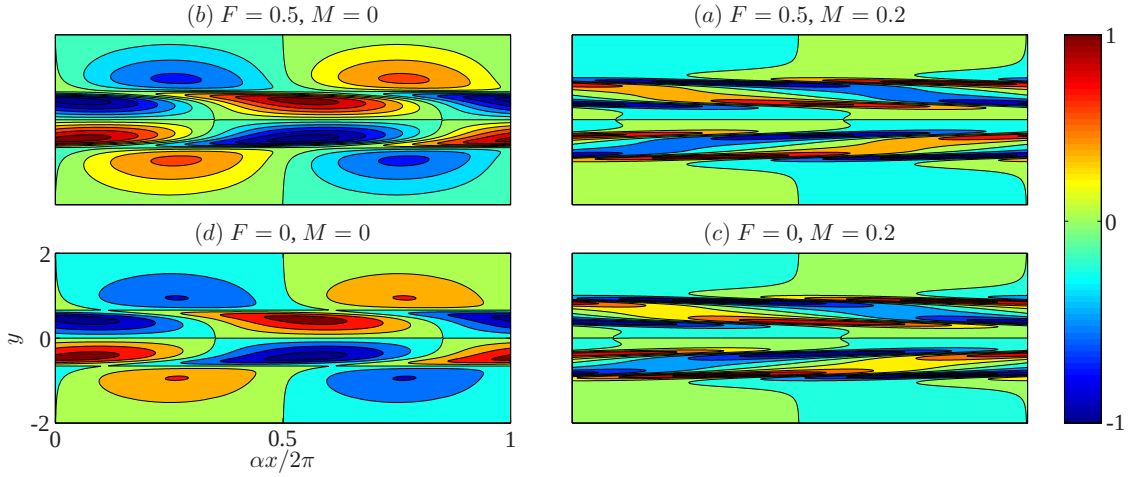

Figure 5.17: Vorticity eigenfunction of the most unstable odd mode of $U_0(y) = \mathrm{sech}^2(y)$, at some selected parameters.

5.5 Long-wave asymptotics

Several features of the instabilities of the hyperbolic-tangent shear layer and the Bickley jet may be clarified by generalising the long-wave asymptotic procedure due originally to Drazin & Howard (1962). We consider the governing equation (5.1), written in the form:

$$Z^2(G'' - \alpha^2 K^2 G) + (Z^2)'G' = 0, \qquad Z^2 = \frac{S^2}{K^2}. \tag{5.16}$$

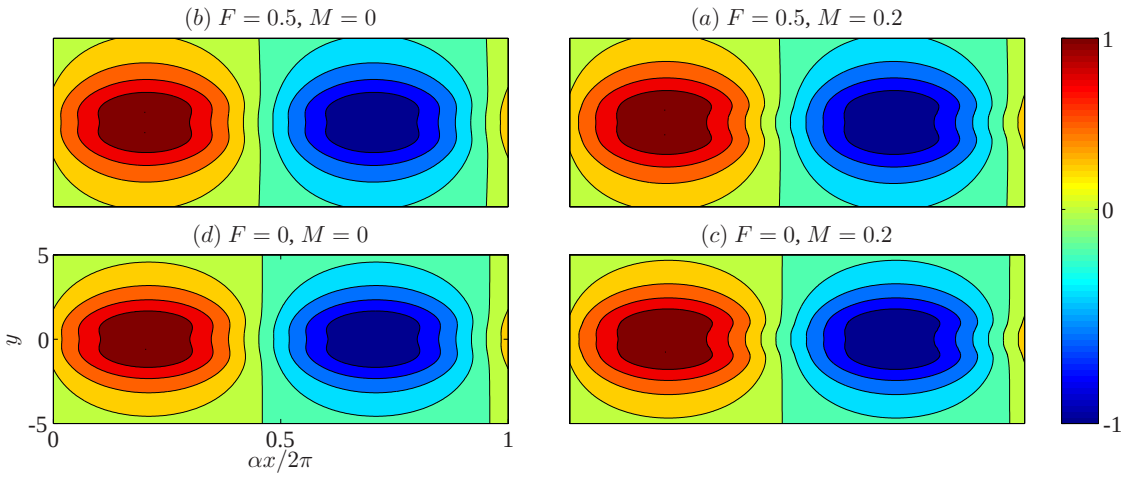

Figure 5.18: Height (pressure) eigenfunction of the most unstable odd mode of $U_0(y) = \text{sech}^2(y)$, at some selected parameters.

We assume that the velocity profiles under consideration are such that $U_\pm = U_0(\pm\infty)$ are well-defined. Then, on choosing an appropriate frame of reference and suitable normalisation for the basic flow, any velocity profile may be designated as either a *shear layer* if $U_\pm = \pm 1$, or as a *jet* if $U_\pm = 0$. The idea is that, for long-wave disturbances, the behaviour of $U_0(y)$ at $y = \pm\infty$ gives the leading order behaviour, with the variations associated with the basic state leading to higher order corrections.

We further assume that U_0' (and so $(Z^2)'$) decays sufficiently rapidly as $|y| \to \infty$. Adopting the same notation as Drazin & Howard (1962), we consider solutions to (5.16), for fixed c, of the form

$$G(y) = \begin{cases} G_+(y) = \chi(y)\exp(-\alpha K_+ y), & y > 0, \\ G_-(y) = \theta(y)\exp(+\alpha K_- y), & y < 0, \end{cases} \tag{5.17}$$

with $\chi, \theta \to$ constant as $y \to \pm\infty$, and where $K_\pm^2 = 1 - F^2 S_\pm^2 = 1 - F^2[(U_\pm - c)^2 - M^2]$. The perturbations must decay as $y \to \pm\infty$; hence $\text{Re}(K_\pm) > 0$. We consider expansions of the functions $\chi(y)$ and $\theta(y)$ of the form

$$\chi(y) = \sum_{n=0}^{\infty} (+\alpha)^n \chi_n(y), \qquad \theta(y) = \sum_{n=0}^{\infty} (-\alpha)^n \theta_n(y), \tag{5.18}$$

with $\chi_0, \theta_0 \to$ constant$(\neq 0)$ and $\chi_n, \theta_n (n > 1) \to 0$ as $y \to \pm\infty$. It turns out to be most convenient to fix $\chi_0(\infty) = \theta_0(-\infty) = 1$, and then to accommodate the necessary degree of freedom in the matching conditions for G at $y = 0$. Without loss of generality, we shall focus

on the equations for χ; those for θ follow in a similar fashion. On substituting expressions (5.17) (with the expansions (5.18)) into (5.16), equating the coefficients at each order of α gives

$$0 = [Z^2\chi_0']', \tag{5.19a}$$

$$0 = [Z^2\chi_1']' - K_+[(Z^2\chi_0)' + Z^2\chi_0'], \tag{5.19b}$$

$$0 = [Z^2\chi_{n+2}']' - K_+[(Z^2\chi_{n+1})' + Z^2\chi_{n+1}] + Z^2(K_+^2 - K^2), \qquad n \geq 0. \tag{5.19c}$$

Equation (5.19a) integrates to $Z^2\chi_0' = C$, with the conditions at infinity then giving $C = 0$. Thus $\chi_0 = \text{constant} = 1$ through our choice of $\chi_0(\infty)$. Integration of equations (5.19b) – (5.19c) then gives, after some algebra,

$$\begin{aligned}
\chi_1 &= \int_\infty^y \left(1 - \frac{Z_+^2}{Z^2}\right)\,\mathrm{d}y_1, \\
\chi_2 &= \int_\infty^y \left[\frac{1}{Z^2}\int_\infty^{y_1}(S^2 - S_+^2)\,\mathrm{d}y_2 + K_+^2\int_\infty^{y_1}\left(1 - \frac{Z_+^2}{Z^2}\right)\,\mathrm{d}y_2\right]\mathrm{d}y_1.
\end{aligned} \tag{5.20}$$

Analogously, we have

$$\begin{aligned}
\theta_0 &= 1, \\
\theta_1 &= K_-\int_{-\infty}^y \left(1 - \frac{Z_-^2}{Z^2}\right)\,\mathrm{d}y_1, \\
\theta_2 &= \int_{-\infty}^y \left[\frac{1}{Z^2}\int_{-\infty}^{y_1}(S^2 - S_-^2)\,\mathrm{d}y_2 + K_-^2\int_{-\infty}^{y_1}\left(1 - \frac{Z_-^2}{Z^2}\right)\,\mathrm{d}y_2\right]\,\mathrm{d}y_1.
\end{aligned} \tag{5.21}$$

Having normalised χ and θ, the matching conditions at $y = 0$ become

$$G_+(0) = \Gamma G_-(0), \qquad \text{and} \qquad G_+'(0) = \Gamma G_-'(0), \tag{5.22}$$

for some constant Γ. Consistency thus implies $G_+(0)G_-'(0) = G_-(0)G_+'(0)$, which gives

$$\begin{aligned}
0 = &\left[\frac{S_+^2}{K_+} + \frac{S_-^2}{K_-}\right] \\
&+ \alpha\left[\int_0^\infty (S^2 - S_+^2)\,\mathrm{d}y + \int_{-\infty}^0 (S^2 - S_-^2)\,\mathrm{d}y\right. \\
&\left. - \frac{S_+^2}{K_+K_-}\int_{-\infty}^0 \left(1 - \frac{S_-^2}{S^2}\right)\,\mathrm{d}y - \frac{S_-^2}{K_+K_-}\int_0^\infty \left(1 - \frac{S_+^2}{S^2}\right)\,\mathrm{d}y\right] + O(\alpha^2),
\end{aligned} \tag{5.23}$$

where the factor of $-1/Z^2$ multiplying the whole of the right hand side has been removed.

Although we have focussed on the case of uniform background magnetic field, it is possible to include a non-uniform background magnetic field in our derivation, subject to imposing conditions analogous to those for the background velocity profile. For the case where there is a underlying topography, we refer the reader to the article of Collings & Grimshaw (1980) for the assumptions required.

5.5.1 Hyperbolic-tangent shear layer

For a shear layer, $U_\pm = \pm 1$, the leading order term of expression (5.23) gives

$$\frac{(1-c^{(0)})^2 - M^2}{\sqrt{1-F^2[(1-c^{(0)})^2 - M^2]}} + \frac{(1+c^{(0)})^2 - M^2}{\sqrt{1-F^2[(1+c^{(0)})^2 - M^2]}} = 0, \tag{5.24}$$

which is exactly the eigenvalue equation of the vortex sheet (4.6). Hence, for any shear layer, $c \to c_\mathrm{v}$ in (4.8) as $\alpha \to 0$. This is perhaps not entirely surprising: sufficiently long waves will, at least to leading order, see the shear layer as a discontinuity. This also suggests that the tongue of instability (cf. Figure 5.1c) is a generic feature of shear layer profiles since long waves are unstable in the tongue region.

Information about the second mode of instability may be obtained at the next order. From the discussion of the vortex sheet in Chapter 4, we know that when F is sufficiently high, the eigenvalue c_v becomes real. Following Blumen *et al.* (1975), we consider $c = c_\mathrm{v} + \alpha c^{(1)} + \cdots$. Choosing $c_\mathrm{v} \in \mathbb{R}^+$, we note that

$$K_{+,0}K_{-,0} = \sqrt{1-F^2[(1-c_\mathrm{v})^2 - M^2}\sqrt{1-F^2[(1+c_\mathrm{v})^2 - M^2} = 1 \tag{5.25}$$

upon writing out c_v in full using (4.8). Assuming $(1-M^2) = O(1)$, to proceed, we need to obtain the $O(\alpha)$ correction to this first term in the square bracket in (5.23), and evaluate the remaining integrals.

Taking $c = c_\mathrm{v} + \alpha c^{(1)}$ and Taylor expand accordingly, we use the $O(1)$ relation that

$$\frac{S_{+,0}^2}{K_{+,0}^2} = -\frac{S_{-,0}^2}{K_{-,0}^2} \tag{5.26}$$

to eliminate terms accordingly. This yields in our case

$$\frac{S_+^2}{K_+^2} + \frac{S_-^2}{K_-^2} = \cdots + \alpha\left[\frac{c^{(1)}}{K_{+,0}}\frac{2}{S_{-,0}^2}4c_\mathrm{v}\sqrt{1+4F^2+4F^4M^2}\right]. \tag{5.27}$$

In the $M = 0$ case this is an equivalent form to that obtained by Blumen *et al.* (1975).

Now, to evaluate the integrals on the right hand side of (5.23). When $U_0 = \tanh(y)$,

$$\int_0^\infty (S^2 - S_+^2)\,\mathrm{d}y + \int_{-\infty}^0 (S^2 - S_-^2)\,\mathrm{d}y = -2. \tag{5.28}$$

For the latter two integrals, using the substitution $v = \tanh(y)$ and partial fractions results in

$$\begin{aligned} -\frac{S_+^2}{K_+K_-}\int_{-\infty}^{0}\left(1-\frac{S_-^2}{S^2}\right)\,\mathrm{d}y - \frac{S_-^2}{K_+K_-}\int_{0}^{\infty}\left(1-\frac{S_+^2}{S^2}\right)\,\mathrm{d}y \\ = -2c_\mathrm{v}\left[\int_{-1}^{0}\frac{-\mathrm{d}v}{1-v}+\int_{0}^{1}\frac{\mathrm{d}v}{1+v}\right] \\ + \frac{1-(c_\mathrm{v}-M)^2}{2M}\int_{-1}^{1}\frac{\mathrm{d}v}{v-M-c_\mathrm{v}} - \frac{1-(c_\mathrm{v}+M)^2}{2M}\int_{-1}^{1}\frac{\mathrm{d}v}{v+M-c_\mathrm{v}}. \end{aligned} \tag{5.29}$$

In (5.29), for the integrals in the square brackets, since there are no singularities on the integration path, the integrals may be evaluated in the usual fashion. For the other two integrals, there is potentially a singularity on the integration path. Since $c_\mathrm{v} \in \mathbb{R}^+$, we deform the contour as a semicircle to go under the singularity[1] at $v = c_\mathrm{v} + M$ and $v = c_\mathrm{v} - M$ respectively. Observing that the singularities are simple poles with residue 1, the final expression is given by

$$\begin{aligned} (5.29) =& \frac{1-(c_\mathrm{v}-M)^2}{2M}\log\left(\frac{1-M-c_\mathrm{v}}{1+M+c_\mathrm{v}}\right)+\delta_1 \\ & - \frac{1-(c_\mathrm{v}+M)^2}{2M}\log\left(\frac{1+M-c_\mathrm{v}}{1-M+c_\mathrm{v}}\right)-\delta_2, \end{aligned}$$

with

$$\delta_1 = \begin{cases} \pi\mathrm{i}, & |c_\mathrm{v}-M|\le 1, \\ 0, & \text{otherwise}, \end{cases} \qquad \text{and} \qquad \delta_2 = \begin{cases} \pi\mathrm{i}, & c_\mathrm{v}+M\le 1, \\ 0, & \text{otherwise}. \end{cases} \tag{5.30}$$

Putting the above together, writing everything out in full and manipulating the expressions a little, we final obtain an expression for $c^{(1)}$ given by

$$\begin{aligned} c^{(1)} =& \mathrm{i}\frac{\sqrt{F^2[(1-c_\mathrm{v})^2-M^2]-1}}{4c_\mathrm{v}^2}\frac{(1+c_\mathrm{v})^2-M^2}{\sqrt{1+4F^2+4F^4M^2}}\times \\ & \left(1+\frac{c_\mathrm{v}^2}{2}\left[\log\left(\frac{(1+c_\mathrm{v})^2-M^2}{(1-c_\mathrm{v})^2-M^2}\right)-\delta_1-\delta_2\right]\right. \\ & \left. +\frac{1-M^2-c_\mathrm{v}^2}{4M}\left\{\log\left(\frac{(1+M)^2-c_\mathrm{v}^2}{(1-M)^2-c_\mathrm{v}^2}\right)+\delta_1-\delta_2\right\}\right), \end{aligned} \tag{5.31}$$

with δ_i given by (5.30). It may be shown that for $M \to 0$, the expression inside the braces is equal to $4M(1-c_\mathrm{v})^{-2} + O(M^2)$, and that equation (5.31) formally reduces to an equivalent form of equation (21) in Blumen *et al.* (1975). Unlike for the leading order result c_v, there is no cut off with increasing F. By expanding c_v given by (4.8) up to powers of F^{-4}, it may though be readily demonstrated from (5.31) that $\mathrm{Im}(c^{(1)}) \to 0^+$ as $F \to \infty$.

The analysis leading to expression (5.31) is valid only for c_v not close to zero, i.e., F^2 not close to $2(1-M^2)^{-1}$ or M not close to 1. When $2 - F^2(1-M^2)^{-1}$ is small, $O(\alpha^{2/3})$ to be precise, we

[1] As we consider $\mathrm{Im}(c_\mathrm{v}) \to 0^+$.

have $c_{\mathrm{v}} \sim \alpha c^{(1)} \sim \alpha^{1/3}$. Performing appropriate rescaling and choosing the appropriate branch so that $\mathrm{Re}(\sqrt{\cdots}) > 0$, gives $c^{(1)}$ as the solution of the cubic equation

$$\frac{6+2M^2}{(1-M^2)^3}c^3 + \left(\frac{2}{1-M^2} - F^2\right)c - \mathrm{i}\alpha\left[\frac{1}{1-M^2} + \frac{1}{2M}\log\frac{1+M}{1-M}\right] = 0, \tag{5.32}$$

for $\alpha^{2/3} \sim 2(1-M^2)^{-1} - F^2 \to 0$. Equation (5.32) formally reduces to equation (23) in Blumen *et al.* (1975). There is an inadmissible root $c = -\mathrm{i}c_i$, and two roots that are either purely imaginary ($c = \mathrm{i}c_i$) or complex ($c = \pm c_r + \mathrm{i}c_i$) depending on F^2. Considering the expansion

$$(5.32) = (c - \mathrm{i}A)^2(c - \mathrm{i}B),$$

the transition to non-zero c_r may be seen to occur at

$$F^2_{\mathrm{cusp}} = \frac{2}{1-M^2} - 3\left[\frac{\alpha^2}{4}\frac{6+2M^2}{(1-M^2)^3}\left(\frac{1}{1-M^2} + \frac{1}{2M}\log\frac{1+M}{1-M}\right)^2\right]^{1/3}. \tag{5.33}$$

This expression reduces to $F^2_{\mathrm{cusp}} = 2 - 3(6\alpha^2)^{1/3}$ when $M \to 0$, as given by Blumen *et al.* (1975). The leading order result with, separately, corrections from the outer and inner expansions, together with the full numerical results, are presented in figure 5.19. The asymptotic results, including the location of the cusp given by equation (5.33), show excellent agreement with the numerically computed values.

5.5.2 Long-wave asymptotics for jets

A general velocity profile is defined as a jet if, in an appropriate frame, $U_\pm = 0$. In this case, expression (5.23) simplifies to

$$0 = \frac{2S_0^2}{K_0} + \alpha\left[\int_{-\infty}^{\infty}(S^2 - S_0^2)\,\mathrm{d}y - \frac{S_0^2}{K_0^2}\int_{-\infty}^{\infty}\left(1 - \frac{S_0^2}{S^2}\right)\,\mathrm{d}y\right] + O(\alpha^2), \tag{5.34}$$

where $S_0^2 = (0-c)^2 - M^2$. Here, for a fixed value of F, we need to consider different regimes for M. For $F^2 = O(1)$, if $M^2 = O(1)$ then c is real at both leading order and at the next order correction. The marginal case is $M^2 \sim \alpha$, but this gives $c^{(0)} = 0$ at leading order. At the next order correction, we choose to balance the first two terms on the right hand side of (5.34). On letting $M^2 = \mu\alpha$ and defining $E = \int_{-\infty}^{+\infty} U^2/2\,\mathrm{d}y$, where E may be assumed to be $O(1)$ via rescaling, we obtain

$$c \sim \mathrm{i}\sqrt{\alpha E - M^2} \qquad \text{as} \qquad M^2 \sim \alpha \to 0,\ F^2 = O(1). \tag{5.35}$$

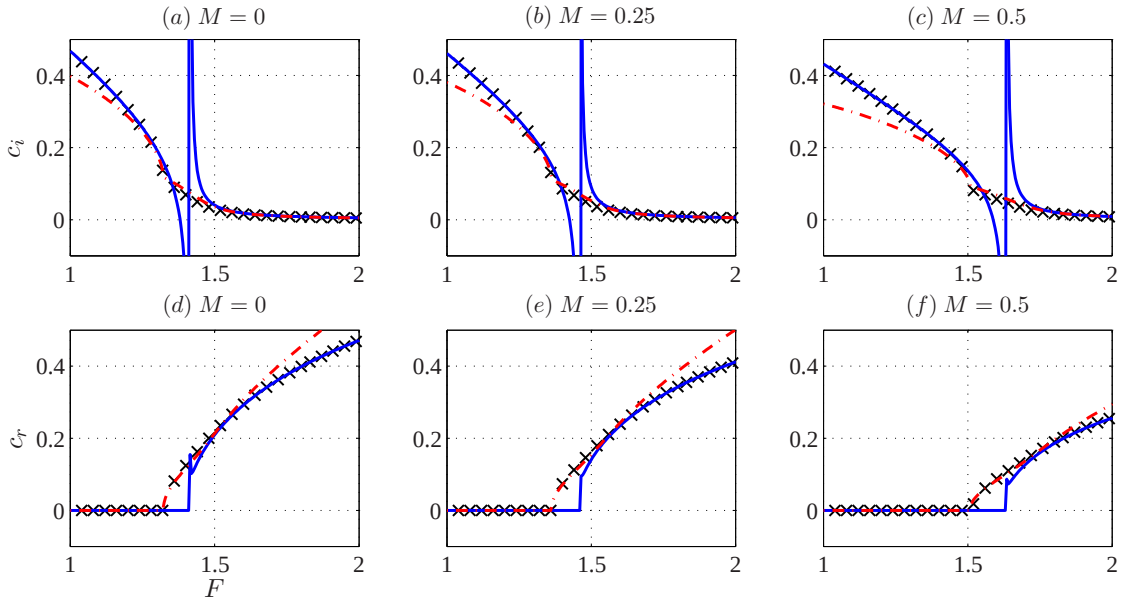

Figure 5.19: Line graphs of $c = c_r + \mathrm{i}c_i$ at $\alpha = 0.01$, varying with F for some values of M, for the shear layer. The crosses are computed results, solid line is the asymptotic result $c_{\mathrm{v}} + \alpha c_1$ with c_1 given by (5.31), and the dot-dashed line is the inner expansion given by the relevant solution to the cubic (5.32).

The corresponding result for the compressible hydrodynamic case was derived by Gill & Drazin (1965), and for the incompressible MHD case by Gedzelman (1973).

For large F, we let $F^2 = \epsilon^{-1} \gg 1$. Then the interesting case is when $M^2 = O(\epsilon)$ and $\alpha \sim \epsilon$. Considering the same balance as above gives the following result:

$$c \sim \mathrm{i}\left[\frac{\alpha^2 F^2 E^2}{2} - M^2 + \sqrt{\alpha^2 E^2 + \frac{\alpha^4 F^4 E^4}{4}}\right]^{1/2} \qquad \text{as} \qquad \frac{1}{F^2} \sim M^2 \sim \alpha \to 0. \tag{5.36}$$

This result reduces formally to (5.34) in the limit of small F.

For the Bickley jet, $\int_{-\infty}^{+\infty} (\mathrm{sech}^2 y)^2 \, \mathrm{d}y = 4/3$. The corresponding long-wave asymptotic results are therefore given by

$$c \sim \mathrm{i}\sqrt{\frac{2}{3}\alpha - M^2} \qquad \text{as} \qquad M^2 \sim \alpha \to 0, \; F^2 = O(1), \tag{5.37}$$

and

$$c \sim \mathrm{i}\left[\frac{2}{9}\alpha^2 F^2 - M^2 + \frac{2}{3}\sqrt{\alpha^2 + \frac{\alpha^4 F^4}{9}}\right]^{1/2} \qquad \text{as} \qquad \frac{1}{F^2} \sim M^2 \sim \alpha \to 0. \tag{5.38}$$

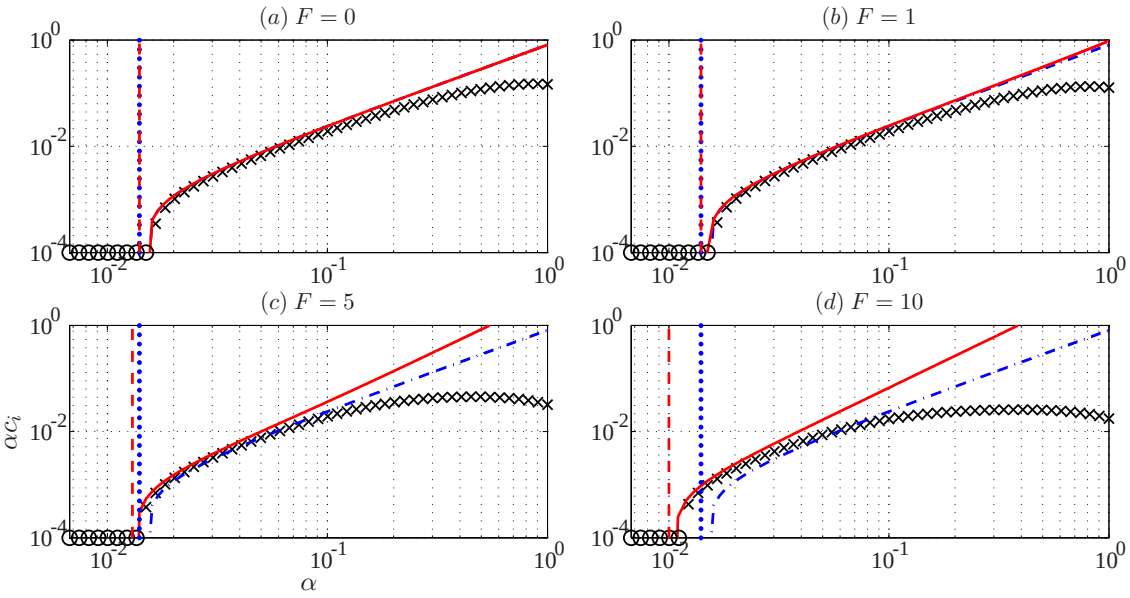

Figure 5.20: Comparison of the computed growth rates (crosses) and the predicted growth rates from the asymptotic results for $U(y) = \mathrm{sech}^2(y)$, at $M = 0.1$: $\alpha\times$(5.37) is given by the dot-dashed line (cutoff plotted as vertical dotted line) and $\alpha\times$(5.38) is given by the solid line (cutoff plotted as vertical dashed line). Circles denote the modes stabilised by the magnetic field.

The growth rate as predicted by (5.37) and (5.38) is plotted against the computed growth rates (of the even mode) in Figure 5.20; it can be seen that the cutoffs due to the magnetic field are accurately predicted.

5.5.3 Consistency issues of long-wave asymptotics for jets

One potential concern is that we have assumed that the second integral in the square brackets in expression (5.34) is negligible in the leading order balance. We show here that

$$\frac{c^2 - M^2}{1 - F^2(c^2 - M^2)} \int_{-\infty}^{+\infty} \left[1 - \frac{c^2 - M^2}{(U_0 - c)^2 - M^2}\right] \mathrm{d}y = O(\epsilon \log \epsilon), \tag{5.39}$$

where ϵ is some small parameter related to the regime of interest. Thus the asymptotic scheme is indeed consistent.

Following Drazin & Howard (1962), we shall assume that $|U_0| \leq A\mathrm{e}^{-a|y|}$, which is satisfied for the Bickley jet considered. This condition may be relaxed: choosing $|U_0| \leq A/(1 + y^{2n})$, where n is an integer, provides a modified version of (5.39) using the approach below. Drazin

& Howard (1962) make the additional assumption that c is 'almost pure imaginary', namely that $|c|/|c_i| \leq N < \infty$. Here we adopt the modified assumption that

$$\frac{|c|^2 + M^2}{c_i^2} \leq N_1 = O(1). \tag{5.40}$$

Although there is no rigourous explanation for why this should hold, it is supported by both our *a posteriori* numerical and asymptotic results.

Consider first the case of $F = 0$. The left hand side of (5.39) is then given by

$$I = (c^2 - M^2) \int_0^\infty \left[1 - \frac{c^2 - M^2}{(U_0 - c)^2 - M^2} \right] \mathrm{d}y, \tag{5.41}$$

where we have taken the integral over the positive real-half line without loss of generality. We split the range of integration as

$$\int_0^\infty = \int_0^{\log(\cdot)} + \int_{\log(\cdot)}^\infty, \qquad \text{where} \quad \log(\cdot) = \log\left(\frac{A}{c}\right)^{1/a}. \tag{5.42}$$

We now proceed by bounding the individual integrals and estimating their leading order size by using the result (5.34). First, using

$$|(U_0 - c)^2 - M^2| \geq c_i^2, \tag{5.43}$$

it is seen that

$$\begin{aligned} (c^2 - M^2) \int_0^{\log(\cdot)} (\cdots)\, \mathrm{d}y &\leq |c^2 - M^2| \int^{\log(\cdot)} \left[1 + \frac{|c|^2 + M^2}{c_i^2} \right] \mathrm{d}y \\ &\leq |c^2 - M^2| \log(\cdot)[1 + N_1] \\ &= O(\alpha \log \alpha), \end{aligned} \tag{5.44}$$

upon also using the assumption that $M^2 = O(\alpha)$, and the derived result (5.34) that $c = O(\alpha^{1/2})$.

We choose to construct an upper bound for the second integral as follows:

$$\begin{aligned} (c^2 - M^2) \int_{\log(\cdot)}^\infty (\cdots)\, \mathrm{d}y &= (c^2 - M^2) \int_{\log(\cdot)}^\infty \left[\frac{U_0^2 - 2U_0 c}{(U - c)^2 - M^2} \right] \\ &\leq \frac{|c^2 - M^2|}{c_i^2} \int_{\log(\cdot)}^\infty [U_0^2 + 2|U_0||c|]\, \mathrm{d}y \\ &\leq N_1 \left[\frac{A^2 \mathrm{e}^{-2a \log(\cdot)}}{2a} + \frac{2A \mathrm{e}^{-a \log(\cdot)}}{a} \right] \\ &= O(\alpha), \end{aligned} \tag{5.45}$$

from which it follows that $I = O(\alpha \log \alpha)$.

For $F^2 = O(1)$, we make the additional assumption that

$$\frac{1}{|1 - F^2(c^2 - M^2)|} \leq \frac{1}{|1 + F^2M^2 - F^2|c|^2|} \leq N_2 = O(1), \tag{5.46}$$

where we have used the triangle inequality in reverse and made use of the facts that $M^2 = O(\alpha)$ and that $c = O(\alpha^{1/2})$ from (5.35). We may immediately conclude that $I = O(\alpha \log \alpha)$ as before. For $F^2 = \epsilon^{-1}$, the corresponding result is (5.35), which states that $c = \tilde{C}\sqrt{\epsilon}$ and $M^2 = \mu\epsilon$; an entirely analogous procedure will give the result $I = O(\epsilon \log \epsilon)$. So indeed we have consistency of the asymptotic scheme for the jet case. For $|U_0| \leq A/(1 + y^{2n})$, an analogous result may be derived by adopting a different splitting of the integral in (5.42). This shows that if we were to calculate the next order correction, we need to be aware that we may obtain terms of $O(\epsilon \log \epsilon)$, something that is perhaps not immediately obvious. A modification of this procedure may be applied to the case where the magnetic field is not uniform.

5.6 Summary and discussion

For the shear layer, we found two types of instabilities. The first of these is what we termed the inflection point instability, possessing the characteristic that $c_r = 0$, and its instability mechanism may be interpreted as the result of a pair of counter-propagating Rossby waves. The other instability we found is the supersonic instability, possessing the characteristic that $c_r \neq 0$, and are generally attributed to gravity waves interacting with the critical levels. The supersonic instabilities were found to be weaker instabilities, so we have focussed our study on the inflection point instabilities.

The inflection-point instability is strongest around the $F = 0$, $M = 0$ case, for which there exists an interpretation for the instability mechanism in terms of counter-propagating Rossby waves. We showed that modifications due to MHD and/or shallow-water effects are present. It was seen that the underlying Rossby wave mechanism necessarily generate vorticity anomalies that counteract the basic instability mechanism, consistent with the observed stabilisation from the numerical results.

A long-wave asymptotic analysis showed that, at leading order, the instability behaves like a vortex sheet instability as discussed in Chapter 4. When there is no leading order instability, there can be instability at $O(\alpha)$, and the resulting analytical expression describes well the supersonic modes

from the numerical calculations. The critical F for which that supersonic instability becomes the preferred mode of instability was also derived from this asymptotic analysis.

For the Bickley jet, the parity result dictates that the eigenfunction is either even or odd about $y = 0$. The even mode is generally found to be more unstable than the odd mode, although there are isolated regions in parameter space where the converse is true. A cutoff of the instability due to the magnetic field at $\alpha \ll 1$ is again observed, and the locations of the cutoffs may be found using an asymptotic analysis.

With regards to the Rossby wave mechanism, there were details that we have not taken into account, such as the changes in the phase-locking mechanism (the induced vorticity anomalies from extra effects accelerates the underlying Rossby waves), or whether it would be applicable even in the tongue region of instability for the shear layer. The mathematical basis appears to be well developed for an extended investigation (e.g., Heifetz *et al.*, 1999, 2004, 2009; Carpenter *et al.*, 2012), and it would be interesting to investigate the modifications to the wave dynamics, potentially revealing the more subtle features possessed by the instability. Since we know that, in the hydrodynamic case, the stability criteria may be interpreted as conditions that allow the relevant mechanisms to occur, one question we may ask is that, if we know the precise details associated with the instability mechanism, can we deduce from this stability criteria (e.g., Heifetz *et al.*, 2009)? This would be particularly interesting since we have not managed to derive stability conditions for this system of equations, and this may provide another avenue to derive stability theorems.

With regards to the supersonic instabilities, it would also be interesting to consider a further investigation into the characteristic of these instabilities, using tools employed by previous works (e.g., Satomura, 1981; Hayashi & Young, 1987; Takehiro & Hayashi, 1992; Balmforth, 1999). It was mentioned also in Balmforth (1999) that one interpretation of these supersonic instabilities is via over-reflection (e.g., Acheson, 1976; Lindzen & Tung, 1978; McIntyre & Weissman, 1978; Lindzen, 1988; Harnik & Heifetz, 2007; Bakas & Farrell, 2010; Benilov & Lapin, 2013), and it would be interesting to derive the modifications to over-reflection in SWMHD to further our understanding on phenomena involving magneto-gravity waves. Furthermore, in the work of Harnik & Heifetz (2007), an attempt was made to reconcile over-reflection and the Rossby wave action-at-a-distance mechanism, and it would also be interesting to see how over-reflection leading to instability may be interpreted in this formalism.

5.7 Appendix: Recovering fields from the eigenfunction G

The quantities $(\hat{u}, \hat{v}, \hat{b}_x, \hat{b}_y, \hat{h})$ may be recovered from knowledge of the eigenfunction G. It may be shown that, for the case where $H \equiv 1$ and $\hat{v} = (U_0 - c)G$

$$\hat{v} = (U_0 - c)G, \tag{5.47a}$$

$$\hat{b}_y = MB_0G, \tag{5.47b}$$

$$\hat{u} = \frac{\hat{v}' + F^2M[B_0'(U_0 - c) + B_0U_0']\hat{b}_y - F^2[(U_0 - c)U_0' + M^2B_0B_0']\hat{v}}{-\mathrm{i}\alpha[1 - F^2[(U_0 - c)^2 - M^2B_0^2]]}, \tag{5.47c}$$

$$\hat{b}_x = \frac{\hat{b}_y' + F^2[(U_0 - c)U_0' + MB_0U_0']\hat{b}_y - F^2M[B_0U_0' + (U_0 - c)B_0')]\hat{v}}{-\mathrm{i}\alpha[1 - F^2[(U_0 - c)^2 - M^2B_0^2]]}, \tag{5.47d}$$

$$\hat{h} = \frac{M(B_0'(U_0 - c) + B_0U_0')\hat{b}_y - [(U_0 - c)U_0' + M^2B_0B_0']\hat{v} + [(U - c)^2 - M^2B_0^2]\hat{v}'}{\mathrm{i}\alpha(U - c)[1 - F^2[(U_0 - c)^2 - M^2B_0^2]]}. \tag{5.47e}$$

In the investigation presented here, the numerical derivatives were calculated by a fourth-order accurate finite-difference approximation using the `weights` routine given in Fornberg (1998). We observe here $\hat{h}$ remains formally at $O(1)$ because of the rescaling $\hat{h} = \hat{\tilde{h}}/F^2$ employed when we wrote down the full non-dimensionalised SWMHD equations. Indeed, since $\hat{h}$ is to be identified with $\hat{p}$ when $F = 0$, it may be shown that we recover the above expression if we start with the equations with $F = 0$ and reconstruct p from $(\hat{u}, \hat{v}, \hat{b}_x, \hat{b}_y)$. The perturbation displacement η, vorticity ω, potential vorticity q and current j are seen to satisfy

$$\frac{\mathrm{D}\eta}{\mathrm{D}t} = v \qquad \Rightarrow \qquad \hat{\eta} = \frac{\hat{v}}{\mathrm{i}\alpha(U_0 - c)}, \tag{5.48a}$$

$$\omega = \frac{\partial v}{\partial x} - \frac{\partial u}{\partial y} \qquad \Rightarrow \qquad \hat{\omega} = \mathrm{i}\alpha\hat{v} - \hat{u}', \tag{5.48b}$$

$$Q + q = \frac{\Omega_0 + \omega}{1 + F^2h} \qquad \Rightarrow \qquad \hat{q} = \hat{\omega} - F^2\Omega_0\hat{h} + O(\text{small}^2), \tag{5.48c}$$

$$j = \frac{\partial b_y}{\partial x} - \frac{\partial b_x}{\partial y} \qquad \Rightarrow \qquad \hat{j} = \mathrm{i}\alpha\hat{b}_y - \hat{b}_x'. \tag{5.48d}$$

Working out vorticity and current from $\hat{\omega}$ and $\hat{j}$ is found to be more accurate than taking derivatives of the full u and v fields. It is found that by taking the numerical solution and inserting it back into the linearised equations (3.3), the largest error as measured by the L_∞ norm is of $O(10^{-2})$ for the choice of numerical tolerance we used for working out G. This occurs in the y-momentum equation; typical diagrams for the errors from an inversion is given in Figure 5.21.

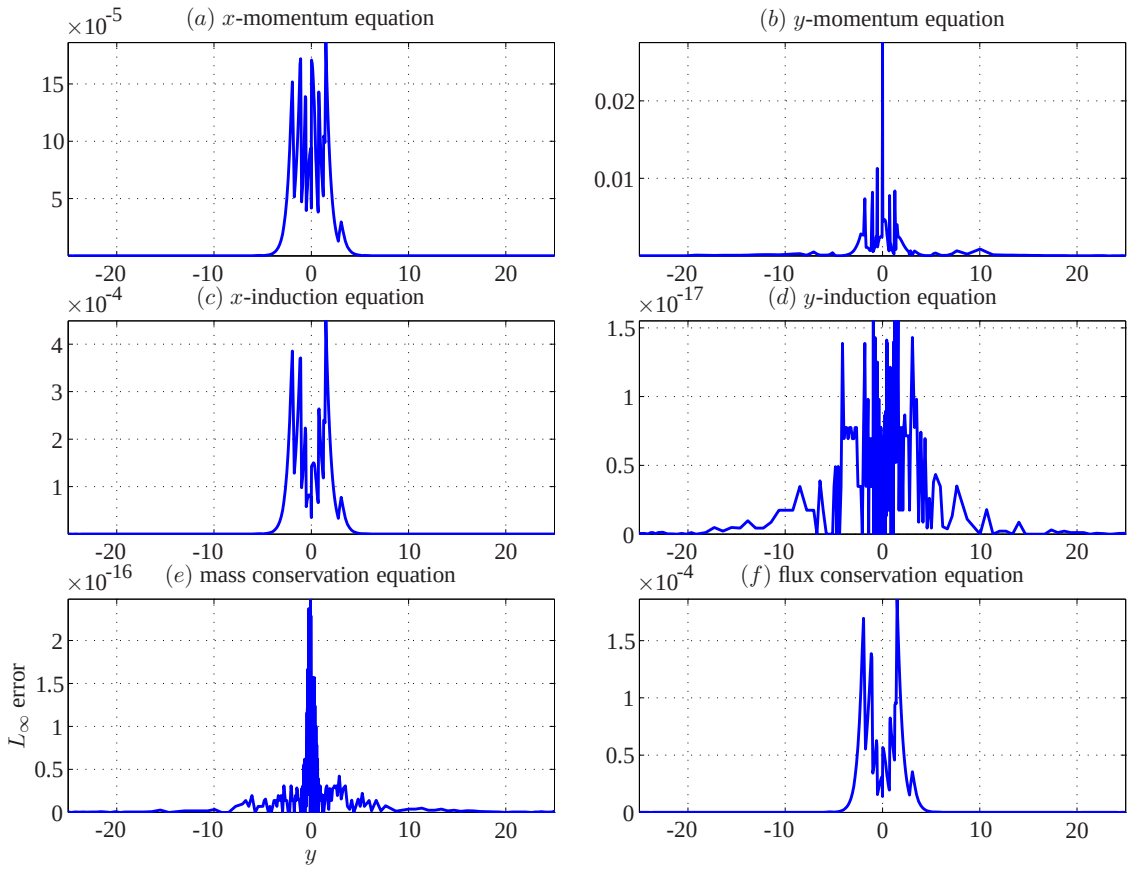

Figure 5.21: L_∞ error of the inverted eigenfunctions for the case $F = 0.7$, $M = 0.2$ and $\alpha = 0.26$, when the numerical solutions are substituted into the linearised SWMHD equations given by (3.3). This diagram is typical of the behaviour of the errors, with the largest errors in the y-momentum equation.

Chapter 6

Nonlinear evolution: two-dimensional incompressible MHD

In the previous chapter the instability characteristics of the shear layer and the Bickley jet profile were investigated. A natural progression now is to investigate the nonlinear evolution of unstable shear flows. In this chapter, we consider the incompressible limit ($F = 0$) to highlight the dynamics due to MHD effects, before moving on to an investigation of the full SWMHD system in Chapter 7. We start by reviewing in some detail the numerical methods we employ. We then review the hydrodynamic case before proceeding to an investigation of the MHD case. A summary and discussion of the results are given at the end of the chapter.

6.1 Mathematical formulation and numerical methods

As in the previous chapter, we consider the case with no topography and a uniform background magnetic field given by $B_0 = 1$, and we will consider either $U_0(y) = \tanh(y)$ or $U_0(y) = \text{sech}^2(y)$; $M = \mathcal{B}/\mathcal{U}$ is then our measure of the field strength. We shall be investigating the nonlinear evolution numerically. Since we only have finite resolution and we expect the evolution to generate small-scales, we need something to damp these small-scale features, in a physical manner, to stabilise our numerical routines. To this end, we reinstate the viscous and Ohmic dissipation. The (two-dimensional) incompressible MHD equations ($F = 0$) in non-dimensional

form are then given by

$$\frac{\partial \boldsymbol{u}}{\partial t} + \boldsymbol{u}\cdot\nabla\boldsymbol{u} - \nabla p - M^2\boldsymbol{b}\cdot\nabla\boldsymbol{b} = \frac{1}{\mathrm{Re}}\nabla^2\boldsymbol{u}, \tag{6.1a}$$

$$\frac{\partial \boldsymbol{b}}{\partial t} + \boldsymbol{u}\cdot\nabla\boldsymbol{b} - \boldsymbol{b}\cdot\nabla\boldsymbol{u} = \frac{1}{\mathrm{Rm}}\nabla^2\boldsymbol{b}, \tag{6.1b}$$

$$\nabla\cdot\boldsymbol{u} = 0, \tag{6.1c}$$

$$\nabla\cdot\boldsymbol{b} = 0. \tag{6.1d}$$

The Reynolds numbers are defined using the velocity and length scales associated with the basic flow, so

$$\mathrm{Re} = \frac{\mathcal{U}\mathcal{L}}{\nu}, \qquad \mathrm{Rm} = \frac{\mathcal{U}\mathcal{L}}{\eta}, \tag{6.2}$$

where ν is the kinematic viscosity, and η is the coefficient of magnetic diffusivity.

We shall be interested in the temporal evolution of the dynamics, and we consider a domain that is periodic in x and wall bounded in y. A domain of length $L_x = 2\pi/\alpha$ will support one wavelength of the instability with wavenumber α, doubling this gives two wavelengths of the instability, and so forth. Although the basic flow profiles are technically defined on an unbounded domain, it is found that by taking the y-boundaries located at $y = \pm L_y$ for L_y sufficiently large, together with appropriate boundary conditions, the dynamical influence of the boundaries can be minimised.

Since $\boldsymbol{u}$ and $\boldsymbol{b}$ are both divergence-free, we write the equations in terms of a streamfunction ψ and a magnetic potential A, here defined as

$$\boldsymbol{u} = \boldsymbol{e}_z\times\nabla\psi, \qquad \boldsymbol{b} = \boldsymbol{e}_z\times\nabla A. \tag{6.3}$$

The vorticity ω and current j are then given by

$$\omega = \nabla^2\psi, \qquad j = \nabla^2 A. \tag{6.4}$$

The divergence-free conditions are automatically satisfied, and the set of equations (6.1) have the equivalent formulation given by

$$\frac{\partial \omega}{\partial t} + \partial(\psi,\omega) - M^2\partial(A,\nabla^2 A) = \frac{1}{\mathrm{Re}}\nabla^2\omega, \tag{6.5a}$$

$$\frac{\partial A}{\partial t} + \partial(\psi, A) = \frac{1}{\mathrm{Rm}}\nabla^2 A, \tag{6.5b}$$

$$\nabla^2\psi = \omega, \tag{6.5c}$$

where

$$\partial(\alpha,\beta) = \frac{\partial\alpha}{\partial x}\frac{\partial\beta}{\partial y} - \frac{\partial\alpha}{\partial y}\frac{\partial\beta}{\partial x} \tag{6.6}$$

is the usual Jacobian term. The corresponding basic states are then given by

$$\Psi_0(y) = \begin{cases} -\log\cosh(y), \\ -\tanh(y), \end{cases} \qquad A_0(y) = -y. \tag{6.7}$$

This set up is convenient in that we do not have to worry about imposing the divergence-free condition at every time step via, for example, splitting methods, projection methods, or semi-implicit methods (e.g., Peyret, 2002).

In our channel geometry, boundary conditions in y need to be imposed accordingly. The no-normal flow condition implies $v = \partial\psi/\partial x = 0$ on $y = \pm L_y$, so ψ is a constant function in x. Then, because momentum is conserved,

$$\iint u \,\mathrm{d}x\mathrm{d}y = \iint \frac{\partial\psi}{\partial y}\,\mathrm{d}x\mathrm{d}y = L_x[\psi(t)]_{-L_y}^{L_y} = \text{constant}, \tag{6.8}$$

so we must have

$$[\psi(t)]_{-L_y}^{L_y} = [\psi(0)]_{-L_y}^{L_y}. \tag{6.9}$$

This is satisfied if

$$\psi(t, \pm L_y) = \psi(0, \pm L_y). \tag{6.10a}$$

The same argument applies to the no-normal flux condition $b_y = 0$, giving

$$A(t, \pm L_y) = A(0, \pm L_y). \tag{6.10b}$$

To mimic a free shear flow, we use stress-free boundary conditions rather than no-slip, so

$$\frac{\partial u}{\partial y} = 0 \qquad \Rightarrow \qquad \frac{\partial^2\psi}{\partial y^2} = \omega(\pm L_y) = 0. \tag{6.10c}$$

The above conditions are then to be enforced at each time-step accordingly.

Additionally, we split the above quantities as a basic state plus a perturbation, i.e.

$$\psi = \Psi_0(y) + \tilde{\psi}, \qquad A = A_0(y) + \tilde{A}, \tag{6.11}$$

and also

$$\omega = \Omega_0(y) + \nabla^2\tilde{\psi} = -U_0'(y) + \nabla^2\tilde{\psi}, \qquad j = J_0(y) + \nabla^2\tilde{A} = 0 + \nabla^2\tilde{A}. \tag{6.12}$$

Inserting this into equation (6.5) and dropping the tildes, we obtain the equivalent formulation

$$\frac{\partial \omega}{\partial t} + U_0 \frac{\partial \omega}{\partial x} + \Omega_0' \frac{\partial \psi}{\partial x} + \partial(\psi, \omega) - M^2 \left[\frac{\partial \nabla^2 A}{\partial x} + \partial(A, \nabla^2 A) \right] = \frac{1}{\mathrm{Re}} \nabla^2 \omega + \frac{1}{\mathrm{Re}} \Omega_0'', \quad (6.13a)$$

$$\frac{\partial A}{\partial t} + U_0 \frac{\partial A}{\partial x} - \frac{\partial \psi}{\partial x} + \partial(\psi, A) = \frac{1}{\mathrm{Rm}} \nabla^2 A, \quad (6.13b)$$

$$\nabla^2 \psi = \omega. \quad (6.13c)$$

At first this seems to be complicating matters somewhat, but there are in fact several benefits to doing this. Using the same arguments for the boundary conditions as above, the conditions to be imposed on equations (6.13) translate to

$$\psi(\pm L_y) = 0, \qquad A(\pm L_y) = 0, \qquad \omega(\pm L_y) = 0. \quad (6.14)$$

We also see that if we manually set the Jacobian terms to zero, we recover the linear equations, and this provides a check on the numerical routines by comparing the results with the linear calculations from the previous chapter. One possible concern is that the viscous dissipation changes the background flow before the instability has a chance to manifest. To combat this, we can switch off the basic state dissipation $\mathrm{Re}^{-1}\Omega_0''$ during the linear phase, and switch it back on when the perturbations are sufficiently large (e.g., measured by the energy). Tests have been carried out comparing this approach to a case where everything (background flow and perturbations) is dissipated and a case where only the perturbation states are dissipated, and the qualitative differences are not large, so we employ this approach in our simulations.

6.2 Numerical methods: Fourier–Chebyshev pseudo-spectral method

We solve the system (6.13) using a pseudo-spectral method, a popular method that is characterised by its high accuracy and that is especially powerful in rectangular domains. We consider a Fourier expansion in x and a Chebyshev expansion in y. We review the basic procedures here for self-containment purposes (for further reading, see, for example, Canuto *et al.* 1993, Fornberg 1998, Trefethen 2000, Boyd 2001, Peyret 2002 or Durran 2010).

6.2.1 Pseudo-spectral methods

A sufficiently smooth quantity u may be expanded in terms of Fourier and Chebyshev modes as

$$u = \sum_k \sum_j a_{jk} \mathrm{e}^{\mathrm{i}kx} T_j(y), \tag{6.15}$$

where $T_j(y)$ are the Chebyshev polynomials of the first kind and the complex exponentials represent the Fourier modes. Although an infinite sum is implied, in practical situations this sum is truncated at some finite N_x and N_y corresponding to the numerical resolution. Effectively we go from a physical space description $u(x_i, y_j)$ to a spectral one where the data of interest are the coefficients a_{jk}. To obtain these coefficients, the data is sampled at special collocation points in physical space, and a spectral transform is employed to switch between physical and spectral representations. For analytical u, a spectral description has a discretisation error which drops off like $O(c^{-N})$, whereas a physical space description has a discretisation error that drops off like $O(N^{-c})$, depending on the order of discretisation. This is due to the fact that a spectral description is inherently global, taking into account the sampled data at every collocation point, whereas a finite-difference type description is local.

Certain operations are easier/faster to do in the relevant spaces. In spectral space, the operators associated with differentiation are usually relatively simple, so solving the corresponding algebraic equations is usually not a problem. However, nonlinear products are costly since a convolution sum is often required. The opposite is true in physical space; there the operators are usually dense and ill-conditioned, but products may be done trivially. To exploit the corresponding advantages, the pseudo-spectral formalism performs the differentiation and linear algebra operations in spectral space, and forms products in physical space, utilising a transform to switch between the two spaces. One of the key ingredients then is an efficient transform routine, and this exists for both Fourier and Chebyshev modes. There are aliasing errors when forming the nonlinear product followed by transforms, but these may be appropriately removed.

6.2.2 Fourier modes

For Fourier modes, the Fast Fourier Transform (FFT; algorithm due originally to Cooley & Tukey 1965) is available; see, for example, Boyd 2001, §10. This lets us transform $u(x_i)$ to $\hat{u}(k) =$

$\sum_i a_k \mathrm{e}^{\mathrm{i}kx_i}$, where the collocation points are given by

$$x_i = \frac{2\pi i}{N_x}, \qquad i = 0, 1, \cdots, N_x - 1. \tag{6.16}$$

The transform is fast in that the number of operations required is $O(N_x \log N_x)$, as opposed to standard discrete Fourier transform algorithms that typically requires $O(N_x^2)$ operations. Differentiation in spectral space is especially simple, given by

$$\frac{\partial}{\partial x} \to \mathrm{i}k. \tag{6.17}$$

Numerical tests of the FFT routines used are given in §6.8.

There are errors from using this pseudo-spectral approach, arising from the fact that there is some ambiguity when sampling a function at a finite number of collocation points. For example, suppose we have $x_i = (0, \pi, 2\pi)$, the sampled values $u(x_i) = (0, 0, 0)$ may well describe $u = \sin(nx)$ for $n \in \mathbb{Z}$; here, the resolution limits the highest harmonic that may be properly described. Normally this is not an issue, but spurious errors do arise when FFTs of nonlinear products are taken, since the combination of the lower harmonics may result in unphysical higher harmonics that are below the truncation level set by the resolution, so introducing spurious oscillations. There are several methods to remove these errors, with Orszag's 2/3 rule (Orszag, 1971) being particularly simple to implement. During the transform stage, we simply set the coefficients of the highest third of the harmonics to zero. In a Fourier representation of the above, we should bear in mind that N_x points give modes from $k = -N_x/2, \cdots 0, 1, \cdots N_x/2$, so in the transform routine, all coefficients with wavenumbers satisfying

$$|k| \geq \lceil (N_x/2)(2/3) \rceil = \lceil N_x/3 \rceil \tag{6.18}$$

are set to zero, where $\lceil (\cdot) \rceil$ is the ceiling function. We have found that dealiased runs are better behaved, especially when the run appears to only be marginally resolved. Another point to note is that the discretised version of the differential equations do not necessarily conserve discretely the physical quantities such as those mentioned in Chapter 2. One way to ensure the discretised equations inherit the conservations laws from the continuous case is to remove the dealiasing errors (e.g., Boyd, 2001, §11). All runs reported here are dealiased using Orszag's 2/3 rule.

The Fourier description allows spatial integration to be done in a particularly convenient fashion. We note that

$$\int_0^{L_x} a_k \mathrm{e}^{\mathrm{i}kx} \, \mathrm{d}x = \begin{cases} L_x a_0, & k = 0, \\ 0, & k = 2\pi n / L_x, \quad n \in \mathbb{N}. \end{cases} \tag{6.19}$$

with L_x the length of the periodic domain. So to integrate in the x-direction, we simply need to pick out the $k = 0$ Fourier mode and multiply it by L_x. This method of numerical integration is spectrally accurate.

We have also the standard Parseval's theorem given by

$$\int_0^{L_x} u^2 \, \mathrm{d}x = L_x \sum_k |a_k|^2. \tag{6.20}$$

This follows from the fact that the Fourier modes are orthogonal with respect to the corresponding inner product on this domain of interest. Indeed, expanding u^2 in Fourier modes automatically gives the result, assuming the order of integration and summation may be exchanged. This allows us for example to work out the global and modal decomposition of quadratic quantities (such as energy) whilst maintaining spectral accuracy.

6.2.3 Chebyshev modes

Chebyshev polynomials of the first kind on $y \in [-1, 1]$ may be defined by the recurrence relation

$$T_0(y) = 1, \qquad T_1(y) = y, \qquad T_{j+1}(y) = 2yT_j(y) - T_{j-1}(y). \tag{6.21}$$

Alternatively, they may be defined as polynomials satisfying

$$T_j(y) = \cos(j \arccos y), \qquad j = 0, 1, \cdots . \tag{6.22}$$

A clear description of this is given in the book of Trefethen (2000), where Chebyshev polynomials are seen as the cosine function wrapped around a cylinder. With this description, there is a clear relationship between the Chebyshev modes and cosine functions, so an adapted FFT serves as the transform.

The collocation points we employ in this case are the Gauss-Lobatto points given by

$$y_j = \cos\left(\frac{\pi j}{N_y}\right), \qquad j = 0, \cdots N_y. \tag{6.23}$$

Aliasing errors will be present if we use the pseudo-spectral approach, but again may be removed by setting to zero the highest third of the wavenumbers.

Differentiation in Chebyshev spectral space is not as straightforward as in Fourier space; however the matrices are still relatively sparse. These differentiation matrices are evaluated via recurrence

relations, and may be shown to be given by (e.g., Peyret, 2002, §3)

$$\hat{u}_j^{(1)} = \frac{2}{c_j} \sum_{p=j+1,\ (p+j)\ \text{odd}}^{N_y} p\hat{u}_p, \qquad j = 0, \cdots N_y - 1 \tag{6.24}$$

and

$$\hat{u}_j^{(2)} = \frac{1}{c_j} \sum_{p=j+1,\ (p+k)\ \text{even}}^{N_y} p(p^2 - j^2)\hat{u}_p, \qquad j = 0, \cdots N_y - 1, \tag{6.25}$$

where the Chebyshev weights c_j are given by

$$c_j = \begin{cases} 2, & j = 0, \\ 1, & j > 0. \end{cases} \tag{6.26}$$

We then see that the differentiation matrices for the first and second derivatives D_1 and D_2 are given by

$$\mathsf{D}_1 = \begin{pmatrix} 0 & 1 & 0 & 3 & 0 & 5 & \cdots \\ & 0 & 4 & 0 & 8 & 0 & \vdots \\ & & 0 & 6 & 0 & 10 & \vdots \\ & & & 0 & 8 & 0 & \vdots \\ & & & & 0 & 10 & \vdots \end{pmatrix}, \qquad \mathsf{D}_2 = \begin{pmatrix} 0 & 0 & 8 & 0 & 64 & 0 & \cdots \\ & 0 & 0 & 48 & 0 & 240 & \vdots \\ & & 0 & 0 & 96 & 0 & \vdots \\ & & & 0 & 0 & 160 & \vdots \\ & & & & 0 & 0 & \vdots \end{pmatrix}, \tag{6.27}$$

where blank entries are zeroes. The matrices take an upper-triangular form. A rescaling is required if the domain is not defined on $y = [-1, 1]$. The corresponding matrices in physical space are dense (e.g., Trefethen, 2000, §6).

In this kind of pseudo-spectral method, boundary conditions are imposed by modifying the rows of the operators corresponding to the highest harmonics. This τ-method introduces a small error (denoted by τ) because we have sacrificed some modes in favour of forcing the boundary condition; however, we still maintain spectral accuracy. Now, the Chebyshev polynomials are seen to satisfy

$$T_j(1) = 1, \qquad T_j(-1) = (-1)^j$$

and

$$T_j'(1) = j^2, \qquad T_j'(-1) = (-1)^{j-1} j^2,$$

so for Dirichlet conditions on the boundaries, we need to replace the bottom two rows of the differential operators by

$$b_+ = \begin{pmatrix} 1 & 1 & \cdots & 1 \end{pmatrix}, \qquad b_- = \begin{pmatrix} 1 & -1 & \cdots & (-1)^{N_y} \end{pmatrix}. \tag{6.28}$$

For Neumann conditions, we need to replace the last two rows by

$$b_+ = \begin{pmatrix} 0 & 1 & \cdots & N_y^2 \end{pmatrix}, \qquad b_- = \begin{pmatrix} 0 & -1 & \cdots & (-1)^{N_y-1} N_y^2 \end{pmatrix}. \tag{6.29}$$

When the operators are modified by the rows enforcing the boundary conditions, the resulting matrix appears to be of a form where appropriate manipulations should result in uncoupled systems that may be solved separately. This is indeed the case when the resulting equation of the form of a constant-coefficient Helmholtz equation, where only second and zero derivatives are involved. For purely Dirichlet or purely Neumann conditions, the resulting system is of the quasi-tridiagonal form, for which a fast solver exists (Thual, 1986). Most equations we need to solve are of this Helmholtz type, and as such we may use the fast solver. The fast solver requires $O(N)$ operations, compared to the standard LU-decomposition with a back-substitution, which typically requires $O(N^3)$ operations. For more details of this fast solver, see Section 6.8.

Spatial integration may be performed via the Clenshaw–Curtis quadrature (Clenshaw & Curtis 1960; see also Trefethen 2000, §12). This is given by

$$\int_{-1}^{1} u \,\mathrm{d}y \approx \mathbf{w}^T \mathbf{a}, \qquad \mathbf{w} = \begin{pmatrix} 2 \\ 0 \\ \dfrac{2}{1-2^2} \\ 0 \\ \vdots \\ \dfrac{2}{1-N_y^2} \end{pmatrix} = \begin{pmatrix} c_0 \times 1 \\ c_1 \times 0 \\ c_2 \times \dfrac{2}{1-2^2} \\ 0 \\ \vdots \\ c_{N_y} \times \dfrac{1}{1-N_y^2} \end{pmatrix}, \tag{6.30}$$

where $\mathbf{a} = (a_j)$ are the Chebyshev coefficients of u. Observe that only the even coefficients make a contribution, since an odd function integrated over an even domain is identically zero.

To calculate the integrals of quadratic quantities, we cannot rely on an analogous Parseval's theorem as the Chebyshev modes are not orthogonal to the weight function $w(y) = 1$. Instead, the relationship between the coefficients of u and u^2 is given by

$$\begin{aligned} u = \sum_{j=0}^{N_y} a_j T_j \Rightarrow u^2 &= \sum_{j=0}^{N_y} \sum_{k=0}^{N_y} a_j a_k T_j T_k \\ &= \sum_{j=0}^{N_y} \sum_{k=0}^{N_y} \frac{a_j a_k}{2} (T_{j+k} + T_{|k-j|}), \end{aligned} \tag{6.31}$$

upon using a standard relation for Chebyshev polynomials. So then

$$\int_{-1}^{1} u \, \mathrm{d}y \approx \sum_{j=0}^{N_y} \sum_{k=0}^{N_y} \frac{a_j a_k}{2} \int_{-1}^{1} (T_{j+k} + T_{|k-j|}) \, \mathrm{d}y, \tag{6.32}$$

and we can evaluate the integral by summing the coefficients multiplied by the relevant Clenshaw–Curtis weights, but truncating when $(j + k) > N_y$. However, we expect this method to be extremely inefficient since we have to perform $O(N_y^2)$ elementary operations. Alternatively, one could take a FFT of u^2 and use the Clenshaw–Curtis quadrature as before. It was found that both methods are comparable in accuracy but the summation method is overly expensive except for relatively small values of N_y; see Section 6.8 for more details.

6.3 Numerical methods: time-stepping by linear multi-step methods

The spatial discretisation turns the system of PDEs into a set of differential equations taking the symbolic form

$$\frac{\partial u}{\partial t} = \mathsf{N}(u) + \mathsf{L}(u). \tag{6.33}$$

Here, u is the state vector of interest, and we will denote the nonlinear and linear operators associated with the problem as N and L respectively. For example, in the one-dimensional advection-diffusion equation, $\mathsf{N}(u) = -u\partial u/\partial x$ and $\mathsf{L}(u) = \nu \partial^2 u/\partial x^2$.

Perhaps the first 'obvious' thing to do is to consider a fully explicit discretisation; that is, something of the form

$$u^{n+1} = \mathsf{A}(\Delta t, u^n, u^{n-1}, \cdots, \mathsf{N}(u^n), \mathsf{N}(u^{n-1}), \cdots, \mathsf{L}(u^n), \mathsf{L}(u^{n-1}), \cdots), \tag{6.34}$$

where the superscript denotes the state variable at the relevant time level, and the precise form of A depends on the time-step method used. The important thing is that only information from the previous time levels are required. When the temporal discretisation is done this way, the time-step required for numerical stability is subject to the CFL condition (e.g., Boyd, 2001, §12)

$$\Delta t \left[\frac{u_{\mathsf{N}} + u_{\mathsf{L}}}{\Delta x} \right] \leq C_{\text{cfl}} = O(1), \tag{6.35}$$

where C_{cfl} is a method dependent number (we refer to this as the CFL number here), and the subscripts denote the relevant terms associated with the physics described by N and L. Physically, this condition places a necessary restriction on the time-step size associated with the phenomenon

represented by the various terms if we are to advance in time in a numerically stable fashion. This turns out to be a severe issue if the diffusion terms are to be treated explicitly; for the Fourier–Chebyshev method we consider here, the constraint on the time-step size can be very severe (e.g., Boyd, 2001, §12).

Such time-step constraints may be bypassed if a fully implicit method is considered; symbolically, this is represented by

$$u^{n+1} = \mathsf{A}(\Delta t, u^{n+1}, u^n, \cdots, \mathsf{N}(u^{n+1}), \mathsf{N}(u^n), \cdots, \mathsf{L}(u^{n+1}), \mathsf{L}(u^n), \cdots). \tag{6.36}$$

Implicit methods tend to be conditionally stable, but can be expensive since an iterative solver is required if nonlinear terms are involved. This shifts the computational burden from the small time-step size to the increased number of operations at each time-step. As a compromise, a semi-implicit method of the form

$$u^{n+1} = \mathsf{A}(\Delta t, u^{n+1}, u^n, \cdots, \mathsf{N}(u^n), \mathsf{N}(u^{n-1}), \cdots, \mathsf{L}(u^{n+1}), \mathsf{L}(u^n), \cdots), \tag{6.37}$$

may be considered. Here, the nonlinear terms are treated explicitly whilst the linear terms are treated implicitly. An iterative solver is usually not required, and the problematic terms are not subject to the CFL condition; we should however bear in mind that stability does not necessarily imply accuracy. This semi-implicit time discretisation is the one we will consider here.

We employ the Adams-Bashforth/Backward-Difference algorithms of order k (AB/BDk; see Peyret 2002, §4) as our time-marching algorithm. For the incompressible case considered in this chapter, we are going to use the variable time-step version of AB/BD3 (because this allows for stable numerical integration at larger time-steps than AB/BD2 and AB2/Crank-Nicolson) given by (e.g., Peyret, 2002, §4)

$$\frac{a_0 u^{n+1} + a_1 u^n + a_2 u^{n-1} + a_3 u^{n-2}}{\Delta t_c} = b_0 \mathsf{N}(u^n) + b_1 \mathsf{N}(u^{n-1}) + b_0 \mathsf{N}(u^{n-2}) + \mathsf{L}(u^{n+1}), \tag{6.38a}$$

$$\begin{aligned} a_0 &= 1 + \frac{1}{1+r_c} + \frac{1}{1+r_c+r_p}, \qquad a_1 = \frac{-(1+r_c)(1+r_c+r_p)}{r_c(r_c+r_p)}, \\ a_2 &= \frac{1+r_c+r_p}{r_c r_p (1+r_c)}, \qquad a_3 = \frac{-(1+r_c)}{r_p(r_c+r_p)(1+r_c+r_p)}, \end{aligned} \tag{6.38b}$$

$$b_0 = \frac{(1+r_c)(1+r_c+r_p)}{r_c(r_c+r_p)}, \qquad b_1 = \frac{-(1+r_c+r_p)}{r_c r_p}, \qquad b_2 = \frac{1+r_c}{r_p(r_c+r_p)}, \tag{6.38c}$$

$$r_c = \frac{\Delta t_{p1}}{\Delta t_c} = \frac{t^n - t^{n-1}}{t^{n+1} - t^n}, \qquad r_p = \frac{\Delta t_{p2}}{\Delta t_c} = \frac{t^{n-1} - t^{n-2}}{t^{n+1} - t^n}. \tag{6.38d}$$

The time-step size Δt is set by the maximum allowable value satisfying

$$\Delta t \left[\frac{\max(U_0 + u)}{\Delta x} + \max\left(\frac{v}{\Delta y} \right) \right] \leq C_{\text{cfl}}, \tag{6.39}$$

where $\boldsymbol{u} = (u, v)$ in (6.39), and the CFL number is an input parameter. See Section 6.9 for a derivation and some of the related numerical tests carried out for the AB/BD3 algorithm.

There are other methods, such as Integrating Factor or Exponential Time Differencing, that could act as an alternative to a semi-implicit discretisation but these all have other associated problems when a Chebyshev discretisation is employed; see, for example, Livermore (2007) for a review and comparison of such methods in the spherical MHD context.

Our subsequent parameter choices for the simulations are chosen after doing convergence tests on the time-step size and spatial resolution, by comparing runs at half the time-step and/or increased resolution (twice the resolution where possible) and looking at, for example, the energy and dissipation time-series. Energy power spectrum for the runs presented here show the energy content at the higher modes are small (below 10^{-5}), indicating our runs are well-resolved; spectrum diagrams have been omitted here.

6.4 Hydrodynamic evolution: a review

We first review what is known about the nonlinear evolution of unstable shear flows in the incompressible, hydrodynamic limit. Although the results presented are not new, we reproduce them here for self-containment, and to demonstrate that our numerical routines are able to reproduce known, well-established results. For the hydrodynamic case, we set M to zero in the governing equation (6.13), and solve only for the vorticity and streamfunction.

6.4.1 Hyperbolic-tangent shear layer

For this flow profile we focus on the case where the domain supports exactly one wavelength of the most unstable mode predicted by the linear theory, so we take $L_x = 2\pi/\alpha$, with $\alpha = 0.44$ (Michalke 1964, and Chapter 5 here). Test runs have found that $L_y = 10$ is sufficiently large for finite-domain effects to be negligible. For this case we choose a resolution of $N_x = 256$ and $N_y = 512$, at Re $= 500$, a compromise between having well-resolved runs and the runs not being

too dissipative. A CFL number of 0.25 is employed for the simulation, its value again found from convergence tests. We initialise the primary instability with some amplitude at fixed phase, and, additionally, extra perturbations at lower amplitudes at random phase. Mathematically, we add the following to the initial vorticity Ω_0:

$$\omega = \left[10^{-3} \cos(\alpha x) + 10^{-5} \sum_{k:\ k/\alpha=2}^{\lfloor N_x/3 \rfloor} \gamma_k \cos(kx - 2\pi\sigma_k) \right] \mathrm{e}^{-y^2}.$$

Here, γ_k and σ_k are randomly generated numbers in the range $[-1, 1]$. Higher harmonics are limited to $\lfloor N_x/3 \rfloor$ where $\lfloor(\cdot)\rfloor$ is the floor function. A Gaussian in y is chosen so that the perturbations are sufficiently localised around $y = 0$. Although we do not initialise with an eigenfunction as calculated from linear theory, the small amplitude perturbation allows for a well-defined linear phase where the perturbations have more than sufficient time to readjust to the optimum configuration. Only ω needs to be initially specified as the first step involves an inversion to give the corresponding ψ. When the domain is large enough to support two or more wavelengths of the primary instability, the initial perturbation is appropriately modified so that the wavenumbers smaller than the primary instability also given a small non-zero amplitude.

Figure 6.1 shows snapshots of the vorticity at several times; the left-column shows the total vorticity, and the right column shows the vorticity with the $k = 0$ Fourier mode removed. Figure 6.1(a) shows that the shear layer starts rolling up and stretches out a thin region of vorticity called the braid. In this case the stagnation point is at $x = 0$, $y = 0$. As the instability develops, fine features form until they are smeared out by viscosity. By $t = 70$ the braids have been diffused and only the large vortex remains. The vortex oscillates and its amplitude is gradually damped by viscosity. The vortex was seen to be long-lived. This qualitative picture agrees with previous results (e.g., Ho & Huerre, 1984). For Figure 6.1(b), we make the observation that at the early stages of the evolution the vorticity pattern resembles Figure 5.5(c), the vorticity eigenfunction obtained from linear theory. This gives us confidence that, although we did not initialise using the eigenfunction, the linear phase is long enough that the perturbations adjust to the optimum configuration.

Another feature in which we might be interested is the evolution of the along-stream mean profile $\overline{u}$, defined by

$$\overline{u} = \frac{1}{L_x} \int_0^{L_x} u \, \mathrm{d}x. \tag{6.40}$$

We also define the shear layer width by the width of the region bounded by the y-locations of

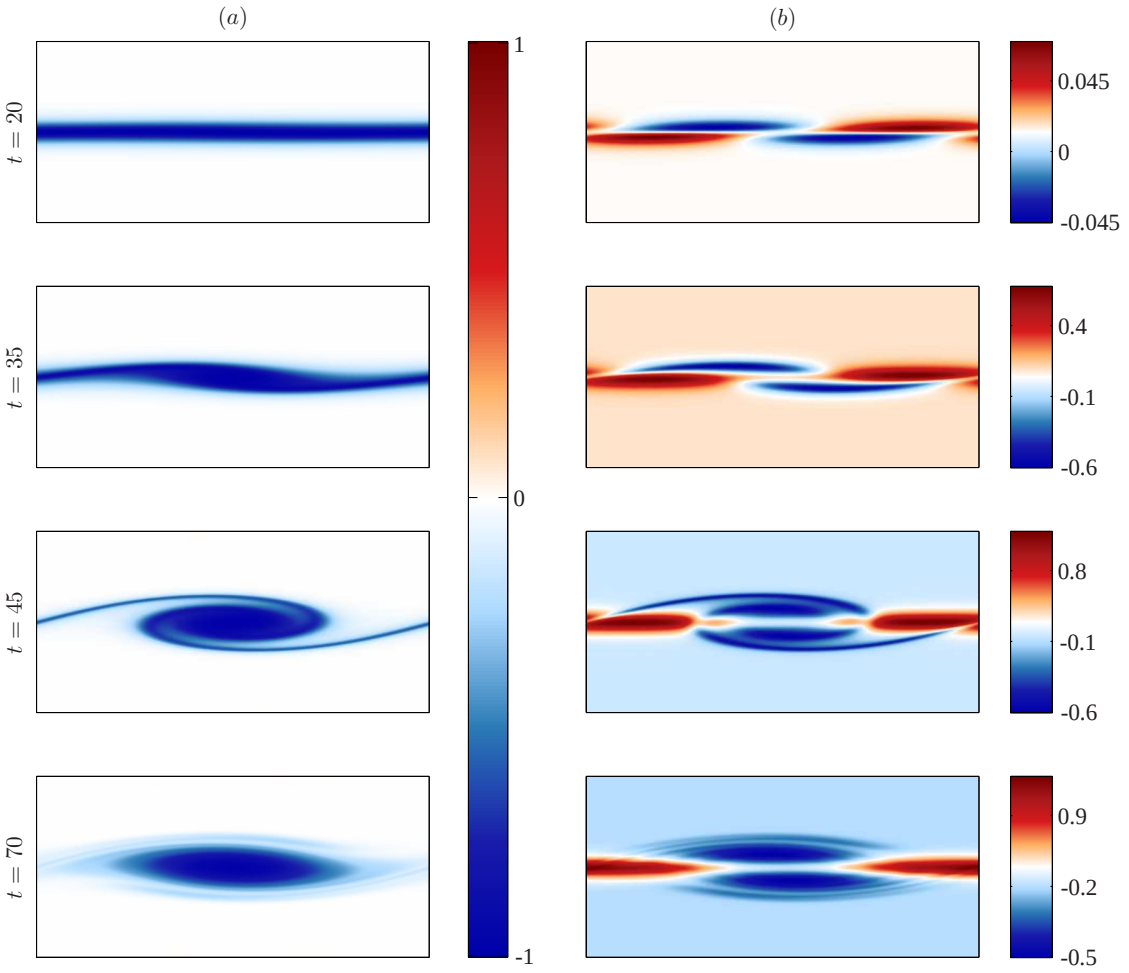

Figure 6.1: Snapshots of vorticity for the shear layer run, at Re $= 500$. Left column shows the full vorticity, whilst the right column shows vorticity with the $k = 0$ Fourier mode removed.

which the difference between $\overline{u}$ and its free-stream value ($u_{\pm\infty} = \pm 1$ in this case) is smaller than some tolerance. Another possible way to define this width would be by the y-location where $\overline{\omega}$ is sufficiently close to its free-stream value ($\overline{\omega} = 0$ in this case). Snapshots of $\overline{u}$ are shown in Figure 6.2.

Here, we see that as the instability develops and the shear layer rolls up, the shear flattens out, leading to an increase of the shear layer width. There does not appear to be much more broadening after the roll-up stage, and any small increases in shear layer width after the roll-up stage we attribute to viscous effects. Although there is still an inflection point, the parallel flow assumption no longer applies, and so to say anything about the stability of the saturated state we would need to consider a linear instability analysis of this state via, for example, a Floquet analysis (e.g.,

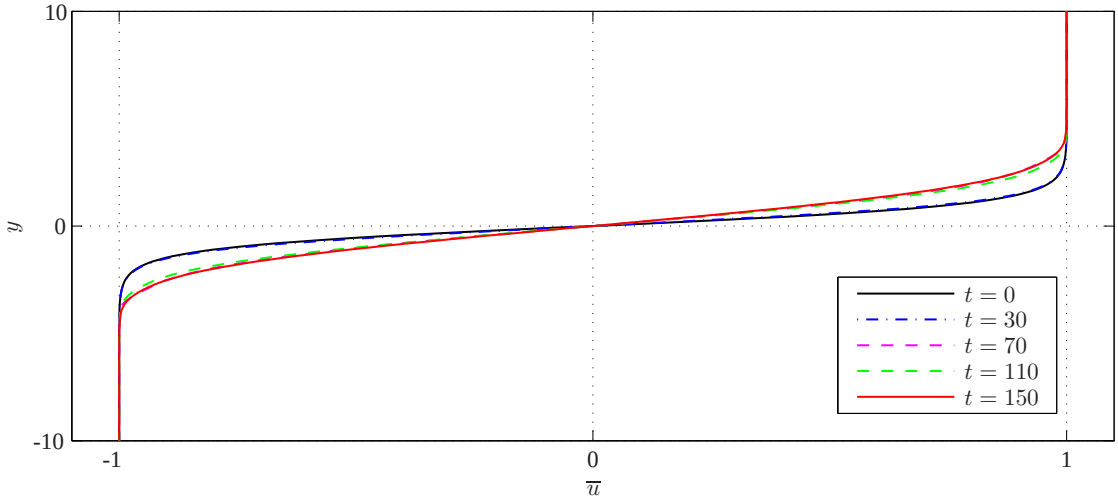

Figure 6.2: Snapshots of $\overline{u}$ for the shear layer run at Re $= 500$.

Klaassen & Peltier, 1985b). The possibility of hydrodynamic secondary instabilities is reviewed at the end of this section.

In the hydrodynamic case, the domain-integrated energy evolution is given by

$$\frac{1}{2}\frac{\mathrm{d}}{\mathrm{d}t}\iint |\nabla\psi|^2 \,\mathrm{d}x\mathrm{d}y = -\frac{1}{\mathrm{Re}}\iint \omega^2 \,\mathrm{d}x\mathrm{d}y. \tag{6.41}$$

We show first in Figure 6.3 a time-series of the domain-integrated kinetic energy. Using Parseval's theorem or otherwise, we separate the energy content into the mean ($k = 0$ Fourier mode) and perturbation ($k \neq 0$ Fourier mode) component. A fitting of the perturbation energy is used to infer a growth rate during the linear phase, and this inferred growth rate 0.185 is close to the growth rate inferred from linear calculations, which is 0.189 (Michalke 1964, and Chapter 5 here). Most of the energy resides in the mean flow during the evolution, and even after saturation the perturbation energy is still around two orders of magnitude less than the mean energy. The dissipation is sufficiently weak that the decrease in total energy is at around 10% (or $E(t = 150)/E(t = 0) \approx 0.9$). One feature that we note is that there is an oscillation in the perturbation energy, indicating that there is continual transfer of energy between the mean flow and the perturbation. This is related to the oscillation in physical space when the vortex is leaning with/against the background shear, a phenomenon known as nutation (e.g., Miura & Sato, 1978). The process may be further quantified by an examination of the Reynolds stresses. However this is not our primary focus here, and so we refer the reader to, for example, Klaassen & Peltier (1985a) or Metcalfe *et al.* (1987) for a detailed discussion.

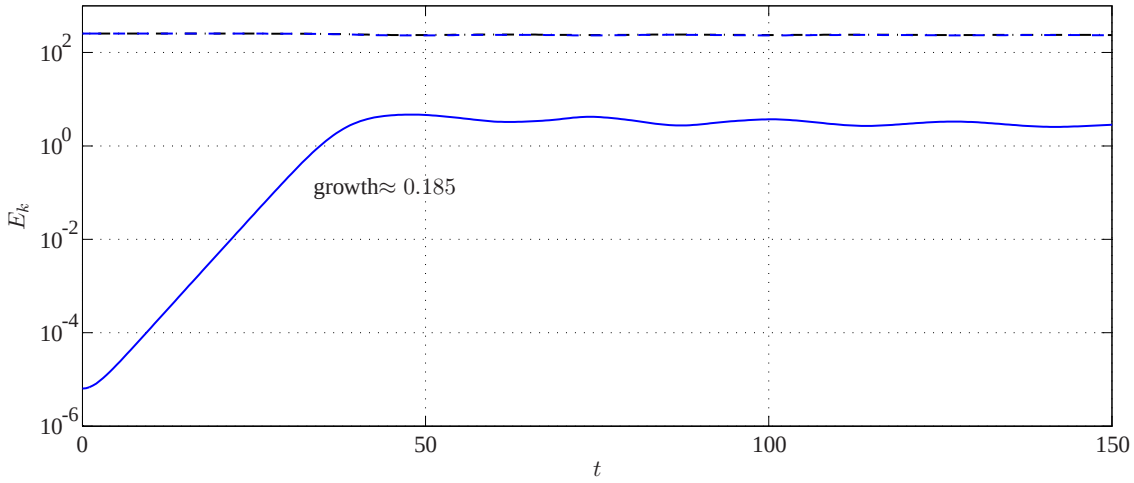

Figure 6.3: Time-series of the energy for the shear layer run at Re $= 500$ (solid $=$ perturbation state; dashed $=$ mean state; black dot-dashed $=$ total energy). Most of the energy still resides in the mean so the total energy and mean energy curve lie on top of each other.

We show in Figure 6.4 the dissipation rate ϵ_{Re} defined by

$$\epsilon_{\text{Re}} = \frac{1}{\text{Re}} \iint \omega^2 \, \mathrm{d}x\mathrm{d}y. \tag{6.42}$$

We observe that ϵ_{Re} is bounded above by its initial value in the diagram; this is because enstrophy (and in fact any function of vorticity) is an ideal invariant of two-dimensional hydrodynamics, and there can be no net enstrophy production in this set up. This is however not the case when MHD effects are present, since the Lorentz force feedback violates the conservation of vorticity, leading to a dissipation rate exceeding the initial rate.

We have also checked that the numerical method conserves x- and y-momentum. The initialisation has no momentum to begin with, as the basic state has zero net momentum, and the disturbances are periodic with zero mean. The numerical integration shows that, for the course of the run, domain-integrated momentum remains at machine level magnitudes.

Hydrodynamic secondary instabilities

Although the primary focus of this flow is the single wavelength case, we have also carried out runs at two wavelengths, and test cases at four wavelengths. It is known that a configuration of a row of like-signed vortices is unstable, and is most unstable to an instability at twice the wavelength

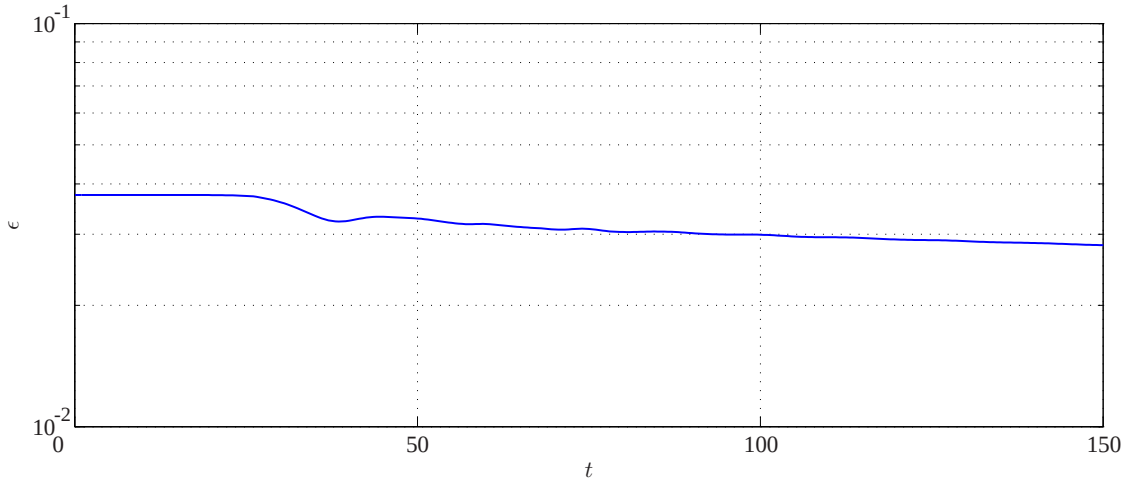

Figure 6.4: A time-series of the dissipation rate ϵ_{Re} for the shear layer run at $\mathrm{Re} = 500$.

of the primary instability (i.e. at wavenumber $\alpha/2$), a result first demonstrated for point vortices by von Kármán (e.g., Lamb, 1932, §7). This subharmonic pairing instability has been investigated analytically (Kelly, 1967; Stuart, 1967) and numerically (Corcos & Sherman, 1984; Metcalfe *et al.*, 1987; Klaassen & Peltier, 1989, 1991; Staquet, 1995; Mashayek & Peltier, 2012a,b) for the shear layer. As the name suggests, this secondary instability causes like-signed vortices to pair up and merge into larger vortices, further broadening the mean profile. We have performed some simulations where only the fundamental wavenumber α receives a non-zero amplitude, but the domain is large enough to support two vortices initially forming, and we find that the vortices do not merge at least for the run duration (up to $t = 200$, where $t = 50$ is approximately the time when the primary instability starts saturating). If instead we initialise in a 'generic' fashion, with non-zero amplitudes at wavenumbers in the subharmonic and higher harmonics, the vortices do merge. Measuring the growth rate numerically at each Fourier mode as (e.g., Klaassen & Peltier 1989)

$$\sigma(k,t) = \frac{1}{2E(k,t)}\frac{\mathrm{d}E(k,t)}{\mathrm{d}t} \tag{6.43}$$

shows that, as a function of time, $\sigma(\alpha,t)$ is initially the largest, then it is superseded by $\sigma(\alpha/2,t^*)$ at some later time t^*. This merging generates further small scale activity as may be seen by an increase in dissipation rate at the time around the merging.

Even in the single-wavelength case, the vortex core formed may be unstable to several secondary instabilities, although most of these are ruled out in our setting; we mention them however for

completeness. One of these is the shear aligned convective instability of Klaassen & Peltier (1985a,b); when stratification is present, a shear flow in the vertical rolls up in to a vortex that entrains heavier fluid and transports it to a region of lighter fluid, which can then be buoyantly unstable. Another instability associated with the vortex core is the instability associated with elliptical streamlines (Pierrehumbert, 1986; Bayly, 1986; Waleffe, 1990). The elliptical instability a wave resonance phenomenon but requires a third spatial dimension, something that we do not have here. This secondary instability plays a role in the breakdown of the two-dimensional flow into three-dimensional turbulence, and is applicable in a variety of laboratory, geophysical and astrophysical flows where elliptic streamlines are found; see Kerswell (2002) for a comprehensive review.

Away from the vortex core, the braid region may also suffer a wide variety of secondary instabilities, which may be of strain or shear type (e.g., Corcos & Sherman, 1976; Metcalfe *et al.*, 1987; Dritschel *et al.*, 1991; Staquet, 1995, 2000; Caulfield & Kerswell, 2000). These have not been observed in our test runs at higher Re, although we only limited ourselves to $\mathrm{Re} = 1000$. The hyperbolic instability investigated by Caulfield & Kerswell (2000) suggests that such braid/stagnation-point instabilities may be more unstable than the elliptic instability associated with the vortex core, and may also contribute to the breakdown of the two-dimensional profile into three-dimensional turbulence; see Mashayek & Peltier (2012a,b).

As observed by various authors, the emergence of such secondary instabilities can delay the subharmonic pairing instability (Metcalfe *et al.*, 1987; Staquet, 1995). Additionally, Mashayek & Peltier (2012a,b) recently demonstrated that secondary instabilities can cause the disruption of the parent vortex before pairing can occur. This is perhaps interesting in that, as mentioned in Mashayek & Peltier (2012a), pairing is almost never seen in nature but is usually seen in numerical simulations. They attribute this to the fact that the Reynolds numbers in numerical simulations were never high enough (until their investigation) for other secondary instabilities to dominate over the pairing mode. We have observed pairing here in our hydrodynamic simulations, but in our physical setting here, the secondary instabilities are weak or not supported.

To summarise, there are a wide variety of secondary instabilities that can cause the breakdown of the flow into three-dimensional turbulence. This breakdown has important consequences in, for example, vertical mixing in the ocean (e.g., Caulfield & Peltier, 2000; Staquet, 2000; Peltier & Caulfield, 2003; Mashayek & Peltier, 2012b).

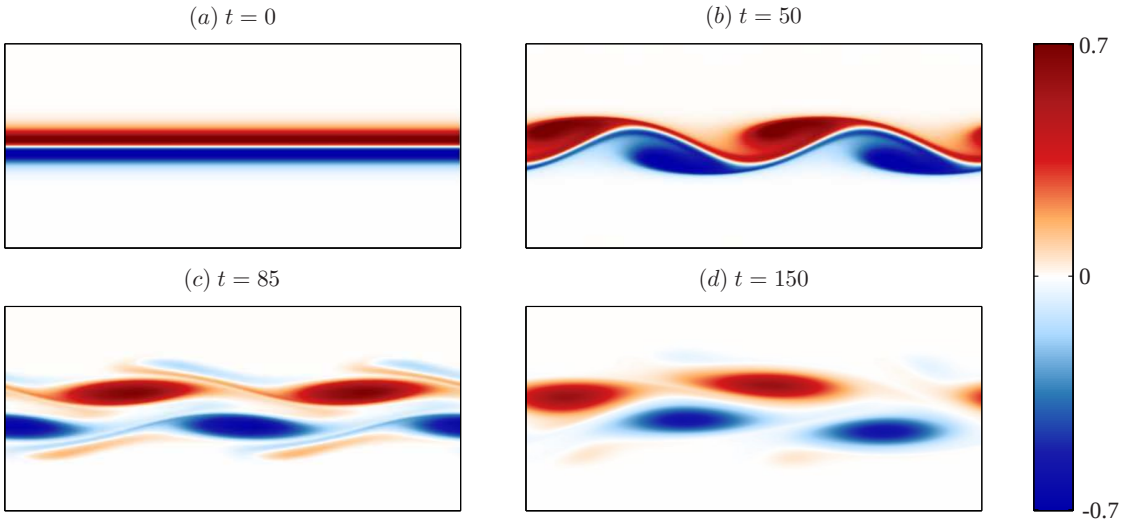

Figure 6.5: Snapshots of vorticity for the Bickley jet, at Re $= 500$.

6.4.2 Bickley jet

We now give a similar account for the Bickley jet profile. From the linear theory calculations (see Figure 5.14), the even mode is generally more unstable, so a generic excitation should trigger the even mode. The most unstable even mode has wavenumber $\alpha \approx 0.9$, and thus we initialise as in the shear layer case, with the primary disturbance at fixed phase, and higher harmonics at a lower amplitude with random phase. To demonstrate that pairing between vortices can occur, we take a domain that supports two wavelengths of the primary instability. The domain size is about 14 by 20 in x and y, using a resolution of $N_x = 256$ and $N_y = 512$, also at Re $= 500$. Figure 6.5 shows snapshots of the vorticity.

We see that, in some sense, the jet profile is like a double shear layer, with two opposite vorticity layers. The instability causes a meandering of the jet, which subsequently breaks, causing the shear regions to roll-up into vortices. These vortices are of different sign and can influence each other to give interesting dynamics. Since we have two wavelengths of the primary instability, there are four primary vortices formed, two of each sign, along with some small, less well-defined satellites, much like what was observed in, for example, Zabusky & Deem (1971) and Sutherland & Peltier (1994). This kind of configuration is not unlike a von Kármán street, whose stability with finite vortex cores has been analysed and is shown to be generically unstable (e.g., Kida, 1982; Jimenez, 1987, 1988). Indeed, at some stage near the end of our run at $t = 150$, two of these

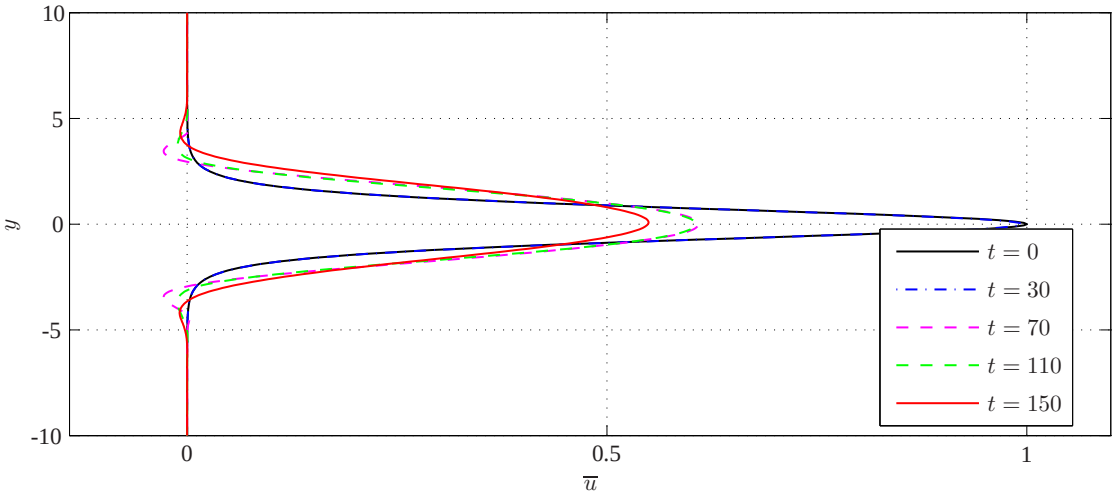

Figure 6.6: Snapshots of the $\overline{u}$ for the Bickley jet run at Re $= 500$. Notice that there is some back flow at the later times.

vortices (usually the two positive vortices) start showing early stages of merging. This then affects how the other vortices propagate, causes a change in the travel angle and results in the vortices propagating towards the y-boundaries. In a longer run not presented here, the vortices then bounce around the domain, deflecting from the boundaries upon impact. The runs are qualitatively similar to those reported by, for example, Zabusky & Deem (1971) and Sutherland & Peltier (1994). We only display results up to $t = 150$ as the dynamical influence of the wall is certainly minimal up to this moment; once the vortices hit the walls, finite-domain effects are obviously non-negligible.

Figure 6.6 shows snapshots of $\overline{u}$. As in the shear layer case, the instability causes the flow profile to broaden out and reduce the shear. We also observe that the maximum flow velocity decreases down to about a half of the initial maximum. It is also interesting to see some mean back flow, shown at later times, a phenomenon that has previous been observed (e.g., Zabusky & Deem, 1971, Figure 9).

Figure 6.7 shows a time-series of the energy. A fitting of the perturbation energy was used to obtain a growth rate 0.152, which agrees well with the growth rate 0.160 obtained from linear calculations. The energy remains largely in the mean state. However, $E(t = 150)/E(t = 0) \approx 0.7$, implying a loss about 30% of the total energy; this should be compared to just under 10% loss for the shear layer run. A test run at higher resolution indicates that this loss of energy is due to the choice of Re and not from the runs being under-resolved. The dissipation rate ϵ_{Re} is plotted in

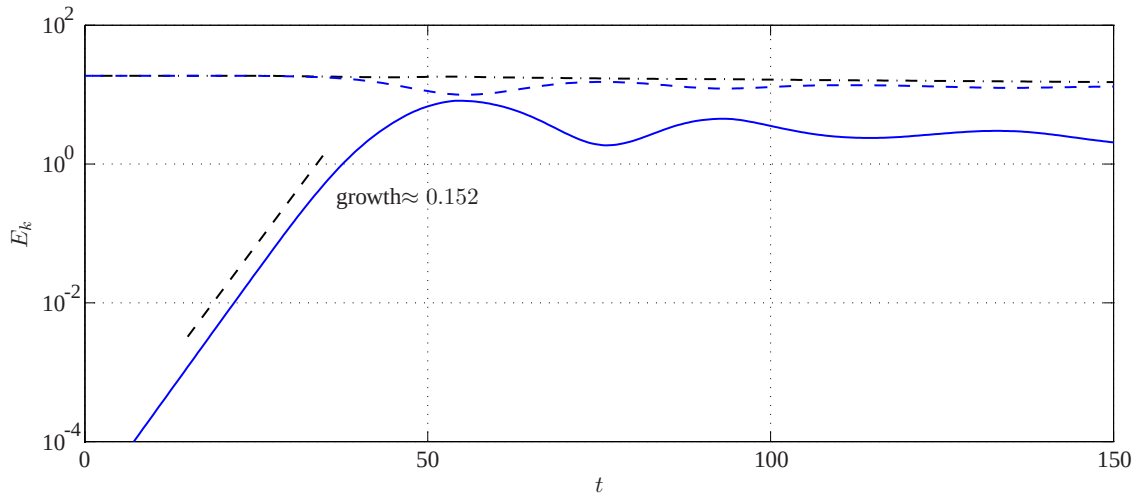

Figure 6.7: Time-series of energy for the Bickley jet run at Re $= 500$ (blue $=$ kinetic; solid $=$ perturbation state; dashed $=$ mean state; black dot-dashed $=$ total energy).

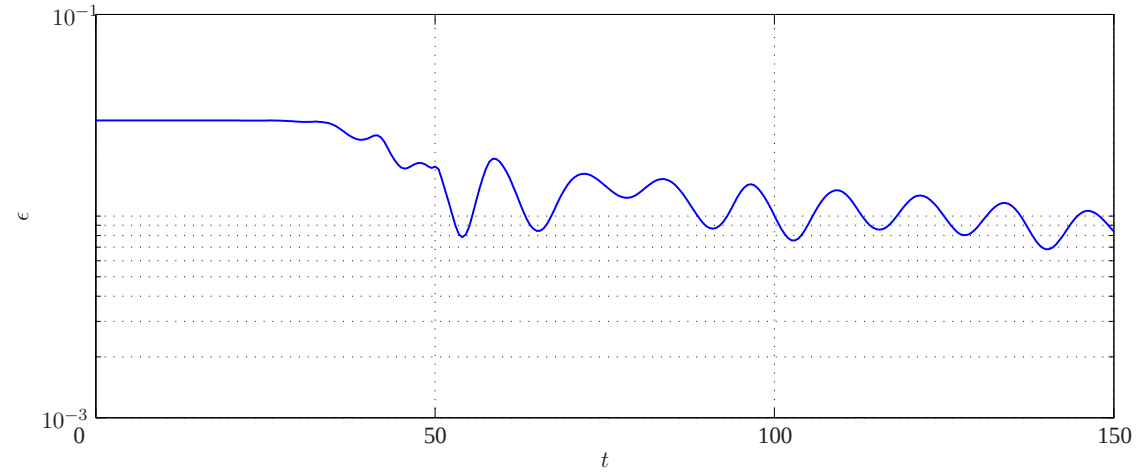

Figure 6.8: Time-series of the dissipation rate ϵ_{Re} for the Bickey jet run at Re $= 500$.

Figure 6.8. The dissipation is again bounded by its initial value as explained before.

6.5 MHD evolution: hyperbolic-tangent shear layer

We now examine the effect of a magnetic field on the nonlinear evolution of unstable shear flows, starting with the shear layer before moving onto the jet profile. We consider an initially uniform magnetic field, so the initial state is not resistively unstable (e.g., Biskamp, 2000, §4). However, the

evolved state may be resistively unstable, and the dynamics may be altered by resistive instabilities.

A priori, we might envisage three MHD regimes:

1. MHD effects are 'strong', so that although the initial state is linearly stable, it could be nonlinearly stable (e.g., suppression of shear layer roll-up);

2. MHD effects are 'weak', and the evolution is much like the hydrodynamic case;

3. some intermediate case between the two, where the vortical motion can wind up the field lines, build up MHD feedback, and modify the nonlinear development.

It is this intermediate case (3) we are particularly interested in; although the field is initially weak (measured by energy ratios for example), MHD effects may not be negligible when the nonlinear evolution is concerned. Naturally, we expect the degree of feedback to depend on the field strength M, the magnetic diffusivity as measured by Rm, and, on the viscosity as measured by Re.

The nonlinear development of the MHD shear layer case has been studied previously (Miura, 1982; Malagoli *et al.*, 1996; Frank *et al.*, 1996; Jones *et al.*, 1997; Keppens *et al.*, 1999; Jeong *et al.*, 2000; Baty *et al.*, 2003; Palotti *et al.*, 2008). However, all these authors have used routines designed for solving compressible MHD. Furthermore, all these works, apart from Palotti *et al.* (2008), rely on resolution dependent numerical dissipation. Palotti *et al.* (2008) investigated the dependence of the evolution on Rm but not on the field strength M, whilst the other works investigated the effects of M and the sonic Mach number on the evolution.

The account we present here is new in that we numerically solve the incompressible MHD system rather than a small Mach number run of compressible MHD, and, furthermore, we investigate the simultaneous dependence of the nonlinear evolution on both M and Rm. The former is perhaps not that significant, as it appears that the more striking aspect of the nonlinear evolution stems from MHD rather than compressible effects (Malagoli *et al.*, 1996; Jones *et al.*, 1997). The nonlinear evolution can result in secondary resistive instabilities since finite Rm leads to reconnection events, which release magnetic stresses back onto the flow, altering the dynamics. The theory of classical resistive instabilities relies on Ohmic dissipation (e.g., Biskamp, 2000, §4), so we argue that, for any attempt to reconcile the numerical results and the theory, employing explicit Ohmic dissipation rather than some numerical artefact is essential. Further, being able to control the strength of

parameter	value
α	0.44
C_{cfl}	0.2
$L_x \times L_y$	$[0, 2\pi/\alpha] \times [-10, 10]$
Re	500
M	0.01, 0.02, 0.03, 0.04, 0.05, 0.06, 0.07, 0.1
Rm	50, 250, 500, 750, 1000
$N_x \times N_y$	512×1024 for Rm $= 1000$
	384×768 for Rm $= 750$
	256×512 otherwise

Table 6.1: Parameter values employed in our investigation for the shear layer profile.

Ohmic dissipation is important in a systematic exploration of parameter space, something that is not possible with resolution-dependent dissipation.

For our investigation, we fix Re $= 500$, and consider several values of Rm ranging from 50 to 1000 (or, effectively, several values of the magnetic Prandtl number Pm $=$ Rm/Re ranging from 0.1 to 2), and a wide range of basic field strengths measured by M. All runs are dealised, and, as a reminder, $M = 1$ guarantees linear stability (from Chapter 5 here). We have focused on small values of M, where the linear growth rates and eigenfunctions are only small perturbations away from the hydrodynamic case. We use the same fundamental wavenumber $\alpha = 0.44$, chosen so that only a single wavelength of the primary instability is supported. Calculations have been carried out at the parameter values given in Table 6.1.

For illustrative purposes, we focus on three sample runs, where Rm $= 500$, and $M = 0.01$, 0.03, and 0.05. At these values of M, the initial magnetic energy is no more than 1% of the initial kinetic energy. Figure 6.9 shows snapshots of vorticity from these runs.

Figure 6.9(a) shows the run at $M = 0.01$, a truly weak field case, for which the evolution resembles the hydrodynamic evolution. In this case there is stretching and shearing of the magnetic field, but the resulting magnetic forces are never strong enough to alter the macro-dynamics in any significant way. This should be contrasted to the $M = 0.03$ run given in Figure 6.9(b). As the shear layer rolls up, the stretched field is now strong enough to feed back on the flow, resulting

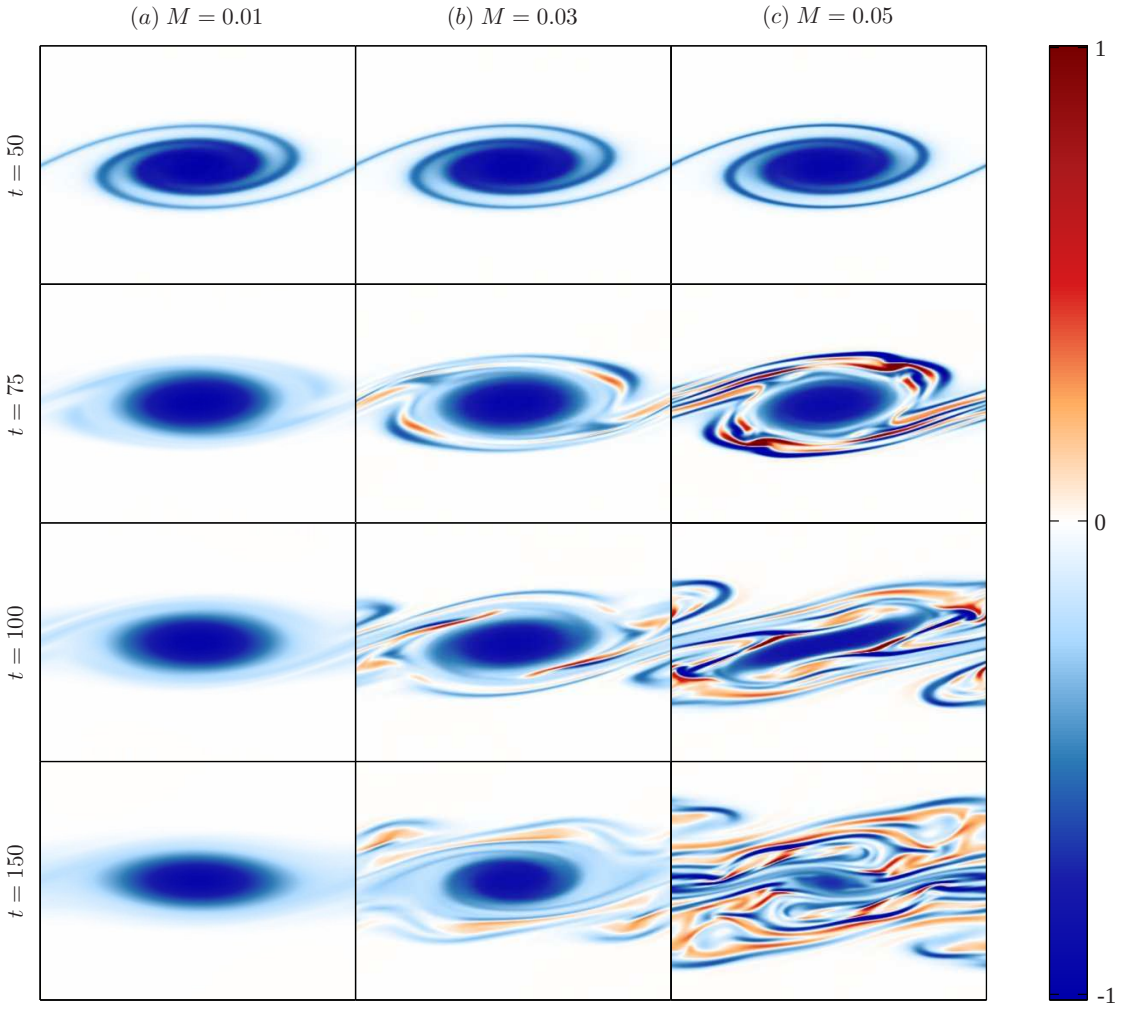

Figure 6.9: Snapshots of vorticity for the shear layer at different field strengths (at Rm $=$ Re $= 500$).

in positive vorticity filaments in the peripheral regions of the vortex. This build up of filaments with strong vorticity however is not sustained, and by $t = 150$ the filaments have been smoothed out by dissipative effects. The final frame of Figure 6.9(b) still bears some resemblance to the corresponding frame for the $M = 0.01$ case, with a clear signature of the vortex, although it has diminished in size. This would perhaps be termed a 'mildly disruptive' case. Figure 6.9(c) shows a 'severely disruptive' case, when $M = 0.05$. The initial roll-up is similar to the other two cases; however very strong regions of vorticity are created. At $t = 100$ the vortex seems to have suffered some elongation and shearing due to the MHD feedback onto the flow. By the end frame, although there are still traces of the vortex remaining, it has been substantially reduced in size, and the dominant features in the domain are now strong vorticity filaments.

For the $M = 0.1$, Rm $= 500$ case (not presented here), what little remains of the parent vortex is destroyed by $t = 150$, and vorticity filaments litter the computational domain. In increasing Rm for the above runs, the behaviour becomes more violent and the observed disruption is stronger. For example, the $M = 0.03$, Rm $= 1000$ run is more like the severely disruptive run presented here in Figure 6.9(c), in contrast to the mildly disruptive run at the same M but Rm $= 500$ shown in Figure 6.9(b). This indicates that there is stronger disruption with increasing M and Rm.

It is informative to see the magnetic field line configuration. This may be done by plotting contours of the magnetic potential A; snapshots of the field lines are given in Figure 6.10 for the three cases presented here. The contours are chosen so that the field lines thread the region $y \in [-2, 2]$ at $t = 0$, with a 0.5 spacing; the field line threading $y = 0$ is omitted for clarity. We see that in Figure 6.10(a), for the non-disruptive case, the field lines are wound up by the vortical motion and form concentrated flux regions on the edges of the vortex; such regions should also be seen as current sheets, which are expected to be resistively unstable. In such a situation with curved field lines, the magnetic tension, given by $T = \boldsymbol{b} \cdot \nabla \boldsymbol{b}$, has a component directed into the vortex. The idea is that the vortical motion winds up the field lines and builds up magnetic stresses, which are then released at a major reconnection event, and act on the vortex. In this weak field case the force is not strong enough to disrupt the vortex in any significant way. By the end time, the magnetic loops inside the vortex have largely been diffused and magnetic flux has been expelled from the centre to the edges of the vortex. This process of flux expulsion has previously been described by Weiss (1966), who, via dimensional arguments, also predicted the strength to which fields could grow. Although his numerical computations were carried out in the kinematic regime, with no feedback on the velocity field via the Lorentz force in the momentum eqauation, the $M = 0.01$ case here is comparable to his results in that the Lorentz force is never significant compared to the fluid inertia even locally, and the kinematic assumptions are well satisfied.

Now we compare the weak case of $M = 0.01$ to the mildly disruptive case of $M = 0.03$ in Figure 6.10(b). The magnetic stresses are now strong enough to cause some disruption. The parent vortex is still present after the mild disruption and a flux expelled state is reached. The $M = 0.03$ case suffers no further disruption events after $t = 150$ in a longer test run we have carried out. This may be explained by the fact that, since the vortex is able to maintain its integrity after the initial disruption, most of the field lines that thread the vortex end up being expelled, so there is nothing left for the surviving vortex to wind up. For the $M = 0.05$ case in Figure 6.10(c), the

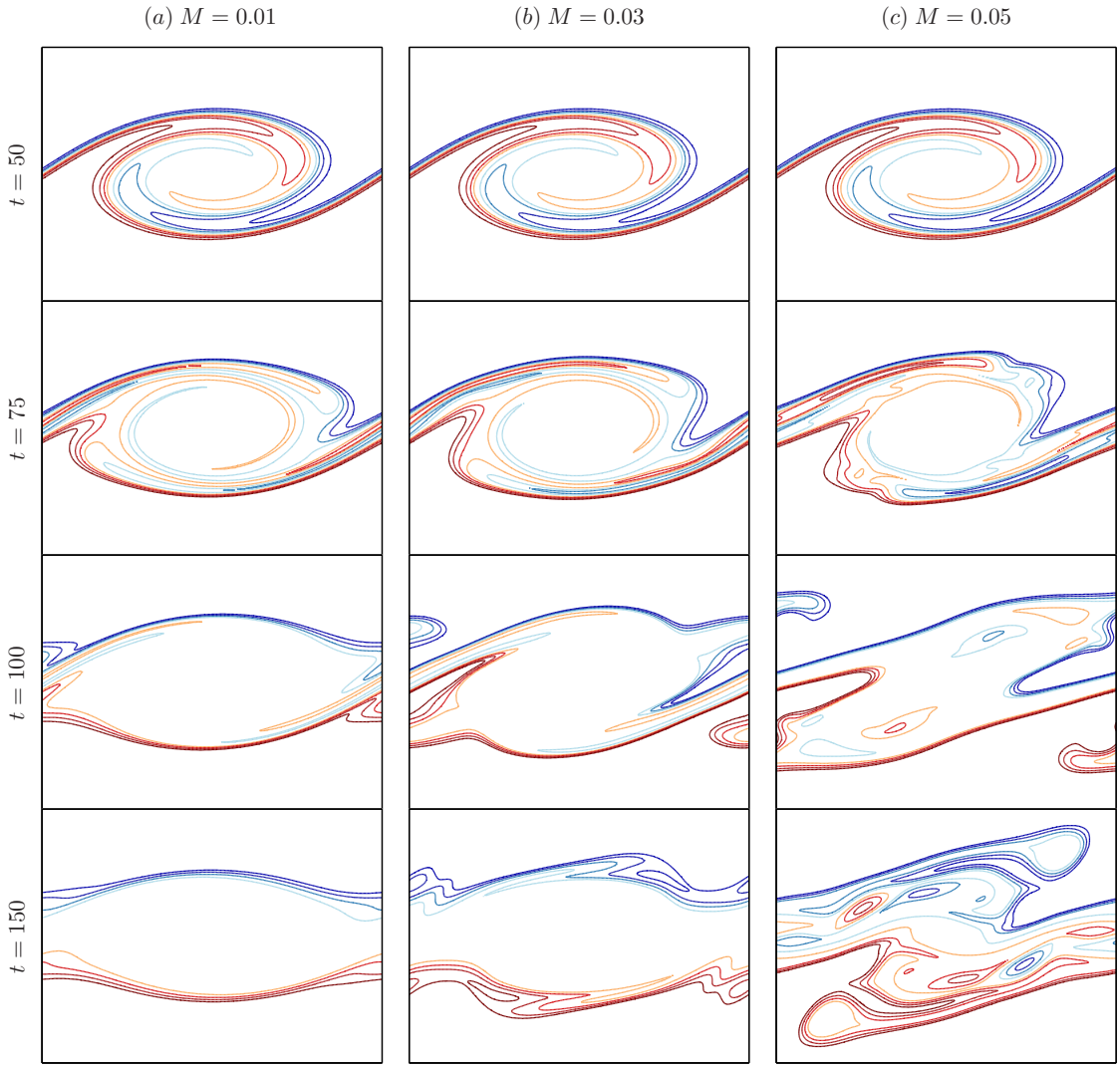

Figure 6.10: Snapshots of field lines for the shear layer runs at several field strengths (at $\mathrm{Rm} = \mathrm{Re} = 500$).

stresses released are even stronger and distort the vortex significantly. The evolution is completely different, with clear signs of magnetic islands, and a flux expelled state is not achieved.

We observe that disruption is a fast phenomenon, occurring in no more than an eddy turnover time. One key point we want to highlight is that the disruption, when it does happen, affects the dynamics well before the flux expelled state has been reached. Also, to demonstrate further that the magnetic tension does act to distort the vortex, we plot in Figure 6.11 the field line configuration with the tension force overlaid as arrows, at a time before a major disruption event has occurred. There is indeed a component directed towards the centre of the vortex.

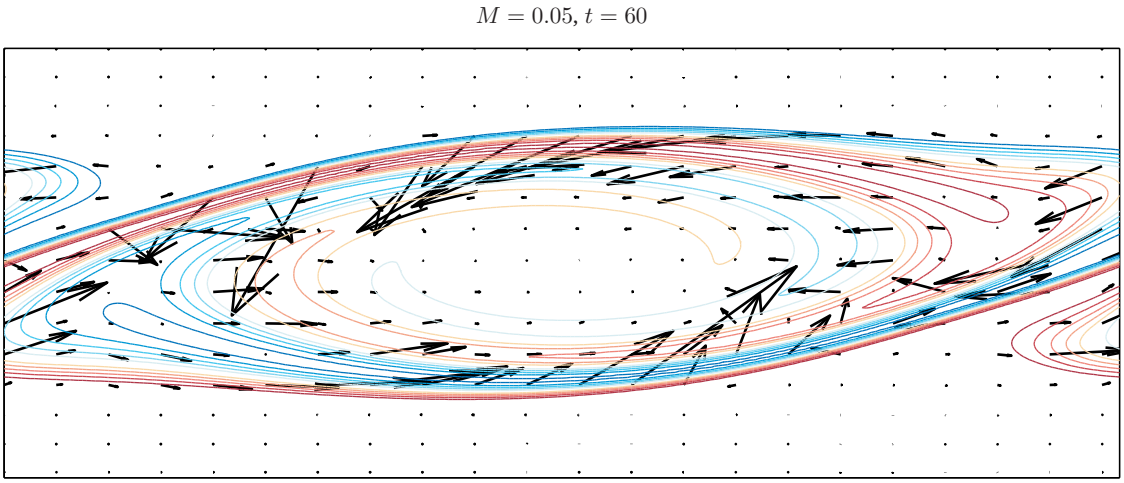

Figure 6.11: Magnetic tension, plotted as arrows, with magnitude proportional to their length, superimposed on a field line plot. The arrow lengths have been magnified by a factor of four for clarity.

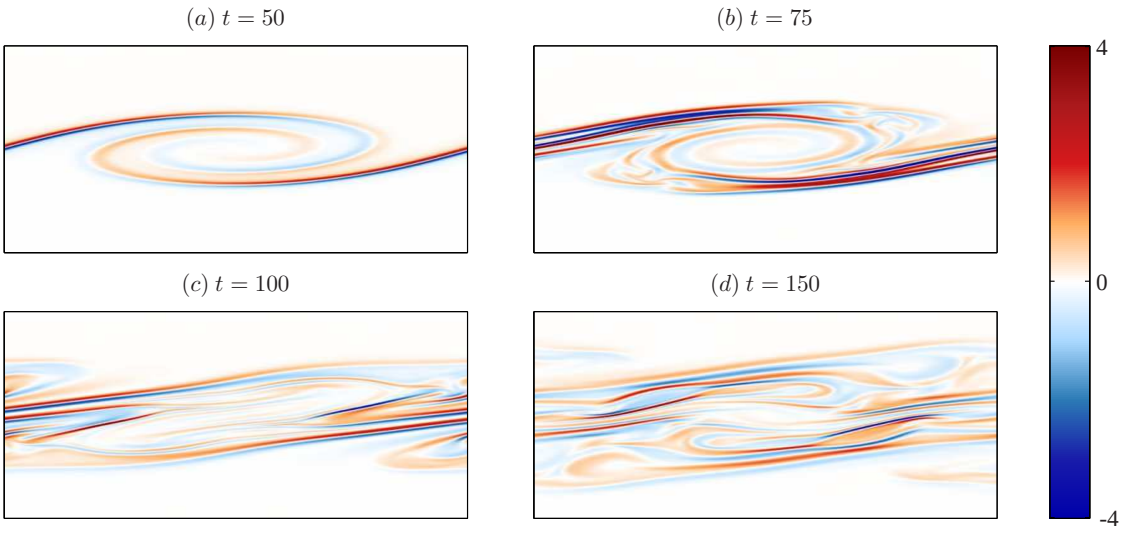

Figure 6.12: Snapshots of current for the shear layer run (at Rm $=$ Re $= 500$, $M = 0.05$).

Figure 6.12 shows snapshots of the current density j for the $M = 0.05$ run. The configuration is consistent with the field line plots in Figure 6.10(c), in that strong current layers are formed on the fringes of the vortex. Such thin layers of current are known to be resistively unstable. Note also that it is not a single current layer, but a double current layer that exists on the edges of the vortex.

One other feature to note in the more violent disruptive cases is that the current distribution bears a noticeable visual resemblance with the vorticity distribution, as has been observed in

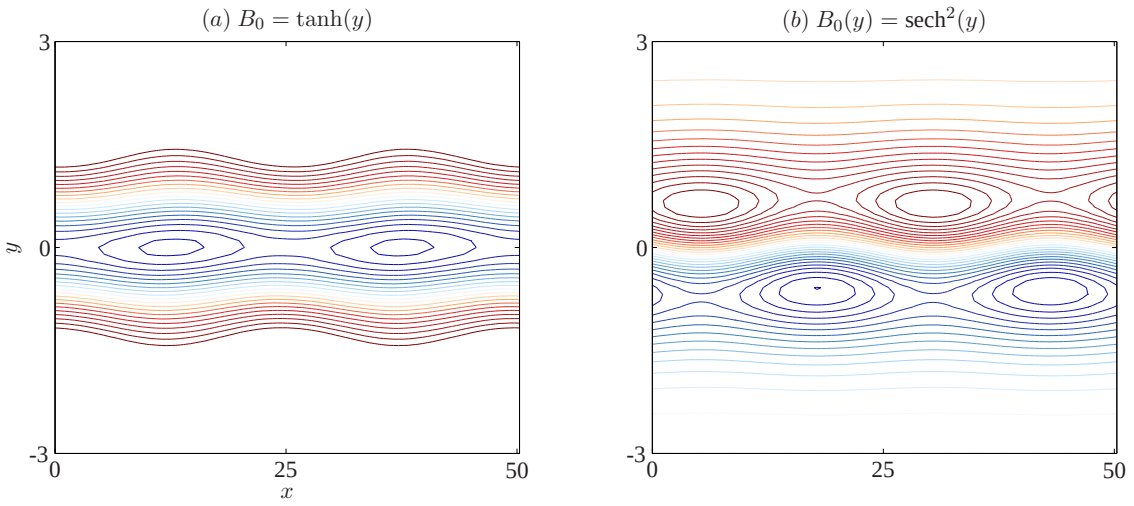

Figure 6.13: Field line configuration from a tearing unstable initialisation, with no background flow.

two-dimensional MHD turbulence simulations (e.g., Biskamp & Welter, 1989; Biskamp, 2003; Dritschel & Tobias, 2012). The shearing of the field lines is strongest at regions with non-zero vorticity so perhaps it is not entirely unexpected that the current is largest around these regions and implying a vorticity-current correlation.

It is known that, in thin current layers, the tearing type instabilities are usually the fastest growing instabilities (e.g., Furth *et al.* 1963; Biskamp 2000, §4; Priest & Forbes 2000, §6). In Figure 6.13 we show the field line configuration from nonlinear simulations, initialising with $B_0(y) = \tanh(y)$ (the single current layer, Figure 6.13*a*) and $B_0(y) = \text{sech}^2(y)$ (a double current layer, Figure 6.13*b*), with no background flow. The tearing instability causes a pinching of the field lines and forms magnetic islands. In other nonlinear simulations in vortical flows (e.g., Biskamp & Welter, 1989), the break up of current layers is often attributed to tearing instabilities, and, in those cases, the break up is often accompanied by balloon like structures in the electric current. These balloon like structures have been observed in some of our nonlinear simulations of shear flows with background magnetic field, so, given that tearing instabilities are usually the most unstable resistive instability in a thin current layer configuration, it seems plausible that these are also in play here. We give some details of our attempt at providing more evidence for pinning down the exact resistive instability at play in the discussion section at the end of the chapter.

Going back to the shear layer case, we show snapshots of $\overline{u}$ for the sample runs in Figure 6.14. Compared to the hydrodynamic cases, we make the observation that disruption events encourage a

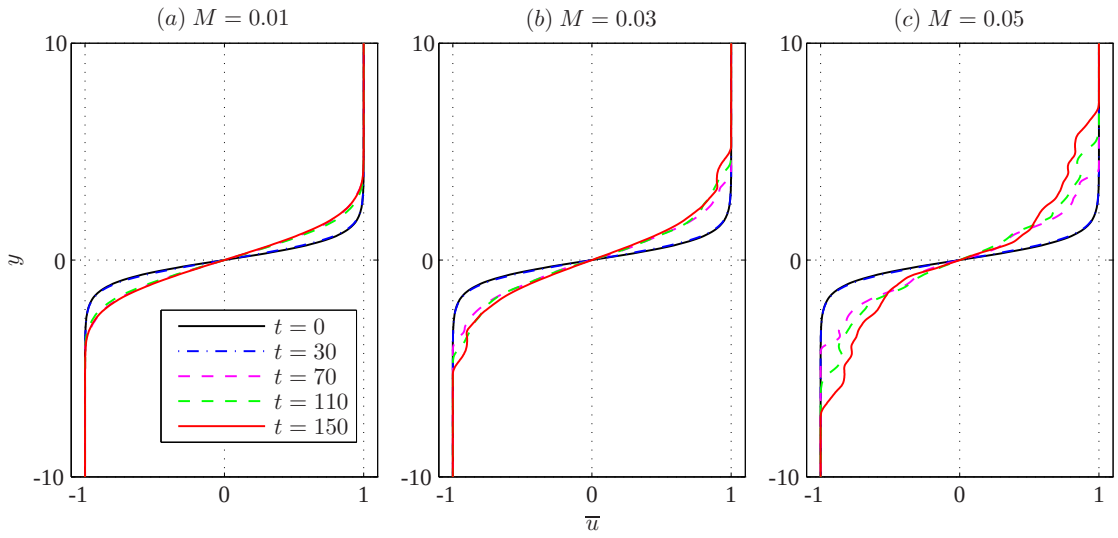

Figure 6.14: Snapshots of $\overline{u}$ for the shear layer runs at different field strengths (at Rm $=$ Re $= 500$).

further broadening of the profile after the initial roll-up, and the shear layer width is increased. Further, the stronger the disruption, the larger the shear layer width. This agrees with the observations made in previous studies (e.g Palotti *et al.*, 2008).

The energy evolution in incompressible MHD is given by

$$\frac{1}{2}\frac{\mathrm{d}}{\mathrm{d}t}\iint (|\nabla\psi|^2 + M^2|\nabla A|^2)\,\mathrm{d}x\mathrm{d}y = -\frac{1}{\mathrm{Re}}\iint \omega^2\,\mathrm{d}x\mathrm{d}y - \frac{M^2}{\mathrm{Rm}}\iint j^2\,\mathrm{d}x\mathrm{d}y, \qquad (6.44)$$

consisting of a kinetic energy term, magnetic energy term, viscous dissipation proportional to enstrophy, and Ohmic dissipation proportional to current squared. We plot in Figure 6.15 a time-series of the energies for the sample runs.

Growth rates for the linear instability are inferred via a fitting of the perturbation kinetic energy as before, and we see that the growth rates are to the hydrodynamic growth rate at 0.185. For the $M = 0.01$ case in Figure 6.15(a), it can be seen that perturbation magnetic energy remains considerably smaller than the perturbation kinetic energy; this is consistent with the observation that MHD effects play a secondary role in the dynamics in this case. The total energy loss is about 10%, comparable with the hydrodynamic case. For the $M = 0.03$ case in Figure 6.15(b), the perturbation magnetic energy is still an order of magnitude smaller than the perturbation kinetic energy. The perturbation magnetic energy is seen to decay from $t = 100$ signifying no significant build up of the magnetic field after the primary disruption. The total energy loss is around 12%, still comparable with the hydrodynamic case. For the $M = 0.05$ case in Figure 6.15(c), the

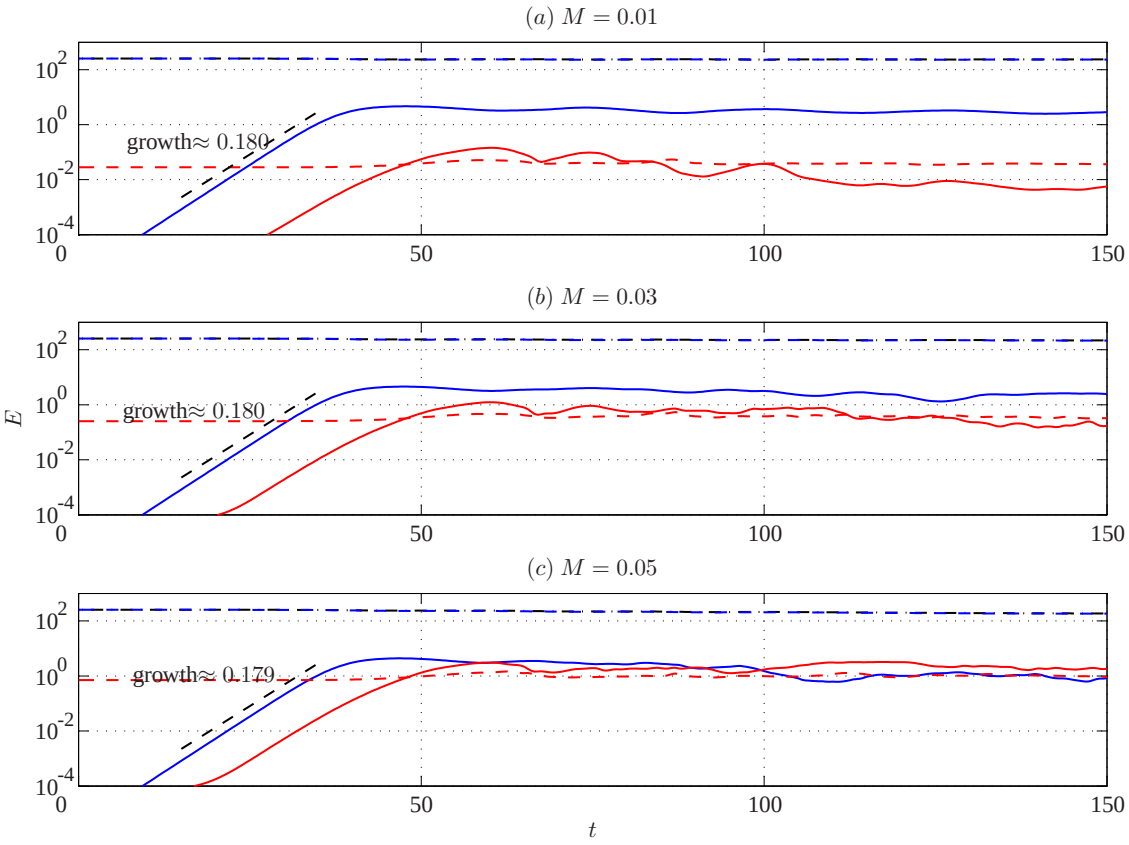

Figure 6.15: Time-series of the energies (blue = kinetic; red = magnetic; solid = perturbation state; dashed = mean state; black dot-dashed line = total energy) for the shear layer runs at different field strengths (at Rm = Re = 500).

perturbation magnetic energy is comparable with the perturbation kinetic energy, and this certainly indicates that the dynamics are significantly influenced by MHD effects. The total energy loss here is higher, at around 17%.

The increase in energy loss observed in Figure 6.15 is perhaps expected; since the Ohmic dissipation rate given by

$$\epsilon_{\mathrm{Rm}} = \frac{M^2}{\mathrm{Rm}} \iint j^2 \, \mathrm{d}x\mathrm{d}y \tag{6.45}$$

is related to the current density, and we have already observed that strong current sheets appear as a result of the vortical motion, this implies that extra dissipation is present, leading to higher energy loss. We plot in Figure 6.16 the viscous dissipation rate ϵ_{Re}, the Ohmic dissipation rate ϵ_{Rm} and the total dissipation for the three sample cases. Indeed, it is seen that the more disruptive case at $M = 0.05$ has a much higher Ohmic dissipation, so much so that Ohmic dissipation is the

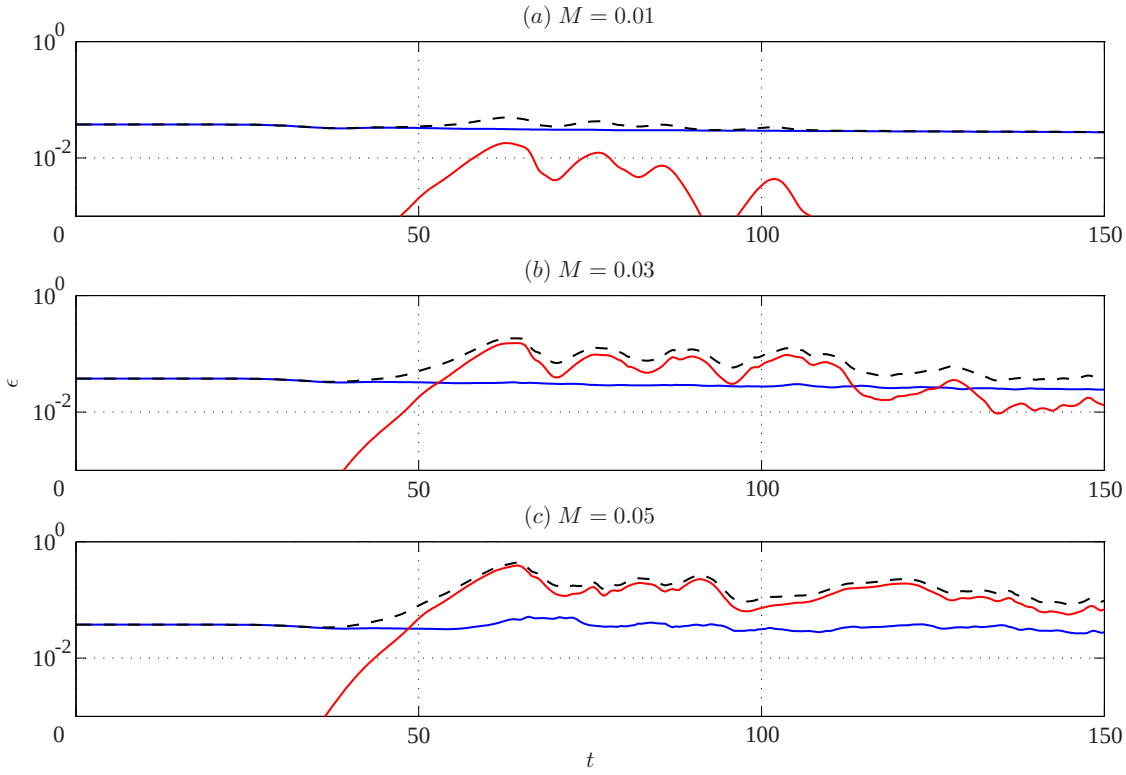

Figure 6.16: Domain-integrated dissipation rate ϵ_{Re} (blue curve), ϵ_{Rm} (red curve) and $\epsilon = \epsilon_{\mathrm{Re}} + \epsilon_{\mathrm{Rm}}$ (black dashed curve) for the shear layer runs, at $\mathrm{Rm} = \mathrm{Re} = 500$.

dominant contribution of the total dissipation. Additionally, Figure 6.16(c) shows that there is an increase in ϵ_{Re} around $t = 70$ for this severely disruptive case, signifying that there is an increase in global enstrophy and hence vorticity production by MHD effects.

Before classifying the computational runs, there are already several questions that one should ask:

1. Can we predict how the growth of the magnetic stress given M, Rm and Re, and, using this, estimate the degree of disruption?

2. What is the dependence of disruption on Re and other hydrodynamic secondary instabilities?

3. Is the break up of the layer caused by a tearing type resistive instability?

We shall now attempt to answer the first question, and provide a kinematic estimate that depends on M and Rm; we defer the latter two question to the discussion section at the end of the chapter.

6.5.1 Regime boundary estimation

We know that if the magnetic stresses built up by the vortical motion are significant before the major reconnection event occurs, then we can expect disruption to occur. The question then is how to quantify the size of the stresses.

The circular motion of the vortex has associated with it a centripetal force. For a fluid with density ρ and permeability μ_0, if a uniform vortex has length scale L_e and velocity U_e, then the centripetal force scales like $\rho U_e^2/L_e$. So we expect there to be significant disruption if the tension force T is comparable to the centripetal force, i.e.

$$T \sim |\rho \boldsymbol{b} \cdot \nabla \boldsymbol{b}| \sim \frac{\rho U_e^2}{L_e}, \tag{6.46}$$

where again $\boldsymbol{b} = \boldsymbol{b}^*/\sqrt{\rho\mu_0}$ is in units of velocity. Then it remains to estimate how large T can get. For this purpose, we employ a kinematic argument similar to that given in Weiss (1966). A kinematic argument should at least give us a first estimate of how large T can grow until it is arrested by dissipative effects.

We start from the (dimensional) induction equation

$$\frac{\partial \boldsymbol{b}}{\partial t} = \nabla \times (\boldsymbol{u} \times \boldsymbol{b}) + \eta \nabla^2 \boldsymbol{b}. \tag{6.47}$$

Now, the initial large-scale field B_0 at length scale L_e may be amplified to a stronger small-scale field b at a smaller length scale ℓ. Away from dissipation scales, flux conservation implies that we have

$$B_0 L_e = b\ell \qquad \Rightarrow \qquad b = \frac{B_0 L_e}{\ell}. \tag{6.48}$$

This amplification is arrested when the advection term $\nabla \times (\boldsymbol{u} \times \boldsymbol{b})$ is comparable to the diffusive term $\eta \nabla^2 \boldsymbol{b}$, i.e.

$$\frac{U_e B_0}{L_e} \sim \frac{\eta b}{\ell^2}, \tag{6.49}$$

implying

$$b \sim \left(\frac{U_e L_e}{\eta}\right)^{1/3} B_0. \tag{6.50}$$

This is the first part of the argument in Weiss (1966), and our b here is his B_1.

Now, since $b \gg B_0$ and $\ell \ll L_e$, we have, using (6.48) and (6.50)

$$T \sim |\rho \boldsymbol{b} \cdot \nabla \boldsymbol{b}| \sim \rho \frac{b^2}{\ell} \sim \rho \frac{b^3}{B_0 L_e} \sim \rho U_e \frac{B_0^2}{\eta}. \tag{6.51}$$

This suggests we are in the disruptive regime when

$$\rho U_e \frac{B_0^2}{\eta} \sim \frac{\rho U_e^2}{L_e} \qquad \Rightarrow \qquad \frac{B_0^2}{\eta} \sim \frac{U_e}{L_e} \sim \Omega_e, \tag{6.52}$$

where Ω_e is the typical scale for vorticity in two-dimensions.

Going back to our non-dimensional set up, a constant field implies that

$$B_0 \to M, \qquad \frac{1}{\eta} \to \mathrm{Rm},$$

so the expected disruption condition (6.46) becomes

$$M^2 \mathrm{Rm} \sim \Omega_e. \tag{6.53}$$

For the shear layer profile considered here, $\Omega_e \sim 1$. The severely disruptive case of $(M, \mathrm{Rm}) = (0.05, 500)$ has $M^2\mathrm{Rm} = 1.25$, the mildly disruptive case of $(M, \mathrm{Rm}) = (0.03, 500)$ has $M^2\mathrm{Rm} = 0.45$, and the non-disruptive case of $(M, \mathrm{Rm}) = (0.01, 500)$ has $M^2\mathrm{Rm} = 0.05$, so this kinematic prediction is then at least consistent with the observed disruption for these three sample cases.

As argued before, the disruption event occurs well before any flux expulsion regime is reached (approximately half to one turnover time compared with three or four turnover times for flux expulsion), so we use the above estimate, which takes into account how much the field lines may be amplified before it is arrested by finite magnetic dissipation. We will test our kinematic estimate here, and discuss the possibilities of a dynamic estimate in the discussion section at the end of the chapter.

6.5.2 Regime classification

We now proceed to classify our set of runs in (M, Rm) space. To do this we need some way of measuring the degree of disruption. There are several features correlated with the observed degree of disruption, such as the dominance of filamentary vorticity structures and the increase of shear layer width. We construct measures that make use of these two observations.

More filamentary structures implies more small-scale activity. In a spectral representation this implies that more modes are required to reconstruct the original profile. Using vorticity as an example, since we have data for vorticity collocated at the relevant points, we consider a

case	k_{cut}	marker
severely disruptive	$k_{\text{cut}} \geq 25$	$\circ$
mildly disruptive	$10 < k_{\text{cut}} < 25$	$\triangle$
no visible disruption	$k_{\text{cut}} \leq 10$	$\times$

Table 6.2: Regime classification for the shear layer in the incompressible case, using the spectral truncation measure.

spectral representation of the data. We then take some truncation wavenumber k_{cut}, and a spectral truncation is carried out by setting to zero the coefficients with wavenumbers $k_{\text{cut}} < k_y \leq N_y$ for Chebyshev modes and $k_{\text{cut}} < k_x \leq N_x/2$ for Fourier modes. The enstrophy associated with $\omega(k = k_{\text{cut}})$ is calculated for increasing k_{cut} until some large percentage of the total enstrophy is recovered, and we record the k_{cut} that achieves this; vorticity fields possessing more filamentary structure will have a higher k_{cut}. As a demonstration, reconstructions of the spectrally truncated vorticity at several values of k_{cut} are given in Figure 6.17, using the $t = 100$ frames of Figure 6.9. The enstrophy capture percentage, given by $\|\omega_{\text{cut}}\|^2/\|\omega_{\text{full}}\|^2$, where $\|\cdot\|$ is interpreted in the L^2 sense, is given underneath the panels. As expected, for a run where the main feature is the parent vortex, only a few modes are needed to capture most of the enstrophy and reproduce the original profile. More modes are required when filamentary structures are present.

For our purpose we choose the k_{cut} that recovers 99% of the enstrophy, i.e.

$$\frac{\|\omega_{\text{cut}}\|^2}{\|\omega_{\text{full}}\|^2} > 0.99, \tag{6.54}$$

and we take k_{cut} maximised over the run time at each (M, Rm). We choose to use enstrophy over the current squared because in our case Re is fixed whilst Rm is not, and a larger Rm allows for thinner current sheets, naturally resulting in a larger k_{cut}. Enstrophy is used over energy because enstrophy provides a sharper measure, as ω is one derivative higher than $\nabla\psi$. The maximum over the run is taken because this takes into account when the activity is at its most vigorous, compared to, say, taking k_{cut} at the end time when diffusion may have already smoothed out some features.

Using Figure 6.17 as a rough visual guide and with some calibration using some sample runs, we classify the runs as in Table 6.2. The raw data from our set of runs is given in Table 6.3; for comparison, the hydrodynamic run at $\text{Re} = 500$ has $k_{\text{cut}} = 7$.

Another measure of the disruption that we consider is the width of the shear layer. As observed

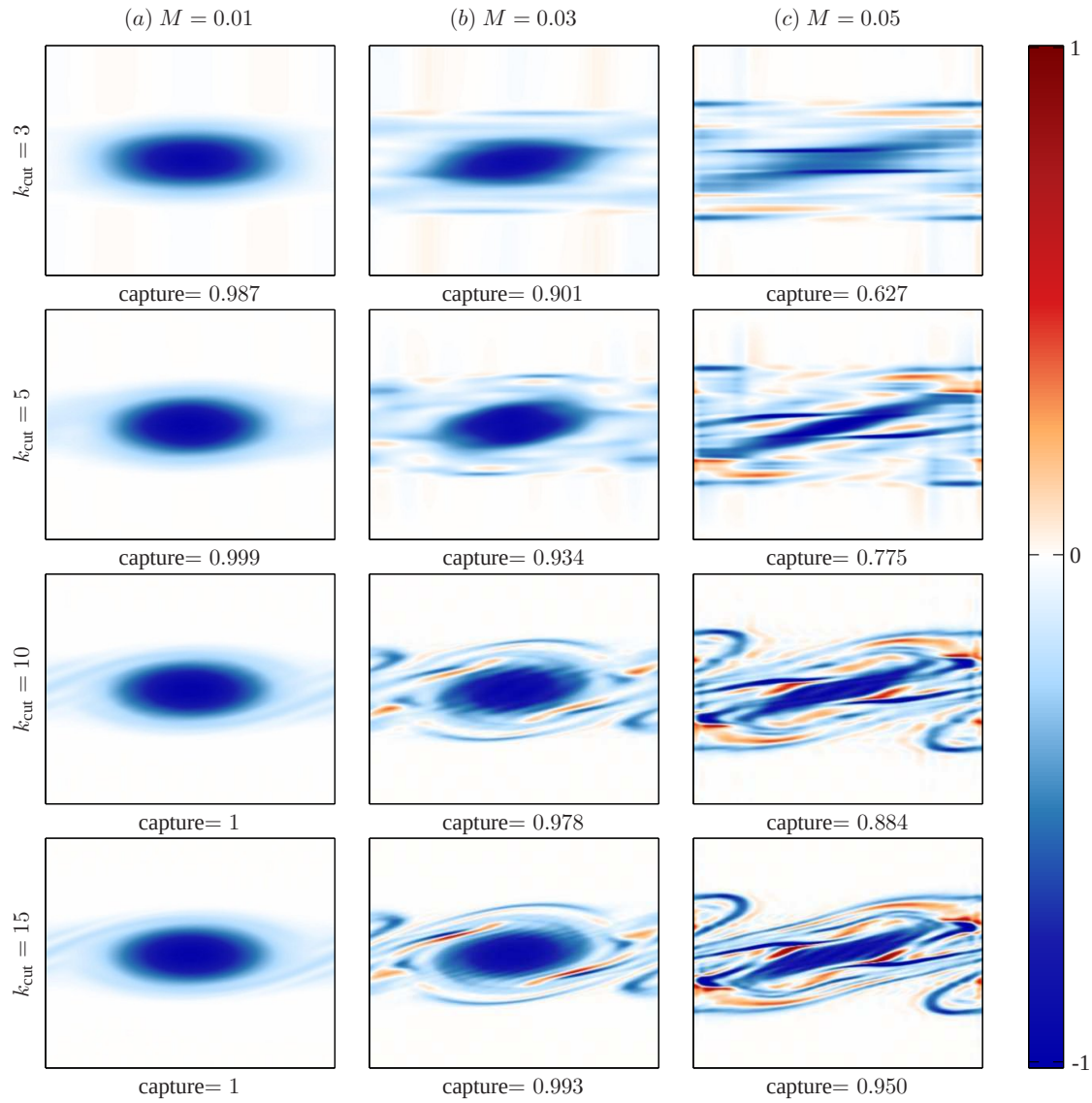

Figure 6.17: Vorticity field truncated spectrally at several levels, for the $t = 100$ snapshot (third row of Figure 6.9). The enstrophy capture ratio given by the left hand side of (6.54) at various truncation levels is also given.

Rm \ M	0.01	0.02	0.03	0.04	0.05	0.06	0.07	0.1
1000	7	17	37	25	55	54	60	60
750	7	14	30	34	34	41	45	60
500	7	7	24	31	33	31	33	46
250	7	7	7	22	27	29	28	31
50	7	7	7	7	8	9	11	14

Table 6.3: Raw data from the set of calculations at Re $= 500$ for the shear layer, with numbers denoting the truncation wavenumber k_{cut} maximised over time. The hydrodynamic case has $k_{\text{cut}} = 7$.

case	layer expansion factor f	marker
severely disruptive	$f \geq 1.5$	$\circ$
mildly disruptive	$1.15 < f < 1.5$	$\triangle$
no visible disruption	$1.15 \leq f$	$\times$

Table 6.4: Regime classification for the shear layer in the incompressible case, using the shear layer width measure.

in Figure 6.14, the more disruptive the run, the larger the shear layer width. To measure the shear layer width, we find the location where $|\overline{u} - \overline{u}_\infty| < 0.01$, with $\overline{u}_\infty$ the free-stream value of the profile ($\overline{u}_\infty = 1$ for the shear layer profile). To give a measure, we fix a snapshot time, and calculate the shear layer width, normalised by the shear layer width in the hydrodynamic case at the corresponding time. For our purposes, we took the layer width at the end time $t = 150$, so

$$f = \frac{\text{layer width of run at } t = 150}{\text{layer width of hydrodynamic run at } t = 150}. \tag{6.55}$$

From this, we classify the runs as in Table 6.4. The raw data is given in Table 6.5. The hydrodynamic case has a factor of 1, with an initial layer width of about 5.9 and an end layer width of 7.65.

Using the two classifications, we plot in Figure 6.18 regime diagrams in (M, Rm) space based on the two measures given, for the single wavelength case at Re $= 500$. Lines of $M^2\text{Rm} = C$, consistent with (6.53), for several values of C are overlaid onto the diagram. There was some calibration required for classifying the simulations; this has been done so that the essentially hydrodynamic runs and the severely disruptive runs are captured as best as possible. There are

Rm \ M	0.1	0.2	0.3	0.4	0.5	0.6	0.7	0.1
1000	1.08	1.30	1.74	1.88	2.11	1.94	2.37	2.46
750	1.07	1.28	1.69	1.81	1.95	1.99	2.37	2.52
500	1.04	1.17	1.37	1.57	1.88	2.01	2.24	2.56
250	1.04	1.07	1.20	1.41	1.67	1.78	2.01	2.40
50	1.03	1.04	1.07	1.07	1.13	1.10	1.25	1.52

Table 6.5: Raw data from the set of calculations at Re $= 500$ for the shear layer. The numbers denote the shear layer width expansion factor (relative to the hydrodynamic run at Re $= 500$, taken at end time). The expansion factor for the hydrodynamic case is defined to be $f = 1$.

one or two differences in classification but these invariably lie close to our regime boundaries. The boundaries were not expected to be sharp, so we argue that the minor differences in this case does not invalidate our conclusions. It appears that $M^2\mathrm{Rm} \geq 0.5$ captures most of the severely disruptive cases. More important, the dependence of vortex disruption by secondary resistive instabilities is well described by the estimate $M^2\mathrm{Rm}$, at least for the range of parameter values we have considered.

6.5.3 Dependence of evolution on Re

In the hydrodynamic case, when the domain is large enough to support two or more wavelengths of the primary instability, vortices formed from the primary instability may pair up. One might ask about the interplay between the pairing modes and the dynamically driven resistive instabilities when the domain is large enough to support pairing instabilities. In the test runs we have carried out, we observed that, disruption, if it occurs, does so before any pairing of the vortices; for severely disruptive cases the vortex can be destroyed before any pairing can happen. For the cases where the disruption is mild, disruption occurs, slightly reducing the vortices in size, then pairing occurs. Assuming this pairing is allowed to take place, one can imagine cases where the primary disruption is weak/mild, but any subsequent pairing results in further build up of magnetic stresses, promoting a weakly/mildly disruptive case to a mildly/severely disruptive case. We have not observed this in any of our test runs, but these were restricted to no more than four wavelengths because of limits on resolution available. In the study of Baty *et al.* (2003), eight wavelengths of the primary instability were allowed, and, in their Figure 15, a promotion to a severely disruptive

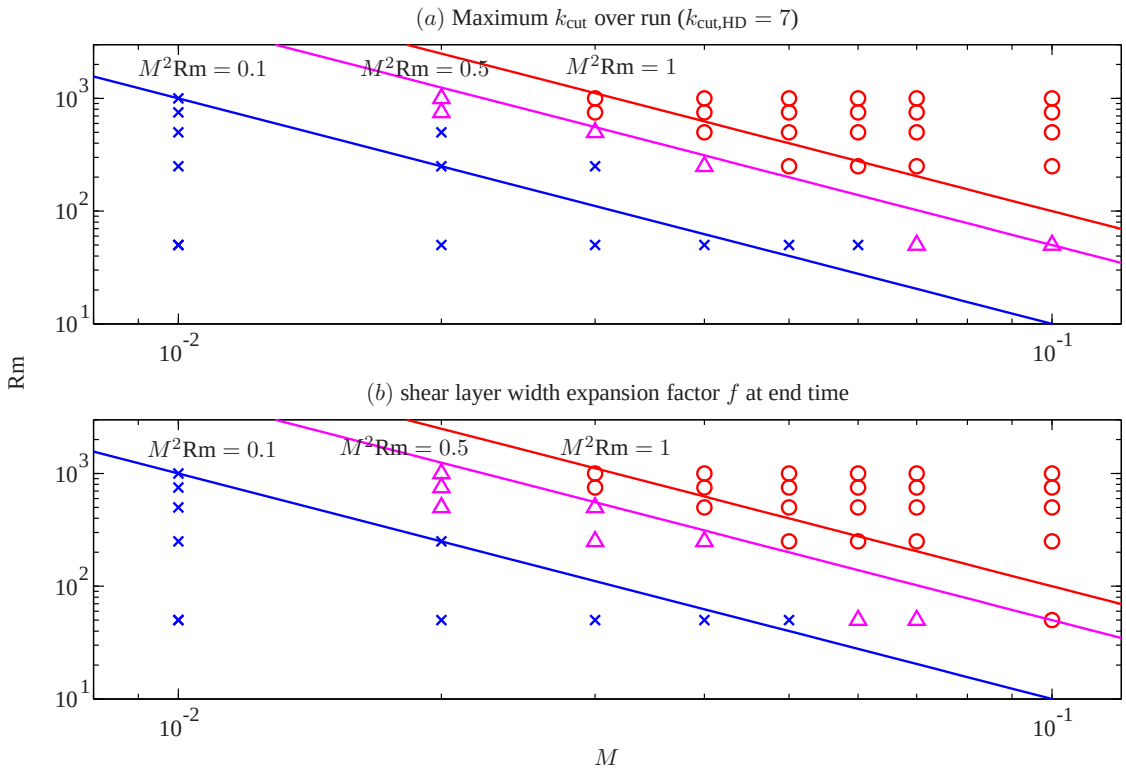

Figure 6.18: Regime diagram, as measured by the spectral truncation wavenumber k_{cut} (maximised over time) and via the shear layer width expansion factor f (taken at end time). The suggested boundary given by (6.53) is plotted for several values of C.

case is seen (their Figure 15 comes from a fully resistive compressible MHD while the other runs in that paper use a numerical dissipation).

Hydrodynamic secondary instabilities were seen also to play a role in the transition to turbulence and are dependent on Re (Mashayek & Peltier, 2012a,b); however, most of these secondary instabilities are excluded in our physical set up. Our simulations are limited to $\mathrm{Re} = 1000$ and as yet it remains inconclusive whether the dependence on Re is weaker than $M^2\mathrm{Rm}$, as suggested by the kinematic estimate; in our tests runs at higher Re we observe that the disruption appears to be more severe.

6.5.4 The cases with larger M

For completeness, Figure 6.19 shows snapshots of the vorticity for runs with larger values of M than those considered previously; recall, from Chapter 5, that $M \geq 1$ guarantees linear stability of this basic state. A larger perturbation to the vorticity was given to compensate for the slower growth rates. We should note that the time snapshots are not comparable to those in Figure 6.9 since the perturbation is of a different magnitude.

For the $M = 0.2$ case in Figure 6.19(a), we observe severe disruption, with regions of very strong vorticity generated even before the vortex has completely formed. The disruption is very rapid and strong filaments litter the domain. Even in this slightly shorter run, the shear layer is observed to have spread to the boundary. For the $M = 0.4$ case in Figure 6.19(b), we perhaps still observe some disruption, but now the background field appears to be strong enough to suppress fluid motion, and by the end frame, we have what would be deemed a laminar state. For the $M = 0.6$ case in Figure 6.19(c), nothing that is characteristic of disruption is observed, and it would appear that even the rolling up motion has been suppressed.

We note then that the disruption estimate $M^2\mathrm{Rm} \sim \Omega_e$ only predicts the degree of disruption where there is a rolling up of the shear layer. The transition location between the disruptive regime and the nonlinearly stable regime has not been investigated here.

6.6 MHD evolution: Bickley jet

We now consider an analogous investigation for the Bickley jet profile. In planar geometry, the evolution of this profile in the incompressible MHD system has been investigated by Biskamp *et al.* (1998); jet-like profiles in the compressible MHD regime have been investigated by, for example, Min (1997a,b) and Baty & Keppens (2006). All these authors find that vortices may be disrupted, and that weak vorticity bands become the dominant feature in the domain. As in the shear layer case, we consider values of M that, according to linear theory, result in growth rates and eigenfunctions that are comparable to the hydrodynamic case. As was done previously, we take $\alpha = 0.9$, with a domain that supports two wavelengths of the primary instability, partly for consistency, and partly to demonstrate that complete disruption may happen before pairing of vortices occur. A summary of the run parameters is given in Table 6.6.

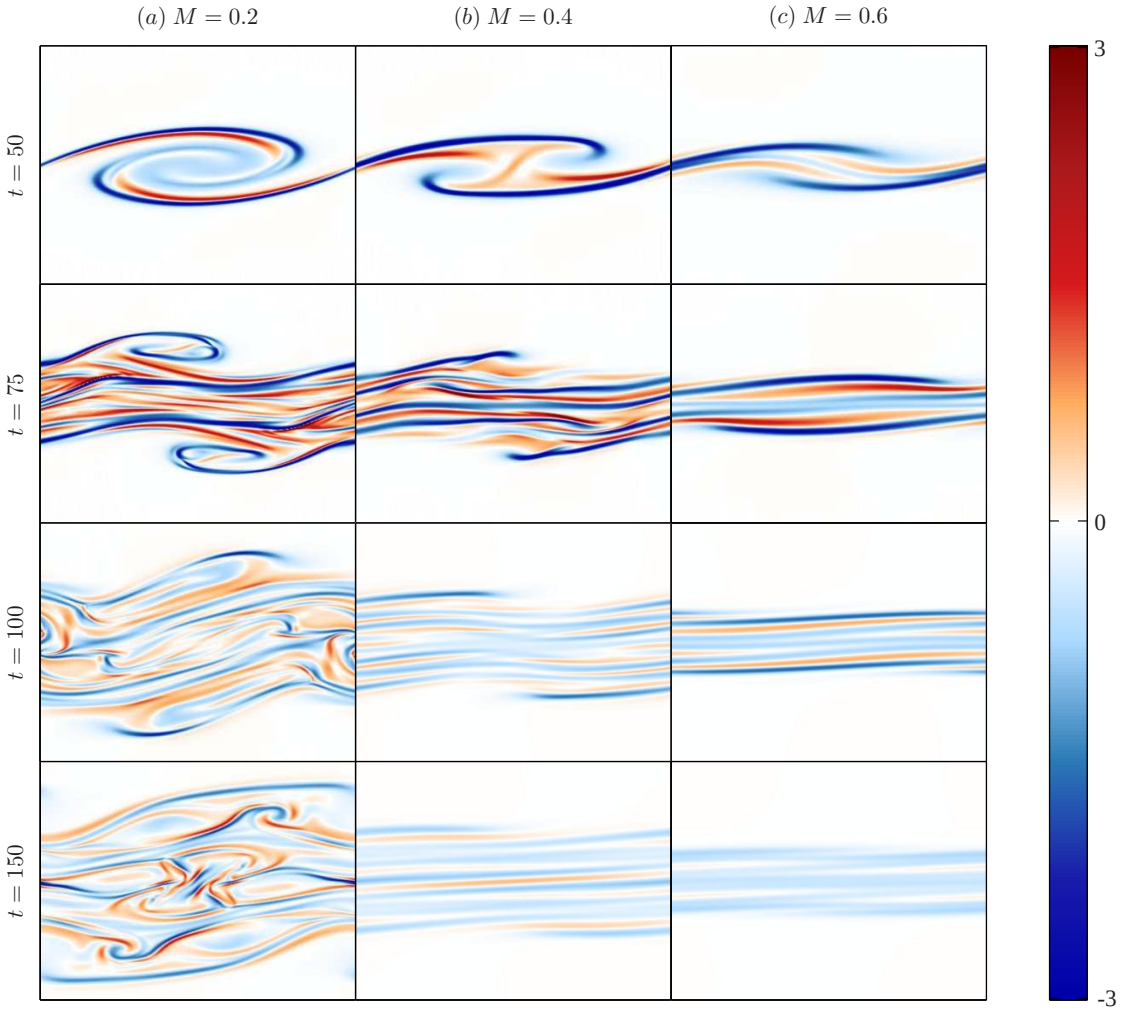

Figure 6.19: Snapshots of vorticity for the shear layer at some larger values of M (at Rm $=$ Re $=$ 500). Note the use of a wider colour scale compared to Figure 6.9, and the simulations were initialised with a larger perturbation than the ones presented in Figure 6.19.

As before, we take three representative runs, carried out at Rm $=$ 500 and $M = 0.01$, 0.03, and 0.05; as a reminder, $M = 0.5$ implies linear stability (see Chapter 5). In Figure 6.20 we show snapshots of the vorticity for these three runs. In all cases, the primary instability causes a meandering and break up of the jet, as in the hydrodynamic case displayed in Figure 6.5. For the $M = 0.01$ case in Figure 6.20(a), at $t = 100$, we see that there is some sort of distortion to the vortices, due to the release of built up magnetic stresses, and the vortices take an almost triangular shape in this frame. The stresses built up in this case however are evidently not very strong, and the vortices are able to recover their elliptical shapes by $t = 150$; at this time, we also see early

parameter	range
α	0.90
C_{cfl}	0.2
$L_x \times L_y$	$[0, 2\pi/\alpha] \times [-10, 10]$
Re	500
M	0.01, 0.02, 0.03, 0.04, 0.05, 0.06, 0.07, 0.1
Rm	50, 250, 500, 750
$N_x \times N_y$	384×768 for Rm $= 750$
	256×512 otherwise

Table 6.6: Parameter values employed in our investigation for the Bickley jet profile.

signs of vortex pairing.

We may contrast this to the other two cases, where thin vorticity layers are seen in the $t = 75$ frames. The resulting magnetic stresses are larger and thus have a more significant impact on the flow. By $t = 100$, the vortices have lost their structure and bands of vorticity become the dominant feature in the domain, as in Biskamp *et al.* (1998). Unlike the shear layer case, however, it appears that disruption is not sustained; there is one primary disruption but this does not trigger further disruptions. We attribute this to the fact that, for the shear layer, the primary disruption results in motion that can tap into the background flow when the layer spreads away from the region near $y = 0$, triggering more disruption. This is not the case for the Bickley jet profile as the flow is primarily supported near $y = 0$. The intensity of vorticity at the late time $t = 150$ is substantially lower than for the $M = 0.01$ case in Figure 6.20(a), signifying that there has been increased dissipation, resulting in a significant decrease in activity.

The associated magnetic field line profiles are plotted in Figure 6.21, again with field lines threading the region $y \in [-2, 2]$ at $t = 0$, at 0.5 spacing; the field line threading $y = 0$ is omitted for clarity purposes. For all cases, it is seen that the regions on the edge of the vortices coincide with regions of strong flux concentration, implying strong current layers at these locations. This strong field region is again not a result of flux expulsion, but rather a result of the vortical motion winding up field lines. For the $M = 0.01$ case in Figure 6.21(a), we observe the formation of some magnetic islands, indicating that reconnection of magnetic field lines has occurred. For the $M = 0.03$ case in Figure 6.21(b), we see very clear traces of magnetic islands even until

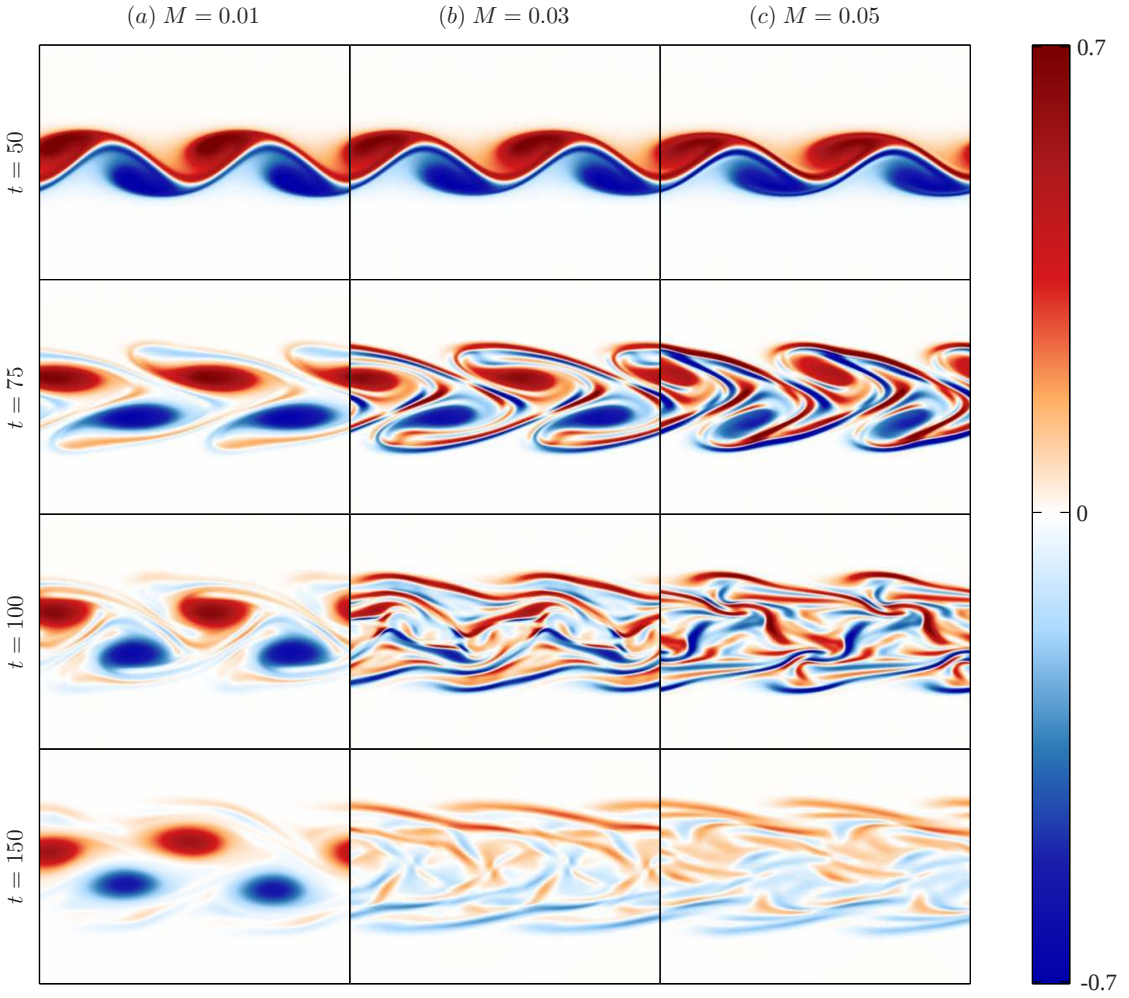

Figure 6.20: Snapshots of vorticity for the Bickley jet at different field strengths (at Rm $=$ Re $= 500$).

$t = 150$, suggesting that the relaxed state is still to be reached. For the $M = 0.05$ case in Figure 6.21(c), it appears that the relaxed state is almost reached, with some distorted field lines but no traces of magnetic islands. This largely diffused state occurs sooner than the $M = 0.03$ case in Figure 6.21(b), indicating that a stronger disruption leads to a quicker relaxation to a state with weaker activity.

Snapshots of the electric current density j for the $M = 0.05$ case are shown in Figure 6.22. As for the shear layer, double current layers are observed at the edges of the vortices rather than single layers; this configuration is expected to be unstable to the family of tearing instabilities. Filaments are again the dominant features in the domain. It is also interesting to see that, in Figure 6.22(d), the intensity of the current at this late time is very low; contrast this to the shear layer case, with

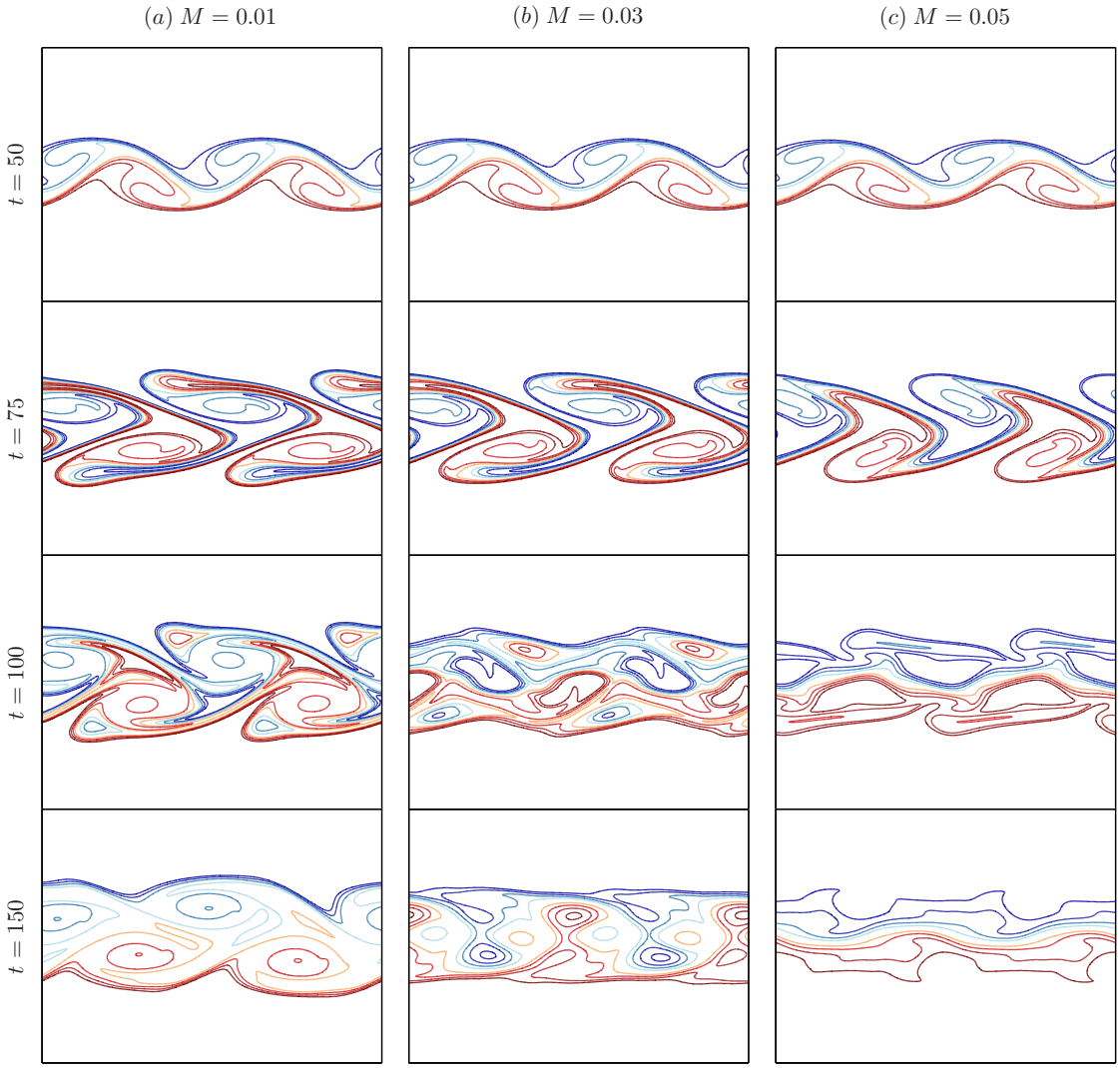

Figure 6.21: Snapshots of field lines for the Bickley jet runs at several field strengths (at Rm $=$ Re $= 500$).

its current profile given in Figure 6.12(d).

In Figure 6.23 we show snapshots of $\overline{u}$. As with the shear layer, there is broadening of $\overline{u}$ as the primary instability saturates and the jet breaks up into vortices. In contrast to the shear layer case however, the jet widths (computed using either $|\overline{u} - \overline{u}_\infty|$ or $|\overline{\omega} - \overline{\omega}_\infty|$ as the measure) for the runs at different field strengths at the end time $t = 150$ are in fact comparable with each other. This seems to be because there is really only one significant disruption event, in contrast to the shear layer case where a cascade of disruptions may occur, leading to a substantial increase of the shear layer width. We do observe, however, that the decrease in peak flow value, given by $\max |\overline{u}(y)|$, is correlated with increasing disruption, with more disruptive runs leading to a larger decrease in

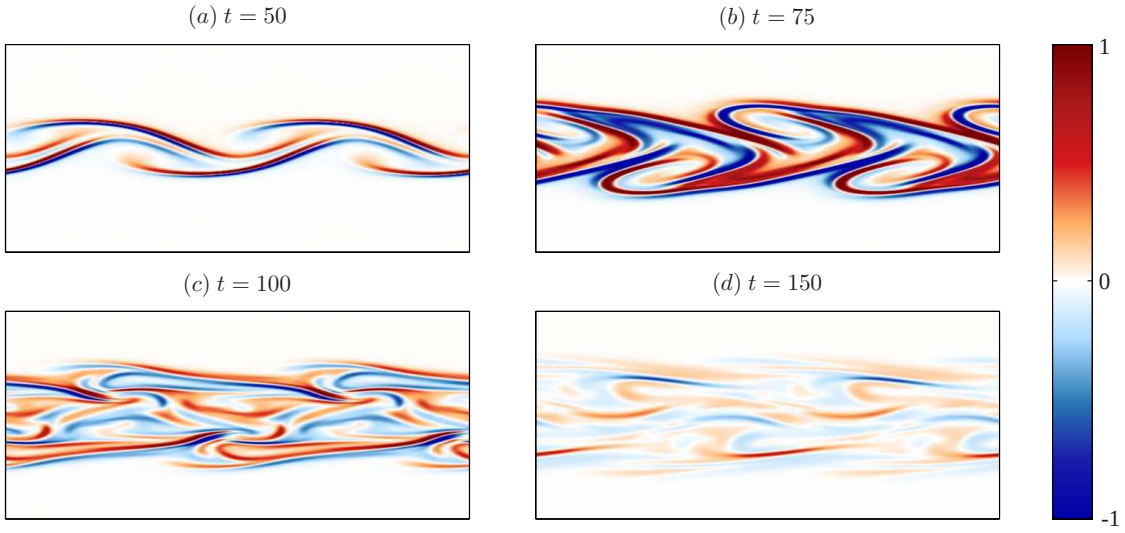

Figure 6.22: Snapshots of electric current for the Bickley jet (at Rm $=$ Re $= 500$, $M = 0.05$).

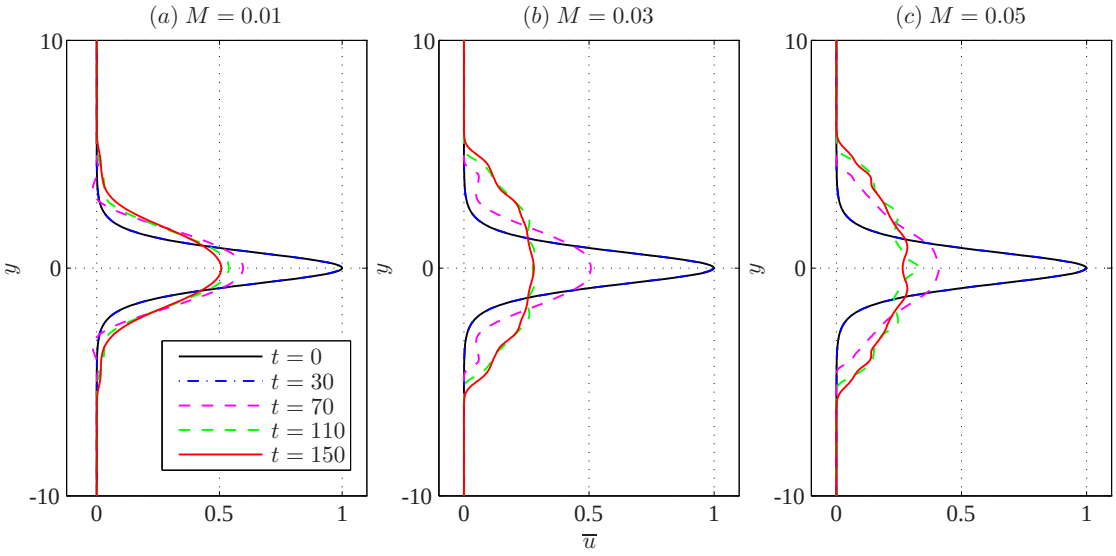

Figure 6.23: Snapshots of $\overline{u}$ for the Bickley jet runs at different field strengths (at Rm $=$ Re $= 500$).

$\max |\overline{u}(y)|$. We use this later to construct a measure of disruption.

Figure 6.24 shows the energy time-series of the representative runs. Again, a growth rate is inferred by a fitting of the perturbation kinetic energy and these values are close to the hydrodynamic dynamic growth rate at 0.160. As in the shear layer runs, we observe that the magnetic energy levels saturate at a different magnitude depending on the initial field strength.

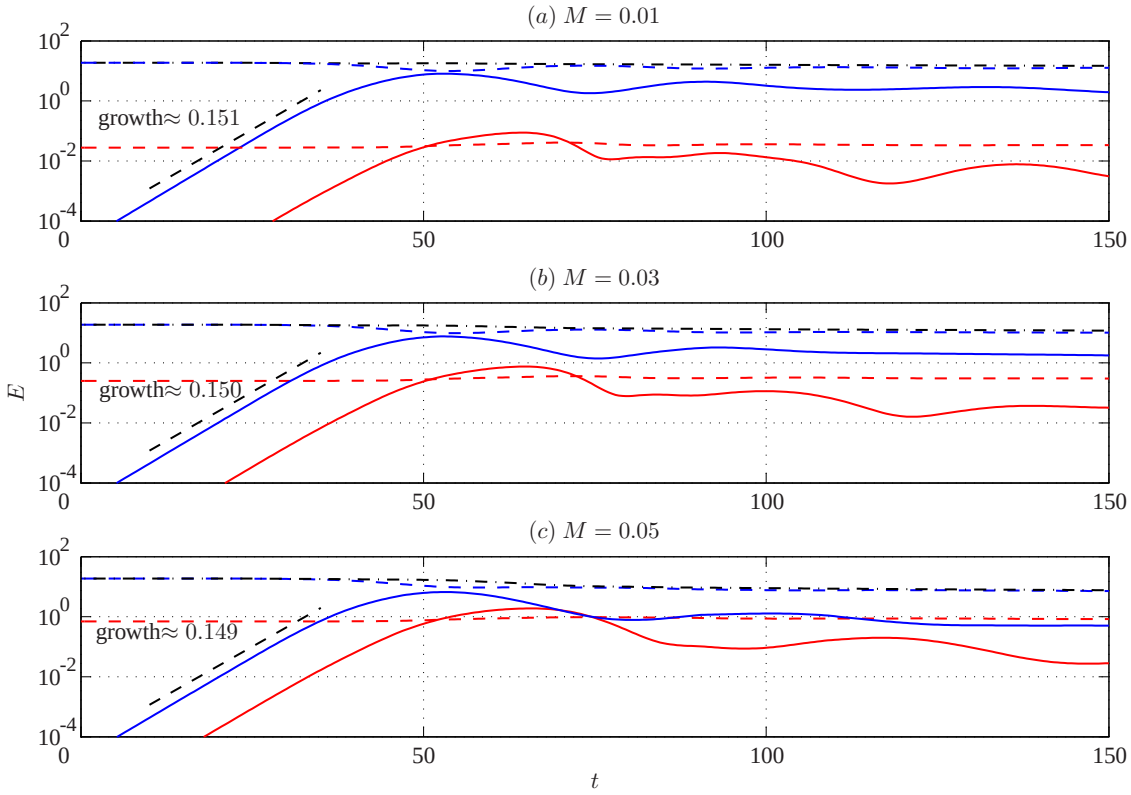

Figure 6.24: Time-series of energies (blue = kinetic; red = magnetic; solid = perturbation state; dashed = mean state; black dot-dashed line = total energy) for the Bickley jet runs (at Rm = Re = 500).

The disruptive cases have the perturbation magnetic and kinetic energies comparable at some point during the run. There is a noticeable loss of total energy; the $M = 0.01$ case in Figure 6.24(a) has a loss of around 30%, comparable with the hydrodynamic case, whilst in the $M = 0.05$ case in Figure 6.24(c), this is around 40%.

In Figure 6.25 we plot the dissipation rates for the three runs. Unlike the shear layer runs, Ohmic dissipation is not necessarily several orders of magnitude higher than the viscous dissipation; however in all three runs they are at some point comparable. The Ohmic dissipation increases to a peak value but then generally decreases afterwards; contrast this to the shear layer case in Figure 6.16 where multiple well-defined peaks in the Ohmic dissipation are observed. This is consistent with the observation that the disruption events are not sustained, and there is really only one primary disruption event.

In this multiple wavelength case there is the possibility of pairing of like-signed vortices; however in the runs where we observe disruption, the destruction of vortices occurs before any vortex

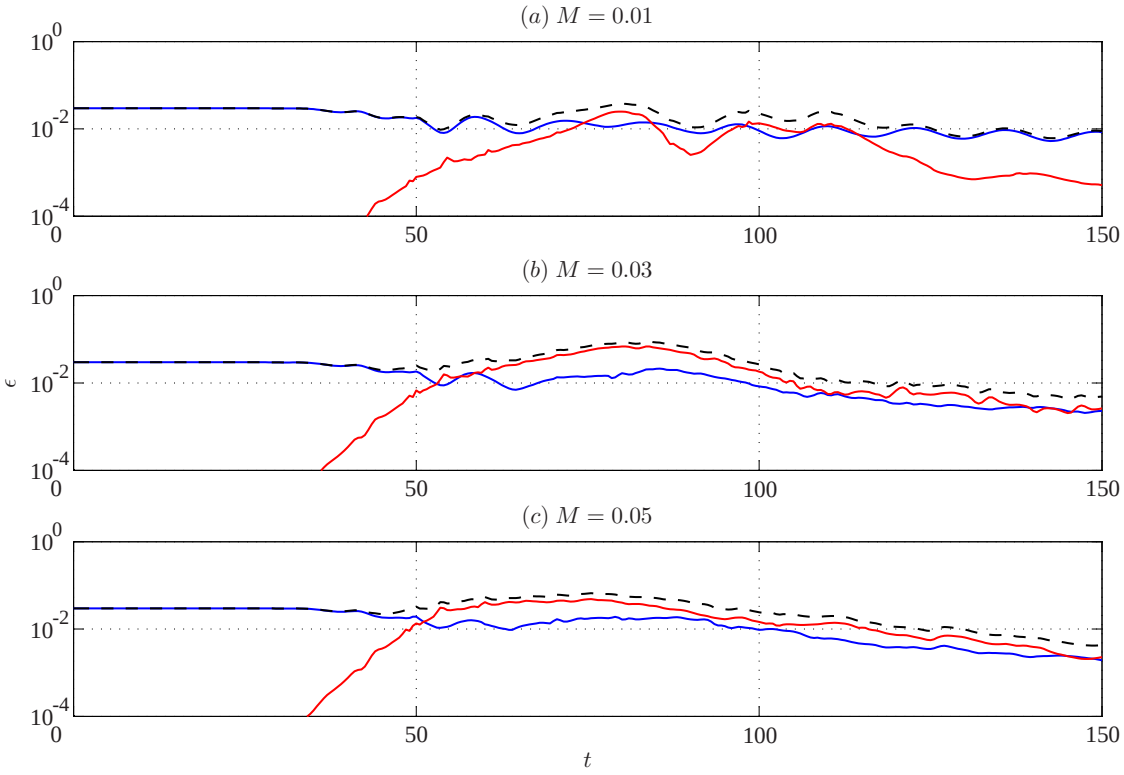

Figure 6.25: Domain-integrated dissipation rate ϵ_{Re} (blue curve), ϵ_{Rm} (red curve) and $\epsilon = \epsilon_{\mathrm{Re}} + \epsilon_{\mathrm{Rm}}$ (black dashed curve) for the Bickley jet runs.

pairing has occurred. When the field is sufficiently weak, vortices form as usual and the evolution is essentially like the hydrodynamic case. One may ask whether multiple pairings can lead to more disruption due to extra winding up of field lines. As discussed in the shear layer case, this certainly seems possible from the work of Baty *et al.* (2003); however we have not observed it in any of our test runs with a larger domain (we have limited ourselves to a domain that supports no more than four wavelengths of the primary instability).

6.6.1 Regime classification

Since we still have vortices winding up field lines, the previous argument in Section 6.5.2 leading to the estimate $M^2\mathrm{Rm} \sim \Omega_e$ is still relevant. In this case, $\Omega_e \sim 0.7$, and the representative runs give values of $M^2\mathrm{Rm}$ consistent with the observed non-disruptive (vortex dominated) and disruptive (band dominated) cases. We have also tried using spectral truncation and jet widths to classify our runs; there is a problem here in that a spectral truncation does not appear to distinguish

case	peak $\overline{u}$ reduction factor	marker
disruptive/bands	< 0.75	$\circ$
not disruptive/vortices	≥ 0.75	$\times$

Table 6.7: Regime classification for the Bickley jet in the incompressible case, using the peak jet strength reduction factor.

Rm \ M	0.01	0.02	0.03	0.04	0.05	0.06	0.07	0.1
750	0.90	0.64	0.48	0.45	0.52	0.52	0.57	0.65
500	0.93	0.69	0.51	0.45	0.51	0.56	0.51	0.65
250	0.96	0.89	0.67	0.51	0.51	0.53	0.51	0.29
50	0.96	0.96	0.93	0.80	0.80	0.40	0.26	0.29

Table 6.8: Raw data from the set of calculations at Re $= 500$ for the Bickley jet. The numbers denote the peak jet strength reduction factor relative to the hydrodynamic case.

between relatively wide bands of vorticity and compact vortices, and we have already made the observation that the jet widths of the saturated states appear to be comparable to each other in our runs. One measure that does seem to be well correlated with the degree of disruption is the peak jet strength value $\max|\overline{u}(y)|$. We will thus take $\max|\overline{u}(y)|$ at the end of the MHD simulations at $t = 150$ and divide this by the peak value of the equivalent hydrodynamic run to give us a reduction factor. We classify the runs using the conditions given in Table 6.7; the corresponding hydrodynamic case of course has a reduction factor of 1, with $\max|\overline{u}(y)| = 0.55$ at $t = 150$ in this case. The raw data is given in Table 6.8 and a regime diagram is given in Figure 6.26.

We see that $M^2\text{Rm} \geq 0.1$ appears to capture all the disruptive cases. More importantly, the dependence of disruption on the combination $M^2\text{Rm}$ appears to be well captured.

6.6.2 The cases with larger M

For completeness, we plot in Figure 6.27 snapshots of the vorticity of a run at larger M, here at $M = 0.25$ ($M = 0.5$ implies linear stability), with Rm $=$ Re $= 500$. The jet appears to meander a little but does not break up into vortices; compare this to the shear layer case where the vortex does not form at larger M. Again, the estimate $M^2\text{Rm} \sim \Omega_e$ requires that we have vortices forming

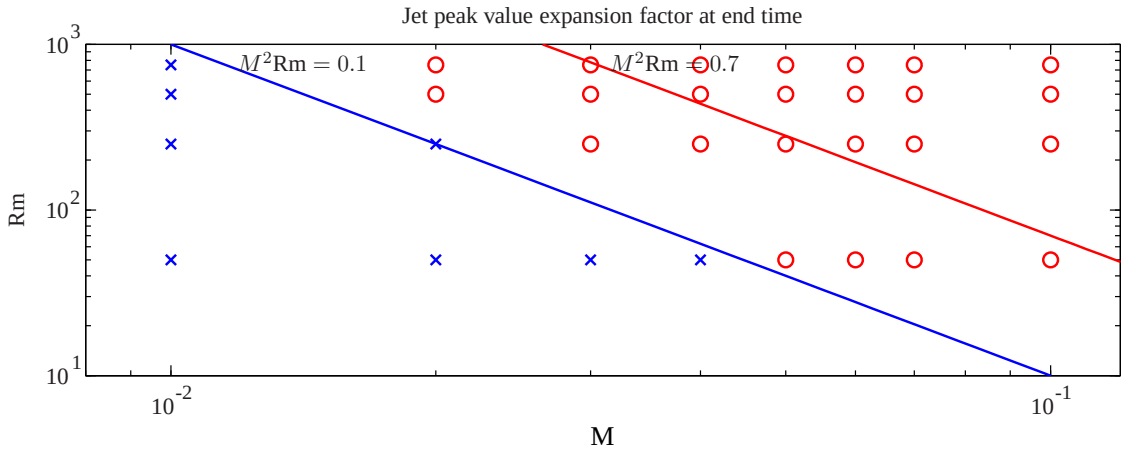

Figure 6.26: Regime diagram, as measured by the reduction of the peak value of $\overline{u}$ at end time as a relative factor to the equivalent hydrodynamic case. Again, $M^2\mathrm{Rm} = C$ is plotted for some values of C.

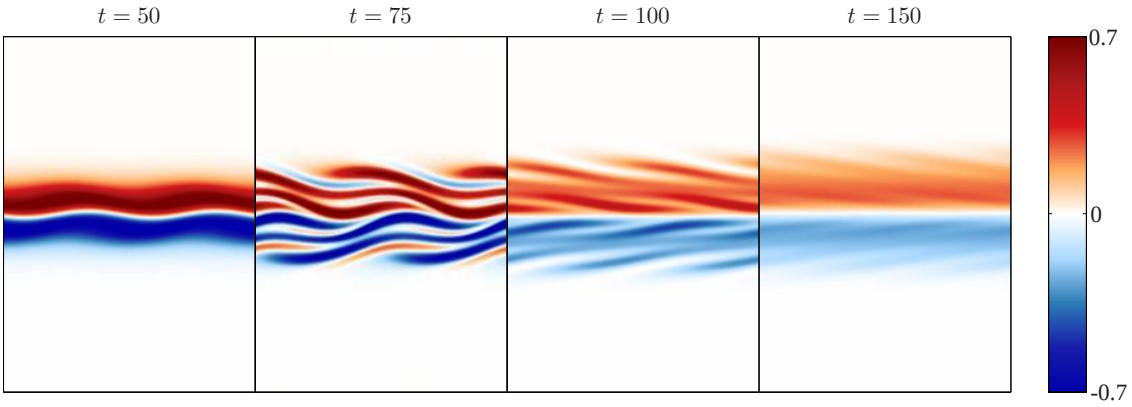

Figure 6.27: Snapshots of vorticity for the Bickley jet run at $M = 0.25$ (at $\mathrm{Rm} = \mathrm{Re} = 500$).

in the first place; the transition between the disruptive and nonlinear stable regime has not been investigated.

6.7 Summary and discussion

To summarise, we have investigated the nonlinear evolution of shear flow instabilities in incompressible MHD, taking $F = 0$. Even for weak background field (in the sense that the initial magnetic energy is much smaller than the initial kinetic energy), it is known from previous work that the vortical motion arising from the hydrodynamic evolution can amplify the magnetic field,

feedback onto the flow, and cause disruption to the coherent structures that would otherwise form. Our work here appears to be the first to investigate the simultaneous dependence of disruption on the basic field strength M and the dissipation parameter, in this case measured by the magnetic Reynolds number Rm, as well as provide an estimate for the dependence of the degree of disruption on the parameter values.

For the shear layer, we focussed on the case where the domain supports a single wavelength of the most unstable mode. In the hydrodynamic case, the shear layer rolls up into a vortex, and in our physical setting, there are no observable hydrodynamic secondary instabilities (e.g., pairing, braid, convective etc.) that affect the stability of the vortex, and the vortex was seen to be long-lived. When a background magnetic field was included, three cases were observed: the case where MHD effects are truly weak, the evolution being essentially hydrodynamic, with the field lines advected passively and eventually reaching a flux expelled regime; the mildly disruptive case, where the vortical motion stretched field lines, releasing stresses, but the vortex survives this disruption, retains its integrity, and a flux expelled regime was also reached; the severely disruptive case, where the MHD feedback was sufficiently strong, disrupting the vortex significantly, a flux expelled regime is not reached, and the resulting dominant features in the domain are vorticity filaments rather than a coherent vortex. The degree of disruption was seen to become more severe on increasing Rm and/or M (assuming that we are still in the nonlinearly unstable regime). It was also seen that the increase of the shear layer width was correlated with the degree of disruption.

With regards to the disruption mechanism, vortical motion winds up magnetic field lines, stretching out a thin current sheet and building up magnetic stresses. This build up is arrested when the current sheet becomes sufficiently thin and breaks (probably due to a resistive instability). This releases the magnetic stress that feeds back onto the flow, potentially causing disruption. With this in mind, we provided an estimate for the degree of observed disruption using a kinematic, dimensional argument. The resulting estimate, $M^2\mathrm{Rm} \sim \Omega_e$, was tested against the numerical data over M and Rm space, with the degree of disruption measured by a spectral truncation wavenumber (maximised over the run) and a shear layer width expansion factor (taken at end of the run). It was seen that, for the shear layer case, $M^2\mathrm{Rm} \geq 0.5$ appears to capture all of the severely disruptive runs, but, more importantly, the degree of disruption exhibited by the data conformed well to the parameter combination $M^2\mathrm{Rm}$.

For the Bickley jet, we focussed on the case where the domain supports two wavelengths of the

most unstable mode. In the hydrodynamic case, it was seen that the jets undergoes a kinking motion before breaking up into vortices, which then subsequently pair up. In the MHD case, either the vortices survive the disruption event, and the evolution proceeds as in the hydrodynamic case, or the vortices are completely disrupted, and vorticity bands form instead. The disruption was observed to be less violent than for the shear layer, in that there appears to be only one significant disruption event, rather than a continued cascade of disruptions. This was attributed to the fact that, in the shear layer, the resulting motion can further tap into the background flow energy away from $y = 0$ for trigger more disruption events, whilst this is not the case for the jet profile as the flow is largely supported around $y = 0$. It was observed from profiles of $\overline{u}$ that the peak value of $\overline{u}$, rather than the jet width or the spectral truncation wavenumber, was better correlated with the disruption observed. Since the physical mechanism leading to disruption is similar to the shear layer case, we also tested the $M^2\text{Rm} \sim \Omega_e$ estimate against the data. It was seen that $M^2\text{Rm} \geq 0.1$ appears to capture all the disruptive runs, and, furthermore, the dependence on the combination $M^2\text{Rm}$ was seen in the regime diagram.

For completeness, we have also performed some runs with larger M, where it appears that we have nonlinear stability, with no rolling up of the shear layer or breaking up of the jet. Our estimate for disruption then requires that we do in fact have vortices forming. The transition location between the disruptive and nonlinearly stable regime has not been investigated here.

Generally, disruption is a fast process, typically occurring in no more than an eddy turnover time. For the shear layer, disruption occurs before a flux expelled regime is reached, and for the jet, disruption can occur before there is any pairing between the vortices. Our estimate, stemming from a particularly simple kinematic and dimensional argument, also highlights that some care is needed when the term 'weak field' is used; in our shear flow problem using our estimate, it is M and Rm in the combination $M^2\text{Rm} \ll 1$ that results in an evolution that is essentially unmodified by MHD effects. The fact that disruption by MHD effects is fast and depends on $M^2\text{Rm}$ indicates that this phenomenon will be a robust feature in the nonlinear development of shear flows in astrophysical systems, since Rm is typically very large. This disruption mechanism from MHD effects also provides another route for transition to turbulence without resorting to other hydrodynamic instabilities that require, for example, stratification effects, and so can operate even in strongly stratified systems where the fluid motion is predominantly horizontal and secondary hydrodynamic instabilities may be weak. This potentially has impact on, for example, mixing

properties in such electrically conducting fluid systems, something that we have not investigated here.

We now discuss some other points relating to the disruption mechanism that were mentioned in the main body of the text.

6.7.1 Dependence on viscosity

All the numerical results presented here were for both the shear layer and the Bickley jet were performed at Re $= 500$, and one might wonder about the effects of increasing Re. We have also conducted some test runs at Re $= 750$ and 1000; one comparison for the shear layer is given in Figure 6.28, where we plot side by side some quantities obtained from the simulations. There are some differences, and it is certainly true that the runs at larger Re appear to result in a more severe disruption, with more vorticity filaments appearing. Since we are restricted here in computing resources, we are unable to probe the parameter region at higher Re, although we do observe that larger Re increases the life-time of the vorticity filaments formed from the shredding of the vortex. We also suspect that, in other systems where other secondary hydrodynamic instabilities operate (e.g., Mashayek & Peltier, 2012a,b), the increase in Re will also lead to a stronger disruption of the vortices formed, except in this case the disruption is due to a combination of both hydrodynamic and resistive secondary instabilities. Larger simulations (or ones employing a different formalism; Dritschel & Tobias 2012) would allow for an investigation of the dynamical dependence on increasing Re and also Rm.

6.7.2 Arresting mechanism: tearing instabilities?

The cause of the major reconnection event in the shear layer runs has largely been attributed to tearing instabilities by previous investigations (e.g., Jones *et al.*, 1997; Keppens *et al.*, 1999; Baty *et al.*, 2003), although we suspect a similar mechanism is at play for the jet runs. In particular, these authors observe in their simulations the appearance of structures that are consistent with the onset of tearing instabilities, such as magnetic islands and chains of plasmoids (e.g., Figure 11 of Keppens *et al.* 1999; Figure 15 of Baty *et al.* 2003). Tearing-type instabilities are generally the most unstable in such a current sheet setting (§4 of Biskamp 2000; §6 of Priest & Forbes 2000). However, we also observe current sheet pinching before current sheet break up in regions centred

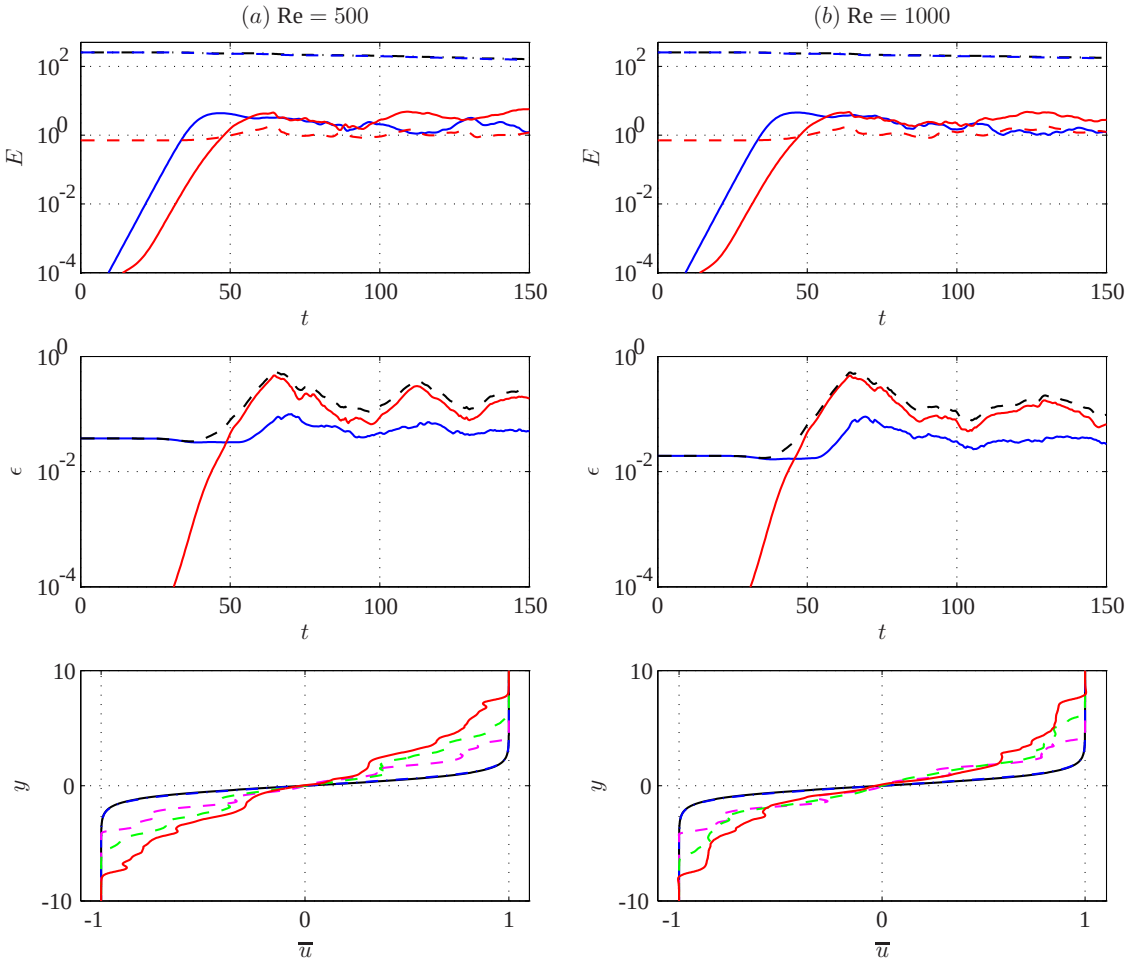

Figure 6.28: Comparison between two shear layer runs at $M = 0.05$, Rm $= 1000$ at two different values of Re. Displayed are the energy time-series (blue = kinetic; red = magnetic), dissipation rates (blue = viscous; red = Ohmic) and snapshots of $\overline{u}$.

around the stagnation point; Figure 6.29 shows snapshots of the current in a higher resolution run, Re $=$ Rm $= 500$ but at 512×1024, with $M = 0.05$, centred around the stagnation point. This pinching is presumably due to the combined effect of the inflow pushing the current sheets together, and the instability causing the sheet to pinch. It would be beneficial if we could separate the effect due to the background flow, and provide more evidence for us to conclude the exact type of resistive instability causing the major reconnection event.

In the time-series of energies shown in Figure 6.15, after the initial peak of perturbation kinetic energy, the perturbation magnetic energy continues to grow a little. One might be convinced that the perturbation magnetic energy grows at a smaller rate purely by observation of the relevant

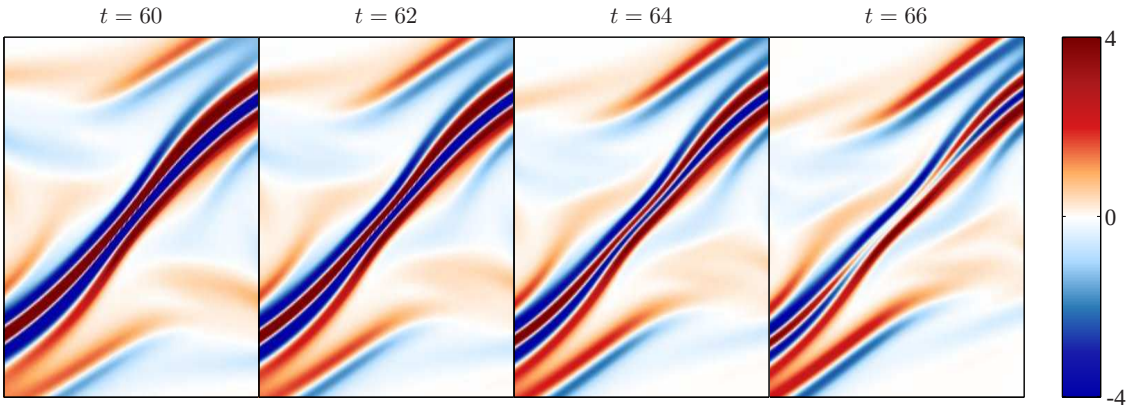

Figure 6.29: Snapshots of current for the shear layer run (at Rm $=$ Re $= 500$, $M = 0.05$), in a small box centred around the stagnation point. A pinching of the current sheet is observed.

figures. If we suppose that might be the case, we could try and infer a growth rate for the tearing instability via a fitting of the available data; using data between $t = 50$ and $t = 55$ for the shear layer runs (just before the first peak in the perturbation magnetic energy in Figure 6.15), a growth rate was inferred for some sample cases at several values of M and Rm. The peak field strength and the length scales of current layers are obtained from the raw data at $t = 50$, and from this a Lundquist number

$$\mathrm{Lu} = \frac{\tau_R}{\tau_A}, \qquad \tau_A = \frac{\ell}{v_A}, \qquad \tau_R = \frac{\ell^2}{\eta} \tag{6.56}$$

was inferred. Here, τ_A is an Alfvén transit time, and τ_R is a resistive time. We know that, classically, the tearing mode with no background flow has a growth rate σ that scales like $\sigma \sim \mathrm{Lu}^{-3/5}$ (Furth *et al.*, 1963). Comparing the inferred growth rates to the theory, the difference between the values is around a factor of 2. This may seem promising; however, we should bear in mind that: (i) we have a background flow and the value of viscosity was not taken into account; (ii) a fitting of 5 time units is probably too small to be meaningful; (iii) the instability, if it really is a tearing-type instability, results from the nonlinear evolution of a shear flow instability with a constantly evolving basic state, and a linear phase may not be well-defined; (iv) it may be a double tearing mode.

We also tried to detect the growth rate of the tearing mode by analysing data taken from a small box around key features of the instabilities . We have tried several locations (centred on the stagnation point, centred on the eye-lid of the vortex formed, centred on the leading braid-region of the vortex formed); however, nothing particularly conclusive resulted from this approach.

We also carried out simulations for the nonlinear evolution of tearing modes with a background flow, as in, for example, Ofman *et al.* (1993), Chen *et al.* (1997), Otto & Fairfield (2000). Both single current layers (e.g., $B_0(y) = \tanh(y)$) and double current layers (e.g., $B_0(y) = \text{sech}^2(y)$) have been tried with and without a background shear layer flow at different shear layer widths. The code manages to reproduce what has been documented previously but does not seem to give any extra information that is relevant to our case here. In particular, we never observe the violent evolution associated with the shear layer profile that is reported here, for several values of Re ranging from 500 to 1000.

Knowing exactly what the arresting mechanism is would complete the dynamical picture concerning disruption induced by vortical motion, as well as provide some explicit suggestions to the parameter dependence we might want to look out for in the regime estimations. It certainly seems plausible that the tearing-type instability acts as the arresting mechanism, but we can not be sure about this until there is more evidence available. We conjecture that it is probably a tearing mode supplemented by the straining experienced by the braid-region/current-layer centred around the stagnation point that ultimately leads to the current layer break up. The interplay between these two mechanisms however is not clear. There are techniques to investigate this but we have not looked at this in much detail.

6.7.3 Validating and improving on the disruption estimate

Supposing for the moment that the dependence of disruption on Re is weak, one interesting and fairly straight forward thing to do would be to see how far the kinematic regime estimation $M^2\text{Rm} \sim \Omega_e$ extends into (M, Rm) space. This would simply involve running larger simulations at higher Rm, possibly using the $M^2\text{Rm} \sim \Omega_e$ estimate as a guide for where to look in parameter space. This may also help clarify the resistive instability point made previously, giving us more evidence towards pinning down the exact type of resistive instability causing the disruption.

One possible and more involved investigation would be to go beyond a kinematic argument and obtain an estimate that takes into account the dynamic feedback. This has been done in the magneto-convection setting by Galloway *et al.* (1978) and Galloway & Moore (1979) via a matched asymptotic technique. It would be interesting to extend those arguments to this perhaps simpler case, since we do not have thermal driving. Perhaps an even simpler case would be to revisit the problem of Weiss (1966), with a vortex in a two-dimensional doubly periodic box and

a uniform background magnetic field, but taking into account the dynamical feedback. Some test simulations we have carried out shows similar disruptive behaviour as those observed here, but we have not studied the parameter dependence in nearly as much detail[1].

[1](At time of final correction) Dritschel & Tobias (private communication) have also reported similar results for the vortex-in-a-box problem.

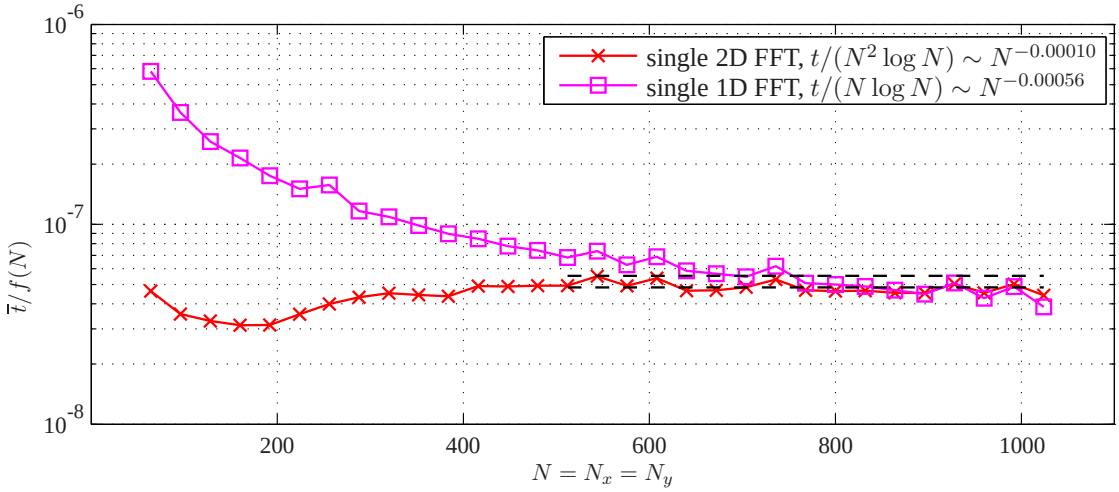

Figure 6.30: Computation time scaling for the FFT commands, averaged over 100 calculations. The computed times for the relevant routines are divided by the theoretical scalings, so the data should fit to a constant function.

6.8 Appendix A: Differentiation and quadrature routines in Fourier–Chebyshev spectral space

6.8.1 Fast Fourier Transform (FFT)

For transforming between physical and spectral space we use the `fft` command native to MATLAB, which is based on the FFTW library. This was adapted as a custom routine here, which has the option for transforming our data between physical space, Chebyshev–Fourier space and intermediate cases. It is well known that a single FFT for an array of length N requires $O(N \log N)$ operations. For our tests, we calculate the computation timings and, from that, infer scalings of these timings with increasing N. Some large number of runs were carried out and the computation time was averaged over the number of runs to give a $\overline{t}$. This is done at increasing values of N to give some $\overline{t}(N) \sim f(N)$. We plot $\overline{t}/f(N)$ in Figure 6.30, where the averaging was done over 100 calculations.

We see then the one-dimensional FFT for transforming from physical to physical-Fourier or physical–Chebyshev space scales like $O(N \log N)$, and the two-dimensional FFT transforming from physical to Chebyshev–Fourier space scales like $O(N^2 \log N)$. Some irregularities are seen, and this may be due to the fact that FFT is a bit faster when N contains many factors of 2.

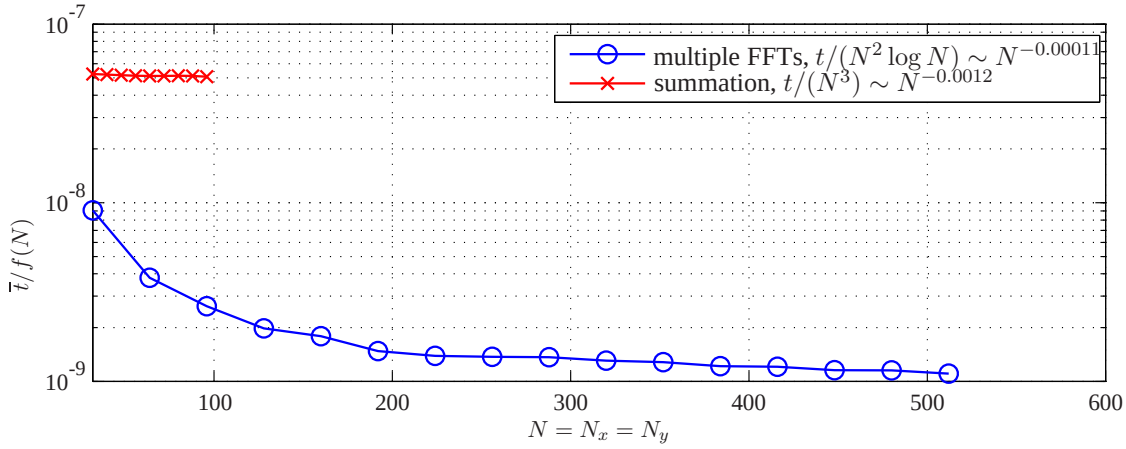

Figure 6.31: Computation time scaling for the commands to evaluate the integrals of quadratic quantities, averaged over 20 calculations. The computed times for the relevant routines have been divided by the theoretical scalings, so the data should fit to a constant function.

6.8.2 Integration of quadratic quantities

As discussed in Section 6.2, we can evaluate in spectral space the integrals of quadratic quantities by summing coefficients in Fourier–Chebyshev spectral space. This is expected to be slow as the summation has to be done individually. Instead, we consider doing the integral as follows:

1. Transform from full spectral space to x-spectral and y-physical space, $f(\hat{x}, \hat{y}) \to f(\hat{x}, y)$;

2. Perform an x-integration using the standard Parseval's theorem, so $f(\hat{x}, y) \to \int f^2(y)\,\mathrm{d}x$;

3. Perform a transform in y and do spectral integration using the Clenshaw–Curtis quadrature, so $\int f^2\,\mathrm{d}x \to \iint f^2\,\mathrm{d}x\mathrm{d}y$.

Two extra FFTs are required but otherwise the relevant computations are fast as they take advantage of vectorisation. The methods are compared and plots analogous to that in the previous section is given as Figure 6.31, averaged at each N over 20 calculations. The summation method was only carried out for small N as the computation time became prohibitively large. Both computation methods maintain spectral accuracy but it is clear that the method utilising extra FFTs is faster and has a better asymptotic scaling.

6.8.3 Quasi-TriDiagonal Solver (QTS)

The fast Helmholtz solver we use is due to Thual (1986); see Appendix B of Peyret (2002) and §4.1 of Canuto *et al.* (1993). Using the inversion step $\nabla^2\psi = \omega$ as an example, we note that in our case the linear system takes the following form in spectral space:

$$\begin{pmatrix} \cdots & \mathsf{D}_2 - k^2\mathsf{I} & \cdots \\ \cdots & b^+ & \cdots \\ \cdots & b^- & \cdots \end{pmatrix} \hat{\psi} = \begin{pmatrix} \hat{\omega} \\ g^+ \\ g^- \end{pmatrix}, \tag{6.57}$$

where $b^\pm$ and $g^\pm$ are the vectors and scalars for enforcing the boundary conditions. Now, there is a recurrence relationship between the second derivative and the zero derivative Chebyshev coefficients, given by

$$P_j\hat{u}^{(2)}_{j-2} + Q_j\hat{u}^{(2)}_j + R_j\hat{u}^{(2)}_{j+2} = \hat{u}_j, \qquad j = 2, 3\cdots N_y, \tag{6.58a}$$

with

$$P_j = \frac{c_{j-2}}{4j(j-1)}, \qquad Q_j = \frac{-e_{j+2}}{2(j^2-1)}, \qquad R_j = \frac{e_{j+4}}{4j(j+1)}, \tag{6.58b}$$

where c_j and e_j are given by

$$c_j = \begin{cases} 2, & j = 0, \\ 1, & \text{otherwise}, \end{cases} \qquad e_j = \begin{cases} 1, & j \le N_y, \\ 0 & j > N_y. \end{cases} \tag{6.58c}$$

We then observe that (6.57) may be written as

$$\begin{aligned} \hat{\psi}^{(2)}_k - k^2\hat{\psi}_k &= \hat{\omega}_k, \qquad k = 0, 1, \cdots N_y - 2, \\ \sum_k b^+_k &= g^+, \\ \sum_k b^-_k &= g^-, \end{aligned} \tag{6.59}$$

so eliminating accordingly, it may be seen that the system given by (6.57) takes the alternative form

$$P'_j\hat{\psi}_{j-2} + Q'_j\hat{\psi}_j + R'_j\hat{\psi}_{j+2} = f_j, \qquad j = 2, \ldots, N_y, \tag{6.60a}$$

where

$$P'_j = k^2P_j, \qquad Q'_j = -k^2Q_j - 1, \qquad R'_j = k^2R_j, \tag{6.60b}$$

and

$$f_j = -(P_j\hat{\omega}_{j-2} + Q_j\hat{\omega}_j + R_j\hat{\omega}_{j+2}). \tag{6.60c}$$

Notice that there are no primes on P, Q and R in the definition of f. The system decouples, and the even and odd coefficients may be solved separately. The resulting decoupled system is of the form

$$\begin{pmatrix} b_0 & b_2 & \cdots & \cdots & \cdots & b_{N_y} \\ P_2' & Q_2' & R_2' & & & \\ & P_4' & Q_4' & R_4' & & \\ & & \ddots & \ddots & \ddots & \\ & & & P'_{N_y-2} & Q'_{N_y-2} & R'_{N_y-2} \\ & & & & P'_{N_y} & Q'_{N_y} \end{pmatrix} \begin{pmatrix} \hat{\psi}_0 \\ \hat{\psi}_2 \\ \hat{\psi}_4 \\ \vdots \\ \vdots \\ \hat{\psi}_{N_y} \end{pmatrix} = \begin{pmatrix} g \\ f_2 \\ f_4 \\ \vdots \\ \vdots \\ f_{N_y} \end{pmatrix} \tag{6.61}$$

where b and g denotes the boundary condition vector and the boundary value appropriately modified, and similarly for the odd coefficients; this system is of quasi-tridiagonal form (a tridiagonal system with one extra row). An analogue of the Thomas algorithm for the tridiagonal system is given as follows:

1. Let I be the length of $b_{\text{even/odd}}$. Define $p = P'_{\text{even/odd}}$, and analogously for Q, R, and f. Let $\hat{\psi} = \hat{\psi}_{\text{even/odd}}$, so we solve for $\hat{\psi}$ and then extract the relevant information to get $\hat{\psi}_{\text{even/odd}}$.

2. Construct

$$X_{I-1} = -\frac{p_I}{q_I}, \qquad Y_{I-1} = \frac{f_I}{q_I}, \tag{6.62}$$

$$X_{i-1} = \frac{-p_i}{q_i + r_i X_i}, \qquad Y_{i-1} = \frac{f_i - r_i Y_i}{q_i + r_i X_i}, \qquad i = I-1, \ldots, 1. \tag{6.63}$$

3. Construct

$$\theta_i = X_{i-1}\theta_{i-1}, \qquad \lambda_i = X_{i-1}\lambda_{i-1} + Y_{i-1}, \qquad i = 1, \ldots, I, \tag{6.64}$$

with $\theta_0 = 1$, $\lambda_0 = 0$.

4. Evaluate

$$\hat{\psi}_0 = \frac{g_{\text{even/odd}} - \Lambda}{\Theta}, \qquad \Theta = \sum_i b_i\theta_i, \qquad \Lambda = \sum_i b_i\lambda_i. \tag{6.65}$$

From this, compute

$$\hat{\psi}_i = X_{i-1}\psi_i + Y_i, \qquad i = 0, \ldots, I-1, \tag{6.66}$$

and extract the data accordingly.

For the inversion problem $\nabla^2\psi = \omega$, we impose the $\psi = 0$ condition, so

$$b_{\text{even}} = \begin{pmatrix} 1 & 1 & \cdots 1 \end{pmatrix}, \qquad g_{\text{even}} = \frac{g_+ + g_-}{2} = 0,$$
$$b_{\text{odd}} = \begin{pmatrix} 1 & 1 & \cdots 1 \end{pmatrix}, \qquad g_{\text{odd}} = \frac{g_+ - g_-}{2} = 0.$$

This algorithm is stable if the system satisfies a diagonally dominant condition given by

$$|q_i| \begin{cases} \geq |p_i| + |r_i| & \text{if} \quad r_i \neq 0, \\ > |p_i| + |r_i| & \text{if} \quad r_i = 0. \end{cases} \tag{6.67}$$

This method may be used if Dirichlet or Neumann boundary conditions are used on both boundaries, but needs to be modified if mixed boundary conditions are used. If the boundary conditions are inhomogeneous and when the domain is not on $[-1, 1]$, extra prefactors will appear in $g_{\text{even/odd}}$.

As for the Thomas algorithm, the number of operations required is $O(N)$, which is substantially smaller than using `LU`$-$decomposition and a back-substitution, which typically requires $O(N^3)$ operations. In Figure 6.32 we plot the computation time for a representative problem (solving for the inversion step of the vorticity for the streamfunction at the first time-step), averaged over 20 calculations, required by the QTS routine as compared to other native commands in MATLAB, namely (i) `linsolve` with no options invoked (denoted as Linsolve in Figure 6.32), and (ii) `lu` followed by `linsolve` with options for solving strictly upper- and lower-triangular systems (denoted as LU in the Figure Figure 6.32). The numerical differences between the computed solutions are of $O(10^{-8})$; however, it is seen that the actual computation time and the suggested asymptotic behaviour of the scaling of the QTS routine compares favourably to `linsolve` and `lu` commands in MATLAB.

6.9 Appendix B: Derivation of AB/BD3

We first derive the BDk algorithms. We discretise $\partial u^{n+1}/\partial t$ by a backward difference formula, knowing the data at three levels before. Chapter 3 of Fornberg (1998) provides the formula for finding the appropriate weights for an arbitrary spaced stencil, essentially rearranging the appropriate Lagrange polynomial and tracing its coefficients. We have

$$F_{ij}(x) = \sum_{k=0}^{i} \frac{c_{ij}^k}{k!} x^k, \qquad f^{(k)}(x) = c_{i0} f(x_0) + \Delta t_c c_{i1} f(x_1) + \cdots, \tag{6.68}$$

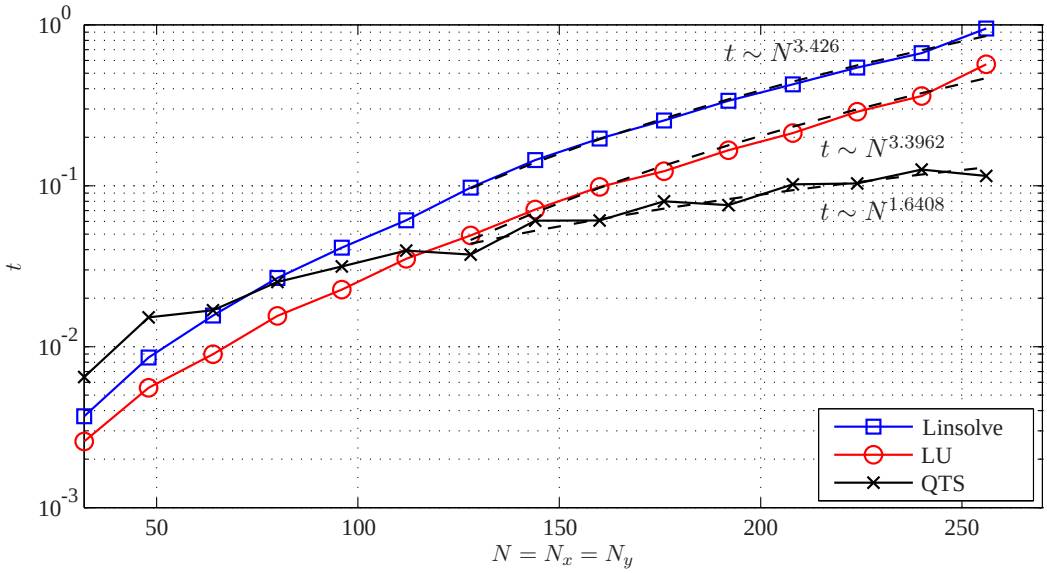

Figure 6.32: Computation time scalings for the linear system solver routines, averaged over 20 calculations.

where k is the derivative required and F_{ij} is the Lagrange polynomial given by

$$F_{ij} = \frac{(x - x_0)\cdots(x - x_{j-1})(x - x_{j+1})\cdots(x - x_i)}{(x_j - x_0)\cdots(x_j - x_{j-1})(x_j - x_{j+1})\cdots(x_j - x_i)}. \tag{6.69}$$

For our case, $k = 3$, and we seek $(c^1_{3,0}, c^1_{3,1}, c^1_{3,2}, c^1_{3,3})$ with

$$(x_0, x_1, x_2, x_3) = (0, -\Delta t_c, -\Delta t_c - \Delta t_{p1}, -\Delta t_c - \Delta t_{p1} - \Delta t_{p2}), \tag{6.70}$$

where Δt with subscripts are defined in Section 6.3.

The Lagrange polynomials are respectively

$$F_{30} = \frac{(x + \Delta t_c)(x + \Delta t_c + \Delta t_{p1})(x + \Delta t_c + \Delta t_{p1} + \Delta t_{p2})}{\Delta t_c(\Delta t_c + \Delta t_{p1})(\Delta t_c + \Delta t_{p1} + \Delta t_{p2})}, \tag{6.71a}$$

$$F_{31} = \frac{x(x + \Delta t_c + \Delta t_{p1})(x + \Delta t_c + \Delta t_{p1} + \Delta t_{p2})}{-\Delta t_c \Delta t_{p1}(\Delta t_{p1} + \Delta t_{p2})}, \tag{6.71b}$$

$$F_{32} = \frac{x(x + \Delta t_c)(x + \Delta t_c + \Delta t_{p1} + \Delta t_{p2})}{-(\Delta t_{p1} + \Delta t_{p2})(-\Delta t_{p1})\Delta t_{p2}}, \tag{6.71c}$$

$$F_{33} = \frac{x(x + \Delta t_c)(x + \Delta t_c + \Delta t_{p1})}{-(\Delta t_c + \Delta t_{p1} + \Delta t_{p2})(-\Delta t_{p1} - \Delta t_{p2})(-\Delta t_{p2})}. \tag{6.71d}$$

The coefficient of x^1 gives

$$\frac{\partial u}{\partial t} \approx \frac{a_0 u^{n+1} + a_1 u^n + a_2 u^{n-1} + a_3 u^{n-2}}{\Delta t_c}, \tag{6.72}$$

with the coefficients a_i given by (6.38).

It then remains to turn this into a AB/BDk scheme by approximating the $f(u^{n+1})$ term by known data. We observe that

$$f(u^{n+1}) = f(u^n) + \Delta t_c f'(u^n) + \frac{(\Delta t_c)^2}{2} f''(u^n) + \cdots, \tag{6.73}$$

so we consider approximating the derivative terms using a one sided difference that is third order accurate. Using the same formula, we seek $(c^1_{2,0}, c^1_{2,1}, c^1_{2,2})$ and $(c^2_{2,0}, c^2_{2,1}, c^2_{2,2})$ with

$$(x_0, x_1, x_2) = (0, -\Delta t_{p1}, -\Delta t_{p1} - \Delta t_{p2}), \tag{6.74}$$

and we obtain

$$F_{20} = \frac{(x + \Delta t_{p1})(x + \Delta t_{p1} + \Delta t_{p2})}{\Delta t_{p1}(\Delta t_{p1} + \Delta t_{p2})}, \tag{6.75a}$$

$$F_{21} = \frac{x(x + \Delta t_{p1} + \Delta t_{p2})}{-\Delta t_{p1}\Delta t_{p2}}, \tag{6.75b}$$

$$F_{22} = \frac{(x + \Delta t_{p1})x}{-\Delta t_{p1}(-\Delta t_{p1} - \Delta t_{p2})}. \tag{6.75c}$$

This gives

$$\Delta t_c c^1_{20} = \frac{2r_c + r_p}{r_c(r_c + r_p)}, \qquad \Delta t_c c^1_{21} = -\frac{(r_c + r_p)}{r_c r_p}, \qquad \Delta t_c c^1_{22} = \frac{r_c}{r_p(r_c + r_p)}, \tag{6.76}$$

and

$$\frac{(\Delta t_c)^2}{2} c^2_{20} = \frac{1}{r_c(r_c + r_p)}, \qquad \frac{(\Delta t_c)^2}{2} c^2_{21} = -\frac{1}{r_c r_p}, \qquad \frac{(\Delta t_c)^2}{2} c^2_{22} = \frac{1}{r_p(r_c + r_p)}, \tag{6.77}$$

which in turn gives us

$$\begin{aligned} f(u^{n+1}) \approx & f(u^n) + \Delta t_c f'(u^n) + \frac{(\Delta t_c)^2}{2} f''(u^n) \\ = & f(u^n) + \Delta t_c (c^1_{20} f(u^n) + c^1_{21} f(u^{n-1}) + c^1_{22} f(u^{n-2})) \\ & + \frac{(\Delta t_c)^2}{2} (c^2_{20} f(u^n) + c^2_{21} f(u^{n-1}) + c^2_{22} f(u^{n-2})) \\ = & b_0 f(u^n) + b_1 f(u^{n-1}) + b_2 f(u^{n-2}), \end{aligned} \tag{6.78}$$

with coefficients given by (6.38). When the step size is constant, these reduce to known formulas (e.g., Peyret, 2002, §4).

To test the time-marching algorithm and the semi-implicit treatment, we use the example given in §4.5 of Peyret (2002), a one-dimensional advection-diffusion problem with forcing where the exact solution is known, and test the AB/BD3 algorithm with $\mathsf{L} = \partial^2/\partial y^2$ in (6.38) against AB/BD2

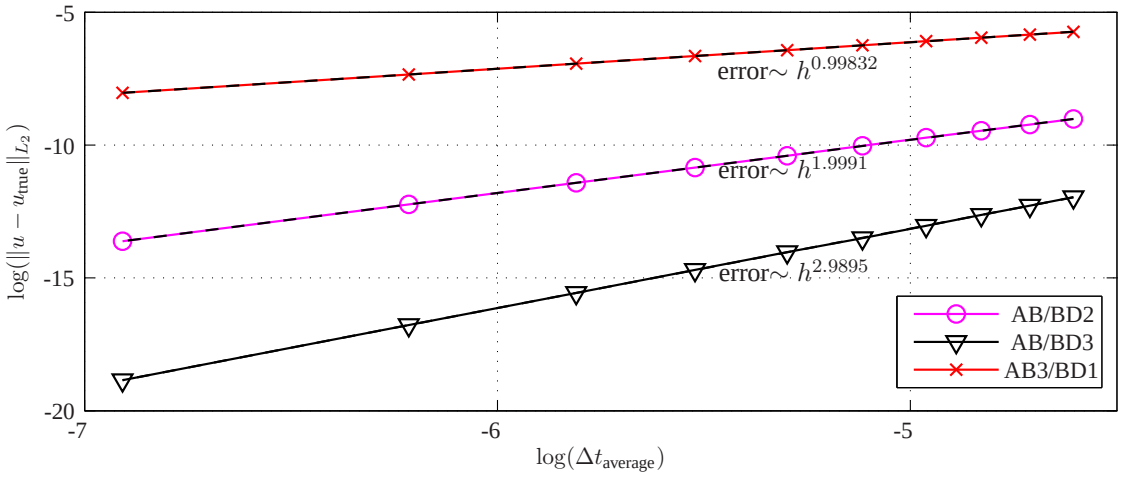

Figure 6.33: (Discrete) L_2 error at the final time of the semi-implicit schemes given by the variable versions of AB/BD2, AB/BD3, and AB3/BD1.

and AB3/BD1 with L similarly treated. To generate the time grid, we specify a step size mean and randomly generate spacings that have Gaussian distribution with small variance (typically around a quarter of the mean); the grid is different at each $\overline{t}$, but all three methods use the same randomly generated grid at the same $\overline{t}$. The results are shown in Figure 6.33, plotted against a measure of the error with mean time-step size. The theoretical decrease in error with decrease in mean-step size is confirmed by the numerical results.

Chapter 7

Nonlinear evolution: shallow-water MHD

Following on from the investigation with $F = 0$ in the previous chapter, we now study the nonlinear evolution of the shear layer and the jet profiles in the SWMHD system where $F > 0$. There are some difficulties with regards to the numerical implementation in the shallow-water case, and we address these first before presenting the results from the simulations. Our focus here is on the $F < 1$ case, and the associated non-zero Froude number modification to the processes highlighted in the previous chapter. Some details with regards to the $F > 1$ cases are given towards the end of the chapter.

7.1 Numerical and mathematical formulation of SWMHD

7.1.1 The choice of dissipation and conservation problems

The SWMHD equations were derived in the ideal setting, but since we expect small-scale features to appear as part of the nonlinear evolution, some sort of diffusion will be required to stabilise the routines. The problem of the form of dissipation to take in the hydrodynamic shallow-water equations has been previously discussed (e.g., Gent, 1993; Ochoa *et al.*, 2011; Gilbert *et al.*, 2013). As an illustrative example, suppose we consider a SWMHD system with dissipation that looks

similar to the incompressible MHD equations given in (6.1), given by

$$\frac{\partial \boldsymbol{u}}{\partial t} + \boldsymbol{u}\cdot\nabla\boldsymbol{u} - M^2\boldsymbol{b}\cdot\nabla\boldsymbol{b} + \nabla h = \frac{1}{\mathrm{Re}}\nabla^2\boldsymbol{u}, \tag{7.1a}$$

$$\frac{\partial \boldsymbol{b}}{\partial t} + \boldsymbol{u}\cdot\nabla\boldsymbol{b} - \boldsymbol{b}\cdot\nabla\boldsymbol{u} = \frac{1}{\mathrm{Rm}}\nabla^2\boldsymbol{b}, \tag{7.1b}$$

$$F^2\frac{\partial h}{\partial t} + \nabla\cdot[(1+F^2h)\boldsymbol{u}] = \frac{F^2}{\mathrm{R}}\nabla^2 h, \tag{7.1c}$$

$$\nabla\cdot[(1+F^2h)\boldsymbol{b}] = 0. \tag{7.1d}$$

Here, R denotes an associated dissipation on h (not necessarily physical). For numerical purposes, there is no reason why we cannot take this form of dissipation; it turns out though that there are physical reasons why the choice of dissipation in (7.1) is a particularly bad one. Regardless of this, there is a fundamental issue that does need to be addressed, and that is the self-consistency of the derivation of the SWMHD equations when finite magnetic dissipation is present. The derivation leading to the SWMHD system assumes there is no magnetic dissipation, and so the free surface is initially and remains a field line. In the ideal case, this is justified, leading to the modified divergence-free condition of the magnetic field, but this is no longer necessarily true when finite magnetic dissipation is present. How do we reconcile this?

For the moment, we argue that for short-time phenomena at large Rm, the frozen-in condition is a reasonable assumption. We then need to be careful with maintaining the equivalent divergence-free condition as well as the conservation laws. As we have noted already in Chapter 2, the equivalent divergence-free condition is absolutely required for the absence of extra sources in the conserved quantities. This frozen-in assumption may be plausible for phenomena on dynamic time-scales, such as shear flow instabilities, but is most certainly not valid for phenomena on dissipative time-scales that occur in, for example, turbulence or dynamo studies. A justification into this fundamental problem of self-consistency must be addressed if the SWMHD equations are to be used for such studies. We revisit this point in the discussion section later.

Suppose we use formulation (7.1). We now show what else can go wrong in terms of conservation laws. In Chapter 2 we already demonstrated the various conservation properties of the ideal SWMHD system (on the left hand side of 7.1), so here we focus on the modifications of the conservation properties resulting from the dissipation terms on the right hand side of (7.1).

Mass conservation

$$\frac{\mathrm{d}}{\mathrm{d}t}\iint h_t \,\mathrm{d}x\mathrm{d}y = \frac{F^2}{\mathrm{R}}\iint \left(\frac{\partial^2}{\partial x^2}+\frac{\partial^2}{\partial y^2}\right) h \,\mathrm{d}x\mathrm{d}y. \tag{7.2}$$

If we have periodicity in x, then we need $F^2\mathrm{R}^{-1}=0$ or $\partial h/\partial y = 0$ on the boundaries for mass conservation.

Momentum conservation violation

Assuming that the divergence-free condition is satisfied for all time, the x-momentum evolution is given by

$$\begin{aligned}\frac{\mathrm{d}}{\mathrm{d}t}\iint h_t u \,\mathrm{d}x\mathrm{d}y &= \iint \left(\frac{1}{\mathrm{Re}}h_t\nabla^2 u + \frac{F^2}{\mathrm{R}}u\nabla^2 h\right)\,\mathrm{d}x\mathrm{d}y \\ &= -F^2\left(\frac{1}{\mathrm{Re}}+\frac{1}{\mathrm{R}}\right)\iint \nabla h_t\cdot\nabla u \,\mathrm{d}x\mathrm{d}y,\end{aligned} \tag{7.3}$$

where we use periodicity in x, $v=0$, $b_y=0$ and additionally $\partial u/\partial y = 0$ as y-boundary conditions. So there is no momentum conservation since the extra terms are not generically zero. Similarly, for the y-momentum equation,

$$\begin{aligned}\frac{\mathrm{d}}{\mathrm{d}t}\iint h_t v \,\mathrm{d}x\mathrm{d}y &= \iint \left(\frac{1}{\mathrm{Re}}h_t\nabla^2 v + \frac{F^2}{\mathrm{R}}v\nabla^2 h\right)\,\mathrm{d}x\mathrm{d}y \\ &= -F^2\left(\frac{1}{\mathrm{Re}}+\frac{1}{\mathrm{R}}\right)\iint \nabla h\cdot\nabla v \,\mathrm{d}x\mathrm{d}y - \int\left[F^2\frac{h^2}{2}+h\right]_{y=-L_y}^{y=L_y}\mathrm{d}x,\end{aligned} \tag{7.4}$$

and we encounter a similar problem.

Flux conservation violation

In addition to problems with momentum conservation, there is also a problem with magnetic flux conservation. Again, assuming the divergence-free condition holds,

$$\begin{aligned}\frac{\mathrm{d}}{\mathrm{d}t}\iint h_t b_x \,\mathrm{d}x\mathrm{d}y &= \iint \left(\frac{1}{\mathrm{Rm}}h_t\nabla^2 b_x + \frac{F^2}{\mathrm{R}}b_x\nabla^2 h\right)\,\mathrm{d}x\mathrm{d}y \\ &= -F^2\left(\frac{1}{\mathrm{Rm}}+\frac{1}{\mathrm{R}}\right)\iint \nabla h\cdot\nabla b_x \,\mathrm{d}x\mathrm{d}y,\end{aligned} \tag{7.5}$$

where periodicity in x, $v=0$, $b_y=0$ and additionally $\partial b_x/\partial y = 0$ as y-boundary conditions have been used. Observe also that

$$\begin{aligned}\frac{\mathrm{d}}{\mathrm{d}t}\iint h_t b_y \,\mathrm{d}x\mathrm{d}y &= \iint \left(\frac{1}{\mathrm{Rm}}h_t\nabla^2 b_y + \frac{F^2}{\mathrm{R}}b_y\nabla^2 h\right)\,\mathrm{d}x\mathrm{d}y \\ &= -F^2\left(\frac{1}{\mathrm{Rm}}+\frac{1}{\mathrm{R}}\right)\iint \nabla h\cdot\nabla b_y \,\mathrm{d}x\mathrm{d}y,\end{aligned} \tag{7.6}$$

so again there are extra contributions to global magnetic flux from extra terms.

Total energy conservation in velocity variables

Constructing the energy budget as before, we see that

$$\begin{aligned}
&\frac{1}{2}\frac{\mathrm{d}}{\mathrm{d}t}\iint \left[h_t(|\boldsymbol{u}|^2 + M^2|\boldsymbol{b}|^2) + F^2h^2\right]\,\mathrm{d}x\mathrm{d}y \\
&\quad= \iint \left[\frac{1}{\mathrm{Re}}(h_t\boldsymbol{u})\cdot\nabla^2\boldsymbol{u} + \frac{M^2}{\mathrm{Rm}}(h_t\boldsymbol{b})\cdot\nabla^2\boldsymbol{b} + \frac{F^2}{\mathrm{R}}\left(\frac{|\boldsymbol{u}|^2 + M^2|\boldsymbol{b}|^2}{2}\nabla^2 h\right) + h\frac{F^2}{\mathrm{R}}\nabla^2 h\right]\,\mathrm{d}x\mathrm{d}y \\
&\quad= -\iint h_t\left\{\left[\frac{1}{\mathrm{Re}}\left(\frac{\partial u_j}{\partial x_i}\right)^2 + \frac{M^2}{\mathrm{Rm}}\left(\frac{\partial b_j}{\partial x_i}\right)^2\right] + \frac{F^2}{\mathrm{R}}\left(\frac{\partial h}{\partial x_i}\right)^2\right\}\,\mathrm{d}x\mathrm{d}y \\
&\qquad - F^2\iint\left[\left(\frac{1}{\mathrm{Re}} + \frac{1}{\mathrm{R}}\right)u_j\frac{\partial h}{\partial x_i}\frac{\partial u_j}{\partial x_i} + M^2\left(\frac{1}{\mathrm{Rm}} + \frac{1}{\mathrm{R}}\right)b_j\frac{\partial h}{\partial x_i}\frac{\partial b_j}{\partial x_i}\right]\,\mathrm{d}x\mathrm{d}y.
\end{aligned} \tag{7.7}$$

Thus we do not have a formally negative-definite dissipation when $F \neq 0$.

Divergence free condition violation

Finally, we observe that

$$\frac{\partial}{\partial t}(h_t\boldsymbol{b}) = \nabla\times(\boldsymbol{u}\times h_t\boldsymbol{b}) + \frac{1}{\mathrm{Rm}}h_t\nabla^2\boldsymbol{b} + \frac{F^2}{\mathrm{R}}\boldsymbol{b}\nabla^2 h, \tag{7.8}$$

and so

$$\frac{\partial}{\partial t}\nabla\cdot(h_t\boldsymbol{b}) = \nabla\cdot\left[\frac{1}{\mathrm{Rm}}h_t\nabla^2\boldsymbol{b} + \frac{F^2}{\mathrm{R}}\boldsymbol{b}\nabla^2 h\right] \neq 0, \tag{7.9}$$

unless $\mathrm{Rm}^{-1} = \mathrm{R}^{-1} = 0$ or $F = 0$. This is particularly problematic, as the divergence-free condition was used implicitly in the calculations of the other conservation laws.

So now we have seen what could go wrong, we consider an alternative implementation of dissipation using the SWMHD equations written in transport variables with $(\boldsymbol{U}, \boldsymbol{B}, h) = (h_t\boldsymbol{u}, h_t\boldsymbol{b}, h)$:

$$\frac{\partial\boldsymbol{U}}{\partial t} + \nabla\cdot\left(\frac{\boldsymbol{U}\boldsymbol{U}}{h_t} - M^2\frac{\boldsymbol{B}\boldsymbol{B}}{h_t}\right) + h_t\nabla h = \frac{1}{\mathrm{Re}}\nabla^2\boldsymbol{U}, \tag{7.10a}$$

$$\frac{\partial\boldsymbol{B}}{\partial t} + \nabla\cdot\left(\frac{\boldsymbol{U}\boldsymbol{B}}{h_t} - \frac{\boldsymbol{B}\boldsymbol{U}}{h_t}\right) = \frac{1}{\mathrm{Rm}}\nabla^2\boldsymbol{B}, \tag{7.10b}$$

$$F^2\frac{\partial h}{\partial t} + \nabla\cdot\boldsymbol{U} = \frac{F^2}{\mathrm{R}}\nabla^2 h, \tag{7.10c}$$

$$\nabla\cdot\boldsymbol{B} = 0. \tag{7.10d}$$

Here, tensor notation is used, with $(\boldsymbol{UB})_{ij} = U_i B_j$. Also note that the form of the dissipation employed in (7.10) is different to that in (7.1). Before going through the same arguments using conservation laws, we first make the observation that the y-component of the momentum equation is given by

$$\frac{\partial V}{\partial t} + \frac{\partial}{\partial x}\left(\frac{UV - M^2 B_x B_y}{h_t}\right) + \frac{\partial}{\partial y}\left(\frac{V^2 - M^2 B_y^2}{h_t}\right) + h_t \frac{\partial h}{\partial y} = \frac{1}{\mathrm{Re}}\nabla^2 V. \tag{7.11}$$

If we take $V = 0$ and $B_y = 0$ as boundary conditions, then, on the y-boundaries, we have

$$h_t \frac{\partial h}{\partial y}\bigg|_{y=\pm L_y} = \frac{1}{\mathrm{Re}} \frac{\partial^2 V}{\partial y^2}\bigg|_{y=\pm L_y}. \tag{7.12}$$

Substituting for $\partial V/\partial y$ using the continuity equation, also evaluated at the y-boundaries, we have

$$h_t \frac{\partial h}{\partial y}\bigg|_{y=\pm L_y} = \frac{1}{\mathrm{Re}} \frac{\partial}{\partial y}\left(\frac{F^2}{\mathrm{R}}\nabla^2 h - F^2 \frac{\partial h}{\partial t} - \frac{\partial U}{\partial x}\right)\bigg|_{y=\pm L_y}. \tag{7.13}$$

Upon swapping the derivatives for the U term and further assuming $\partial U/\partial y = 0$ on the y-boundaries, this gives

$$\frac{F^2}{\mathrm{Re}} \frac{\partial}{\partial t} \frac{\partial h}{\partial y}\bigg|_{y=\pm L_y} = \left(\frac{1}{\mathrm{Re}} \frac{F^2}{\mathrm{R}}\nabla^2 - h_t\right) \frac{\partial h}{\partial y}\bigg|_{y=\pm L_y}. \tag{7.14}$$

For the simulations presented later, we will take $R^{-1} = 0$, and so if $\partial h/\partial y = 0$ initially, then $\partial h/\partial y = 0$ on the boundaries for all subsequent time.

Mass conservation

The continuity equation has not been modified, so periodicity in x and $\partial h/\partial y = 0$ on the boundaries leads again to mass conservation.

Momentum conservation

Assuming the divergence-free condition for $\boldsymbol{B}$ holds,

$$\frac{\mathrm{d}}{\mathrm{d}t}\iint U \,\mathrm{d}x\mathrm{d}y = \frac{1}{\mathrm{Re}}\iint \nabla^2 U \,\mathrm{d}x\mathrm{d}y = 0, \tag{7.15}$$

since we have periodicity, $V = 0$, $B_y = 0$ and if we take $\partial U/\partial y = 0$ on the y-boundaries. Similarly,

$$\frac{\mathrm{d}}{\mathrm{d}t}\iint V \,\mathrm{d}x\mathrm{d}y = \frac{1}{\mathrm{Re}}\iint \nabla^2 V \,\mathrm{d}x\mathrm{d}y - \int \left[F^2 \frac{h^2}{2} + h\right]_{y=-L_y}^{y=L_y} \mathrm{d}x \tag{7.16}$$

using the same set of boundary conditions. No extra terms appear in this setting.

Flux conservation

Again, assuming the divergence-free condition holds,

$$\frac{\mathrm{d}}{\mathrm{d}t}\iint B_x \,\mathrm{d}x\mathrm{d}y = \frac{1}{\mathrm{Rm}}\iint \nabla^2 B_x \,\mathrm{d}x\mathrm{d}y = 0, \tag{7.17}$$

using periodicity, $V = 0$, $B_y = 0$, and if we take $\partial B_x/\partial y = 0$ on the y-boundaries. Similarly,

$$\begin{aligned}\frac{\mathrm{d}}{\mathrm{d}t}\iint B_y \,\mathrm{d}x\mathrm{d}y =& \frac{1}{\mathrm{Rm}}\iint \nabla^2 B_y \,\mathrm{d}x\mathrm{d}y \\ =& \frac{1}{\mathrm{Rm}}\iint \frac{\partial^2 B_y}{\partial y^2}\,\mathrm{d}x\mathrm{d}y - \frac{1}{\mathrm{Rm}}\iint \frac{\partial}{\partial x}\frac{\partial B_x}{\partial y}\,\mathrm{d}x\mathrm{d}y = 0,\end{aligned} \tag{7.18}$$

upon using the same set of boundary conditions.

Total energy conservation

Since the equations are formulated for $\boldsymbol{U}$ and $\boldsymbol{B}$, we first need to work out what the implied dissipation operators for $\boldsymbol{u}$ and $\boldsymbol{b}$ are. Suppose that

$$\frac{\partial \boldsymbol{u}}{\partial t} + \cdots = \mathsf{D}_{\mathrm{Re}}, \tag{7.19}$$

then we have

$$\frac{\partial (h_t \boldsymbol{u})}{\partial t} + \cdots = h_t \mathsf{D}_{\mathrm{Re}} + \frac{F^2}{\mathrm{R}}\boldsymbol{u}\nabla^2 h. \tag{7.20}$$

The right hand side must be equivalent to $\mathrm{Re}^{-1}\nabla^2\boldsymbol{U}$ in (7.10a), so

$$\mathsf{D}_{\mathrm{Re}} = \frac{1}{\mathrm{Re}}\frac{\nabla^2\boldsymbol{U}}{h_t} - \frac{F^2}{\mathrm{R}}\frac{\boldsymbol{u}}{h_t}\nabla^2 h. \tag{7.21}$$

A similar manipulation implies that

$$\mathsf{D}_{\mathrm{Rm}} = \frac{1}{\mathrm{Rm}}\frac{\nabla^2\boldsymbol{B}}{h_t} - \frac{F^2}{\mathrm{R}}\frac{\boldsymbol{b}}{h_t}\nabla^2 h. \tag{7.22}$$

Then the energy equation is

$$\begin{aligned}&\frac{1}{2}\frac{\mathrm{d}}{\mathrm{d}t}\iint \left[h_t(|\boldsymbol{u}|^2 + M^2|\boldsymbol{b}|^2) + F^2h^2\right]\,\mathrm{d}x\mathrm{d}y \\ &\quad= \frac{1}{2}\frac{\mathrm{d}}{\mathrm{d}t}\iint \left[(\boldsymbol{U}\cdot\boldsymbol{u} + M^2\boldsymbol{B}\cdot\boldsymbol{b}) + F^2h^2\right]\,\mathrm{d}x\mathrm{d}y \\ &\quad= \iint \left[\frac{1}{\mathrm{Re}}\boldsymbol{u}\cdot\nabla^2\boldsymbol{U} + \frac{M^2}{\mathrm{Rm}}\boldsymbol{b}\cdot\nabla^2\boldsymbol{B} + \frac{F^2}{\mathrm{R}}\left(\frac{|\boldsymbol{u}|^2 + M^2|\boldsymbol{b}|^2}{2}\right)\nabla^2 h + h\frac{F^2}{\mathrm{R}}\nabla^2 h\right]\,\mathrm{d}x\mathrm{d}y \\ &\quad= -\iint h_t\left\{\left[\frac{1}{\mathrm{Re}}\left(\frac{\partial u_j}{\partial x_i}\right)^2 + \frac{M^2}{\mathrm{Rm}}\left(\frac{\partial b_j}{\partial x_i}\right)^2\right] + \frac{F^2}{\mathrm{R}}\left(\frac{\partial h}{\partial x_i}\right)^2\right\}\,\mathrm{d}x\mathrm{d}y \\ &\qquad + F^2\iint\left[\left(\frac{1}{\mathrm{R}} - \frac{1}{\mathrm{Re}}\right)u_j\frac{\partial h}{\partial x_i}\frac{\partial u_j}{\partial x_i} + M^2\left(\frac{1}{\mathrm{R}} - \frac{1}{\mathrm{Rm}}\right)b_j\frac{\partial h}{\partial x_i}\frac{\partial b_j}{\partial x_i}\right]\,\mathrm{d}x\mathrm{d}y.\end{aligned} \tag{7.23}$$

So, in the hydrodynamic shallow-water system, we can in fact obtain a negative-definite dissipation if we choose Re $=$ R (as in Poulin & Flierl 2003). We will be taking $R^{-1} = 0$, so we do not end up with negative-definite disspation; however, it will be seen the extra contributions arising from this choice is small compared to negative-definite contribution for all the $F < 1$ results we present.

Divergence-free condition

We see that

$$\frac{\partial \boldsymbol{B}}{\partial t} = \nabla \times \left(\frac{\boldsymbol{U}}{h_t} \times \boldsymbol{B} \right) + \frac{1}{\mathrm{Rm}} \nabla^2 \boldsymbol{B}, \tag{7.24}$$

and so

$$\frac{\partial}{\partial t}(\nabla \cdot \boldsymbol{B}) = \nabla \cdot \left[\nabla \times (\cdots) + \boldsymbol{u}(\nabla \cdot \boldsymbol{B}) + \frac{1}{\mathrm{Rm}} \nabla^2 \nabla \cdot \boldsymbol{B} \right]. \tag{7.25}$$

Thus an initially divergence-free field remains divergence-free in the continuous time setting. So certainly formulation (7.10) in transport variables maintains more (but not all) of the conservation laws than formulation (7.1) in velocity variables. In particular, the divergence-free condition (7.10d) is maintained by the formulation of the SWMHD equations given by (7.10).

7.1.2 Arguments for employing (7.10)

Despite some of the flaws that are present with formulation (7.10), namely the lack of negative-definite energy dissipation in the general case with R, Re and Rm distinct, we will be using this formulation and here we give our reasons for this.

With regards to momentum dissipation, several other possibilities have been given in Ochoa *et al.* (2011) and Gilbert *et al.* (2013); our choice here is option III of Ochoa *et al.* (2011). Some of the other possibilities, used in the absence of a dissipation term in the continuity equation, have the property that they give a negative-definite dissipation and maintain other conservation laws. However, the forms of these dissipation terms are not particularly convenient to treat numerically in our pseudo-spectral, semi-implicit-in-time formalism, mainly because the associated dissipation terms involve nonlinear combinations of h and $\boldsymbol{U}$.

There is of course the possibility of taking Re $=$ R in (7.10), which does give a negative-definite dissipation of energy (as in Poulin & Flierl, 2003). We have not done this here and for the results

presented later, we have $\mathrm{R}^{-1} = 0$. This is partly because, when $\mathrm{R}^{-1} \neq 0$, the resulting equation for h to be solved is of fourth rather than second order in y. The fast solver does not appear to have a generalisation to the fourth order problem, and thus another solver needs to be used. In the test runs at some values of F, we compared the case where $\mathrm{R} = \mathrm{Re}$ (using LU for inversion of h) and $\mathrm{R}^{-1} = 0$ (using the fast solver). The runs were qualitatively comparable, but the routine using LU takes anything upwards of five times the amount of time to run compared to the routine using the fast solver.

With regards to the other dissipative terms when $\mathrm{R}^{-1} = 0$, given in the hydrodynamic case by $F^2 \iint u_j(\partial_i h)(\partial_i u_j)\,\mathrm{d}x\mathrm{d}y$, we see that these terms are contains factors of F^2 and involve ∇h. We expect that, for F small, steepening should not be an issue so ∇h is small, and hence the extra contributions to dissipation are also going to be small. As a matter of convenience, we numerically implement (7.10) with $\mathrm{R}^{-1} = 0$, and track $F^2 \iint u_j(\partial_i h)(\partial_i u_j)\,\mathrm{d}x\mathrm{d}y$. In our test runs, we found that, in this particular shear flow problem and at the values of F at which we focussed most of our attention ($F < 1$), the absolute value of the extra contributions is only a small percentage of the total dissipation. There were some issues with test runs at $F > 1$, which we defer to later discussions. So this choice of dissipation is unlikely to cause major problems, using this *a posteriori* validation.

For the MHD case, if we bypass the fundamental issue of field-line slippage and insist on satisfying this divergence-free condition, then we need a magnetic dissipation that maintains this condition. There are several possible choices (Andrew Gilbert, private communication), with ours being one of them; see Section 7.6 for more details. The alternative choices are such that, in the absence of dissipation in the continuity equation, a negative-definite dissipation may be achieved. However, the terms are nonlinear and are problematic to treat in our formalism. So, again mainly for simplicity and also because we expect the extra contributions to be small in the $F < 1$ regime, we employ the setting as in (7.10) and track the extra contributions to magnetic dissipation, here given by $F^2 \iint b_j(\partial_i h)(\partial_i b_j)\,\mathrm{d}x\mathrm{d}y$; these are again seen to be small compared to the total dissipation in our test runs.

In summary, we numerically solve for the SWMHD equations given in (7.10), with $\mathrm{R}^{-1} = 0$. This formulation is an improvement over the formulation in velocity variables as more conservation laws are maintained. In particular, the divergence-free condition is maintained. We should note, however, that energy dissipation in this set up is not negative-definite; tests have shown that, in

this particular problem and at the values of F we consider, the fact that we do not formally have negative-definite dissipation is unlikely to be a significant problem since the extra contribution is only a small percentage of the total dissipation, demonstrated later for some representative cases.

We note in passing that there is also a possibility to employ the vorticity ω, divergence δ (with the associated potentials) and the height field h as fundamental variables (e.g., Polvani *et al.*, 1994; Cho & Polvani, 1996a,b; Scott & Polvani, 2008). This is in fact the preferred method when the domain is doubly periodic, since a spectral method employing either Fourier modes or spherical harmonics allows for a straightforward solution of the resulting Poisson equation. For the channel geometry we have here, there is the added complication of lateral boundary conditions that need to be imposed. In this case the formulation in terms of (ω, δ, h) leads to a coupled elliptic system to be solved at the inversion step at every time-step (Salmon, 2009). This is expensive as an iterative solver will then be required; this formalism has not been tested here.

To maintain the divergence-free condition, we employ a flux function such that

$$\boldsymbol{B} = \boldsymbol{e}_z \times \nabla A. \tag{7.26}$$

This reduces to the magnetic potential in two-dimensional incompressible MHD when $F = 0$. The equations that we will be solving are given by

$$\frac{\partial U}{\partial t} + \frac{\partial}{\partial x}\left(\frac{U^2 - M^2 B_x^2}{1 + F^2 h} + \frac{F^2 h^2}{2}\right) + \frac{\partial}{\partial y}\left(\frac{UV - M^2 B_x B_y}{1 + F^2 h}\right) + \frac{\partial h}{\partial x} = \frac{1}{\mathrm{Re}}\nabla^2 U, \tag{7.27a}$$

$$\frac{\partial V}{\partial t} + \frac{\partial}{\partial x}\left(\frac{UV - M^2 B_x B_y}{1 + F^2 h}\right) + \frac{\partial}{\partial y}\left(\frac{V^2 - M^2 B_y^2}{1 + F^2 h} + \frac{F^2 h^2}{2}\right) + \frac{\partial h}{\partial y} = \frac{1}{\mathrm{Re}}\nabla^2 V, \tag{7.27b}$$

$$\frac{\partial A}{\partial t} + \frac{U}{1 + F^2 h}\frac{\partial A}{\partial x} + \frac{V}{1 + F^2 h}\frac{\partial A}{\partial y} = \frac{1}{\mathrm{Rm}}\nabla^2 A, \tag{7.27c}$$

$$F^2 \frac{\partial h}{\partial t} + \frac{\partial U}{\partial x} + \frac{\partial V}{\partial y} = 0, \tag{7.27d}$$

where we have taken $\mathrm{R}^{-1} = 0$. When $F = 0$, the above equations formally reduce to that of incompressible MHD. In two-dimensional planar MHD, it is well-known that there is no dynamo action (Zel'dovich, 1957); an anti-dynamo result may be shown (due to Andrew Gilbert, private communication); see Section 7.6. We once again the choice of dissipation is an *ad hoc* choice and does not stem from a self-consistent derivation from the Boussinesq MHD equations; we comment on the possibility of deriving a set of thin-layer equations in a self-consistent way at the end of this chapter.

To satisfy as many of the conservation properties as possible, the take the boundary conditions

$$V = 0, \quad \frac{\partial U}{\partial y} = 0, \quad \frac{\partial h}{\partial y} = 0, \quad A = 0 \quad \text{on} \quad y = \pm L_y. \tag{7.28}$$

From (7.27c), we observe that the boundary condition $A = 0$ implies that, on the boundaries, all terms on the left hand side and $\partial^2 A/\partial x^2$ are zero, and so this implies $\partial^2 A/\partial y^2 = \partial B_x/\partial y = 0$ on the boundaries. With such boundary conditions, waves hitting the boundaries will be reflected back into the domain. Test runs have shown that the gravity waves generated for $F < 1$ are small in amplitude and do not appear to have a significant effect on the macro-dynamics. There are methods to absorb impacting gravity waves, such as inserting sponge-layers or modifying the boundary conditions (e.g., Durran, 2010, §8), but these are not employed here.

7.1.3 Presence of fast waves

Unlike the incompressible case, fast gravity waves are supported in shallow-water systems. If we were to consider an explicit treatment of all terms except the dissipation terms, then we would have a restriction on Δt of the form

$$\Delta t \times \max\left\{ \left(\frac{u_{\mathsf{N}}}{\Delta x} + \frac{v_{\mathsf{N}}}{\Delta y} \right), \left(\frac{u_{\mathsf{G}}}{\Delta x} + \frac{v_{\mathsf{G}}}{\Delta y} \right) \right\} \leq C_{\text{cfl}} = O(1). \tag{7.29}$$

For numerical stability, Δt needs to be small enough so that the fastest process supported by the system is evolved in a stable fashion. From Chapter 2, we expect that $(u_{\mathsf{G}}, v_{\mathsf{G}}) \sim O(F^{-1})$, and this places severe restrictions on the time-step, particularly for small F.

There are several ways around this restriction, for example by employing splitting methods or semi-implicit treatments (see e.g., Peyret, 2002; Durran, 2010). We will consider here a semi-implicit treatment of the relevant terms, namely the ∇h terms in equations (7.27a) and (7.27b), and the divergence terms in equation (7.27d).

Another issue we address before giving the full details of the time discretisation is the stability properties of the time-marching scheme for wave propagation. To illustrate this, it is perhaps easiest to consider the one-dimensional, inviscid, hydrodynamic shallow-water equations, with a uniform background flow; in the ideal case, there is no difference between using velocity or

transport variables, so we use velocity variables temporarily. The linearised equations are

$$\frac{\partial u}{\partial t} + \frac{\partial u}{\partial x} + \frac{\partial h}{\partial x} = 0, \tag{7.30a}$$

$$F^2 \left[\frac{\partial h}{\partial t} + \frac{\partial h}{\partial x} \right] + \frac{\partial u}{\partial x} = 0. \tag{7.30b}$$

To analyse the stability of the scheme, we carry out a von Neumann stability analysis (e.g., Durran, 2010, §3), using the AB/BD2 method, rather than AB/BD3 employed in the previous chapter, to demonstrate the differences in the stability properties between this second and third order time-marching scheme. A discretisation with $\partial h/\partial x$ and $\partial u/\partial x$ treated implicitly then gives

$$a_0 u^{n+1} + a_1 u^n + a_2 u^{n-1} + \Delta t U_0 \frac{\partial}{\partial x}(b_0 u^n + b_1 u^{n-1}) + \Delta t \frac{\partial h^{n+1}}{\partial x} = 0, \tag{7.31a}$$

$$F^2(a_0 h^{n+1} + a_1 h^n + a_2 h^{n-1}) + F^2 \Delta t U_0 \frac{\partial}{\partial x}(b_0 h^n + b_1 h^{n-1}) + \frac{\partial u^{n+1}}{\partial x} = 0, \tag{7.31b}$$

where the AB/BD2 coefficients are given by (Peyret, 2002, §4)

$$a_0 = \frac{2 + r_c}{1 + r_c}, \qquad a_1 = -1 - \frac{1}{r_c}, \qquad a_2 = \frac{1}{1 + r_c}, \tag{7.32a}$$

$$b_0 = 1 + \frac{1}{r_c}, \qquad b_1 = -\frac{1}{r_c}, \tag{7.32b}$$

$$r_c = \frac{\Delta t_{p1}}{\Delta t_c} = \frac{t_n - t_{n-1}}{t_{n+1} - t_n}. \tag{7.32c}$$

Now, since the system given by (7.31) is a function of x only, we consider solutions of h and u of the form $(u^n, h^n) \sim A^n \exp(\mathrm{i}kx)$, where $A \in \mathbb{C}$. If $|A| > 1$, then the numerical solution will grow at each time-step and thus be numerically unstable. Denoting $z = \mathrm{i}k\Delta t$, we obtain the linear system

$$\begin{pmatrix} \mathsf{V}_{AB/BD2}(A, U_0, z) & zA^2 \\ zA^2 & F^2 \mathsf{V}_{AB/BD2} \end{pmatrix} \begin{pmatrix} \hat{u} \\ \hat{h} \end{pmatrix} = 0, \tag{7.33}$$

where we have used the shorthand

$$\mathsf{V}_{AB/BD2} = a_0 A^2 + (a_1 + U_0 b_0 z)A + (a_2 + U_0 b_1 z). \tag{7.34}$$

Choosing F and U_0, we can solve this system for A on a $z = z_r + \mathrm{i}z_i$ grid. Choosing the appropriate branch of solutions, we can plot the stability contour $|A| = 1$ in the complex z plane, with numerical stability ($|A| < 1$) to the left of the contour, and instability otherwise. In Figure 7.1 we plot the stability region of AB/BD2 along with the corresponding results for AB/BD3, AB3/Crank-Nicolson, and AB2/Crank-Nicolson, for several F values. Since $z = \mathrm{i}k\Delta t$,

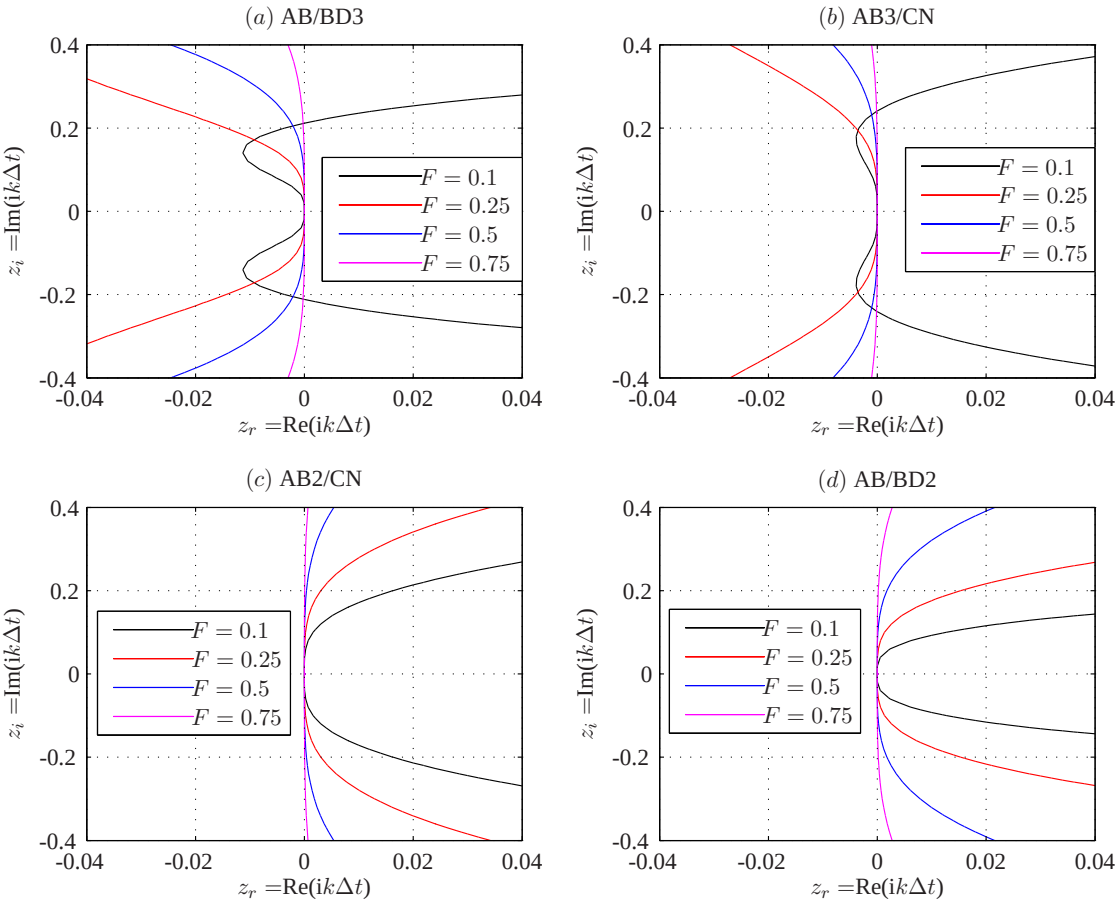

Figure 7.1: Numerical stability boundaries of various time-marching schemes for the one-dimensional, linear, hydrodynamic shallow-water equations, plotted at several F values. The schemes are stable for z values left of the contours.

if the scheme is unstable on some of the $z_r = 0$ line then we have a restriction on Δt. We see that when AB3 schemes are employed in this setting, we have a severe restriction on Δt when $F \ll 1$, whilst the AB2 scheme does not appear to exhibit this undesirable behaviour. The AB/BD3 version of the code is easily adapted to AB/BD2 since the only things that needs changing are the relevant coefficients a_j and b_j, given in equation (7.32); thus we employ the AB/BD2 scheme as the time-marching algorithm in this chapter.

As a final test of the AB/BD2 scheme, we solve numerically the two-dimensional linearised SWMHD equations. These are solved with the AB/BD2 scheme using the semi-implicit formalism presented earlier, appropriately initialised with exact gravity wave solutions given by (2.48). First an elliptic equation for h is solved, then u and v are updated at each time-step, with a

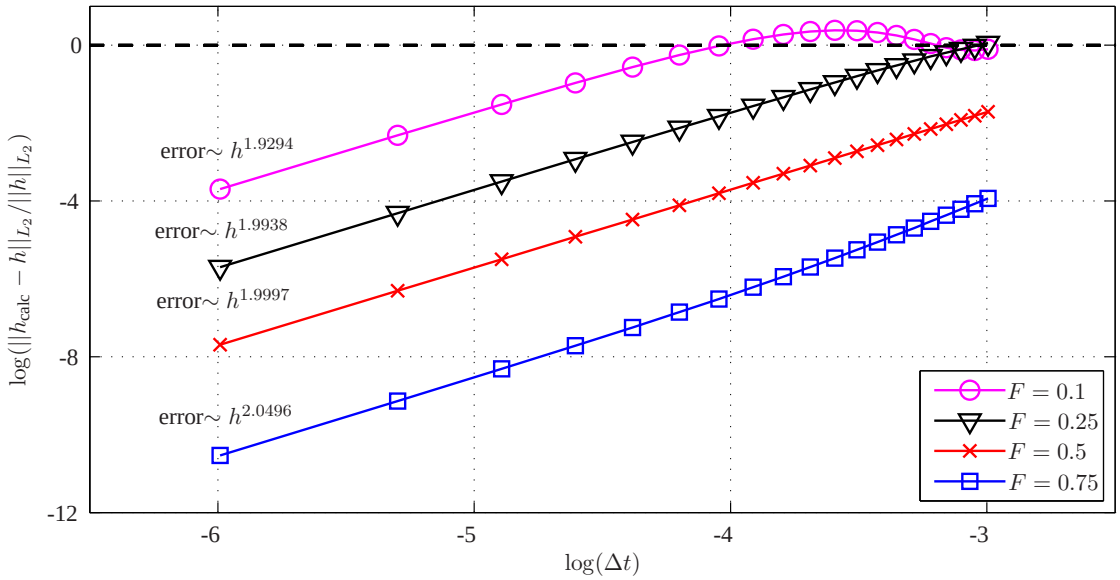

Figure 7.2: Relative L_2 errors for a two-dimensional, linear SWMHD evolution of a single gravity wave initialisation, at several F values; $U_0 = 1$, $M = 0.1$, wavenumber $(k, l) = (6, 1)$ and $(L_x, L_y) = (2\pi, 1)$, with $N_x = N_y = 32$.

Chebyshev discretisation in y and Fourier discretisation in x as in Chapter 6, using $v = 0$, $b_y = 0$ and $\partial h/\partial y = 0$ as the y-boundary conditions. The initial wave profile was evolved for 10 periods, and the relative spatial L_2 error was calculated at the end time. Figure 7.2 shows a typical error diagram, with errors diminishing at the correct theoretical rate. Note that even for relatively large Δt, the scheme is stable as predicted; the chief source of error is presumably due to dispersion. Tests with polychromatic initialisations show similar qualitative and quantitative behaviour. Although results here only show cases with $F < 1$, it is seen that such a semi-implicit treatment using the AB/BD2 scheme maintains numerical stability for linear dynamics even for $F \geq 1$.

Returning to the SWMHD system (in transport variables), a corresponding semi-implicit treatment

in time using the AB/BD2 discretisation results in the scheme

$$\left(a_0 - \frac{\Delta t}{\mathrm{Re}}\nabla^2\right) U^{n+1} = \mathsf{N}(U) - \Delta t \frac{\partial h^{n+1}}{\partial x}, \tag{7.35a}$$

$$\left(a_0 - \frac{\Delta t}{\mathrm{Re}}\nabla^2\right) V^{n+1} = \mathsf{N}(V) - \Delta t \frac{\partial h^{n+1}}{\partial y}, \tag{7.35b}$$

$$\left(a_0 - \frac{\Delta t}{\mathrm{Rm}}\nabla^2\right) A^{n+1} = \mathsf{N}(A), \tag{7.35c}$$

$$a_0 F^2 h^{n+1} + \Delta t \left(\frac{\partial U^{n+1}}{\partial x} + \frac{\partial V^{n+1}}{\partial y}\right) = F^2 \mathsf{N}(h), \tag{7.35d}$$

where N denotes the relevant terms that are evaluated at the levels below $n+1$. Taking the divergence of the momentum equation then gives

$$\left(a_0 - \frac{\Delta t}{\mathrm{Re}}\nabla^2\right)\left(\frac{\partial U^{n+1}}{\partial x} + \frac{\partial V^{n+1}}{\partial y}\right) = \left(\frac{\partial \mathsf{N}(U)}{\partial x} + \frac{\partial \mathsf{N}(V)}{\partial y}\right) - \Delta t \nabla^2 h^{n+1}, \tag{7.36}$$

and so we have the following elliptic equation to solve for h:

$$\begin{aligned}\left[(\Delta t)^2\nabla^2 - a_0 F^2\left(a_0 - \frac{\Delta t}{\mathrm{Re}}\nabla^2\right)\right] h^{n+1} \\ = \Delta t\left(\frac{\partial \mathsf{N}(U)}{\partial x} + \frac{\partial \mathsf{N}(V)}{\partial y}\right) - F^2(a_0 - \nu\Delta t\nabla^2)\mathsf{N}(h).\end{aligned} \tag{7.37}$$

Once h^{n+1} is known, the other equations may be appropriately advanced in time. Since this is a second order scheme, the first time-step is taken using an Euler/Crank-Nicolson scheme with a similar semi-implicit treatment.

Note that the algorithm also works for $F = 0$, and in this case h is to be identified with the pressure field p. There is however a subtlety in the inversion step for h when solving the Poisson equation (7.37); see Section 7.7 for details. The shallow-water program may be used to solve for incompressible dynamics, and results from this program have been checked against those obtained from the program employing the streamfunction-vorticity formulation. The qualitative and quantitative results (e.g., agreement of shear layer width at end time, general behaviour of energy time-series and dissipation rates) from the two programs agree with each other, but the program using the streamfunction-vorticity formulation runs faster because it has one less equation to solve.

7.2 Hydrodynamic evolution

We focus first on cases with $F < 1$. We have found that, for the nonlinear runs using AB/BD2, the CFL number needs to be reduced from around 0.15 for the small F cases to about 0.05 for larger F

in order to retain numerical stability, with the transition at around $F \approx 0.4$. In these shallow-water runs, we initialise with a linear eigenfunction (appropriately scaled) at specified α, and add to this higher wavenumber perturbations at lower amplitude with random phase. The initial total energy of the perturbations is fixed at 10^{-5}. As before, we switch off the dissipation of the basic state until the perturbations are sufficiently large, using the same energy criteria as in Chapter 6.

7.2.1 Hyperbolic-tangent shear layer

Table 7.1 shows a summary of the parameter values employed for the shear layer runs. Again, we focus on the case where the domain supports a single wavelength of the primary instability. The optimal α for these cases are close to $\alpha = 0.44$. We will focus our investigation on $F = 0$, 0.1 and 0.5; the runs at $F = 0.25$ and $F = 0.75$ are comparable to those at $F = 0.1$ and $F = 0.5$ respectively.

parameter	range
F	0, 0.1, 0.25, 0.5, 0.75
Re	500
$N_x \times N_y$	256×512
C_{cfl}	0.15 for $F < 0.5$
	0.05 for $F \geq 0.5$
α	0.44

Table 7.1: Parameter values used in our investigation of the nonlinear SWMHD equations for the shear layer profile.

We show in Figure 7.3 snapshots of the potential vorticity $q = \omega/h_t$ (this reduces to the regular vorticity when $F = 0$). Figure 7.3(a) is the case with $F = 0$, i.e. the incompressible case; the evolution for this case has already been described in the previous chapter. The vortex does not lie in the centre of domain as in Figure 6.1 because of a phase difference in the initialisation. For the case with $F = 0.1$ in Figure 7.3(b), the evolution is largely similar to the incompressible case. For $F = 0.5$ in Figure 7.3(c), the rolling up stage is delayed somewhat but otherwise the evolution is similar to the other two cases. The saturated state at this large F value is a slightly elongated vortex compared to the small F cases.

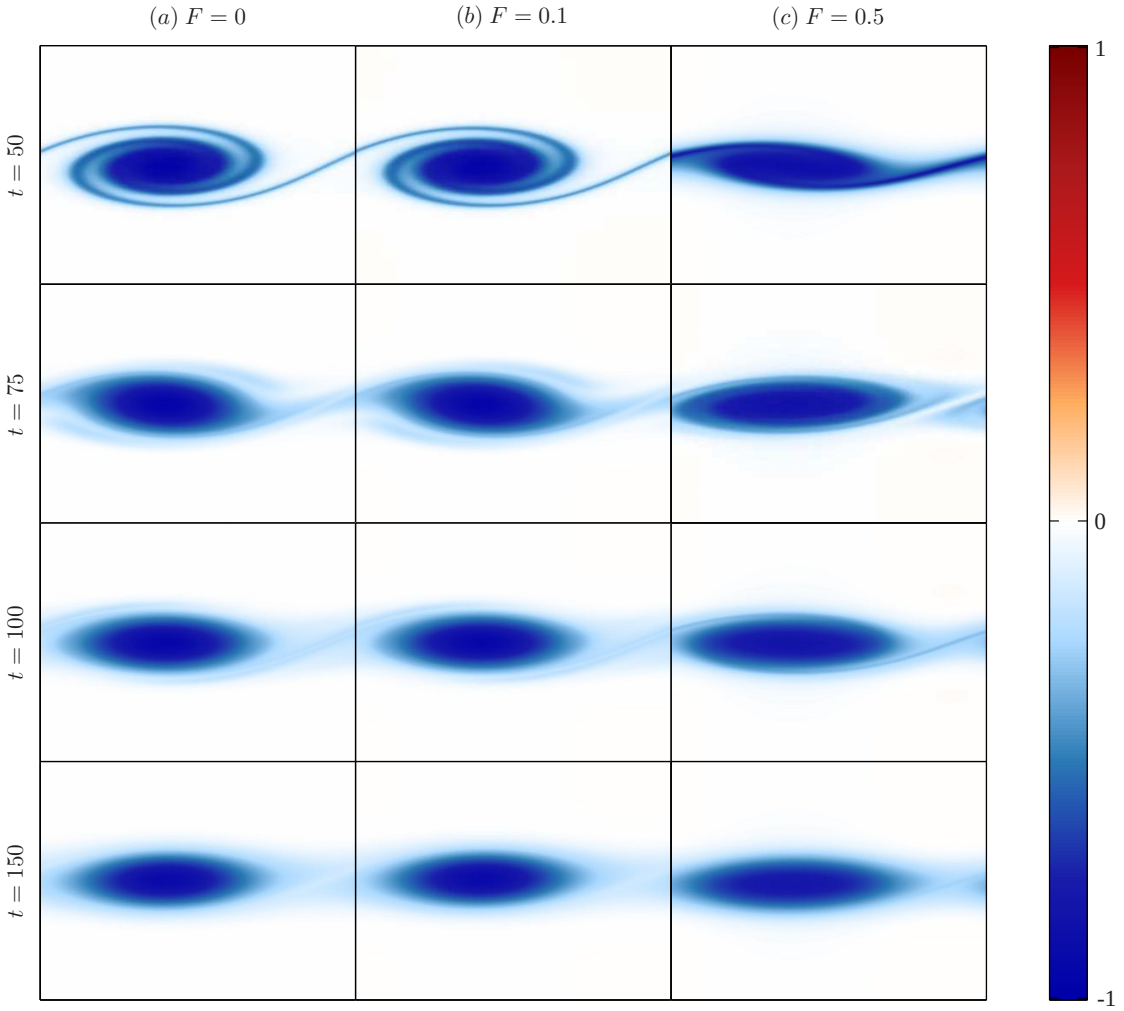

Figure 7.3: Snapshots of potential vorticity at some different values of F for the shear layer runs (at Re $=$ 500). The $F = 0$ case may be compared to Figure 6.1.

In Figure 7.4 we show the height field for the $F = 0.5$ case at early times; the $F = 0.1$ case is qualitatively similar except that the quantities are about an order of magnitude smaller. In Figure 7.4(a) we plot the deviation from the basic height field F^2h. We can clearly see that the pattern is growing in amplitude; however, no other activity is seen because the component corresponding to the fundamental mode dominates. In Figure 7.4(b) we plot the same quantity but with the first Fourier harmonic filtered out, in order to remove a portion of the fundamental mode of instability. We can now see more small-amplitude activity, corresponding to gravity waves travelling around the domain, reflecting from the y-boundaries accordingly. These waves are invariably of small amplitude and do not seem to affect the macro-dynamics significantly.

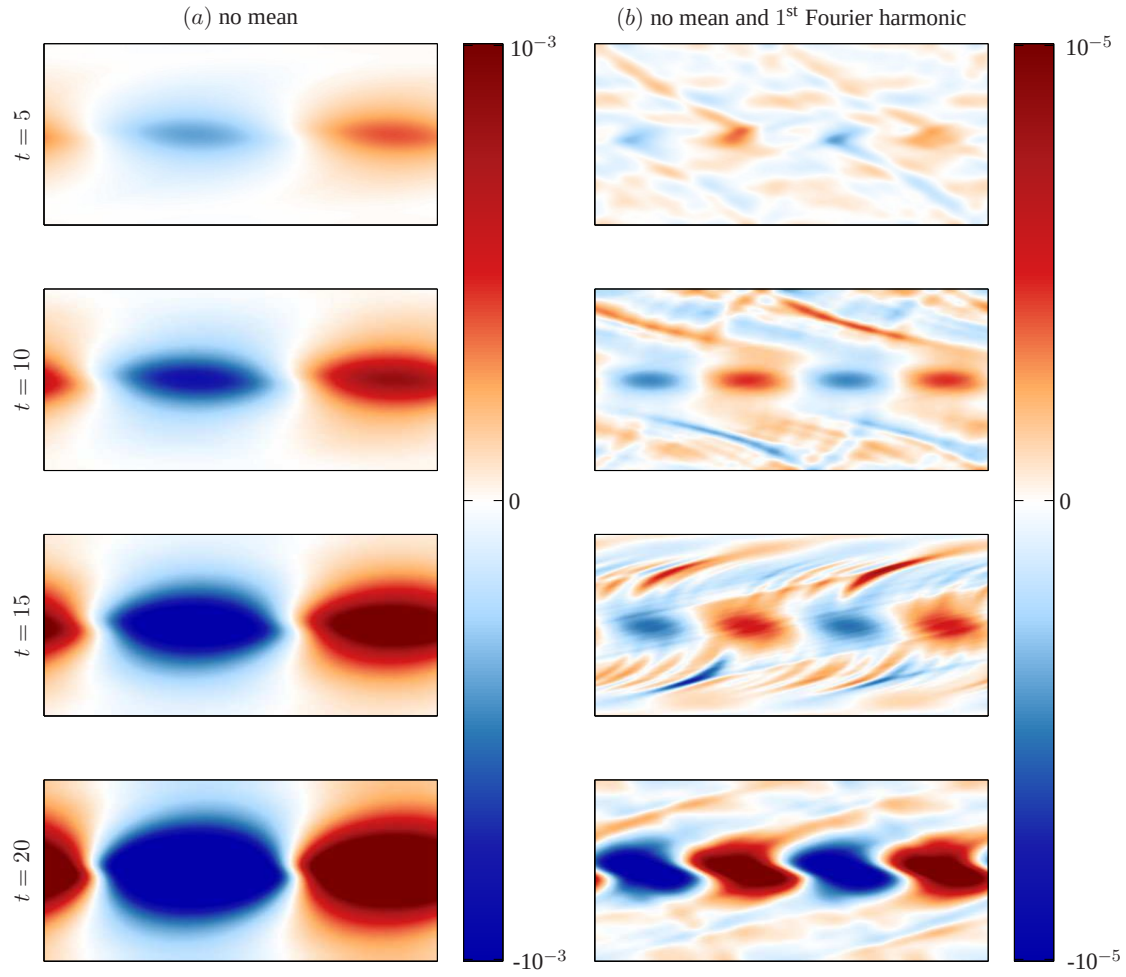

Figure 7.4: Snapshots of the height field for the $F = 0.5$ run at some early times, for the shear layer run (at Re $= 500$). The left column has the mean height ($H = 1$) removed, while the right column has the mean and first Fourier harmonic removed.

Figure 7.5 shows snapshots of $\overline{u}$ for the representative cases; it can be seen that there is no great difference between the three plots. The rolling up of the shear layer increases the shear layer width, with the widths being comparable in all three cases once the saturated state has been reached.

In Figure 7.6 we show the energy time-series (kinetic and potential) for the three cases. Growth rates are inferred by a fitting of the perturbation kinetic energy and these agree well with calculations from linear theory (at 0.185, 0.184 and 0.140 for $F = 0$, 0.1 and 0.5 respectively). When $F \neq 0$, kinetic energy can also be transformed into potential energy, equal to $\iint F^2 h^2/2 \, \mathrm{d}x\mathrm{d}y$. We first observe that the potential energy is larger for $F = 0.5$ than $F = 0.1$, since there is a larger deformation to the free surface $F^2 h$. Another feature that we observe from

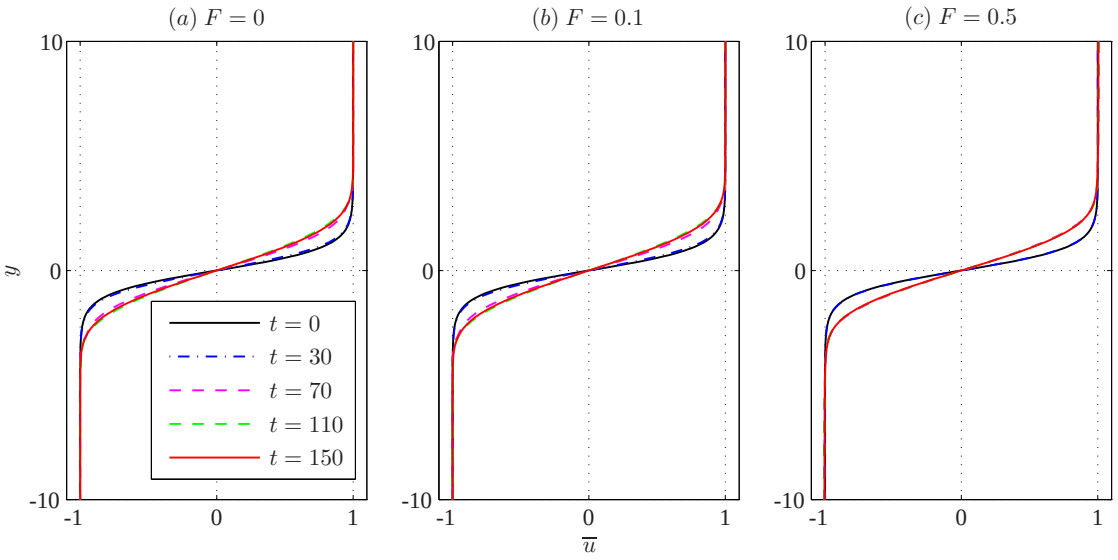

Figure 7.5: Snapshots of $\overline{u}$ for the shear layer runs (at Re $= 500$).

the energy plots is that the evolution of the perturbation potential energy largely follows that of the perturbation kinetic energy. The oscillations in the kinetic energy are again related to vortex nutation, and the similarity in the evolution of the two energy profiles is due to the height field adjusting to the oscillations in velocity accordingly. The total energy loss for all three cases is comparable to the incompressible case, at around 10%.

The right hand side of the energy balance equation (7.23) is given by

$$\tilde{\epsilon}_{\mathrm{Re}} = \frac{1}{\mathrm{Re}} \iint \left[h_t \left(\frac{\partial u_j}{\partial x_i} \right)^2 + F^2 u_j \frac{\partial h}{\partial x_i} \frac{\partial u_j}{\partial x_i} \right] \mathrm{d}x\mathrm{d}y. \tag{7.38}$$

In Figure 7.7 we show the time-series of the domain-integrated terms representing dissipation. The solid curve is a time-series of $\tilde{\epsilon}_{\mathrm{Re}}$, whilst the dashed line is the absolute value of $\mathrm{Re}^{-1} F^2 \iint u_j (\partial_i h)(\partial_i u_j) \, \mathrm{d}x\mathrm{d}y$. It turns out that $\tilde{\epsilon}_{\mathrm{Re}}$ is positive definite whilst the cross term, which may be of either sign (but tends to be negative) is much smaller than the sign-definite term. As we can see, for the purely incompressible case with $F = 0$, there is no extra contribution since the cross term is multiplied by a factor of F^2. For the other two cases, the size of the cross term increases with F; however it is still only a small percentage of the total contribution. We conclude therefore that, even though we do not have sign-definite dissipation of energy, the effects of this choice of dissipation operator on this particular shear instability problem are unlikely to be significant.

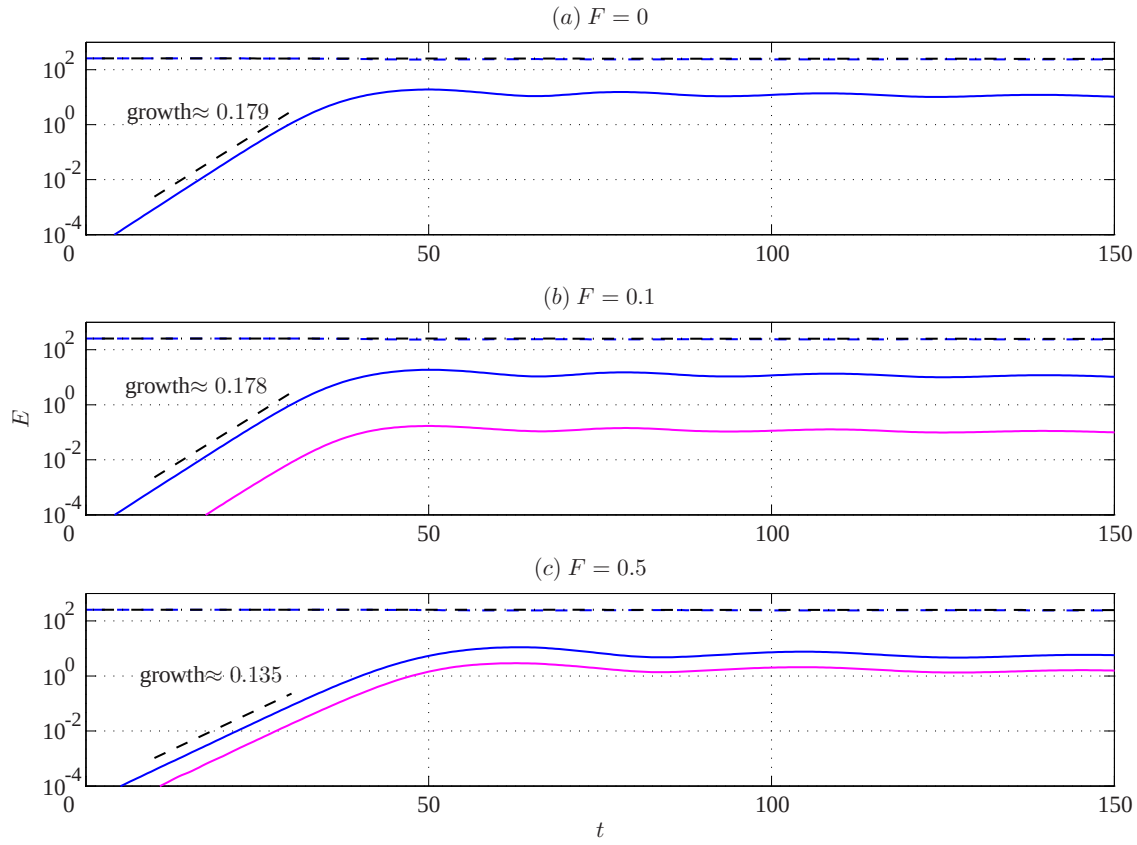

Figure 7.6: Time-series of energies (blue = kinetic; magenta = potential; solid = perturbation state; dashed = mean state; black dot-dashed line = total energy), for the shear layer runs (at Re = 500).

Finally, Figure 7.8 shows the time-series of the domain-integrated momentum. We choose here to use linear scales to highlight the rapid sign changes in the signal. The domain-integrated y-momentum, given by the red solid curve (note the different axes used for the panels), initially starts off very small, then grows somewhat but remains numerically small. The corresponding curve for the domain-integrated x-momentum is given by the blue curve (the initialisation has no x-momentum to begin with); the values are consistently around $O(10^{-11})$ and variations of this signal are not visible at this axis scale. The source of the growth in the y-momentum appears to be due to the h terms in equation (7.16). We have tried tracking values from both sides and integrating both sides as a function of time to see whether the two terms are correlated; there appears to be reasonable agreement, but we have a noisy signal and so the integration is not particularly accurate. We have also tracked the domain-integrated mass to verify mass conservation; and mass is conserved at an error no more than $O(10^{-8})$ (not shown).

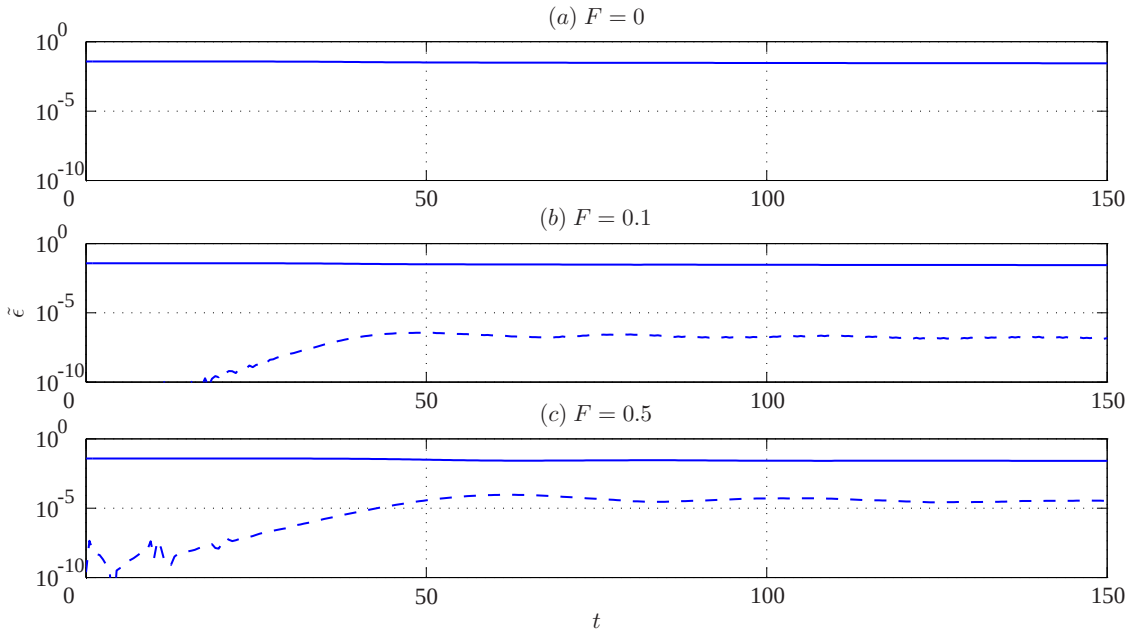

Figure 7.7: Domain-integrated dissipation rate $\tilde{\epsilon}_{\mathrm{Re}}$ (solid curve) and contribution from the cross term (dashed curve) for the shear layer runs.

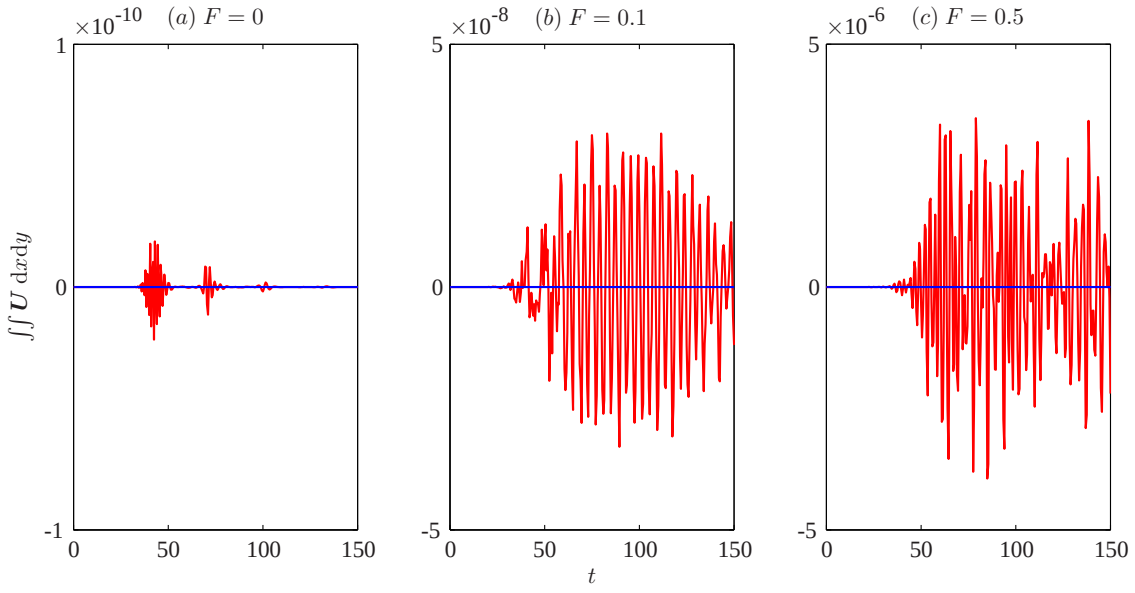

Figure 7.8: Domain-integrated momentum for the shear layer runs. The red curve represents the domain-integrated y-momentum (which is not expected to be conserved). The blue curve, which represents the domain-integrated x-momentum (also should be zero) has variations that are not visible at this axis scale.

We have also considered the case of multiple wavelengths; pairing occurs as in the incompressible case without substantial difference.

7.2.2 Bickley jet

For the Bickley jet, the calculations in Chapter 5 indicate that the even mode is more unstable than the odd mode for any α within the unstable bandwidth, so we initialise the nonlinear simulation with the even eigenfunction, normalised so that the total initial energy is fixed at 10^{-5}. We use the same parameter values as in the shear layer case except we take $\alpha = 0.9$, with the domain large enough to support two wavelengths of the primary instability, as in Chapter 6. Linear theory tells us that, at the values of F we are considering, the even mode has a growth rate similar to the incompressible case, with hardly any noticeable perturbation of the eigenfunctions. The question then is whether the nonlinear evolution is significantly different. From our investigation of the shear layer, we might suspect that the evolution will not be noticeably different to the incompressible case provided $F < 1$.

Figure 7.9 shows snapshots of the potential vorticity at the three different values of F we are considering; it would appear in this case that there is almost no difference in the evolution, with all the panels being visually identical to each other. Although not our focus here, when rotational effects are present, it is well known that there is an asymmetry between the stability properties of cyclones and anti-cyclones (vortices of positive and negative vorticity respectively), where modifying F can have a more noticeable effect (e.g., Polvani *et al.*, 1994; Poulin & Flierl, 2003).

In Figure 7.10 we show the height field for the $F = 0.5$ case, to show that there is small-amplitude activity in the height field and thus the presence of small amplitude gravity waves. The corresponding diagram for $F = 0.1$ is similar but the plotted quantities are at least an order of magnitude smaller.

In Figure 7.11 we show snapshots of $\overline{u}$ for the jet profile. Once again, the profiles are virtually indistinguishable from each other, with the same behaviour as in the incompressible hydrodynamic case. The jet profile broadens and reduces in magnitude, with some reverse flow observed.

The time-series of the energy for the Bickley jet profile is plotted in Figure 7.12. Growth rates are inferred from a fit of the perturbation kinetic energy, and these agree well with the linear theory (which are 0.160, 0.160 and 0.157 for $F = 0$, 0.1 and 0.5 respectively). The growth rates are

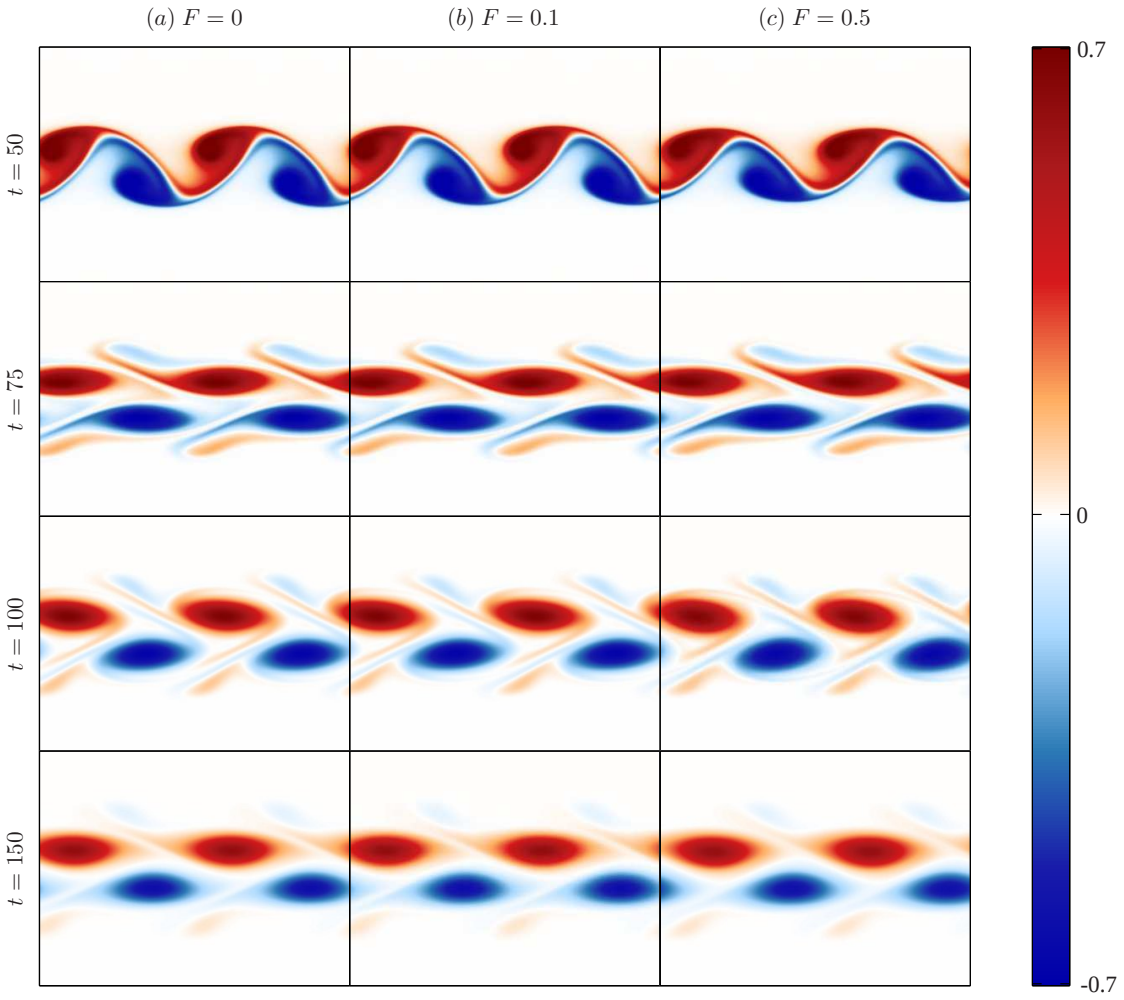

Figure 7.9: Snapshots of potential vorticity at various values of F for the Bickley jet profile (at Re $= 500$). The $F = 0$ case may be compared to Figure 6.5.

also comparable to each other, with a slight difference for the $F = 0.5$ case. We see that the perturbation potential energy is a few orders of magnitude smaller than the kinetic energy, but the potential energy increases with F. The total loss of energy is comparable to the incompressible case, at around 30%.

Figure 7.13 shows the dissipation rates represented by the terms in (7.38). Again, we notice that the extra contribution from the cross term is several orders of magnitude less than the sign-definite dissipation, and thus our choice of dissipation is unlikely to cause a significant problem in this shear instability problem, even though it is not formally sign-definite.

The domain-integrated perturbation momentum is plotted in Figure 7.14. In this case there is a

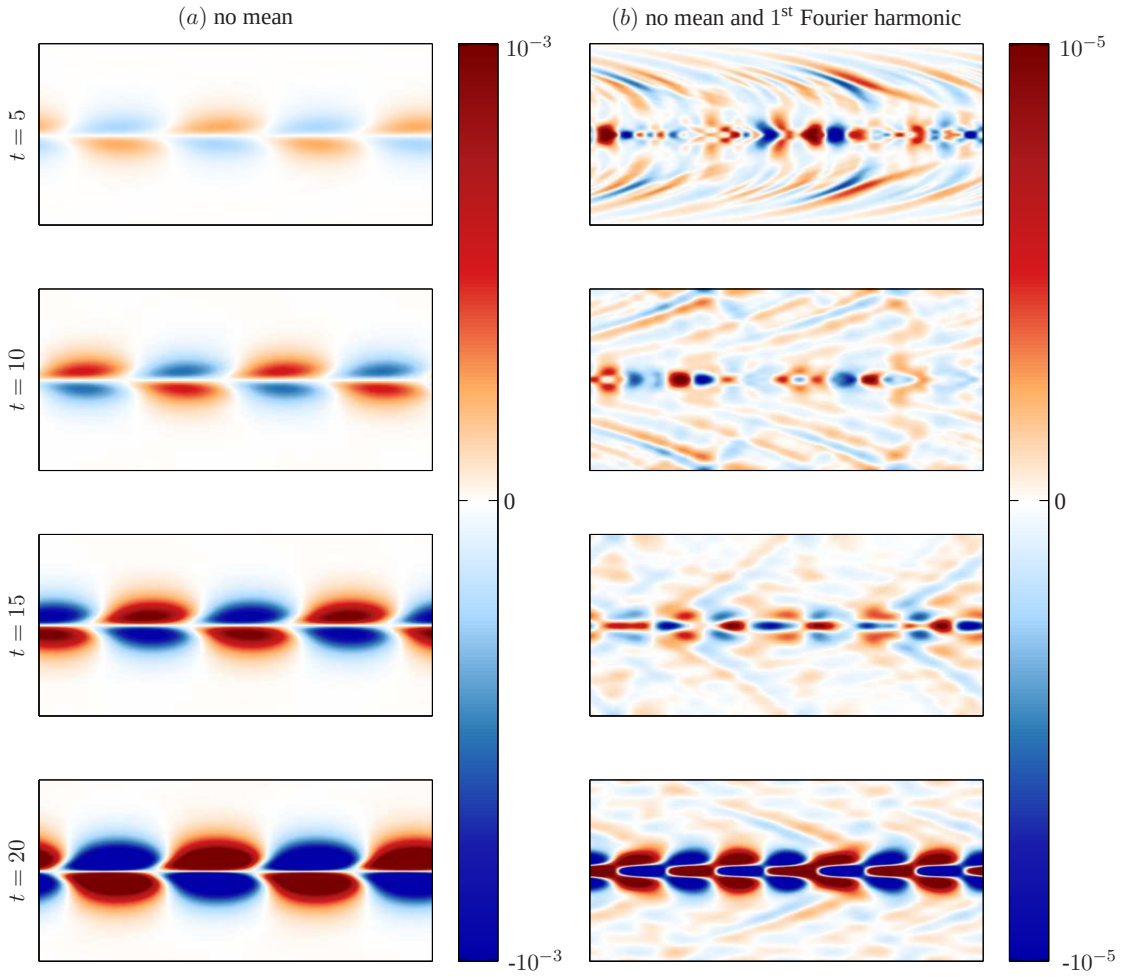

Figure 7.10: Snapshots of the height field for the $F = 0.5$ run at some early times, for the Bickley jet profile (at Re $= 500$). The left column has the background height field $H = 1$ removed, while the right column has both the background height field and first Fourier mode removed.

background flow with non-zero x-momentum; the momentum contribution of this was removed to give a deviation from momentum conservation. Even when this has been done, we see that the largest deviation from zero comes from the y-momentum signal, given by the red curve. The blue curve representing the x-momentum has been overlaid for visibility purposes, and at this scale any variations are not visible. The errors are small and should have a negligible effect on the overall dynamics. A similar integration of the signal as discussed for the shear layer case has been tried and the conclusions are broadly similar.

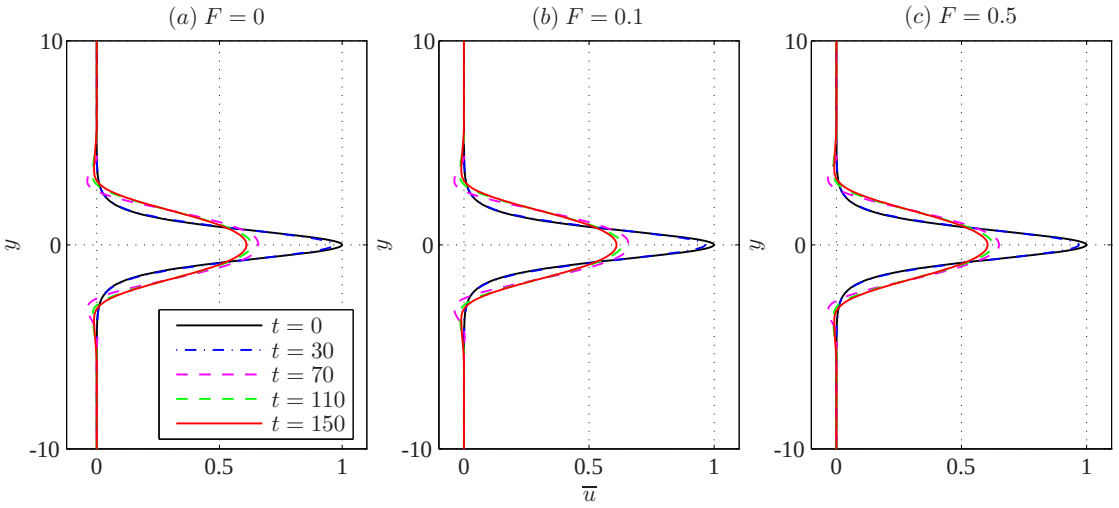

Figure 7.11: Snapshots of $\overline{u}$ for the Bickley jet runs (at Re $= 500$).

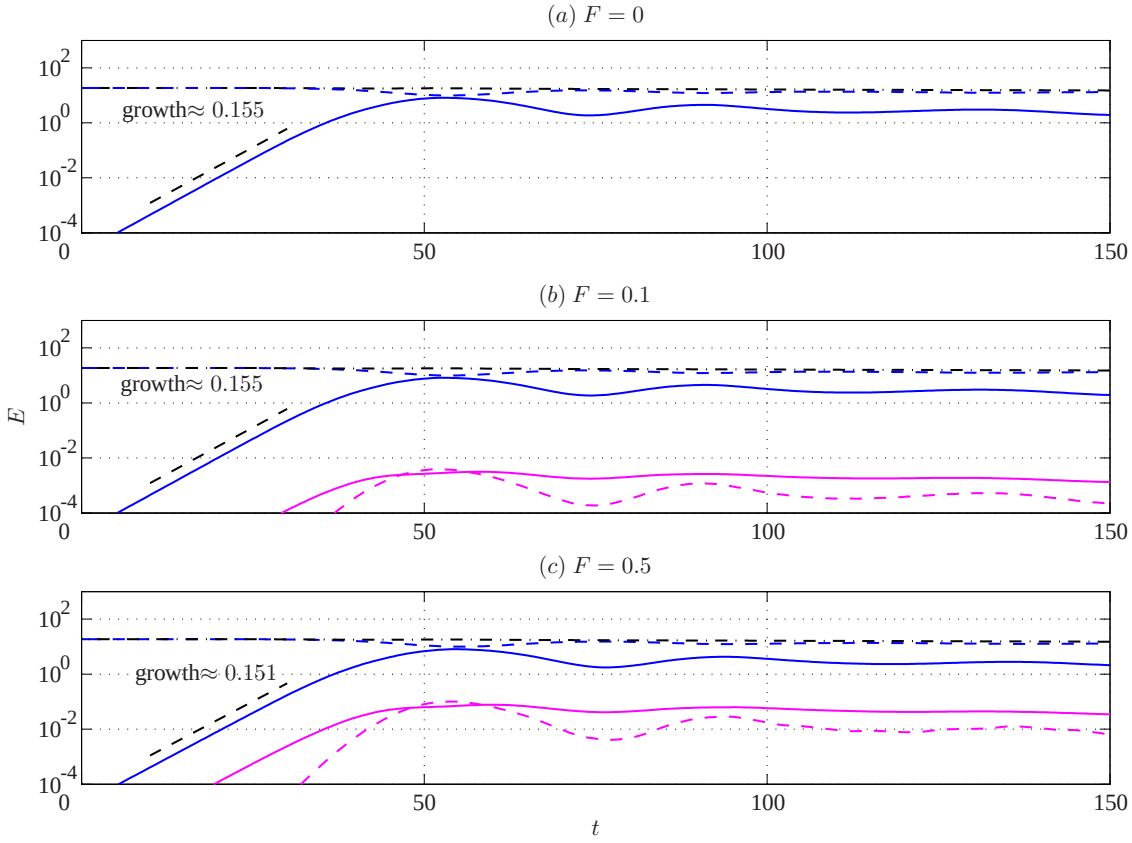

Figure 7.12: Time-series of energies (blue = kinetic; magenta = potential; solid = perturbation state; dashed = mean state; black dot-dashed line = total energy) for the Bickley jet runs (at Re $= 500$).

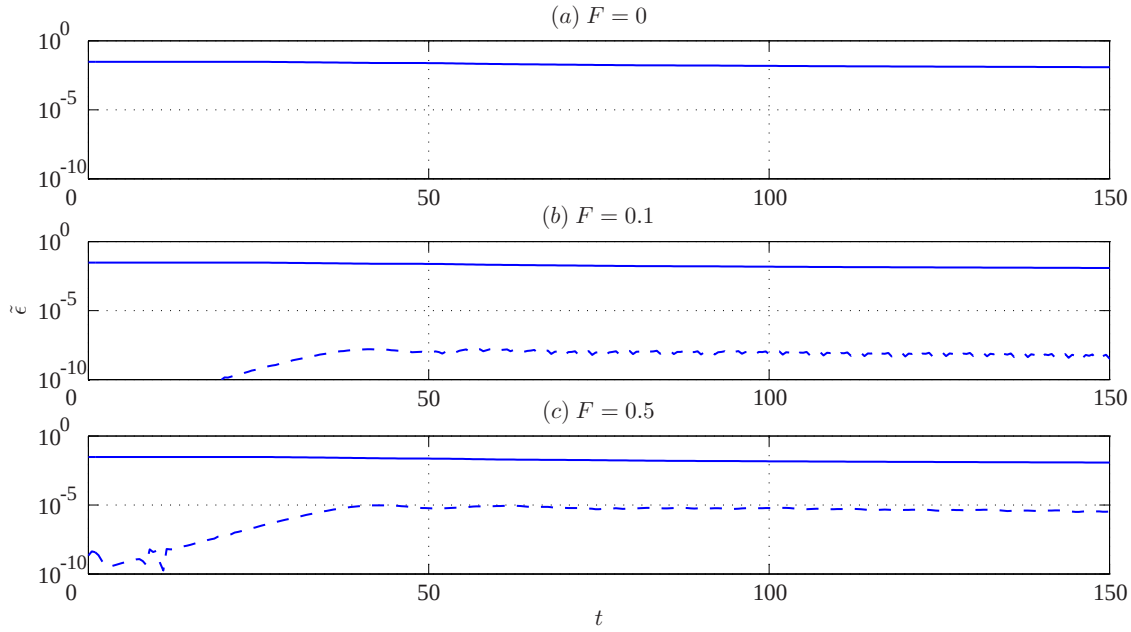

Figure 7.13: Domain-integrated dissipation rate $\tilde{\epsilon}_{\mathrm{Re}}$ (solid curve) and contribution from the cross term (dashed curve) for the Bickley jet runs. The cross term contribution increases in magnitude with increasing F.

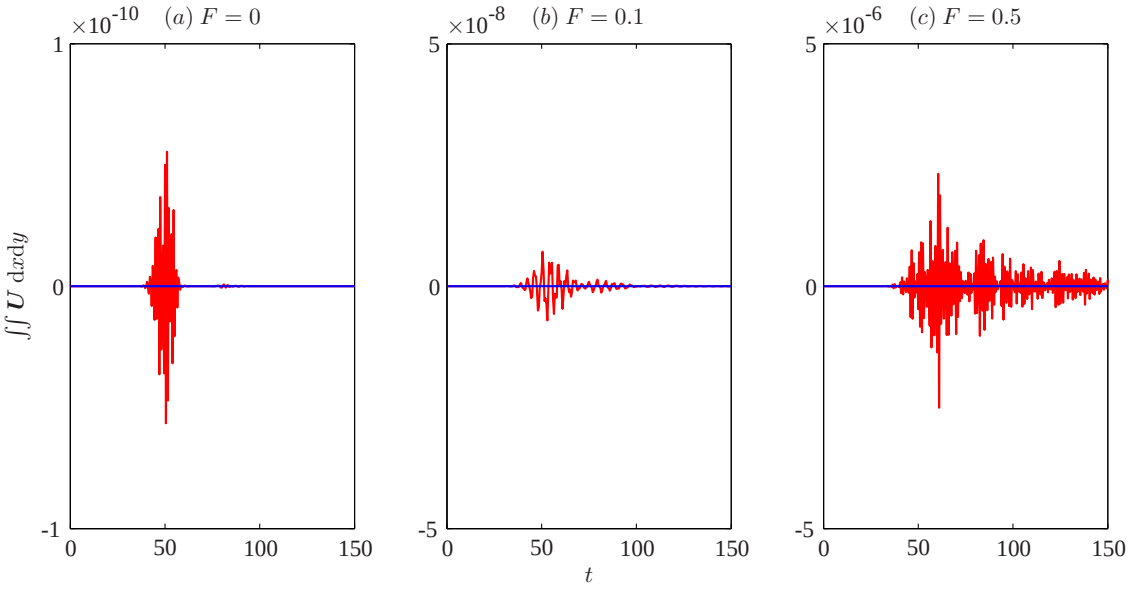

Figure 7.14: Domain-integrated pertubation momentum for the Bickley jet profile. The red curve represents the domain-integrated y-momentum (which is not formally conserved), and the blue curve represented the domain-integrated x-momentum with the background state removed.

7.3 MHD evolution

We now turn to the cases with $M > 0$, again with a uniform background magnetic field. We first discuss the evolution of the shear layer profile with increasing F before moving on to the Bickley jet profile.

7.3.1 Hyperbolic-tangent shear layer: $F = 0.1$

At such a small value of F we do not expect a large deviation from the conclusions drawn from the $F = 0$ incompressible case. As such, we will not go into so much detail as we have done previously, but concentrate on highlighting the differences that do arise. We focus on the regime of small M as before and use the Re $= 500$, Rm $= 500$ and $M = 0.01$, 0.03 and 0.05 runs as our three representative cases.

Figure 7.15 shows snapshots of the potential vorticity at different values of M. These are comparable to the corresponding diagrams for the incompressible case (Figure 6.9). The three cases show various degrees of disruption as before, with increased disruption with increasing M and Rm. The vortex winds up field lines, builds magnetic stresses, and stretches out thin current sheets that are resistively unstable. The breakup of the current layer releases the stresses, impacts back on the vortex, and potentially causes disruption. In the weakly disruptive cases, the surviving vortex would expel field lines to the edges of the vortex as before. We will use the spectral truncation parameter later to measure the severity of disruption for the runs at different parameter values.

The plots related to the magnetic quantities are largely similar to those given in the incompressible case and have been omitted. Plotting the height field shows traces of small-amplitude waves, but we omit this here also as it does not appear to show any particularly interesting features that are obviously associated with MHD effects.

Figure 7.16 shows snapshots of $\overline{u}$; we see again that the degree of disruption is correlated with the resulting shear layer width. Later on we will use the layer width expansion factor to quantify the degree of disruption, as was done previously for the incompressible case.

Figure 7.17 shows the time-series of the energy for these sample runs. The behaviour of the magnetic energy is largely as observed in Figure 6.15 for the incompressible case, with a different

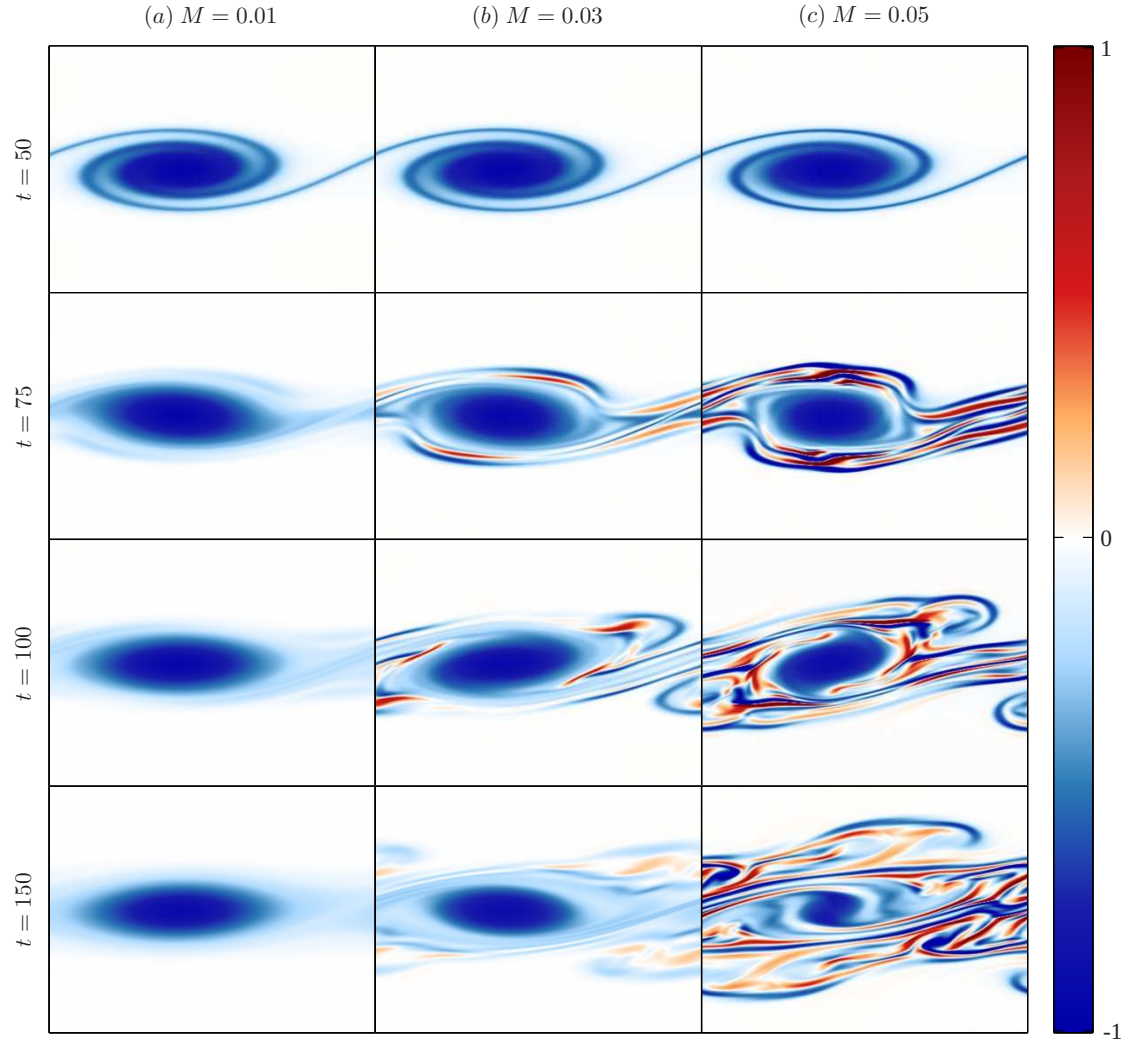

Figure 7.15: Snapshots of potential vorticity at $F = 0.1$ and different values of M for the shear layer (at $\mathrm{Re} = \mathrm{Rm} = 500$). Compare this to Figure 6.9.

saturation level correlated with the degree of disruption observed. In the mildly disruptive cases, the behaviour of the potential energy is similar to that of Figure 7.6, with the perturbation potential energy mimicking the evolution of the perturbation kinetic energy.

As before, we monitor the contributions to dissipation from the sign-definite terms and sign-indefinite terms in the runs; a time-series of these quantities for these three sample runs is given in Figure 7.18. In this case and at this value of F, the contribution from the extra cross terms is several orders of magnitude smaller than the total dissipation, so we expect that the effects of employing this dissipation operator are, for this problem and at this value of F, unlikely to

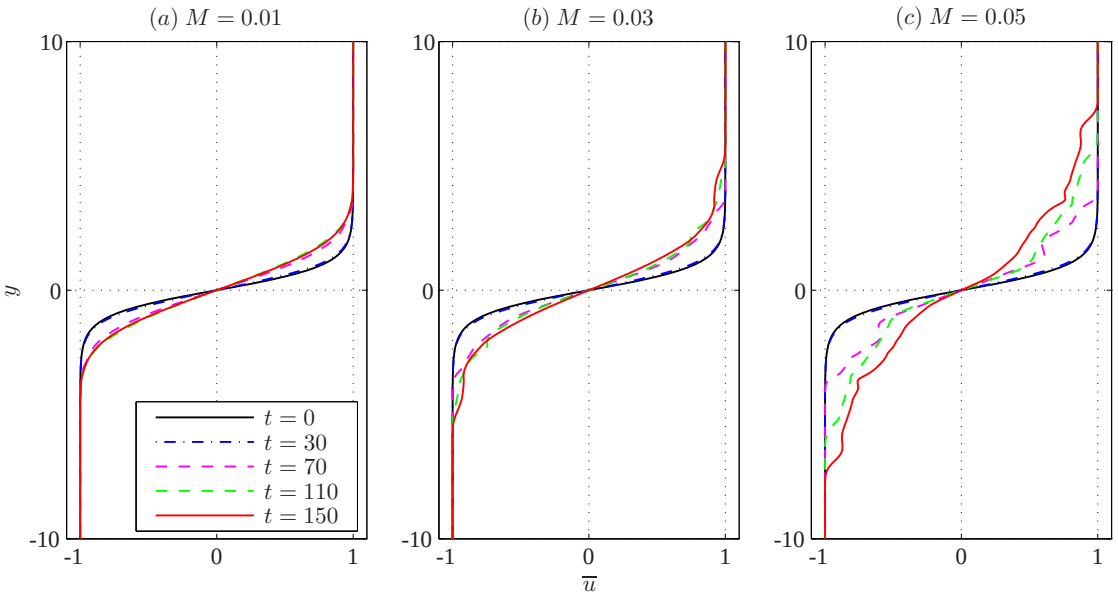

Figure 7.16: Snapshots of $\overline{u}$ with $F = 0.1$ for the shear layer runs (at Re $=$ Rm $= 500$). Compare this to Figure 6.14.

contribute significantly to the resulting dynamics.

We have also looked at the time-series of the other conservation quantities, namely momentum, magnetic flux and mass. The time-series of domain-integrated momentum is again very noisy and the main error comes from the y-momentum signal, which fluctuates about zero with an amplitude of $O(10^{-7})$; the x-momentum is of $O(10^{-11})$ for the duration of the runs. The graph looks similar to the middle panel of Figure 7.8 and have been omitted. The conservation of magnetic flux is very well maintained, with errors for both x- and y-flux kept at no more than $O(10^{-10})$. In light of the well-behaved conservation of the magnetic flux and mass, the corresponding time-series have also been omitted.

To classify the runs, we use again the spectral truncation parameter (equation 6.54, maximised over all times for which we have data for) and the shear layer width expansion factor (equation 6.55, taken at the end time) as a measure of the disruption. The same regime boundaries in the previous chapter given in Table 6.2 and 6.4 are used for comparison purposes, and the same kinematic estimate $M^2\text{Rm} \sim \Omega_e$ as derived previously will be tested with this set of data. The hydrodynamic case has $k_{\text{cut}} = 7$ and an expansion factor of 1, with an initial layer width of 5.92 and an end layer width of 7.54 in our non-dimensional units. The regime diagram is given in Figure 7.19, and the

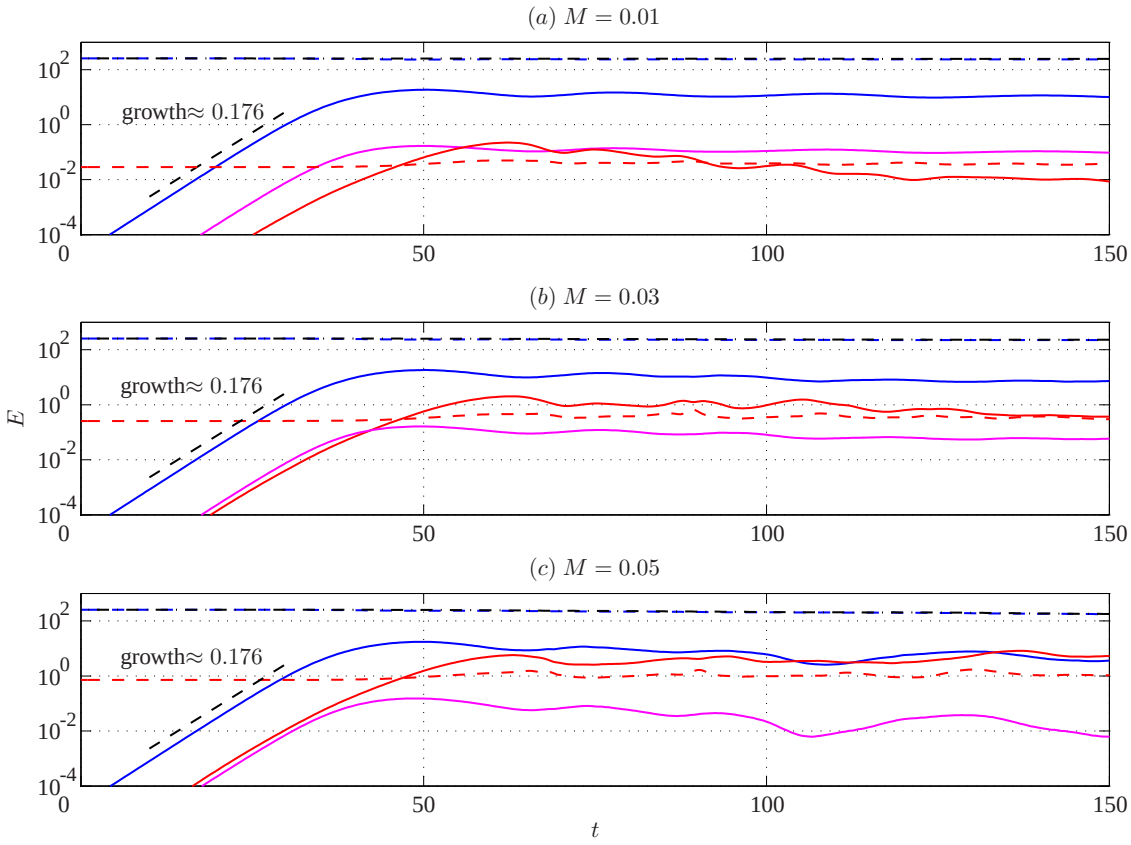

Figure 7.17: Time-series of energies (blue = kinetic; red = magnetic; magenta = potential; solid = perturbation state; dashed = mean state; black dot-dashed line = total energy) for the shear layer runs (at Rm = Re = 500, $F = 0.1$).

raw data in Tables 7.2 and 7.3.

The raw data may be compared with the data for the $F = 0$ case given in Tables 6.3 and 6.5, and only one of the runs has been classified differently. This particular run is on the borderline of the regime boundary in the $F = 0$ case anyway so this discrepancy is not a concern. Consequently, the regime diagram given in Figure 7.19 is largely similar to that for the case $F = 0$ (given by Figure 6.18, without the Rm $= 1000$ data and with one marker changed). We see again that the degree of disruption is well described by the suggested parameter dependence M^2Rm, with $M^2\text{Rm} \geq 0.5$ capturing the runs that are classified as severely disrupted.

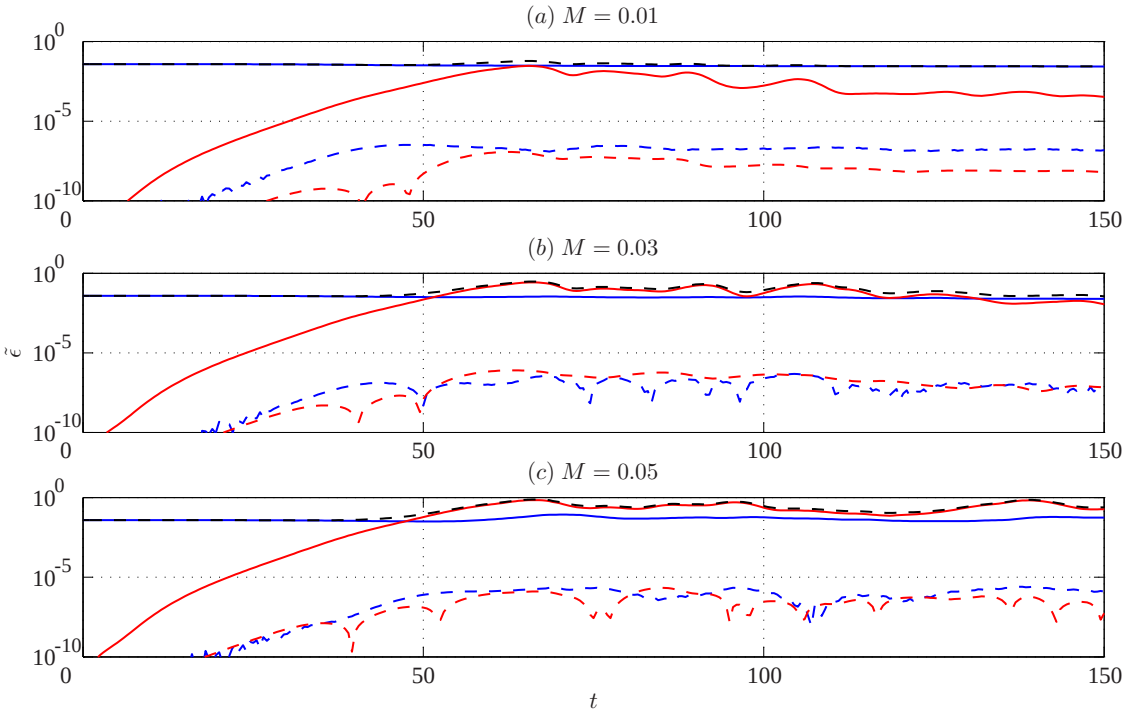

Figure 7.18: Domain-integrated dissipation rate $\tilde{\epsilon}_{\mathrm{Re}}$ (solid curve) and contribution from the cross term (dashed curve), for the shear layer at $F = 0.1$; blue represents the terms associated with momentum dissipation, and red represents the terms associated with flux dissipation.

Rm \ M	0.01	0.02	0.03	0.04	0.05	0.06	0.07	0.1
750	7	18	35	47	42	38	48	54
500	7	7	23	36	44	36	36	44
250	7	7	8	18	25	31	32	26
50	7	7	7	8	8	10	11	13

Table 7.2: Raw data from the set of calculations at Re $= 500$ for the shear layer runs at $F = 0.1$. The numbers denote the truncation wavenumber k_{cut} (taking the maximum over time). The hydrodynamic case at $F = 0.1$ has $k_{\mathrm{cut}} = 7$. See Figure 7.19 for colour codes.

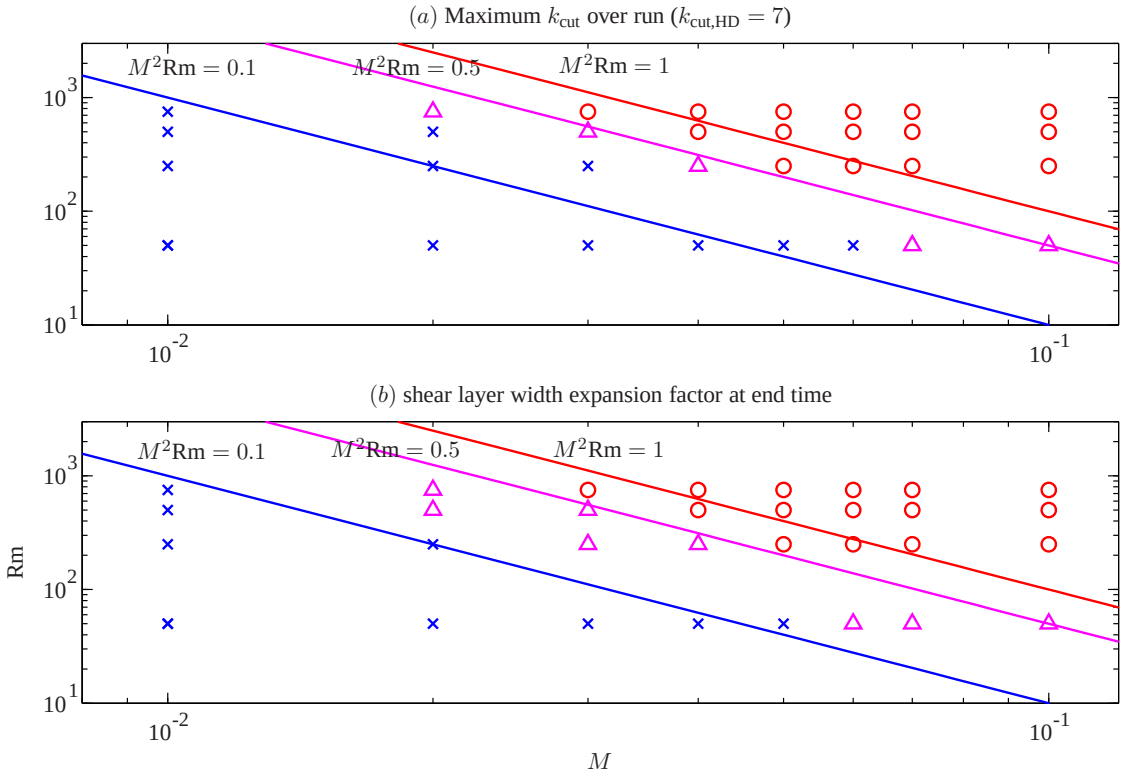

Figure 7.19: Regime diagram for the shear layer runs at $F = 0.1$, as measured by the spectral truncation parameter $k_{\rm cut}$ and via the shear layer width at the end of the run. The suggested boundaries given by $M^2\mathrm{Rm} = C$ are plotted for several values of C. The colours are as before, with blue denoting non-disruptive cases, magenta denoting mildly disruptive cases, and red denoting strongly disruptive cases.

Rm \ M	0.1	0.2	0.3	0.4	0.5	0.6	0.7	0.1
750	1.02	1.19	1.60	1.80	1.94	2.42	2.33	2.57
500	1.02	1.16	1.43	1.71	1.97	2.00	2.14	2.65
250	1.02	1.05	1.26	1.49	1.64	1.86	2.04	2.42
50	1.00	1.02	1.03	1.05	1.07	1.10	1.16	1.36

Table 7.3: Raw data from the set of calculations at $\mathrm{Re} = 500$ for the shear layer runs at $F = 0.1$. The numbers denote the shear layer width expansion factor (relative to the hydrodynamic run at $\mathrm{Re} = 500$ and $F = 0.1$, taken at end time). The expansion factor for the hydrodynamic case is defined to be $f = 1$. See Figure 7.19 for colour codes.

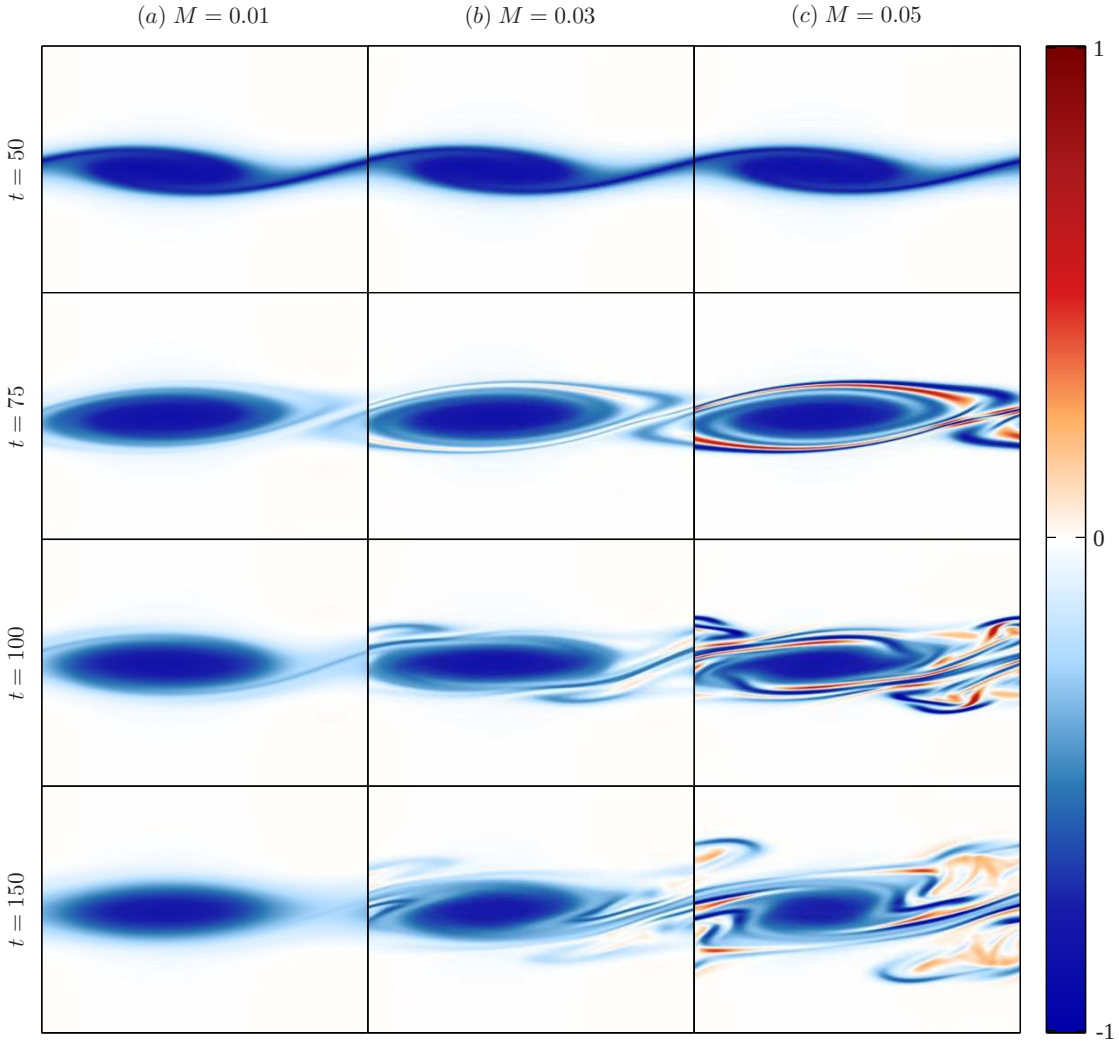

Figure 7.20: Snapshots of vorticity at $F = 0.5$ at some different values of M for the shear layer (at Re $=$ Rm $= 500$).

7.3.2 Hyperbolic-tangent shear layer: $F = 0.5$

Having seen that the small F case does not seem to be very different to the incompressible case, we now consider a case where F is slightly larger. We still use Rm $=$ Re $= 500$, with $M = 0.01$, 0.03 and 0.05 as our three representative cases. We again use $\alpha = 0.44$, even though this is not the optimal wavenumber at these parameter values (the optimal wavenumber here is around $\alpha = 0.40$).

Figure 7.20 shows snapshots of the potential vorticity. Comparing this to Figure 7.15 and 6.9,

we see that the runs appear less disruptive. The $M = 0.01$ case in Figure 7.20(a) resembles the hydrodynamic case, with the vorticity concentrated in the (if somewhat slightly more elongated) vortex. For the $M = 0.03$ case in Figure 7.20(b), there are some hints of vorticity regions outside the vortex but these are distinctly fainter than in the corresponding $F = 0.1$ or $F = 0$ case. The vortex here is of a similar size to the smaller M case, in contrast to the $F = 0.1$ case, where the resulting vortex for $M = 0.03$ is smaller than that for $M = 0.01$. For the $M = 0.05$ case in Figure 7.20(c), this was previously a severely disruptive case at this value of M and Rm, but now the disruption is noticeably milder. Although strong vorticity filaments are seen and the vortex appears to have reduced in size, it retains its integrity up to the end time $t = 150$. A longer run shows that, for this $M = 0.05$ case, the filaments eventually get smeared out but the vortex remains, unlike the analogous case when F is smaller, with the vortex completely destroyed. The equivalent diagrams for current and height do not appear to show any new features and have been omitted.

There are some plausible explanations for this decrease in the observed disruption. One possibility is that the magnetic stresses build up as before, and any stresses that are released act on the fluid column. However, now that the fluid column is also allowed to move vertically, a portion of this built up stress ends up as work done against gravity, and this cushioning effect results in a milder disruption. The suppression of filamentation due to the shorter range of interaction when $F > 0$ has been previously reported by, for example, Waugh & Dritschel (1991).

Figure 7.21 shows snapshots of $\overline{u}$ for these runs. We note that the final time shear layer width of the $M = 0.03$ case is not noticeably different to that of $M = 0.01$, unlike the equivalent diagrams for smaller F given in Figures 7.16 and 6.14. The shear layer width for $M = 0.05$ is also only marginally larger than for the other two cases, unlike the smaller F cases. If we use the shear layer width as a measure of the disruption then we again conclude that, keeping $(M, \mathrm{Rm}, \mathrm{Re}, \alpha)$ fixed, we expect runs to be classified as having suffered a milder disruption with increasing F.

The time-series of the energies are plotted in Figure 7.22. The growth rates are again inferred and these are consistent with the growth rates obtained from the linear calculation. The potential energy for all three runs here is larger than in the equivalent diagram in Figure 7.17, for $F = 0.1$.

In Figure 7.23 we show the domain-integrated dissipation terms. The sign-indefinite contribution is larger here than for $F = 0.1$; however, it is still only a small percentage of the total dissipation. The conservation properties of other quantities have been checked and are well-maintained by the

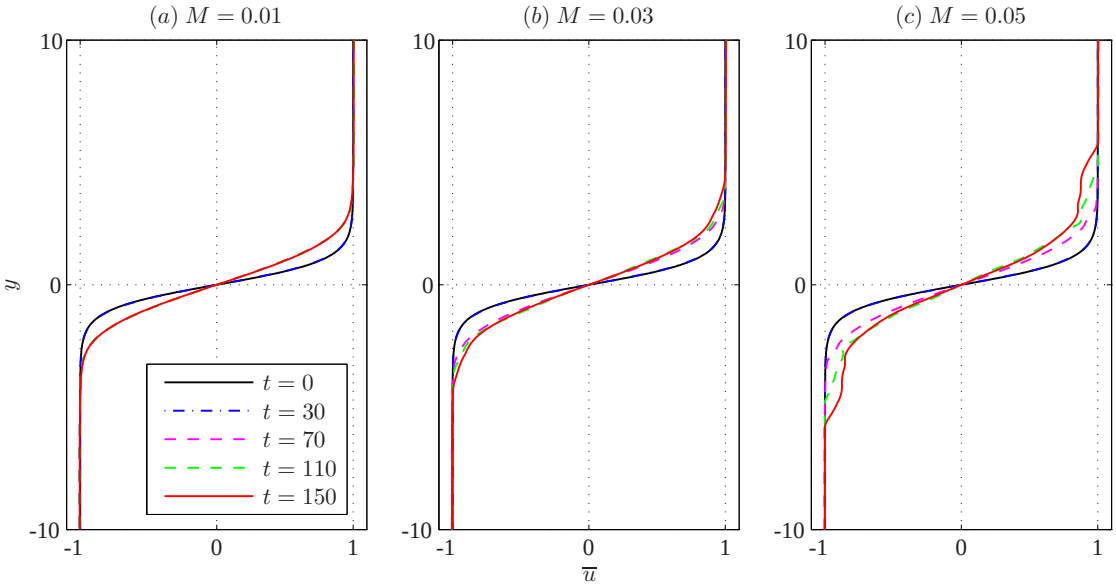

Figure 7.21: Snapshots of $\overline{u}$ with $F = 0.5$ for the shear layer runs (at Re $=$ Rm $= 500$).

Rm \ M	0.01	0.02	0.03	0.04	0.05	0.06	0.07	0.1
750	5	5	24	35	42	42	40	55
500	5	5	15	27	31	29	35	32
250	5	5	5	10	20	23	23	21
50	5	5	5	5	5	6	7	10

Table 7.4: Raw data from the set of calculations at Re $= 500$ for the shear layer at $F = 0.5$. The numbers denote the truncation wavenumber k_{cut} (taking the maximum over time). The hydrodynamic case has $k_{\text{cut}} = 5$.

numerical scheme, with errors do not exceed $O(10^{-7})$; these diagrams have been omitted.

In order to classify the runs and for comparison purposes, we use the same measures and regime boundaries as in the $F = 0.1$ and $F = 0$ cases, measured against the hydrodynamic run at $F = 0.5$. The regime diagram in (M, Rm) space is given in Figure 7.24. The raw data for the MHD runs is given in Tables 7.4 and 7.5, for the spectral truncation parameter and shear layer width expansion respectively; the hydrodynamic run has $k_{\text{cut}} = 5$ (maximised over the times for which we have data) and $f = 1$, with the shear layer width of 7.65 units (taken at $t = 150$).

We observe that there are several runs previously classified as severely/mildly disruptive that are

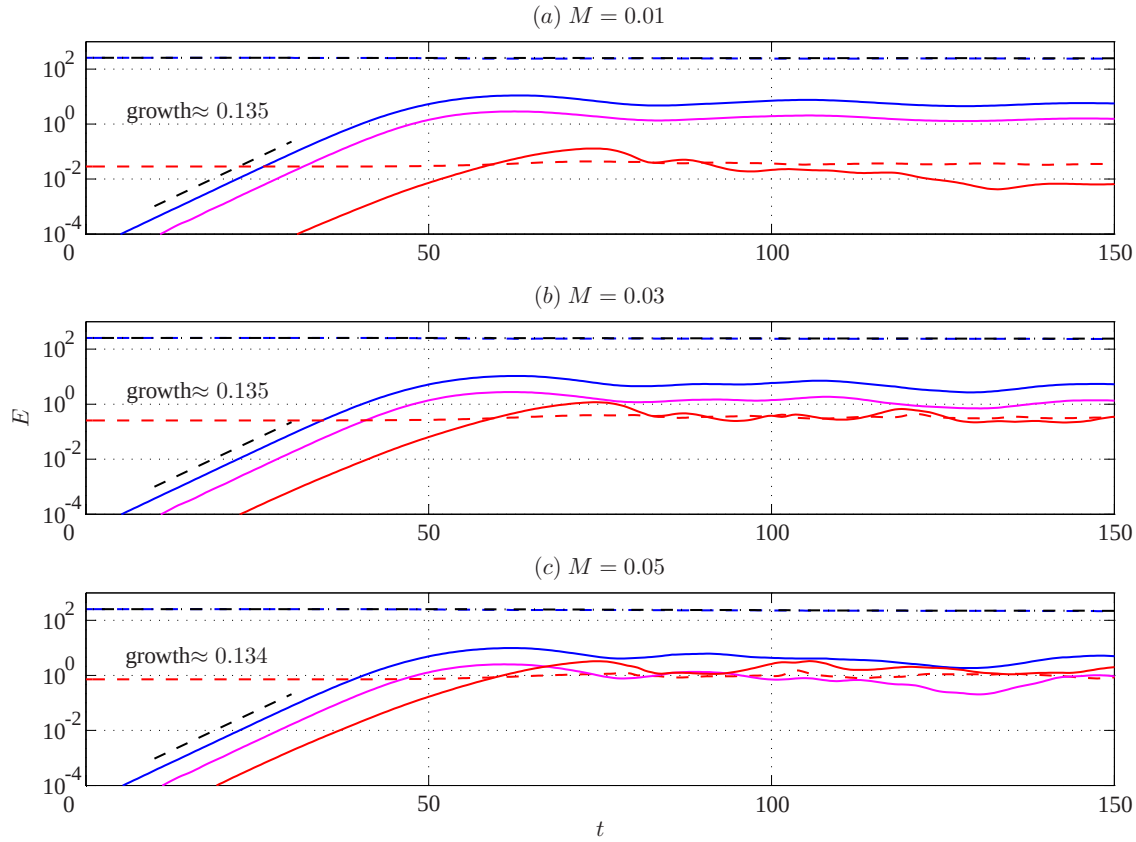

Figure 7.22: Time-series of energies (blue = kinetic; red = magnetic; magenta = potential; solid = perturbation state; dashed = mean state; black dot-dashed line = total energy) for the shear layer runs (at Rm = Re = 500, $F = 0.5$).

Rm \ M	0.1	0.2	0.3	0.4	0.5	0.6	0.7	0.1
750	1.00	1.02	1.13	1.47	1.63	1.60	1.74	2.61
500	1.00	1.01	1.10	1.29	1.48	1.63	1.61	2.09
250	1.00	1.01	1.03	1.15	1.26	1.40	1.53	1.82
50	1.00	1.00	1.00	1.00	1.00	1.01	1.01	1.03

Table 7.5: Raw data from the set of calculations at Re = 500 for the shear layer at $F = 0.5$. The numbers denote the shear layer width expansion factor (relative to the hydrodynamic run at Re = 500, taken at end time). The expansion factor for the hydrodynamic case is defined to be $f = 1$.

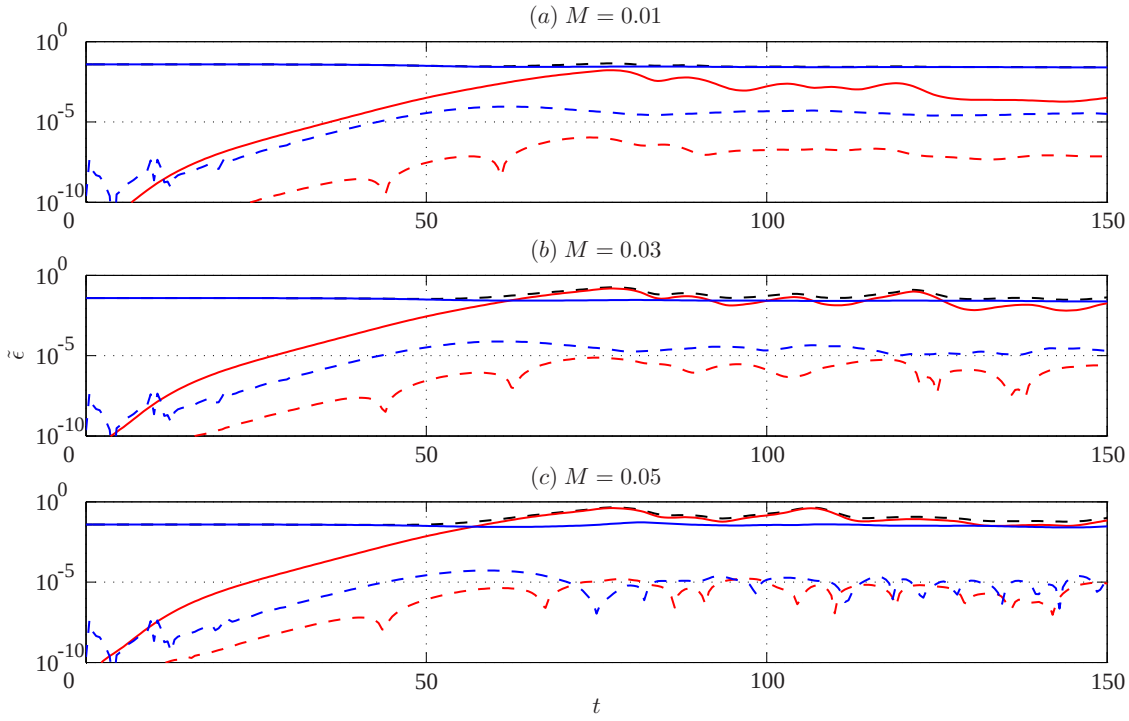

Figure 7.23: Domain-integrated dissipation rate $\tilde{\epsilon}_{\mathrm{Re}}$ (solid curve) and contribution from the cross term (dashed curve) for the shear layer runs at $F = 0.5$ blue represents the momentum dissipation terms, and red represents the flux dissipation terms.

now classified as mildly/non-disruptive. There are also some discrepancies between the two measures. Considering that the regime boundaries were calibrated using only data from the incompressible case, this discrepancy is perhaps not unexpected. The regime changeovers still appear to closely follow the dependence $M^2\mathrm{Rm} = C$ well, at least for the coverage of (M, Rm) space we have here. The region $M^2\mathrm{Rm} \geq 0.5$ now contains some runs that are classified as mildly disruptive, in contrast to the smaller F cases, consistent with the runs generally suffering a weaker disruption at higher F (compared to Figure 7.19). In conclusion, we expect the disruption to follow the dependence $M^2\mathrm{Rm} = f(F)$, with f a decreasing function of F.

7.3.3 Bickley jet: $F < 1$

We have already observed in Section 7.2.2 that the effects of $F \leq 1$ appear to be weak for the nonlinear evolution of the Bickley jet in the hydrodynamic, shallow-water case. In Figure 7.25 we show snapshots of the potential vorticity at $F = 0.5$, again for $\mathrm{Rm} = \mathrm{Re} = 500$, and $M = 0.01$,

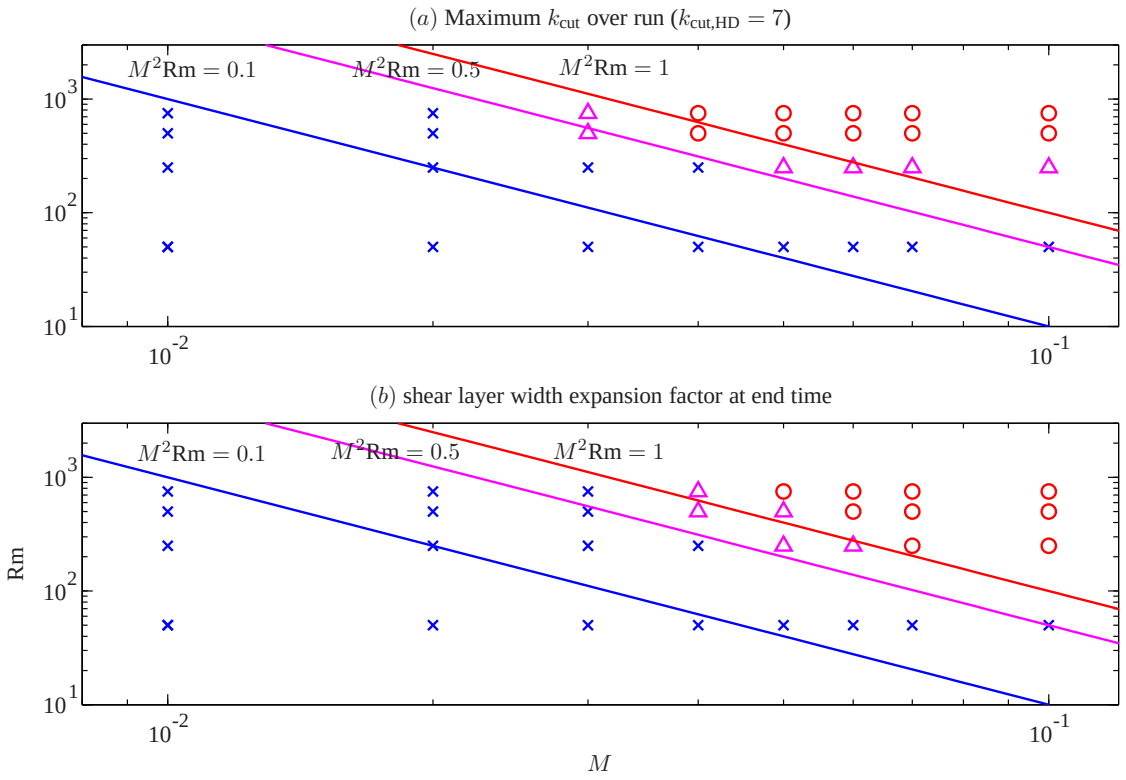

Figure 7.24: Regime diagram for the shear layer at $F = 0.5$, as measured by the spectral truncation parameter k_{cut} and via the shear layer width at the end of the run. The suggested boundaries given by $M^2\text{Rm} = C$ are plotted for several values of C.

0.03, and 0.05 as our representative cases.

We observe here that, compared to Figure 6.20, there are some differences in the transients for the more disruptive cases; however the end result is qualitatively similar, with the appearance of weak bands of vorticity. What is slightly different in this case is that, in the end frame of the $M = 0.05$ case, there appears to be slightly more activity compared to the corresponding $M = 0.03$ case, contrary to the corresponding comparison when $F = 0$ given in Figure 6.20. For the weak field case, the disruption is slight, only deforming the vortices slightly but not destroying them, and the vortices recover their elliptical shape by the end frame. A reduction in the amplitude and spreading of the jet may also be seen in the profiles of $\overline{u}$.

The other diagrams (profiles of $\overline{u}$, time-series of energies, dissipation and conservation of quantities) and the regime diagram are virtually indistinguishable to those given for the incompressible case in Chapter 6 and have been omitted. So it would appear that the effect of

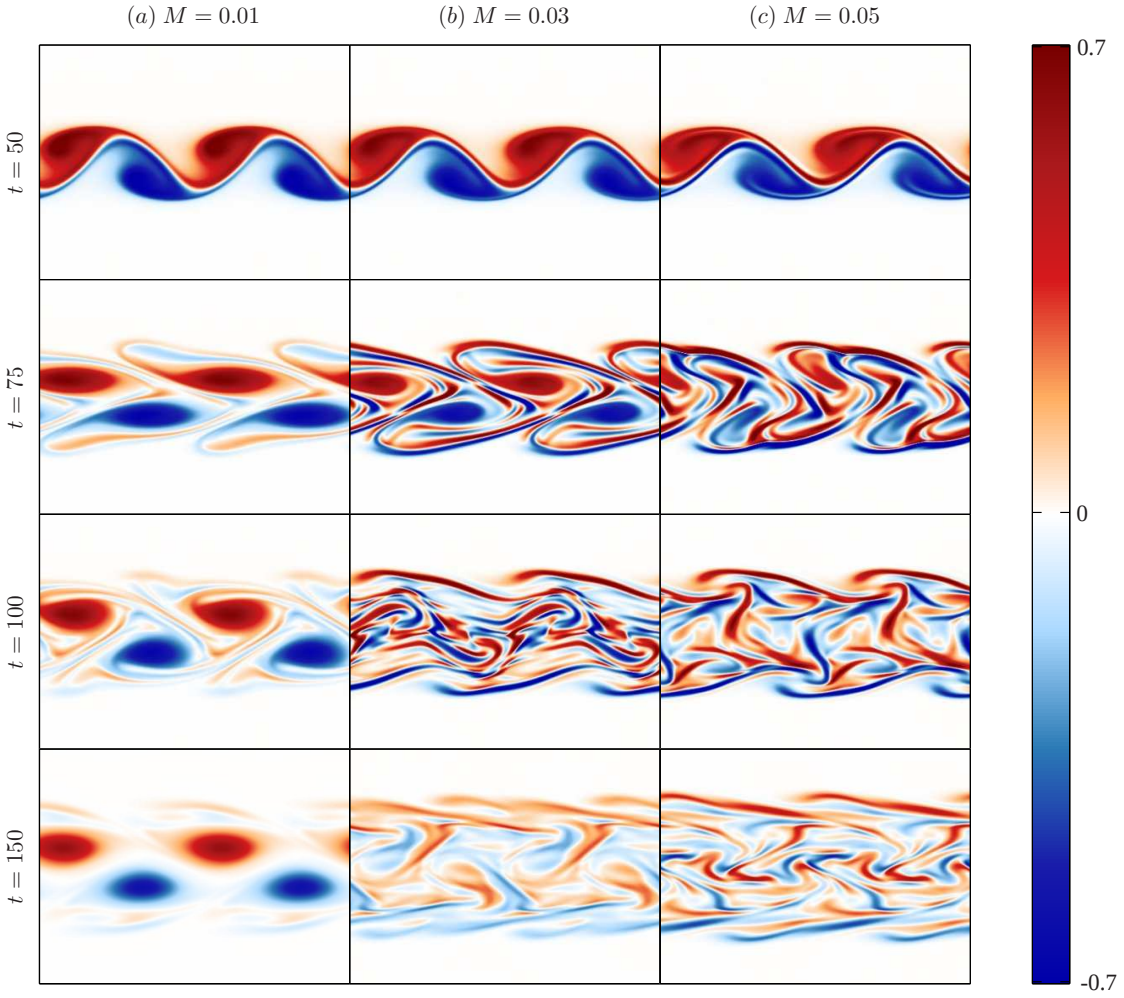

Figure 7.25: Snapshots of potential vorticity at $F = 0.5$ and different values of M for the Bickley jet profile (at Re $=$ Rm $= 500$).

$F \leq 1$ on the evolution of the Bickley is relatively weak. Again, this may not be true when rotational effects are present, since we then expect vortex asymmetry to play a role in the dynamics.

7.4 The case of $F \geq 1$

It would appear that the nonlinear dynamics in the $F < 1$ regime is not significantly different to the $F = 0$ limit, so it is of interest to investigate the $F \geq 1$ regime where, for example, supersonic instabilities are present. However, we ran into some serious numerical problems when considering the $F \geq 1$ cases. In Figure 7.26 we plot the perturbed free surface for a shear layer

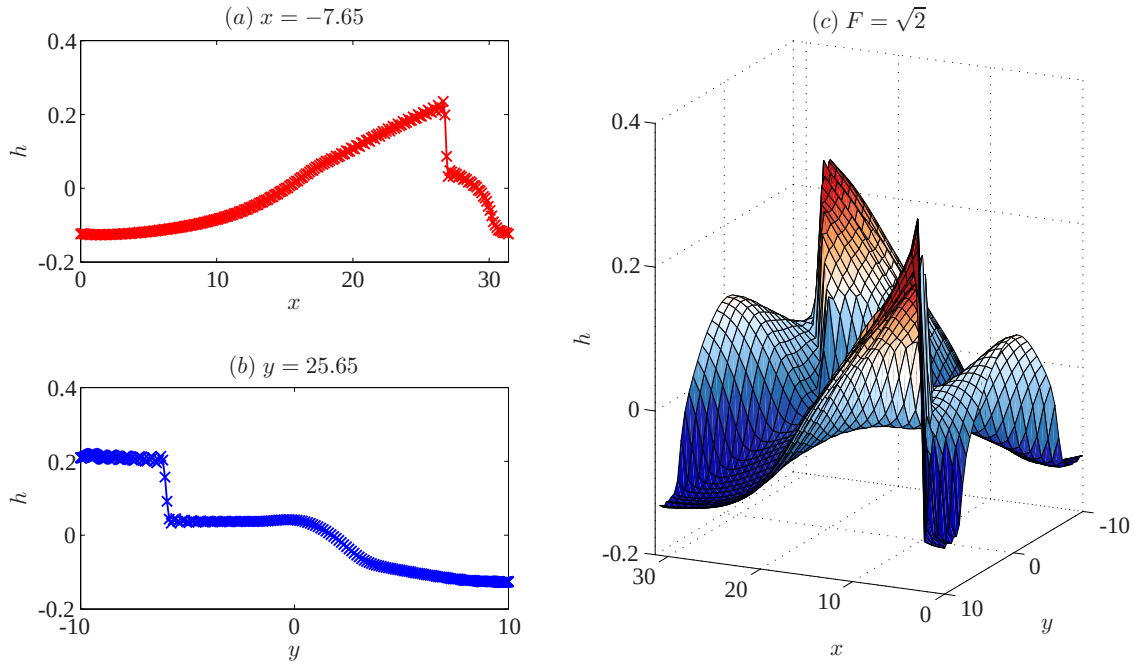

Figure 7.26: Perturbed free surface plots h for the shear layer at $M = 0$, $F = \sqrt{2}$, at a snapshot taken a short while before the numerical routine crashes. (a) and (b) shows cross-sections of h, and (c) shows a surface plot of h. For image rendering purposes, (c) is produced using only a fifth of the total data points.

test run, at $M = 0$ and $F = \sqrt{2}$, initialised using the eigenfunction calculated from linear theory. It can be seen that there is nonlinear steepening of the free surface. Steepening was also observed for the Bickley jet simulations with $F \geq 1$. It is during the nonlinear phase of the instability, where the background flow starts being modified by the perturbations, that we start seeing this steepening. It should be noted that, for the linear shallow-water case, our time-stepping scheme at this CFL number is stable for $F \geq 1$; we still observe steepening when the CFL number has been decreased. The code crashes shortly after this time-snapshot. Overturning of the free surface and shock formation has been observed in previous shallow-water simulations of shear instabilities (e.g., Chu, 2010, and references within), so we believe this steepening is a generic feature arising from the dynamics and is not a numerical artefact.

As shallow-water theory is a long-wave theory (dynamics have a small aspect ratio), shock formation leads to the breakdown of the assumption of hydrostatic balance, and therefore breakdown of shallow-water theory. There are methods to deal with steepening (numerical, modifying or augmenting shallow-water theory) and these are discussed in the discussion section

at the end of this chapter.

7.5 Summary and discussion

We assumed that the free surface is forced to stay a field line, resulting in the condition $\nabla \cdot (h\boldsymbol{b}) = 0$. Putting to one-side the validity of this assumption for the moment, it was seen that seen that the SWMHD equations written in terms of the transport variables $\boldsymbol{U} = h_t\boldsymbol{u}$ and $\boldsymbol{B} = h_t\boldsymbol{b}$, with a Laplacian operator acting on $\boldsymbol{U}$ and $\boldsymbol{B}$ to mimic dissipation, maintain more conservation laws than the analogous approach employing velocity variables. A particularly important point is that our approach here maintains the divergence-free condition $\nabla \cdot \boldsymbol{B} = 0$, implicitly required in deriving the conservation laws even in the ideal case. The approach we employ is particularly convenient to implement in our pseudo-spectral, semi-implicit-in-time approach, but it does not provide a formally negative-definite dissipation. We have though tracked the formally sign-indefinite term in our simulations and have found this extra contribution to be only a small percentage of the total dissipation for our $F < 1$ simulations, so is unlikely to play a significant role in the dynamics. We conjecture that there should be mathematically consistent way of deriving shallow-water with magnetic dissipation, and we suspect that, for our problem, our approach is a good approximation to the 'exact' theory since the errors introduced appear to be small. As fast waves are present, certain terms in the shallow-water system were treated implicitly to relieve the CFL condition. It was also found, via a von Neumann analysis, that the AB/BD2 scheme possessed better stability properties than AB/BD3, so numerical routines for the shallow-water system used AB/BD2 as the time-marching scheme.

We focussed on the $F < 1$ cases. For the shear layer, we again considered the case where the domain supports a single wavelength of the primary instability. We first investigated the effect of increasing F when $M = 0$. At small values of F, small-amplitude gravity waves are present; however, they do not seem to affect the nonlinear dynamics very much, and the evolution was largely like the incompressible case, with a long-lived vortex forming. For larger values of F, small-amplitude gravity waves are again present, although these are at a larger amplitude than the small F cases. The vortex formed is more elongated than for the incompressible and small F cases, but is also seen to be long-lived. When a magnetic field is included, the degree of disruption observed in the small F cases was comparable to the incompressible case. For larger F, however,

the disruption is seen to be milder. One explanation for this is that when the magnetic stresses are released on the fluid column, some of this is converted into deforming the free surface and thus does work against gravity. Like the incompressible case, disruption, when it occurs, is a fast phenomenon, occurring within one or two eddy turnover times after the formation of the vortex.

We also tested our kinematic regime estimate $M^2\mathrm{Rm} \sim \Omega_e$ against the data from the shallow-water runs. We classified the runs using the same regime boundaries as those used in the incompressible case. It is seen that, for small F, the classifications are largely the same as the incompressible case. For larger F, the runs appear to suffer a milder disruption, with some runs that were previously severe/mildly disruptive classified as mildly/non-disruptive. Thus our estimate $M^2\mathrm{Rm} \sim \Omega_e$ over-estimates the degree of disruption at the ranges of M and Rm we covered. The data points still follow the $M^2\mathrm{Rm} = f(F)$ dependence reasonably well, with f a decreasing function of F.

For the Bickley jet, when $F < 1$ in both the hydrodynamic and MHD regime, the evolution is still effectively like the incompressible case, except for the fact that the presence of small-amplitude gravity waves, although these do not appear to influence the vortex dynamics very much. The transients are slightly different but the disruption observed appears to depend mainly on M and Rm and only weakly on F. The regime classifications are also largely similar to the incompressible case and so the results were not presented.

Once F exceeds $O(1)$, there are numerical difficulties for both profiles, where overturning of the free surface was observed. This points to a breakdown of shallow-water theory as the small aspect ratio and hydrostatic balance assumption becomes invalid, and further numerical and/or mathematical modification or a different model is required to investigate the dynamics.

We now provide a discussion of several issues that arose during this investigation, in decreasing order of severity.

Numerical treatment of gravity wave terms

One not so crippling numerical issue we had was that the CFL number required for numerical stability was somewhat low when $F \neq 0$. As a reminder, the nonlinear term $(1 + F^2 h)\nabla h$ was split into a linear term that was treated implicitly, whilst the nonlinear term was treated explicitly. We suspect this decrease in CFL number is due to this explicit treatment of the nonlinear terms,

and it might be an idea to try for a more implicit treatment to give a larger stable time-step. We could treat the nonlinear term as implicitly as possible whilst maintaining linearity at level $n+1$. To do this, we observe that

$$h^{n+1}\nabla h^{n+1} \approx \left(h^n + \Delta t \left.\frac{\partial h}{\partial t}\right|_n + \cdots \right) \nabla h^{n+1}, \tag{7.39}$$

so taking an approximation of the time derivative term using data from level n and $n-1$ (but not level $n+1$ in order to maintain linearity at level $n+1$) gives

$$h_t \nabla h \approx \{1 + F^2[(1+b_0\Delta t)h^n + b_1 \Delta t h^{n-1}]\}\nabla h^{n+1}, \tag{7.40}$$

where the b_i coefficients are given in (7.32). If we then form the equation for h in our semi-implicit approach, we observe that we need to take a divergence of $h_t\nabla h$, and we will end up with an inversion for h that involves operators involving second as well as first derivatives. Not only can we not use the fast solver as we no longer have a Helmholtz equation to solve, we also have spatially varying coefficients multiplying the differential operators. So, in the shallow-water cases, finite-difference/volume methods are perhaps more suitable since no spectral representation (so no convolution sums) is required. Other formulations (in vorticity-divergence or otherwise) may also lead to other numerical schemes (e.g., Mohebalhojeh & Dritschel, 2000, 2001; Dritschel & Viúdez, 2007).

Although we have not considered inserting sponge-layers to absorb outgoing gravity waves (e.g., Durran, 2010, §8), this may be done in principle, to better mimic the free-shear flow problem. In this shear instability problem it is possibly not a major concern as the gravity waves are small-amplitude and do not seem to alter the vortex dynamics all that much. Although not our focus here, in studies of gravity wave generation by shear flows where the outward flux is of concern (e.g., Sutherland *et al.*, 1994; Sutherland & Peltier, 1994; Staquet & Sommeria, 2002; Bakas & Farrell, 2009a,b), ways to stop waves reflecting from the boundaries are required.

Nonlinear steepening when $F \geq 1$

Our investigation was restricted to the regime $F < 1$ where we do not appear to encounter steepening that causes the routines to crash. The $F \geq 1$ region contains, for the shear layer, the portion of parameter space where supersonic modes are unstable, as well as the tongue region (when MHD effects are present), and, for the Bickley jet, the region where perhaps the nonlinear dynamics would be more different than the $F < 1$ case we have considered here.

Steepening points to the breakdown of shallow-water theory, which is a system of equation obtained at leading order in the aspect ratio. Going to the next order in aspect ratio, the equations obtained includes dispersion effects that can counter the steepening; the set of equations are known as the Green–Naghdi equations (Green & Naghdi 1976; see also Dellar 2003b and Pearce & Esler 2010). This may perhaps be required for investigating the dynamics in the region where wave steepening occurs.

There are several numerical methods that deal with nonlinear steepening and shock formation, but we have not tested any of these in any detail to judge their relative merits. One possibility is to employ a dissipation of h as in Poulin & Flierl (2003); such a dissipation may represent physical mechanism (e.g., radiative damping), and its additional consequences on the conservation laws have already been discussed. A second possibility is to employ shock capturing methods used in compressible or shallow-water dynamics (e.g., Toro, 2001; Chu, 2010), and these would involve using a finite-difference/volume method. One other possibility that prevents nonlinear steepening in shallow-water is to modify the pressure term ∇h in the momentum equation appropriately, as in Bühler (1998).

Form of the dissipation

We have already highlighted that finite magnetic diffusivity implies field line slippage, something that is not entirely consistent with the derivation of the SWMHD equations as we have here. Another potential problem is that the dissipation that we did employ does not guarantee a sign-definite energy dissipation. We discuss the latter point before the more fundamental question of the self-consistency of the SWMHD system when finite magnetic diffusion is present.

We consider first the form of momentum dissipation. The problems associated with the form of momentum dissipation in the hydrodynamic case have been previously discussed in the literature (e.g., Ochoa *et al.*, 2011; Gilbert *et al.*, 2013). The recent papers of Ochoa *et al.* (2011) and Gilbert *et al.* (2013) conclude that, to ensure momentum conservation, the dissipation should be expressed in terms of the divergence of a symmetric stress tensor, with the correct factors of h to account for the fact that momentum in shallow-water is given by $\boldsymbol{U} = h\boldsymbol{u}$ (see also Bühler, 2000). It then remains to check whether we have negative-definite energy dissipation. The form of dissipation employed here, given by $\nabla^2\boldsymbol{U}$ in the transport variable formulation (corresponding to option III of Ochoa *et al.* 2011) satisfies the momentum condition, but does not give a formally

negative-definite dissipation. Other forms of the dissipation that do maintain momentum and negative-definite dissipation are given in Ochoa *et al.* (2011) and Gilbert *et al.* (2013). None of these are particularly well suited to a pseudo-spectral, semi-implicit-in-time treatment, because the terms are nonlinear in the fundamental variables, so finite-difference/volume methods are perhaps better suited for this line of investigation.

With regards to the form of the magnetic dissipation, we have noted that, if we were to enforce the frozen-in property, then we would need a magnetic dissipation that maintains the divergence-free condition in the magnetic field. A general form of magnetic dissipation that satisfies this property was suggested by Andrew Gilbert (private communication); see Section 7.6. The main point is although there is the possibility for a magnetic diffusion that also gives negative-definite dissipation of magnetic energy, the dissipation terms appear in nonlinear combinations, much like the issue encountered in the choice of momentum dissipation. Again, a finite-difference/volume approach is perhaps more suitable to implement these types of dissipation.

Returning to the more fundamental question of self-consistency, we argued that, for phenomena on short dynamical time-scales such as shear flow instabilities, the frozen-in approximation is perhaps a plausible one. Although our method is *ad hoc*, we conjecture that it is perhaps a good approximation to the 'exact' theory, to be derived self-consistently starting from the Boussinesq three-dimensional MHD equations, because the errors introduced with our approach is small and our integration times are short. The same argument is almost certainly not going to be true for studies that require dynamics to be simulated on resistive time-scales, such as turbulence or dynamo problems (overlooking the possibility of an anti-dynamo theorem for the moment). Studies that do utilise the SWMHD equations with finite magnetic diffusivity and the frozen-in approximation need to justify not only the form of the dissipation used, but also the validity of the underlying approximations on a case by case basis. As a case in point, we feel that this issue has not been appropriately addressed in the article by Lillo *et al.* (2005), who study the possibility of dynamo action in some sort of system resembling the SWMHD system here. As we have alluded to already, there is also the possibility of anti-dynamo results depending on the form of the dissipation if the frozen-in approximation is used (see Section 7.6).

It should be possible to derive a self-consistent form of the SWMHD equations with dissipation included in the derivation by, for example, matching the magnetic field in the fluid layer onto some external magnetic field profile. The question then is whether the approximations that are required

are realistic, and whether one actually gains anything from doing an approximation, as some of the advantages of employing the shallow-water system (such as the system being explicitly dependent on only two spatial dimensions) may be lost. The derivation of the SWMHD system with field-line slippage has not been investigated in much detail here, but is a fundamental question that needs to be addressed, especially if the SWMHD system is to be employed for modelling nonlinear physical phenomena, such as global tachocline or hot exoplanet dynamics.

7.6 Appendix A: Other forms of magnetic dissipation in SWMHD

In the absence of dissipation in the continuity equation, consider

$$\frac{\partial \boldsymbol{B}}{\partial t} + \nabla \cdot \left(\frac{\boldsymbol{U}\boldsymbol{B}}{h_t} - \frac{\boldsymbol{B}\boldsymbol{U}}{h_t} \right) = \frac{h_t}{\mathrm{Rm}} \mathsf{D}, \tag{7.41}$$

with

$$h_t \mathsf{D} = -\nabla \times (h_t^p \nabla \times (h_t^q \boldsymbol{b})), \tag{7.42}$$

where p and q are free parameters for the moment and h_t is the total fluid column (Andrew Gilbert, private communication). The factor of h_t multiplying D is to account for dissipation of the total fluid column. It is obvious that this form of dissipation maintains the divergence-free condition of the magnetic field, and reduces accordingly in the incompressible case. The case that we used in (7.10), in transport variables with $\nabla^2 \boldsymbol{B}$ (where only energy dissipation was an issue), is the case where $p = 0$ and $q = 1$. In general, we have

$$\begin{aligned} \frac{1}{2}\frac{\mathrm{d}}{\mathrm{d}t} \iint h_t |\boldsymbol{b}|^2 \, \mathrm{d}x\mathrm{d}y &= \cdots + \iint h_t \boldsymbol{b} \cdot \frac{\partial \boldsymbol{b}}{\partial t} \, \mathrm{d}x\mathrm{d}y \\ &= \cdots + \frac{1}{\mathrm{Rm}} \iint h_t \boldsymbol{b} \cdot \mathsf{D} \, \mathrm{d}x\mathrm{d}y \\ &= \cdots - \frac{1}{\mathrm{Rm}} \iint h_t^p (\nabla \times \boldsymbol{b}) \cdot (\nabla \times (h^q \boldsymbol{b})) \, \mathrm{d}x\mathrm{d}y. \end{aligned} \tag{7.43}$$

Then we see that, for our case ($p = 0$ and $q = 1$), the energy dissipation is not negative-definite, as observed already. If instead we take $p = 1$ and $q = 0$, then we have a negative-definite dissipation, with the dissipation related to the domain integrated current $\iint h_t j^2 \, \mathrm{d}x\mathrm{d}y$. The numerical advantage of the $p = 0$, $q = 1$ case is that it leads to terms that are particularly easy to treat in our pseudo-spectral formalism. The $p = 1$, $q = 0$ case contains nonlinear terms which may be treated accordingly in the finite-difference/volume approach, in contrast to the pseudo-spectral approach we employed here.

7.6.1 Anti-dynamo result

The following results are also due to Andrew Gilbert (private communication), included here for completeness. In the ideal SWMHD system, the induction equation in terms of the flux function (with $h_t = 1 + F^2 h$)

$$h_t \boldsymbol{b} = \mathrm{e}_z \times \nabla A \tag{7.44}$$

is given by (Dellar, 2002)

$$\frac{\partial A}{\partial t} + \boldsymbol{u} \cdot \nabla A = 0. \tag{7.45}$$

With our choice of dissipation, $p = 0$ and $q = 1$ in equation (7.42), we have

$$\frac{\partial A}{\partial t} + \boldsymbol{u} \cdot \nabla A = \frac{1}{\mathrm{Rm}} \nabla^2 A. \tag{7.46}$$

In the shallow-water case, the argument is that the maximum point $A = A_{\max}$ cannot increase in time and so there is no dynamo, at least in terms of magnetic flux. In full, suppose we have

$$A_{\max}(t) = A(\boldsymbol{x}_{\max}(t), t)). \tag{7.47}$$

Then

$$\nabla A\big|_{\boldsymbol{x}_{\max}} = 0, \qquad \nabla^2 A\big|_{\boldsymbol{x}_{\max}} \leq 0, \tag{7.48}$$

and so

$$\begin{aligned} \frac{\mathrm{d}A_{\max}}{\mathrm{d}t} =& \frac{\mathrm{d}\boldsymbol{x}_{max}}{\mathrm{d}t} \cdot \nabla A\big|_{\boldsymbol{x}_{\max}} + \frac{\partial A_{\max}}{\partial t} \\ =& - \boldsymbol{u} \cdot \nabla A\big|_{\boldsymbol{x}_{\max}} + \frac{1}{\mathrm{Rm}} \nabla^2 A\big|_{\boldsymbol{x}_{\max}} \leq 0. \end{aligned} \tag{7.49}$$

The maximum $A_{\max}$ cannot increase, so a dynamo that has increasing magnetic flux with time is impossible.

For the case $p = 1$ and $q = 0$ which gives negative-definite dissipation, it may be shown that the induction equation in terms of the streamfunction is given (in our notation) by

$$\frac{\partial A}{\partial t} + \boldsymbol{u} \cdot \nabla A = \frac{1}{\mathrm{Rm}} \nabla^2 A - \frac{1}{\mathrm{Rm}} \frac{F^2}{1 + F^2 h} (\nabla h) \cdot (\nabla A). \tag{7.50}$$

When $F = 0$ this reduces to the incompressible case. A similar anti-dynamo result may be shown since the extra term has a ∇A contribution, which is zero at $\boldsymbol{x}_{\max}$.

7.7 Appendix B: Numerical scheme when $F = 0$

When $F = 0$, the inversion for h in (7.37) becomes ill-defined when $k = 0$ since we have a second order differential equation with two Neumann boundary conditions. This corresponds to the issue that, in the incompressible case, pressure effectively acts as a Lagrange multiplier to ensure incompressibility at every time-step, but since it only appears through a derivative (unlike the shallow-water case where there is a specific evolution equation for h), the mean component

of the pressure is defined up to a constant. Although this mean component plays no role in the dynamics, it does however lead to a non-unique inversion. To fix this constant, we observe that, in the incompressible case, the Poisson equation for p is given by

$$\nabla^2 p = \nabla \cdot (\boldsymbol{u} \cdot \nabla \boldsymbol{u} - M^2 \boldsymbol{b} \cdot \nabla \boldsymbol{b}) + \frac{1}{\mathrm{Re}} \nabla^2 \boldsymbol{u}. \tag{7.51}$$

Taking an x-average, using the divergence-free conditions for $\boldsymbol{u}$ and $\boldsymbol{b}$, and the condition $\partial u/\partial y = 0$ on the y-boundaries, we end up with

$$\frac{\partial^2 \overline{p}}{\partial y^2} = \frac{\partial^2}{\partial y^2} (\overline{v^2 + M^2 b_y^2}). \tag{7.52}$$

Integrating once gives

$$\frac{\partial \overline{p}}{\partial y} = 2 \left(\overline{v \frac{\partial v}{\partial y} + M^2 b_y \frac{\partial b_y}{\partial y}} \right) + C. \tag{7.53}$$

The constant C is zero since $\partial p/\partial y$, v and b_y are zero on the y-boundaries. Integrating once again gives another constant that is irrelevant for the dynamics, hence may be set to zero. We notice then since v and b_y are zero on the boundaries, then $\overline{p} = 0$ on the boundaries also. To implement this in our numerical routine, an extra option was written in so that, when $F = 0$ and $k = 0$, instead of implementing homogeneous Neumann conditions on both walls (solved using the fast solver), one of the boundary conditions was changed to a homogeneous Dirichlet condition (to take into account we set the constant to be zero) and solved using LU decomposition.

Chapter 8

Conclusions and further work

8.1 Summary of results

We have investigated the problem of shear flow instabilities in the single layer SWMHD system, in planar geometry with no rotation. General properties of the SWMHD system were reviewed, paying particular attention to the conservation properties.

For the onset of the instabilities, the linearised problem was first formulated in the usual manner, looking at the temporal evolution of normal mode solutions and formulating an eigenvalue problem. Some results for general basic states were derived. We then focussed on the simpler problem with no underlying topography and a uniform background magnetic field. Instability characteristics of two piecewise-constant profiles, the vortex sheet and the rectangular jet, and two smooth profiles, the hyperbolic-tangent shear layer and the Bickley jet, were investigated via numerical and asymptotic methods. For the shear layer, two modes of instabilities were identified, the inflection-point and supersonic instabilities. The inflection-point instabilities have larger growth rates, are standing waves, resemble the vortex sheet instability at small α, and their associated instability mechanism is normally attributed to the constructive interference of a pair of counter-propagating Rossby waves. The supersonic instabilities are found when $F > 1$, have growth rates that are smaller than the inflection-point modes, arise as a pair of propagating waves, and the associated instability mechanism is normally attributed to gravity wave interaction with critical layers. The Bickley jet was found to possess two modes of instability, classified as either even or odd about $y = 0$. For the shear layer, the instabilities close to the $F = 0$, $M = 0$

case are normally attributed to counter-propagating Rossby waves, and here we also investigated modifications to this mechanism introduced by shallow-water and MHD effects. It was seen that the underlying Rossby wave action-at-a-distance mechanism generates vorticity anomalies that counteract the basic mechanism, leading to stabilisation of the instability. A long-wave asymptotic procedure was employed to provide analytical expressions to complement the numerical results.

For the nonlinear evolution, it was seen that vortices that form as the shear layer rolls up or as the jet profile breaks up may suffer disruption when MHD effects were present. Focussing first on the incompressible case, this disruption was seen to depend on the basic field strength M and the magnetic dissipation parameter, here characterised by the magnetic Reynolds number Rm. An estimate from a kinematic argument suggests that the dependence of the disruption on the parameter values scales as $M^2\mathrm{Rm} \sim \Omega_e$, where Ω_e is the typical vorticity magnitude of the vortices formed. A range of runs from both profiles were classified accordingly and it was seen that the data conforms well to the $M^2\mathrm{Rm}$ dependence. Although we have restricted ourselves to studying the dependence of M and Rm, some tests runs at larger Re suggests that disruption is more severe also at increasing Re; this is perhaps expected as the dissipation acts less on the vorticity filaments, prolonging it's lifetime, contribution to the amount of small-scale activity. In the shallow-water case, we focussed on the $F < 1$ case as $F \gtrsim 1$ appears to lead to overturning of the free surface, and thus leads to the breakdown of shallow-water theory as the initial assumptions used in deriving the set of equations becomes invalid. For small values of F, the evolution was essentially like the incompressible case. For the shear layer at moderate values of F, it was seen that the disruption appears to be milder. For the Bickley jet, all $F < 1$ cases appear to be qualitatively similar, with minimal differences between these $F < 1$ runs and the incompressible runs, except for the presence of small-amplitude gravity waves, which do not seem to interact significantly with the vortical motions. The kinematic estimate $M^2\mathrm{Rm} \sim \Omega_e$ was tested against the numerical data from the shallow-water runs, and the degree of disruption appears still to depend closely on $M^2\mathrm{Rm}$.

More in-depth summaries and relevant discussions may be found at the end of the individual chapters.

8.2 Conclusions

We have provided a thorough investigation into the characteristics of shear instabilities associated with free-shear flows, focusing on shear layer and jet profiles. In particular, we have attempted to provide an investigation into the underlying instability mechanism and its modifications by other physical effects.

With regards to disruption by MHD effects, since Rm is typically large in astrophysical systems of interest and the fact that disruption occurs on dynamical time-scales (no more than a few eddy turnover times), we expect disruption to be a robust feature in unstable shear flows, causing the breakdown of coherent structures and the transition of laminar flows into chaotic, turbulent motion. The key feature of these secondary resistive instabilities is that they may operate in strongly stratified systems with large Richardson number when other secondary hydrodynamic instabilities are comparatively weak.

Our disruption estimate $M^2\mathrm{Rm} \sim \Omega_e$ is a kinematic one, relying only on the fact that vortices wind up the magnetic field. It should therefore serve as a first estimate even for shear flows in other physical systems, for example, where the system is stratified and velocity shear is in the vertical, i.e. the Kelvin–Helmholtz scenario. The extent to which the kinematic estimate is true has not been investigated for the large Rm region as larger runs are required.

Understanding the breakdown of coherent structures into turbulent motion is not only interesting from a fluid dynamical point of view, but it also has important physical consequences. One such example is in turbulent mixing, physically relevant in both geophysical and astrophysical systems. We have not looked at the consequences on mixing in this case, but it is certainly an interesting problem to consider in the future.

8.3 Some possible further work

Extension of Ripa's theorem

As mentioned in Chapter 3 and 5, one result in shallow-water that we have not managed to generalise to the SWMHD system is an analogue of Ripa's theorem (Ripa, 1983). Ripa's theorem states that, for the rotating, hydrodynamic shallow-water system in planar geometry,

if the Rayleigh–Fjørtoft condition (for potential vorticity) and a subsonic condition is satisfied, then the basic state is formally stable, i.e. linearly stable to infinitesimal disturbances. The approach adopted in the derivation is to make use of the underlying symmetries possessed by the equations to construct a norm and to find the extremal states via a variational problem, an idea dating back to Arnol'd (1965a,b, 1966a,b). These norms may be constructed directly from the governing equations although some ingenuity may be required (e.g., Taylor, 1915; Drazin & Howard, 1966; Bretherton, 1966b; Blumen, 1971; Satomura, 1981; Eliassen, 1983), or may be constructed more systematically for general ideal fluid systems by making use of the underlying Hamiltonian structure (e.g., Holm *et al.*, 1985; Shepherd, 1990). For the shallow-water system, Ripa's theorem may be derived via this method (Shepherd 1990, 1992; see also Ripa 1991 for the multi-layer case), while in the incompressible MHD case, Rayleigh–Fjørtoft type stability criteria have been derived previously via similar methods (e.g., Holm *et al.*, 1985; Vladimirov & Moffatt, 1995; Vladimirov *et al.*, 1996). The SWMHD system has been shown to possess a Hamiltonian structure (Dellar, 2002, 2003a), and it remains to derive stability conditions for this system; this is currently being investigated.

Modification to the Rossby wave mechanism by other physical effects

In Chapter 5 we attributed the inflection-point instabilities to interacting Rossby waves, and considered modifications to the underlying mechanism when other physical effects were involved. It should be possible to quantify in more detail the modification of the Rossby waves by MHD effects. One approach is to consider the piecewise-linear mixing layer profile (sometimes known as the Rayleigh strip), which may be solved exactly in the hydrodynamic case. The mathematical basis appears to be well established (e.g., Heifetz *et al.*, 1999, 2004; Heifetz & Methven, 2005; Heifetz *et al.*, 2006; Harnik & Heifetz, 2007; Heifetz *et al.*, 2009; Carpenter *et al.*, 2012), employing, for example: the Generalised Stability Theory formalism of Farrell & Ioannou (1996a,b) to obtain information about the optimum configuration and information about transient growth; pseudo-energy/momentum (related also to the Hamiltonian formalism discussed earlier) to quantify wave activity responsible for instability in simulations; wave kernels (or Green's functions) to described the wave-interaction effects. It would be informative to see how the inclusion of a background magnetic field would alter the underlying Rossby (or Rossby-Alfvén) wave dynamics and its role in generating the instability.

Supersonic modes, gravity wave interaction, and over-reflection

As demonstrated in the shallow-water system, instability can also arise owing to gravity wave interaction with critical layers in the system (e.g., Satomura, 1981; Hayashi & Young, 1987; Takehiro & Hayashi, 1992; Balmforth, 1999). It would be interesting to further investigate these supersonic modes via the WKB/numerical approach of Takehiro & Hayashi (1992) and the matched asymptotics approach of Balmforth (1999) in the SWMHD system. Related to wave interaction is the process of over-reflection (e.g., Acheson, 1976; Lindzen & Tung, 1978; Lindzen, 1988; Benilov & Lapin, 2013). There have also been attempts to interpret the over-reflection phenomenon by an analogous Rossby wave action-at-a-distance mechanism (Harnik & Heifetz, 2007). It would also be interesting to see in detail the MHD modifications to the underlying mechanisms associated with gravity waves, in order to provide a better understanding of phenomena associated with magneto-gravity waves.

Disruption mechanism and regime estimates

A fairly simple extension of the work carried out here would be to test the kinematic estimate $M^2\mathrm{Rm} \sim \Omega_e$ with larger runs at higher Rm and Re, and to see how well this estimate extends into parameter space. The probing of parameter space would employ the kinematic estimate as a guide to where to look, and to see whether the $M^2\mathrm{Rm}$ dependence holds true for more extreme values in parameter space.

Going beyond the kinematic estimate, it would be desirable to obtain estimates that consider the full dynamical problem so that effects in the incompressible and shallow-water regimes are taken into account. A dynamical estimate was previously given for the magneto-convection by Galloway *et al.* (1978); see also the numerical investigation in Galloway & Moore (1979). Although the physical settings are different, it should be possible to adapt their asymptotic techniques to our problem in order to provide estimates of the magnetic field strength before disruption occurs. An even simpler problem may be to consider a vortex in a doubly-periodic box (as in Weiss 1966), but with dynamical feedback. Some test runs of this vortex-in-a-box problem have shown that the vortex may also be disrupted by MHD effects, so this problem would complement our shear flow study in understanding the underlying mechanism, as well as providing another testing ground for our theoretical predictions.

One component in the disruption mechanism that we have not been able to clarify is the resistive instability leading to release of magnetic stresses. We suspect that it is a tearing-type instability, since tearing instabilities tend to be the fastest growing instabilities in thin currents. Larger resolution runs should provide more data and possibly show clearer signatures of the resistive instabilities in these thin current sheets. We also have the shear flow as well as vortex-in-a-box problem as testing grounds to investigate the nature of the resistive instabilities in current sheets arising from vortical motion.

A complementary approach to the pseudo-spectral method we have employed here would be to consider the vortex in a box problem and/or the shear flow problem using contour dynamics, such as the Contour Advective Semi-Lagrangian algorithm (CASL; e.g., Mohebalhojeh & Dritschel, 2009) or the newer version, the Combined Lagrangian Advection Method (CLAM; e.g., Dritschel & Fontane, 2010). The routines are based on semi-Lagrangian methods advecting (potential) vorticity contours, and are formally Re $= \infty$ methods (the process of contour surgery removes small-scale, sharp features not covered by the numerical resolution). The CASL/CLAM codes have been tested in various settings and are known to be able to reproduce results obtained via, for example, pseudospectral methods, at an impressive fraction of the cost in terms of both time and computing power (e.g., Dritschel & Scott, 2009). The MHD version of CLAM has been employed in a recent study of two-dimensional MHD turbulence (Dritschel & Tobias, 2012) and it was seen that the results are comparable to runs performed using pseudospectral methods, for low magnetic Prandtl number ($\nu \ll \eta \ll 1$), again at a tiny fraction of the cost. This would provide another approach for investigating the dependence of the dynamics on Re.

$F \geq 1$ regime and shallow-water with dissipation

We have not been able to investigate the nonlinear evolution of shear flows in the $F \geq 1$ regime because of nonlinear steepening leading to overturning of the free surface. Shock formation is something that our numerical routines cannot deal with at the moment, but also points to the breakdown of shallow-water theory, since the initial assumptions (small-aspect ratio and hydrostatic balance) become invalid. Other models, such as shallow-water theory with dispersion (Green–Naghdi equations for example), will be required for probing the dynamics at the regimes where steepening occurs.

As discussed already in Chapter 8, the forms of dissipation that provide the desired conservation

properties (such as momentum and magnetic flux conservation, negative-definite dissipation of energy, maintenance of the divergence-free conditions) occur in nonlinear combinations of the fundamental variable, which causes problems in a pseudo-spectral but not in a finite-difference/volume approach. Our choice of dissipation in the $F < 1$ regime led to extra sign-indefinite contributions to energy dissipation (although these were seen to be small for this dynamical problem), and it would certainly be more satisfactory if we use something that gives us the desired physics, including conservation of various quantities and dissipation being negative-definite.

At a more fundamental level, the self-consistency issue of SWMHD with finite magnetic dissipation needs to be addressed if the SWMHD system is to be used as model of, for example, the solar tachocline. It should be possible to include finite magnetic dissipation in the derivation, starting from the Boussinesq incompressible MHD equations, perhaps by matching onto some sort of external magnetic field profile, leading to some other set of equations. It then remains to see whether we can do the approximation in such a way as to preserve certain conservation laws, and whether such an approximation is in fact beneficial as we may lose, for example, the two-dimensional aspect of shallow-water. On the other hand, since we expect there to be no dynamo when magnetic flux is conserved in the layer of fluid, we may have the possibility of dynamo action when the flux conservation is relaxed.

Other physical effects: stratification, rotation, geometry, etc.

Beyond our simple case of a single-layer, non-rotating, shallow-water system in planar geometry, various extensions are possible. For example, multi-layer models may be considered to mimic stratification; a derivation of the multi-layer models has been achieved (Sam Hunter, private communication), assuming that magnetic flux is conserved in each layer. This system should serve as a simplified model for investigating the interplay between stratification and MHD effects.

Rotation effects may also be considered, and, in particular, an analogue of the quasi-geostrophic (QG) equations is of particular interest due to its simplicity, and some provisional work has been performed. Taking a different route to Gilman (1967a,b,c), who considered taking an analogue of the QG limit of the continuously stratified MHD equations before taking layers, we started from the layered shallow-water models under the frozen-in approximation, took an analogue of the QG limit, and we derived the same set of equations given in Gilman (1967a,b,c). The difference is

that, done this way, it was clear why there is no explicit coupling of the magnetic field in the different layers in the momentum or induction equation. The initial idea of using this magneto-quasi-geostrophic model (mQG perhaps; see also Umurhan, 2013, on arXiV) was to investigate the jet formation problem in MHD (e.g., Tobias *et al.*, 2007); this is however beyond the scope of this study and will be developed elsewhere.

The shear flow problem in the spherical case has been considered already, as mentioned in Chapter 1 (Dikpati & Gilman, 2001; Rempel & Dikpati, 2003; Dikpati *et al.*, 2003; Dikpati & Gilman, 2005). These works are linear studies, and it would be interesting to consider the nonlinear behaviour, bearing in mind the discussion we presented with regards to the form of the dissipation employed.

Going beyond shallow-water, the shear flow problem with MHD effects in the Kelvin–Helmholtz problem, i.e. vertical shear with vertical stratification (and possibly with a third spatial dimension) would merit an investigation. This would then introduce the other well-known hydrodynamic secondary instabilities into play, alongside the expected disruption arising from MHD effects. These would presumably contribute to the breakdown of coherent structures into turbulence, with implications for turbulent mixing, for example. This is an important area of study as it would have implications for the mixing properties in stratified MHD systems, such as the tachocline.

It is hoped that this study contributes to the larger study of MHD by investigating in some detail the dynamics in a simpler setting, highlighting some fundamental features that should be present even when other physical effects might be in play. Shear instabilities play an important role in the transition into turbulence, and this investigation was kept sufficiently theoretical to provide a fundamental understanding to the underlying dynamics that forms part of this larger physical problem.

Bibliography

ACHESON, D. J. 1976. On over-reflexion. *J. Fluid Mech.*, **77**, 433–472.

ARNOL'D, V. I. 1965a. Conditions for nonlinear stability of stationary plane curvilinear flows of an ideal fluid. *Soviet Math.*, **6**, 773–777.

ARNOL'D, V. I. 1965b. Variational principle for three-dimensional steady-state flows of an ideal fluid. *J. Appl. Math. Mech.*, **29**, 1002–1008.

ARNOL'D, V. I. 1966a. On an *a priori* estimate in the theory of hydrodynamical stability. *Amer. Math. Soc. Transl. Ser.*, **79**, 267–269.

ARNOL'D, V. I. 1966b. Sur la géometrie differéntielle des groups de Lie de dimension infinie et ses applications à l'hydrodynamique des fluids parfaits. *Ann. Inst. Fourier 16*, **1**, 316–361.

BAINES, P. G., & MITSUDERA, H. 1994. On the mechanism of shear instabilities. *J. Fluid Mech.*, **276**, 327–342.

BAKAS, N. A., & FARRELL, B. F. 2009a. Gravity waves in a horizontal shear flow. Part I: Growth mechanisms in the absence of potential vorticity perturbations. *J. Phys. Oceanogr.*, **39**, 481–496.

BAKAS, N. A., & FARRELL, B. F. 2009b. Gravity waves in a horizontal shear flow. Part II: Interaction between gravity waves and potential vorticity perturbations. *J. Phys. Oceanogr.*, **39**, 497–511.

BAKAS, N. A., & FARRELL, B. F. 2010. The role of nonnormality in overreflection theory. *J. Atmos. Sci.*, **67**, 2547–2558.

BALMFORTH, N. J. 1999. Shear instability in shallow water. *J. Fluid Mech.*, **387**, 97–127.

BARSTON, E. M. 1980. Circle theorems for inviscid steady flows. *Int. J. Engng Sci.*, **18**, 477–489.

BATY, H., & KEPPENS, R. 2006. Kelvin-Helmholtz disruptions in extended magnetized jet flows. *Astron. Astrophys.*, **447**, 9–22.

BATY, H., KEPPENS, R., & COMTE, P. 2003. The two-dimensional magnetohydrodynamic Kelvin-Helmholtz instability: Compressibility and large-scale coalescence effects. *Phys. of Plasmas*, **10**, 4661–4674.

BAYLY, B. J. 1986. Three-dimensional instability of elliptical flow. *Phys. Rev. Lett.*, **57**, 2160–2163.

BAZDENKOV, S. V., & POGUTSE, O. P. 1983. Supersonic stabilization of a tangential shear in a thin atmosphere. *JETP Lett.*, **37**, 375–377.

BENILOV, E. S., & LAPIN, V. N. 2013. On resonant over-reflection of waves by jets. *Geophys. Astrophys. Fluid Dyn.*, **107**, 304–327.

BETCHOV, R., & CRIMINALE, W. O. 1967. Stability of parallel flows. *Applied Math. and Mech.*, **10**.

BISKAMP, D. 2000. *Magnetic reconnection in plasmas*. Cambridge University Press.

BISKAMP, D. 2003. *Magnetohydrodynamic turbulence*. Cambridge University Press.

BISKAMP, D., & WELTER, H. 1989. Dynamics of decaying two-dimensional magnetohydrodynamic turbulence. *Phys. Fluids B*, **1**, 1964–1979.

BISKAMP, D., SCHWARZ, E., & ZEILER, A. 1998. Instability of a magnetized plasma jet. *Phys. Plasmas*, **5**, 2485–2488.

BLUMEN, W. 1970. Shear layer instability of an inviscid compressible fluid. *J. Fluid Mech.*, **40**, 769–781.

BLUMEN, W. 1971. On the stability of plane flow with horizontal shear to three-dimensional nondivergent disturbances. *Geophys. Astrophys. Fluid Dyn.*, **2**, 189–200.

BLUMEN, W., DRAZIN, P. G., & BILLINGS, D. F. 1975. Shear layer instability of an inviscid compressible fluid. Part 2. *J. Fluid Mech.*, **71**, 305–316.

BOYD, J. P. 2001. *Chebyshev and Fourier Spectral Methods*. Dover, New York.

BRETHERTON, F. P. 1966a. Baroclinic instability and the short wavelength cut-off in terms of potential vorticity. *Q. J. Roy. Met. Soc.*, **92**, 335–345.

BRETHERTON, F. P. 1966b. Critical layer instability in baroclinic flows. *Q. J. Roy. Met. Soc.*, **92**, 325–334.

BÜHLER, O. 1998. A shallow-water model that prevents nonlinear steepening of gravity waves. *J. Atmos. Sci.*, **55**, 2884–2891.

BÜHLER, O. 2000. On the vorticity transport due to dissipating or breaking waves in shallow-water flow. *J. Fluid Mech.*, **407**, 235–263.

BÜHLER, O. 2009. *Waves and mean flows*. Cambridge University Press.

BÜHLER, O., & MCINTYRE, M. E. 1998. On non-dissipative wave-mean interactions in the atmopsheres or oceans. *J. Fluid Mech.*, **354**, 301–343.

BÜHLER, O., & MCINTYRE, M. E. 2003. Remote recoil: a new wave-mean interaction effect. *J. Fluid Mech.*, **492**, 207–230.

CANUTO, C., HUSSAINI, M. Y., QUARTERONI, A., & ZANG, T. A. 1993. *Spectral Methods In Fluid Dynamics*. Springer.

CARPENTER, J. R., TEDFORD, E. W., HEIFETZ, E., & LAWRENCE, G. A. 2012. Instability in stratified shear flow: Review of a physical interpretation based on interacting waves. *Appl. Mech. Rev.*, **64**, 061001.

CAULFIELD, C. P., & KERSWELL, R. R. 2000. The nonlinear development of three-dimensional disturbances at hyperbolic stagnations points: A model of the braid region in mixing layers. *Phys. Fluids*, **12**, 1032–1043.

CAULFIELD, C. P., & PELTIER, W. R. 2000. The anatomy of the mixing transition in homogeneous and stratified free shear layers. *J. Fluid Mech.*, **413**, 1–47.

CHANDRASEKHAR, S. 1981. *Hydrodynamic and Hydromagnetic Stability*. Dover edn. Dover Publications Inc.

CHEN, Q., OTTO, A., & LEE, L. C. 1997. Tearing instability, Kelvin-Helmholtz instability, and magnetic reconnection. *J. Geophys. Res.*, **102**, 151–161.

CHIMONAS, G. 1970. The extension of the Miles-Howard theorem to compressible fluids. *J. Fluid Mech.*, **43**, 833–836.

CHO, J. Y.-K., & POLVANI, L. M. 1996a. The formation of jets and vortices from freely-evolving shallow water turbulence on the surface of a sphere. *Phys. Fluids*, **8**, 1531–1552.

CHO, J. Y.-K., & POLVANI, L. M. 1996b. The morphogenesis of bands and zonal winds in the atmospheres on the giant outer planets. *Science*, **273**, 335–337.

CHRISTENSEN-DALSGAARD, J., & THOMPSON, M. J. 2007. Observational results and issues concerning the tachocline. *In:* HUGHES, D. W., ROSNER, R., & WEISS, N. O. (eds), *The Solar Tachocline*. Cambridge University Press.

CHU, V. H. 2010. Shear instability, wave and turbulence simulations using shallow-water equations. *J. Hydro-environ. Res.*, **3**, 173–178.

CLENSHAW, C. W., & CURTIS, A. R. 1960. A method for numerical integration on an automatic computer. *Numerische Mathematik*, **2**, 197–205.

COLLINGS, I. L., & GRIMSHAW, R. H. J. 1980. The effect of topography on the stability of a barotropic coastal current. *Dyn. Atmos. Ocean.*, **5**, 83–106.

COOLEY, J. W., & TUKEY, J. W. 1965. An algorithm for the machine calculation of complex Fourier series. *Math. Comput.*, **19**, 297–301.

CORCOS, G. M., & SHERMAN, F. S. 1976. Vorticity concentration and the dynamics of unstable free shear layers. *J. Fluid Mech.*, **73**, 241–264.

CORCOS, G. M., & SHERMAN, F. S. 1984. The mixing layer: Deterministic models of a turbulent flow. Part 1. Introduction and the two-dimensional flow. *J. Fluid Mech.*, **139**, 29–65.

CRIMINALE, W. O., JACKSON, T. L., & JOSLIN, R. D. 2003. *Theory and computation in hydrodynamic stability*. Cambridge University Press.

DE STERCK, H. 2001. Hyperbolic theory of the "shallow water" magnetohydrodynamics equations. *Phys. Plasmas*, **8**, 3293–3304.

DELLAR, P. J. 2002. Hamiltonian and symmetric hyperbolic structures of shallow water magnetohydrodynamics. *Phys. Plasmas*, **9**, 1130–1136.

DELLAR, P. J. 2003a. Common Hamiltonian structure of the shallow water equations with horizontal temperature gradients and magnetic fields. *Phys. Fluids*, **15**, 292–297.

DELLAR, P. J. 2003b. Dispersive shallow water magnetohydrodynamics. *Phys. Plasmas*, **10**, 581–590.

DIKPATI, M., & GILMAN, P. A. 2001. Analysis of hydrodynamic stability of solar tachocline latitudinal differential rotation using a shallow-water model. *Astrophys. J.*, **551**, 536–564.

DIKPATI, M., & GILMAN, P. A. 2005. A shallow-water theory for the Sun's active longitudes. *Astrophys. J. Lett.*, **635**, L193–L196.

DIKPATI, M., GILMAN, P. A., & REMPEL, M. 2003. Stability analysis of tachocline latitudinal differential rotation and coexisting toroidal band using a shallow-water model. *Astrophys. J.*, **596**, 680–697.

DIKPATI, M., GILMAN, P. A., CALLY, P. S., & MIESCH, M. S. 2009. Axisymmetric MHD instabilities in solar/stellar tachoclines. *Astrophys. J.*, **692**, 1421–1431.

DRAZIN, P. G., & HOWARD, L. N. 1962. The instability to long waves of unbounded parallel inviscid flow. *J. Fluid Mech.*, **14**, 257–283.

DRAZIN, P. G., & HOWARD, L. N. 1966. Hydrodynamic stability of parallel flow of inviscid fluid. *Advan. Appl. Mech.*, **9**, 1–89.

DRAZIN, P. G., & REID, W. H. 1981. *Hydrodynamic Stability*. 2nd edn. Cambridge University Press.

DRITSCHEL, D. G. 1988. Nonlinear stability bounds for inviscid, two-dimensional, parallel or circular flows with monotonic vorticity, and the analogous three-dimensional quasi-geostrophic flows. *J. Fluid Mech.*, **191**, 575–581.

DRITSCHEL, D. G., & FONTANE, J. 2010. The combined Lagrangian advection method. *J. Comput. Phys.*, **229**, 5408–5417.

DRITSCHEL, D. G., & SCOTT, R. K. 2009. On the simulation of nearly inviscid two-dimensional turbulence. *J. Comput. Phys.*, **228**, 2707–2711.

DRITSCHEL, D. G., & SCOTT, R. K. 2011. Jet sharpening by turbulent mixing. *Phil. Tran. Roy. Soc. A*, **369**, 754–770.

DRITSCHEL, D. G., & TOBIAS, S. M. 2012. Two-dimensional magnetohydrodynamic turbulence in the small magnetic Prandtl number limit. *J. Fluid Mech.*, **703**, 85–98.

DRITSCHEL, D. G., & VANNESTE, J. 2006. The instability of a potential vorticity front. *J. Fluid Mech.*, **561**, 237–254.

DRITSCHEL, D. G., & VIÚDEZ, A. 2007. The persistence of balance in geophysical flows. *J. Fluid Mech.*, **570**, 365–383.

DRITSCHEL, D. G., HAYNES, P. H., JUCKES, M. N., & SHEPHERD, T. G. 1991. The stability of a two-dimensional vorticity filament under uniform strain. *J. Fluid Mech.*, **230**, 647–665.

DRITSCHEL, D. G., POLVANI, L. M., & MOHEBALHOJEH, A. R. 1999. The contour-advective semi-Lagrangian algorithm for the shallow water equations. *Mon. Weather Rev.*, **127**, 1551–1564.

DURRAN, D. R. 2010. *Numerical methods for fluid dynamics*. 2nd edn. Springer.

ELIASSEN, A. 1983. The Charney-Stern theorem on barotropic-baroclinic instability. *Pure Appl. Geophys.*, **121**, 563–572.

FARGE, M., & SADOURNY, R. 1989. Wave-vortex dynamics in rotating shallow water. *J. Fluid. Mech.*, **206**, 433–462.

FARRELL, B. F., & IOANNOU, P. J. 1996a. Generalized stability theory. Part I: Autonomous operators. *J. Atmos. Sci.*, **53**, 2025–2040.

FARRELL, B. F., & IOANNOU, P. J. 1996b. Generalized stability theory. Part II: Non-autonomous operators. *J. Atmos. Sci.*, **53**, 2041–2053.

FORD, R. 1994. The instability of an axisymmetric vortex with monotonic potential vorticity in rotating shallow water. *J. Fluid Mech.*, **280**, 303–334.

FORD, R., MCINTYRE, M. E., & NORTON, W. A. 2000. Balance and the slow quasimanifold: Some explicit results. *J. Atmos. Sci.*, **57**, 1236–1254.

FORNBERG, B. 1998. *A practical guide to pseudospectral methods*. Cambridge University Press.

FRANK, A., JONES, T. W., RYU, D., & GAALAAS, J. B. 1996. The MHD Kelvin-Helmholtz instability: A two-dimensional numerical study. *Astrophys. J.*, **460**, 777–793.

FURTH, H. P., KILLEEN, J., & ROSENBLUTH, M. N. 1963. Finite resistivity instabilities of a sheet pinch. *Phys. Fluids*, **6**, 459–484.

GALLOWAY, D. J., & MOORE, D. R. 1979. Axisymmetric convection in the presence of a magnetic field. *Geophys. Astrophys. Fluid Dyn.*, **12**, 73–105.

GALLOWAY, D. J., PROCTOR, M. R. E., & WEISS, N. O. 1978. Magnetic flux ropes and convection. *J. Fluid Mech.*, **87**, 243–261.

GARAUD, P. 2007. Magnetic confinement of the solar tachocline. *In:* HUGHES, D. W., ROSNER, R., & WEISS, N. O. (eds), *The solar tachocline*. Cambridge University Press.

GEDZELMAN, S. D. 1973. Hydromagnetic stability of parallel flow of an ideal heterogeneous fluid. *J. Fluid Mech.*, **58**, 777–794.

GENT, P. R. 1993. The energetically consistent shallow-water equations. *J. Atmos. Sci.*, **50**, 1323–1325.

GILBERT, A. D., RIEDINGER, X., & THUBURN, J. 2013. Note on the form of the viscous term for two dimensional Navier-Stokes flows. *Submitted to Quart J. Mech. Appl. Math.*

GILL, A. E. 1965. Instabilities of "top-hat" jets and wakes in compressible fluids. *Phys. Fluids*, 1428–1430.

GILL, A. E. 1982. *Atmospheric-Ocean Dynamics*. Academic Press.

GILL, A. E., & DRAZIN, P. G. 1965. Note on instability of compressible jets and wakes to long-wave disturbance. *J. Fluids Mech.*, **22**, 415.

GILMAN, P. A. 1967a. Stability of baroclinic flows in a zonal magnetic field: Part I. *J. Atmos. Sci.*, **24**, 101–118.

GILMAN, P. A. 1967b. Stability of baroclinic flows in a zonal magnetic field: Part II. *J. Atmos. Sci.*, **24**, 119–129.

GILMAN, P. A. 1967c. Stability of baroclinic flows in a zonal magnetic field: Part III. *J. Atmos. Sci.*, **24**, 130–143.

GILMAN, P. A. 2000. Magnetohydrodynamic "shallow water" equations for the solar tachocline. *Astrophys. J.*, **544**, L79–L82.

GILMAN, P. A., & CALLY, P. S. 2007. Global MHD instabilities of the tachocline. *In:* HUGHES, D. W., ROSNER, R., & WEISS, N. O. (eds), *The Solar Tachocline*. Cambridge University Press.

GOUGH, D. O. 2007. An introduction to the solar tachocline. *In:* HUGHES, D. W., ROSNER, R., & WEISS, N. O. (eds), *The Solar Tachocline*. Cambridge University Press.

GOUGH, D. O., & MCINTYRE, M. E. 1998. Inevitability of a magnetic field in the Sun's radiative interior. *Nature*, **394**, 755–757.

GREEN, A. E., & NAGHDI, P. M. 1976. A derivation of equations for wave propagation in water of variable depth. *J. Fluid Mech.*, **78**, 237–246.

GRIFFITHS, R. W., KILLWORTH, P. D., & STERN, M. E. 1982. Ageostrophic instability of ocean currents. *J. Fluid Mech.*, **117**, 343–377.

GRIFFITHS, S. D. 2008. The limiting form of inertial instability in geophysical flows. *J. Fluid Mech.*, **605**, 115–143.

HARNIK, N., & HEIFETZ, E. 2007. Relating overreflection and wave geometry to the counter-propagating Rossby wave perspective: Toward a deeper mechanistic understanding of shear instability. *J. Atmos. Sci.*, **64**, 2238–2261.

HAYASHI, Y.-Y., & YOUNG, W. R. 1987. Stable and unstable shear modes of rotating parallel flows in shallow water. *J. Fluid Mech.*, **184**, 477–504.

HAZEL, P. 1972. Numerical studies of the stability of inviscid stratified shear flows. *J. Fluid Mech.*, **51**, 39–61.

HEIFETZ, E., & METHVEN, J. 2005. Relating optimal growth to counter-propagating Rossby Waves in shear instability. *Phys. Fluids*, **17**, 064107.

HEIFETZ, E., BISHOP, C. H., & ALPERT, P. 1999. Counter-propagating Rossby waves in the barotropic Rayleigh model of shear instability. *Q. J. Roy. Met. Soc.*, **125**, 2835–2853.

HEIFETZ, E., BISHOP, C. H., HOSKINS, B. J., & METHVEN, J. 2004. The counter-propagating Rossby-wave perspective on baroclinic instability. I: Mathematical basis. *Q. J. Roy. Met. Soc.*, **130**, 211–231.

HEIFETZ, E., REUVENI, Y., GELFGAT, A., KIT, E., & METHVEN, J. 2006. The counterpropagating Rossby wave perspective on Kelvin Helmholtz instability as a limiting case of a Rayleigh shear layer with zero width. *Phys. Fluids*, **18**, 018101.

HEIFETZ, E., HARNIK, N., & TAMARIN, T. 2009. Canonical Hamiltonian representation of pseudoenergy in shear flows using counter-propagating Rossby Waves. *Q. J. Roy. Met. Soc.*, **135**, 2161–2167.

HENG, K., & SPITKOVSKY, A. 2009. Magnetohydrodynamic shallow water waves: Linear analysis. *Astrophys. J.*, **703**, 1819–1831.

HO, C-. M., & HUERRE, P. 1984. Perturbed free shear layers. *Annu. Rev. Fluid Mech.*, **16**, 365–424.

HØILAND, E. 1953. On two-dimensional perturbation of linear flow. *Geopfys. Publ.*, **18**, 333–342.

HOLM, D.D., MARSDEN, J.E., RATIU, T.S., & WEINSTEIN, A. 1985. Nonlinear stability of fluid and plasma equilibria. *Phys. Rep.*, **123**, 1–116.

HOSKINS, B. J., MCINTYRE, M. E., & ROBERTSON, A. W. 1985. On the use and significance of isentropic potential vorticity maps. *Q. J. Roy. Met. Soc.*, **111**, 877–946.

HOWARD, L. N. 1961. Note on a paper of John W. Miles. *J. Fluid Mech.*, **10**, 509–512.

HOWARD, L. N. 1963. Neutral curves and stability boundaries in stratified flow. *J. Fluid Mech.*, **16**, 333–342.

HUGHES, D. W., & TOBIAS, S. M. 2001. On the instability of magnetohydrodynamic shear flows. *Proc. R. Soc. Lond. A*, **457**, 1365–1384.

HUGHES, D. W., ROSNER, R., & WEISS, N. O. 2007. *The Solar Tachocline*. Cambridge University Press.

JEONG, H., RYU, D., JONES, T. W., , & FRANK, A. 2000. The magnetohydrodynamic Kelvin-Helmholtz instability. III. The role of sheared magnetic field in planar flows. *Astrophys. J.*, **529**, 536–547.

JIMENEZ, J. 1987. On the linear stability of the inviscid Kármán vortex street. *J. Fluid Mech.*, **178**, 177–194.

JIMENEZ, J. 1988. Linear stability of a non-asymmetric, inviscid, Kármán street of small uniform vortices. *J. Fluid Mech.*, **189**, 337–348.

JONES, T. W., GAALAAS, J. B., RYU, D., & FRANK, A. 1997. The MHD Kelvin-Helmholtz instability. II. The role of weak and oblique fields in planar flows. *Astrophys. J.*, **482**, 230–244.

KELLY, R. E. 1967. On the stability of an invsicid shear layer which is periodic in space and time. *J. Fluid Mech.*, **27**, 657–689.

KEPPENS, R., TOTH, G., WESTERMANN, R. H. J., & GOEDBLOED, J. P. 1999. Growth and saturation of the Kelvin-Helmholtz instability with parallel and anti-parallel magnetic fields. *J. Plasma Phys.*, **61**, 1–19.

KERSWELL, R. R. 2002. Elliptical instability. *Annu. Rev. Fluid Mech.*, **34**, 83–113.

KIDA, S. 1982. Stabilizing effects of finite core on Kármán vortex street. *J. Fluid Mech.*, **122**, 487–504.

KLAASSEN, G. P., & PELTIER, W. R. 1985a. Evolution of finite amplitude Kelvin-Helmholtz billows in two spatial dimensions. *J. Atmos. Sci.*, **42**, 1321–1339.

KLAASSEN, G. P., & PELTIER, W. R. 1985b. The onset of turbulence in finite-amplitude Kelvin-Helmholtz billows. *J. Fluid Mech.*, **155**, 1–35.

KLAASSEN, G. P., & PELTIER, W. R. 1989. The role of transverse secondary instabilities in the evolution of free shear layers. *J. Fluid Mech.*, **202**, 367–402.

KLAASSEN, G. P., & PELTIER, W. R. 1991. The influence of stratification on secondary instability in free shear layers. *J. Fluid Mech.*, **227**, 71–106.

KOCHAR, G. T., & JAIN, R. K. 1979a. Note on Howard's semicircle theorem. *J. Fluid Mech.*, **91**, 489–491.

KOCHAR, G. T., & JAIN, R. K. 1979b. On Howard's semi-circle theorem in hydromagnetics. *J. Phys. Soc. Jpn.*, **47**, 654–658.

LAHAYE, N., & ZEITLIN, V. 2012. Decaying vortex and wave turbulence in rotating shallow water model, as follows from high-resolution direct numerical simulations. *Phys. Fluids*, **24**, 115106.

LAMB, H. 1932. *Hydrodynamics*. 6th edn. Cambridge University Press.

LILLO, R., MININNI, P. D., & GÓMEZ, D. O. 2005. Toward a dynamo model for the solar tachocline. *Physica A*, **349**, 667–674.

LIN, C. C. 1955. *The theory of hydrodynamics stability*. Cambridge University Press.

LINDZEN, R. S. 1988. Instability of plane parallel shear flow (Towards a mechanistic picture of how it works). *PAGEOPH*, **16**, 103–121.

LINDZEN, R. S., & TUNG, K. K. 1978. Wave overreflection and shear instability. *J. Atmos. Sci.*, **35**, 1626–1632.

LIPPS, F. B. 1962. The barotropic stability of the mean winds in the atmosphere. *J. Fluid Mech.*, **12**, 397–407.

LIVERMORE, P. W. 2007. An implementation of the exponential time differencing scheme to the magnetohydrodynamic equations in a spherical shell. *J. Comput. Phys.*, **220**, 824–838.

MALAGOLI, A., BODO, G., & ROSNER, R. 1996. On the nonlinear evolution of magnetohydrodynamic Kelvin-Helmholtz instabilities. *Astrophys. J.*, **456**, 708–716.

MASHAYEK, A., & PELTIER, W. R. 2012a. The 'zoo' of secondary instabilities precursory to stratified shear flow transition. Part 1 Shear aligned convection, pairing, and braid instabilities. *J. Fluid Mech*, **708**, 5–44.

MASHAYEK, A., & PELTIER, W. R. 2012b. The 'zoo' of secondary instabilities precursory to stratified shear flow transition. Part 2 The influence of stratification. *J. Fluid Mech*, **708**, 45–70.

MCINTYRE, M. E., & SHEPHERD, T. G. 1987. An exact local conservation theorem for finite-amplitude disturbances to non-parallel shear flows, with remarks on Hamiltonian structure and on Arnol'd's stability theorems. *J. Fluid Mech.*, **181**, 527–565.

MCINTYRE, M. E., & WEISSMAN, M. A. 1978. On radiating instabilities and resonant overreflection. *J. Atmos. Sci.*, **35**, 1190–1196.

METCALFE, R. W., ORSZAG, S. A., BRACHET, M. E., & RILEY, J. J. 1987. Secondary instability of a temporally growing mixing layer. *J. Fluid Mech.*, **184**, 207–243.

MICHAEL, D. H. 1953. Stability of a combined current and vortex sheet in a perfectly conducting fluid. *Proc. Camb. Phil. Soc.*, **51**, 528–532.

MICHALKE, A. 1964. On the inviscid instability of the hyperbolic-tangent velocity profile. *J. Fluid Mech.*, **19**, 543–556.

MILES, J. W. 1958. On the disturbed motion of a vortex sheet. *J. Fluid Mech.*, **4**, 538–552.

MIN, K. W. 1997a. Numerical simulation of the individual mode evolution in a slab jet. *Mon. Not. R. Astron. Soc.*, **285**, 191–200.

MIN, K. W. 1997b. Simulation of the Kelvin-Helmholtz instability in the magnetized jet. *Astrophys. J.*, **482**, 733–746.

MIURA, A. 1982. Nonlinear evolution of the magnetohydrodynamic Kelvin-Helmholtz instability. *Phys. Rev. Lett.*, **49**, 779–782.

MIURA, A., & SATO, T. 1978. Theory of vortex nutation and amplitude oscillation in an inviscid shear instability. *J. Fluid Mech.*, **86**, 33–47.

MOHEBALHOJEH, A. R., & DRITSCHEL, D. G. 2000. On the representation of gravity waves in numerical models of the shallow water equations. *Q. J. Roy. Met. Soc.*, **126**, 669–688.

MOHEBALHOJEH, A. R., & DRITSCHEL, D. G. 2001. Hierarchies of balance conditions for the f-plane shallow water equations. *J. Atmos. Sci.*, **58**, 2411–2426.

MOHEBALHOJEH, A. R., & DRITSCHEL, D. G. 2009. The diabatic contour-advective semi-Lagrangian algorithms for the spherical shallow water equations. *Mon. Weather Rev.*, **137**, 2979–2994.

NYCANDER, J. 2003. Stable vortices as maximum or minimum energy flows. *In:* O. U. VELASCO FUENTES, J. SHEINBAUM, J. OCHOA (ed), *Nonlinear Processes in Geophysical Fluid Dynamics*. Kluwer.

OCHOA, J., SHEINBAUM, J., & JIMÉNEZ, A. 2011. Lateral friction in reduced-gravity models: Parametrizations consistent with energy dissipation and conservation of angular momenum. *J. Phys. Oceanogr.*, **41**, 1894–1901.

OFMAN, L., MORRISON, P. J., & STEINOLFSON, R. S. 1993. Nonlinear evolution of resistive tearing mode instability with shear flow and viscosity. *Phys. Fluids B*, **2**, 376–387.

ORSZAG, S. A. 1971. On the elimination of aliasing in finite-difference schemes by filtering high-wavenumber components. *J. Atmos. Sci.*, **28**, 1074.

OTTO, A., & FAIRFIELD, D. H. 2000. Kelvin-Helmholtz instability at the magnetotail boundary: MHD simulation and comparison with geotail observations. *J. Geophys. Res.*, **105**, 21175–21190.

PALDOR, N. 1983. Linear stability and stable modes of geostrophic fronts. *Geophys. Astrophys. Fluid Dyn.*, **24**, 299–326.

PALOTTI, M. L., HEITSCH, F., ZWEIBEL, E. G., & HUANG, Y. M. 2008. Evolution of unmagnetized and magnetized shear layers. *Astrophys. J.*, **678**, 234–244.

PEARCE, J. D., & ESLER, J. G. 2010. A pseudo-spectral algorithm and test cases for the numerical solution of the two-dimensional rotating Green-–Naghdi shallow water equations. *J. Comput. Phys.*, **229**, 7594–7608.

PEDLOSKY, J. 1964. The stability of currents in the atmosphere and the ocean: Part I. *J. Atmos. Sci.*, **21**, 201–219.

PEDLOSKY, J. 1987. *Geophysical Fluid Dynamics*. 2nd edn. Springer-Verlag.

PELTIER, W. R., & CAULFIELD, C. P. 2003. Mixing efficiency in stratified shear flows. *Annu. Rev. Fluid Mech.*, **35**, 135–167.

PEYRET, R. 2002. *Spectral methods for incompressible viscous flow*. Springer AMS.

PIERREHUMBERT, R. T. 1986. Universal short-wave instability of two-dimensional eddies in an inviscid fluid. *Phys. Rev. Lett.*, **57**, 2157–2159.

PLOTKA, H., & DRITSCHEL, D. G. 2012. Quasi-geostrophic shallow-water vortex-patch equilibria and their stability. *Geophys. Astrophys. Fluid Dyn.*, **106**, 574–595.

POLVANI, L. M., MCWILLIAMS, J. C., SPALL, M., & FORD, R. 1994. The coherent structures of shallow water turbulence: Deformation radius effects, cyclone/anticyclone asymmetry and gravity wave generation. *Chaos*, **4**, 177–186.

POULIN, F. J., & FLIERL, G. R. 2003. The nonlinear evolution of barotropically unstable jets. *J. Phys. Oceanogr.*, **33**, 2173–2192.

PRIEST, E. R., & FORBES, T. G. 2000. *Magnetic reconnection: MHD theory and applications*. Cambridge University Press.

REMPEL, M., & DIKPATI, M. 2003. Storage and equilibrium of toroidal magnetic fields in the solar tachocline: A comparison between MHD shallow-water and full MHD approaches. *Astrophys. J.*, **584**, 524–527.

RIPA, P. 1982. Nonlinear wave-wave interactions in a one-layer reduced-gravity model on the equatorial β plane. *J. Phys. Oceanogr.*, **12**, 97–111.

RIPA, P. 1983. General stability conditions for zonal flows in a one-layer model on the β-plane or the sphere. *J. Fluid Mech.*, **126**, 463–489.

RIPA, P. 1987. On the stability of elliptical vortex solution of the shallow-water equations. *J. Fluid Mech.*, **183**, 343–363.

RIPA, P. 1991. General stability conditions for a multi-layer model. *J. Fluids Mech.*, **222**, 119–137.

ROSSMANITH, J. A. 2002. *A wave propagation method with constrained transport for ideal and shallow water magnetohydrodynamics*. Ph.D. thesis, University of Washington.

SADOURNY, R. 1975. The dynamics of finite-difference models of the shallow-water equations. *J. Atmos. Sci.*, **32**, 680–689.

SALMON, R. 1998. *Lectures on Geophysical Fluid Dynamics*. Oxford University Press.

SALMON, R. 2009. A shallow water model conserving energy and potential enstrophy in the presence of boundaries. *J. Mar. Res.*, **67**, 779–814.

SATOMURA, T. 1981. An investigation of shear instability in a shallow water. *J. Met. Soc. Japan*, **59**, 148–170.

SCHECTER, D. A., BOYD, J. F., & GILMAN, P. A. 2001. "Shallow-water" magnetohydrodynamic waves in the Solar tachocline. *Astrophys. J.*, **551**, L185–L188.

SCHMID, P. J., & HENNINGSON, D. S. 2001. *Stability and Transition In Shear Flows*. Applied Mathematical Sciences, vol. 142. Springer.

SCOTT, R. K., & POLVANI, L. M. 2008. Equatorial superrotation in shallow atmospheres. *Geophys. Res. Lett.*, **35**, L24202.

SHEPHERD, T. G. 1990. Symmetries, conservation laws, and Hamiltonian structure in geophysical fluid dynamics. *Adv. Geophys.*, 287–338.

SHEPHERD, T. G. 1992. Arnold stability applied to fluid flow: Successes and failures. *In:* CARNEVALE, G.F., & R.T. PIERREHUMBERT, EDS. (eds), *Nonlinear Phenomena In Atmospheric and Oceanic Sciences*. Springer-Verlag.

SHEPHERD, T. G. 2003. Ripa's theorem and its relatives. *In:* O. U. VELASCO FUENTES, J. SHEINBAUM, J. OCHOA (ed), *Nonlinear Processes in Geophysical Fluid Dynamics*. Kluwer.

SHIVAMOGGI, B. K., & DEBNATH, L. 1987. Stability of magnetohydrodynamic stratified shear flows. *Acta Mech.*, **68**, 33–42.

SHOWMAN, A. P. 2007. Numerical simulations of forced shallow-water turbulence: Effects of moist convection on the large-scale on circulation of Jupiter and Saturn. *J. Atmos. Sci.*, **64**, 3132–3157.

SHOWMAN, A. P., & POLVANI, L. M. 2011. Equatorial superrotation on tidally locked exoplanets. *Astrophys. J.*, **738**, 71–94.

SMYTH, W. D., & MOUM, J. N. 2012. Ocean mixing by Kelvin-Helmholtz instability. *Oceanography*, **25**, 140–149.

SPIEGEL, E. A., & ZAHN, J. P. 1992. The Solar tachocline. *Astron. Astrophys.*, **265**, 106–114.

STAQUET, C. 1995. Two-dimensional secondary instabilities in a strongly stratified shear layer. *J. Fluid Mech.*, **296**, 73–126.

STAQUET, C. 2000. Mixing in a stably stratified shear layer: Two- and three-dimensional numerical experiments. *Fluid Dyn. Res.*, **27**, 367–404.

STAQUET, C., & SOMMERIA, J. 2002. Internal gravity waves: From instabilities to turbulence. *Annu. Rev. Fluid Mech.*, **34**, 559–593.

STEGNER, A., & DRITSCHEL, D. G. 2000. A numerical investigation of the stability of isolated vortices beyond the quasi-geostrophic regime. *J. Phys. Oceanogr.*, **30**, 2562–2573.

STUART, J. T. 1967. On finite amplitude oscillations in laminar mixing layers. *J. Fluid Mech.*, **29**, 417–440.

SUTHERLAND, B. R., & PELTIER, W. R. 1992. The stability of stratified jets. *Geophys. Astrophys. Fluid Dyn.*, **66**, 101–131.

SUTHERLAND, B. R., & PELTIER, W. R. 1994. Turbulence transition and internal wave generation in density stratified jets. *Phys. Fluids*, **6**, 1267–1284.

SUTHERLAND, B. R., CAULFIELD, C. P., & PELTIER, W. R. 1994. Internal gravity wave generation and hydrodynamic instability. *J. Atmos. Sci.*, **51**, 3261–3280.

TAKEHIRO, S. I., & HAYASHI, Y. Y. 1992. Over-reflection and shear instability in a shallow-water model. *J. Fluid Mech.*, **236**, 259–279.

TAYLOR, G. I. 1915. Eddy motion in the atmosphere. *Phil. Trans. Roy. Soc. Lond. A*, **115**, 1–26.

THUAL, O. 1986. *Transition vers la turbulence dans des systeèmes dynamique apparentés á la convection*. Ph.D. thesis, Univresité de Nice-Sophia Antipolis.

THUBURN, J., & HAYNES, P. H. 1996. Bounds on the growth rate and phase velocity of instabilities in non-divergent barotropic flow on a sphere: A semicircle theorem. *Q. J. Roy. Met. Soc.*, **122**, 779–787.

TOBIAS, S. M., & WEISS, N. O. 2007. The solar dynamo and the tachocline. *In:* HUGHES, D. W., ROSNER, R., & WEISS, N. O. (eds), *The solar tachocline*. Cambridge University Press.

TOBIAS, S. M., DIAMOND, P. H., & HUGHES, D. W. 2007. β-plane magnetohydrodynamic turbulence in the Solar tachocline. *Astrophys. J.*, **667**, L113–L116.

TORO, E. F. 2001. *Shock-Capturing Methods for Free-Surface Shallow Flows*. Wiley.

TREFETHEN, L. N. 2000. *Spectral Methods in MATLAB*. SIAM.

VALLIS, G. K. 2006. *Atmospheric and Oceanic Fluid Dynamics*. Cambridge University Press.

VLADIMIROV, V. A., & MOFFATT, H. K. 1995. On general transformations and variational principles for the magnetohydrodynamics of ideal fluids. Part 1. Fundamental principles. *J. Fluid Mech.*, **283**, 125–139.

VLADIMIROV, V. A., MOFFATT, H. K., & ILIN, K. I. 1996. On general transformations and variational principles for the magnetohydrodynamics of ideal fluids. Part 2. Stability criteria for two-dimensional flows. *J. Fluid Mech.*, **329**, 187–205.

WALEFFE, F. 1990. On the three-dimensional instability of strained vortices. *Phys. Fluids A*, **2**, 76–80.

WATSON, M. 1981. Shear instability of differential rotation in stars. *Geophys. Astrophys. Fluid Dyn.*, **16**, 285–298.

WAUGH, D. W., & DRITSCHEL, D. G. 1991. The stability of filamentary vorticity in two-dimensional geophysical vortex-dynamics models. *J. Fluid Mech.*, **231**, 575–598.

WEISS, N. O. 1966. The expulsion of magnetic flux by eddies. *Proc. Roy. Soc. Lond. A*, **293**, 310–328.

WOOD, T., & MCINTYRE, M. E. 2011. Polar confinement of the Sun's interior magnetic field by laminar magnetostrophic flow. *J. Fluid Mech.*, **677**, 445–482.

WOOD, T., MCCASLIN, J., & GARAUD, P. 2011. The Sun's meridional circulation and interior magnetic field. *Astrophys. J.*, **738**, 47.

YOUNG, W. R. 1986. Elliptical vortices in shallow water. *J. Fluid Mech.*, **171**, 101–119.

ZABUSKY, N. J., & DEEM, G. S. 1971. Dynamical evolution of two-dimensional unstable shear flows. *J. Fluid Mech.*, **47**, 353–379.

ZAQARASHIVILI, T. V., OLIVER, R., BALLESTER, J. L., & SHERGELASHVILI, B. M. 2008. Rossby waves in "shallow water" magnetohydrodynamics. *A. & A.*, **470**, 815–820.

ZAQARASHIVILI, T. V., CARBONELL, M., OLIVER, R., & BALLESTER, J. L. 2010. Magnetic Rossby waves in the solar tachocline and Rieger-type periodicities. *Astrophys. J.*, **709**, 749–758.

ZEL'DOVICH, YA. B. 1957. The mangetic field in the two-dimensional motion of a conducting turbulent fluid. *Sov. Physics JETP*, **4**, 460–462.